

EXCITON AND CARRIER DYNAMICS IN QUANTUM DOT ASSEMBLIES AND
TWO-DIMENSIONAL PEROVSKITES

Daniel B. Straus

A DISSERTATION

in

Chemistry

Presented to the Faculties of the University of Pennsylvania

in

Partial Fulfillment of the Requirements for the

Degree of Doctor of Philosophy

2018

Supervisor of Dissertation

Cherie R. Kagan

Steven J. Angello Professor of Electrical and Systems Engineering, Materials Science
and Engineering, and Chemistry

Graduate Group Chairperson

David W. Christianson

Roy and Diana Vagelos Professor of Chemistry and Chemical Biology

Dissertation Committee:

Christopher B. Murray, Richard Perry University Professor

Joseph E. Subotnik, Professor of Chemistry

Zahra Fakhraai, Associate Professor of Chemistry

Dedication

To Lizzy

Acknowledgments

Completing my Ph.D. would not have been possible without the support of many people who all share in my accomplishments.

Most importantly, I would like to thank my wife Tanya for her endless supply of kindness, guidance, love, and especially encouragement during difficult times throughout my doctoral studies. Thank you to Lizzy for being such a great daughter and a source of happiness for me, and especially for understanding that I couldn't play while writing this dissertation. Thank you to the rest of my family for your support.

Cherie, I could not have been anywhere near as successful without your mentorship, both in experimental and analytical skills as well as career guidance.

Thank you to my dissertation committee for your time, suggestions, and guidance.

Restoring the lab so quickly after the fire would not have been possible without Scott Stinner and everyone in Engineering Operations, and without them, this dissertation would have taken many additional months to complete.

Thank you to Harold "Buddy" Borders for helping out with all of our machining needs, and I always appreciate the pleasant conversation.

I thank the National Science Foundation for awarding me a Graduate Research Fellowship, especially because external funding allowed me to pursue the otherwise unfunded projects in Part II. I also thank the Department of Energy for funding the projects in Part I including the construction of the time-resolved microwave

conductivity apparatus described in Chapter 2.

Lastly, I would like to acknowledge the contributions of my colleagues and collaborators in the Kagan, Murray, Kikkawa, Rappe, and Subotnik groups at Penn, the Penn Chemistry crystallographers, and the Owen and Roy groups at Columbia. A special thanks to Ed Goodwin, Leo Zhao, Han Wang, Scott Stinner, S. J. Oh, Yuming Lai, Natasha Iotov, Ben Diroll, Ashley Gaulding, Sebastian Hurtado-Parra, Julian Gebhardt, Tavi Semonin, and Giselle Elbaz for collaborating on experiments and including me on publications.

ABSTRACT

EXCITON AND CARRIER DYNAMICS IN QUANTUM DOT ASSEMBLIES AND
TWO-DIMENSIONAL PEROVSKITES

Daniel B. Straus

Cherie R. Kagan

Reducing the size of a semiconductor to the natural length scale of carriers and excitons provides a unique opportunity to tailor the semiconductor's electronic structure and optical properties through quantum and dielectric confinement effects. In this dissertation, we analyze the dynamics of free carriers and excitons in two emerging classes of semiconductors: zero-dimensional coupled quantum dot (QD) assemblies and two-dimensional organic-inorganic hybrid perovskites (2DHPs).

QDs are prized for their size-dependent band gaps and can be assembled with surface ligand tunable inter-QD coupling. However, control over carrier type, concentration, mobility, and lifetime remains an important challenge to their device applications. Post-synthesis modification of QD assemblies provides a route to couple QDs as well as dope and passivate QD surfaces. In PbSe QD assemblies, we modify the Pb:Se ratio to change the dominant carrier type and doping level, and in CdSe QD assemblies, we modulate the conductivity through indium doping. To study the optoelectronic properties of these and other QD assemblies, we built a time-resolved microwave conductivity (TRMC) apparatus to contactlessly probe mobility and lifetime. We correlate changes in carrier density and conductivity from surface modification with the mobility and lifetime measured in TRMC and with field-effect transistor mobilities. We show that the carrier lifetime increases with doping as the Fermi level moves near the band edges and electronically passivates trap states.

2DHPs consist of metal-halide monolayers separated by organoammonium cations and resemble interfacial defect-free quantum well superlattices. Strong confinement of carriers in the inorganic monolayers results in a large exciton binding energy, allowing exciton and carrier dynamics to be probed optically. At temperatures <75 K, we find regularly spaced fine structure resonances in excitonic absorption and photoluminescence spectra of the 2DHP phenethylammonium lead iodide, which we hypothesize are caused by excitons coupling to phonons in the organic framework. We also observe higher energy hot photoluminescence resonances which result from competition between vibrational relaxation and radiative recombination. By synthesizing and characterizing a family of phenethylammonium lead iodide derivatives with single atom substitutions on the phenyl group, we tailor the packing of the organic framework, the energetic disorder, and the rate of photoluminescence.

Contents

Preface	xii
I Photochemistry of Quantum Dot Thin Films	1
1 Introduction to Quantum Dots	2
1.1 Quantum Confinement in Zero Dimensions	2
1.2 Deposition and Ligand Exchange	4
1.3 References	6
2 Theory of Time-Resolved Microwave Conductivity	9
2.1 Introduction	9
2.2 Theory	10
2.2.1 Microwave Absorption in Semiconductors	10
2.2.2 Waveguide Modes	13
2.2.3 Resonant Cavity	14
2.2.4 Complex Propagation Constant	16
2.3 Experimental	17
2.4 The Sensitivity Constant	19
2.4.1 The Analytical Method	19

2.4.2	The Computational Method	23
2.5	Other Types of Samples	26
2.6	References	29
3	The Effects of Inorganic Surface Treatments on Photogenerated Carrier Mobility and Lifetime in PbSe Quantum Dot Thin Films	31
3.1	Introduction	32
3.2	Experimental Methods	35
3.2.1	Synthesis	35
3.2.2	PbSe QD Thin Film Deposition	36
3.2.3	Structural, Optical, and Electrical Characterization	37
3.2.4	Flash-Photolysis Time-Resolved Microwave Conductivity	38
3.3	Results and Discussion	39
3.3.1	Structural and Optical Characterization of PbSe QD Thin Films	40
3.3.2	Electrical Transport Measurements in PbSe QD Field-Effect Transistors	43
3.3.3	Flash-Photolysis Time-Resolved Microwave Conductivity	44
3.4	Conclusion	52
3.5	References	52
4	Increased Carrier Mobility and Lifetime in CdSe Quantum Dot Thin Films Through Surface Trap Passivation and Doping	58
4.1	Introduction	59
4.2	Experimental Methods	60
4.2.1	Synthetic Methods	60
4.2.2	Time-Resolved Microwave Conductivity	62
4.3	Results and Discussion	64

4.4	Conclusion	73
4.5	References	74
II Optical Spectroscopy of Two-Dimensional Hybrid Perovskites		78
5	Introduction to Two-Dimensional Hybrid Perovskites	79
5.1	Introduction	79
5.2	Quantum and Dielectric Confinement	81
5.3	Band Structure	83
5.4	Length of the Organic Cation	84
5.5	Dielectric Constant of the Organic Cation (ϵ_2)	84
5.6	Cross-sectional Area of the Organic Cation	85
5.7	Cationic Phase Transitions	86
5.8	Halide and Metal Substitutions	87
5.9	Length Scale of Excitons	89
5.10	Anisotropic Optical Properties	90
5.11	Conclusion	90
5.12	References	91
6	Direct Observation of Electron-Phonon Coupling and Slow Vibrational Relaxation in Organic-Inorganic Hybrid Perovskites	97
6.1	Introduction	98
6.2	Experimental Methods	100
6.3	Computational Methods	102
6.4	Results and Discussion	104
6.5	Conclusion	118

6.6	References	118
7	Tailoring the Organic Framework and Energetic Disorder in Excitonic 2D Hybrid Perovskites	122
7.1	Introduction	123
7.2	Methods	126
7.3	Results and Discussion	130
7.3.1	Structural Characterization	130
7.3.2	Optical Characterization	134
7.4	Conclusion	148
7.5	References	149
8	Controlling Exciton Dynamics, Fine Structure, and Hot Photoluminescence Through Cation Modification in 2D Hybrid Perovskites	156
8.1	Introduction	156
8.2	Methods	158
8.3	Results and Discussion	159
8.3.1	Structural Characterization	159
8.3.2	Optical Characterization	161
8.3.3	Exploring Other Causes for Hot Exciton PL	173
8.4	Conclusion	174
8.5	References	174
9	Concluding Remarks	178
	Appendices	181
A	Additional Tables	182

B List of Publications	186
C List of Figures	189
D List of Tables	205

Preface

The unique properties of semiconductors are at the foundation of the technological advances of the 20th and 21st centuries. They are more resistive than insulators but less conductive than metals, and their utility comes from the ability to modulate the carrier concentration and therefore conductivity from insulating to conducting through internal chemical modification and through external stimuli such as electric fields or light. Controlling the carrier concentration is crucial to device applications: the conductivity of field-effect transistors is controlled by an applied electric field, allowing them to act as amplifiers in analog electronics and as switches in digital circuits; solar cells absorb light and extract the photogenerated excess charge carriers.

Semiconductors have band gaps that overlap the ultraviolet, visible, or infrared spectrum, and the intrinsic carrier concentration exponentially decays with increasing band gap. The band gap is a fundamental material property in bulk semiconductors: single-element semiconductors such as silicon and binary semiconductors such as cadmium selenide have a fixed band gap. To tune the band gap, the conventional approach is to alloy semiconductors into ternary or quaternary materials. The advent of quantum confined materials provides an additional method to tailor the chemical and physical properties of semiconductors. Instead of synthesizing a new compound to have specific optoelectronic properties, existing compounds can be transformed into zero-dimensional quantum dots (QDs), one-dimensional nanowires or two-dimensional

quantum wells, and quantum confinement results in size-tunable properties including an increased band gap and exciton binding energy. In this dissertation, we study zero- and two-dimensional materials. Part I focuses on quantum confinement in semiconductor QDs and their assemblies.

In Chapter 1, we briefly review QD fundamentals. First, we introduce quantum confinement in zero dimensions, which is the origin of their size-dependent electronic properties. To use QDs as the building blocks for optoelectronic devices, they first must be deposited into thin film assemblies. Depositing QDs is not enough to make devices, however. As-synthesized, colloidal QDs are capped with long insulating ligands that do not permit QDs to electronically couple. To couple QDs, the native ligands are replaced with shorter ligands through a process known as ligand exchange. We introduce the two classes of ligand exchange: solution-phase and solid-state.

Chapter 2 details the Time-Resolved Microwave Conductivity (TRMC) technique, which we use to contactlessly measure the mobility and lifetime of photoexcited carriers in coupled QD assemblies, which is used in Chapters 3 and 4. Chapter 3 studies PbSe QD assemblies. We use surface treatments to vary the Pb:Se ratio, which controls the carrier type and concentration. In Chapter 4, we n-dope CdSe QD assemblies with varying amounts of indium. In both systems, we use TRMC and field-effect transistor measurements to quantify the conductivity, mobility, and lifetime. We find that doping the QD assemblies electronically passivates traps by moving the Fermi level closer to the band edge.

Part II studies two-dimensional hybrid perovskites (2DHPs), which are composed of inorganic metal halide sheets separated by organoammonium cations that electronically form quantum well superlattices. Carriers in 2DHPs experience strong quantum and dielectric confinement effects.

Chapter 5 introduces the chemistry and physics of 2DHPs. In Chapter 6, we

use variable-temperature absorption and photoluminescence measurements to study excitonic dynamics and fine structure in the 2DHP phenethylammonium lead iodide. We find that the excitonic absorption and photoluminescence couple strongly to vibrational modes on the organic cation, and hot exciton photoluminescence out of excited vibrational levels results from competition between vibrational relaxation and radiative recombination. In Chapters 7 and 8, we synthesize a family of phenethylammonium lead iodide derivatives with single atom substitutions on the cation. We find that longer cations increase the energetic disorder in 2DHPs while still exhibiting signatures of coupling to vibrational modes on the organic cation (Chapter 7). Wider cations are known to strain the inorganic framework, and we find that wider cations affect the dynamics of exciton relaxation (Chapter 8). In some of the species with wider cations, we find that the proportion of hot exciton photoluminescence increases by an order of magnitude compared to unsubstituted phenethylammonium lead iodide. The vibrational modes that couple to the exciton are greatly reduced in energy compared to unsubstituted phenethylammonium lead iodide and its derivatives with longer cations.

Part I

Photochemistry of Quantum Dot Thin Films

Chapter 1

Introduction to Quantum Dots

1.1 Quantum Confinement in Zero Dimensions

A nanocrystal is a nanometer-sized semiconductor particle. What makes a quasi-spherical semiconductor nanocrystal a quantum dot (QD) is that in a QD, the diameter $2R$ of the particle is smaller than semiconductor's Bohr radius, so the QD experiences intermediate or strong quantum confinement. QDs are thus considered a zero-dimensional material because they are confined in all dimensions. While quantum dots are never perfectly spherical because of crystal faceting, a useful model for quantum dots is a particle in an infinite spherical potential well.^{1,2} This model is qualitatively similar to the one-dimensional "particle in a box."

Consider a spherical QD with radius R . The potential is

$$\begin{aligned} V(r) &= 0 & r &\leq R \\ V(r) &= \infty & r &> R \end{aligned}$$

The time-independent Schrodinger equation is:

$$\left(-\frac{\hbar^2}{2m^*}\nabla^2 + V\right)\psi = E\psi \quad (1.1)$$

where m^* is the carrier's effective mass.

Unlike the Schrodinger equation for the hydrogen atom, there is no $1/r$ electrostatic potential term, which profoundly impacts the solution. In spherical coordinates, the wavefunction ψ is separable:

$$\psi_{n,l,m}(r, \theta, \phi) = N_{n,l,m}j_l(k_{n,l}r)Y_{l,m}(\theta, \phi) \quad (1.2)$$

where $j_l(k_{n,l}r)$ is the l th spherical Bessel function, $Y_{l,m}(\theta, \phi)$ is a spherical harmonic, and $N_{n,l,m}$ is a constant to normalize the wavefunction.

The boundary condition is:

$$\psi_{n,l,m}(r = R, \theta, \phi) = 0 \quad (1.3)$$

for all θ, ϕ because of the infinite potential outside the sphere. Equation 1.3 holds when $k_{n,l}$ is the n th zero of j_l . Applying Equation 1.1 to $\psi_{n,l,m}$ yields the energy levels

$$E_{n,l} = \frac{\hbar^2 k_{n,l}^2}{2m^* R^2} \quad (1.4)$$

where $n, l = 0, 1, 2, \dots$

The lack of the electrostatic potential in Equation 1.1 results in no restriction on allowed values of l . It is completely normal to consider the $1p$ excitonic state in QDs.³ m takes on the usual values of $0, \pm 1, \pm 2, \dots, \pm l$.

This simple model does not allow for any electronic communication between

quantum dots. A better approximation for the potential is

$$\begin{aligned} V(r) &= 0 & r &\leq R \\ V(r) &= C & r &> R \end{aligned}$$

where $C > 0$. Under this model, the wavefunction is evanescent and exponentially decays for $r > R$ in bound states ($E < C$), similar to the one-dimension particle in a finite square well.² The additional physical insight from this model is that by packing quantum dots closely, they can electronically couple to one another when the evanescent wavefunctions overlap. Additionally, free particle states above the ionization threshold ($E > C$) may be able to be accessed.⁴

1.2 Deposition and Ligand Exchange

Colloidal QDs are synthesized using wet chemical techniques and are a solution processable material, allowing QD assemblies to be deposited using low-cost, large-area deposition methods such as spin- and spray-casting.⁵ Their size-tunable properties^{5,6} make QDs an attractive material for next-generation electronic and optoelectronic devices, and QDs have been used in devices such as field-effect transistors,⁷⁻¹⁵ solar cells,^{10,16-20} photodetectors,^{18,21-23} and light-emitting diodes.^{24,25} As synthesized, colloidal QDs are capped with long, insulating ligands that help determine the size and shape resulting from synthesis as well as stabilize the particles in nonpolar solvents.²⁶ QDs cannot communicate with one another unless the insulating ligands are replaced with shorter organic or inorganic ligands in a process known as a ligand exchange, which allows QDs to pack more tightly so the wavefunctions of adjacent QDs overlap.^{5,27}

There are two general classes of ligand exchange for colloidal QDs.^{5,28} The first class is a solid-state ligand exchange, in which long ligand-capped QDs are deposited into a

solid (*e.g.*, by spin-casting). Subsequently, the long ligands are replaced with short insulating ligands while the QDs remain assembled in a solid. The solid-state method is compatible with a wide variety of ligand chemistries, but QD films experience a large volume contraction that typically results in crack formation. Multiple QD depositions and ligand exchange steps are usually performed to fill in the cracks.^{5,28} A second class is a solution-phase ligand exchange, in which QDs in solution have their ligands replaced in-situ and are subsequently dispersed in a compatible (typically polar) solvent.^{8,29–31} However, solution-phase exchanges require QDs to be electrostatically stabilized in solution post-exchange, which makes solution-phase exchanges less universally applicable than solid-state exchanges.^{5,28} After a solution-phase exchange, only a single deposition step is needed to form large-area, crack free films, which is a major advantage compared to solid-state exchanges.^{5,28}

Even after ligand exchange, there are many challenges for efficient charge transport in coupled QD assemblies.⁵ Ligand exchange processes have the potential to introduce surface defects, such as by stripping surface atoms and leaving dangling bonds^{32,33} that serve as recombination sites for electrons and holes.^{34,35} To improve the performance of optoelectronic devices fabricated from QD thin films, these defects must be passivated either through treatments to heal the defects or through doping so the Fermi level is higher than the energy of the defect states.^{5,36} Furthermore, when considering the properties of the QD thin film, the composition of ligands and any other components in the interparticle space must be taken into account.^{37,38} The size- and surface-tunable properties of QDs present a unique set of advantages and challenges for synthetic and physical chemists.

1.3 References

- (1) Blinder, S. M. Particle in an Infinite Spherical Well. <http://demonstrations.wolfram.com/ParticleInAnInfiniteSphericalWell/>.
- (2) Griffiths, D. J., *Introduction to Quantum Mechanics*, 2nd; Pearson Prentice Hall: 2004.
- (3) Shum, K.; Wang, W. B.; Alfano, R. R.; Jones, K. M. *Phys. Rev. Lett.* **1992**, *68*, 3904–3907.
- (4) Shabaev, A.; Efros, A. L.; Efros, A. L. *Nano Lett.* **2013**, *13*, 5454–61.
- (5) Kagan, C. R.; Murray, C. B. *Nat. Nanotechnol.* **2015**, *10*, 1013–1026.
- (6) Murray, C. B.; Norris, D. J.; Bawendi, M. G. *J. Am. Chem. Soc.* **1993**, *115*, 8706–8715.
- (7) Choi, J.-H.; Oh, S. J.; Lai, Y.; Kim, D. K.; Zhao, T.; Fafarman, A. T.; Diroll, B. T.; Murray, C. B.; Kagan, C. R. *ACS Nano* **2013**, *7*, 8275–83.
- (8) Fafarman, A. T.; Koh, W.-k.; Diroll, B. T.; Kim, D. K.; Ko, D.-K.; Oh, S. J.; Ye, X.; Doan-Nguyen, V.; Crump, M. R.; Reifsnnyder, D. C.; Murray, C. B.; Kagan, C. R. *J. Am. Chem. Soc.* **2011**, *133*, 15753–61.
- (9) Lee, J.-S.; Kovalenko, M. V.; Huang, J.; Chung, D. S.; Talapin, D. V. *Nat. Nanotechnol.* **2011**, *6*, 348–52.
- (10) Liu, Y.; Tolentino, J.; Gibbs, M.; Ihly, R.; Perkins, C. L.; Liu, Y.; Crawford, N.; Hemminger, J. C.; Law, M. *Nano Lett.* **2013**, *13*, 1578–1587.
- (11) Oh, S. J.; Berry, N. E.; Choi, J.-H.; Gaulding, E. A.; Lin, H.; Paik, T.; Diroll, B. T.; Muramoto, S.; Murray, C. B.; Kagan, C. R. *Nano Lett.* **2014**, *14*, 1559–1566.

- (12) Oh, S. J.; Wang, Z.; Berry, N. E.; Choi, J.-h.; Zhao, T.; Gauldin, E. A.; Paik, T.; Lai, Y.; Murray, C. B.; Kagan, C. R. *Nano Lett.* **2014**, *14*, 6210–6216.
- (13) Stinner, F. S.; Lai, Y.; Straus, D. B.; Diroll, B. T.; Kim, D. K.; Murray, C. B.; Kagan, C. R. *Nano Lett.* **2015**, *15*, 7155–7160.
- (14) Talapin, D. V.; Lee, J.-S.; Kovalenko, M. V.; Shevchenko, E. V. *Chem. Rev.* **2010**, *110*, 389–458.
- (15) Talapin, D. V.; Murray, C. B. *Science* **2005**, *310*, 86–9.
- (16) Chuang, C. C.-h. M.; Brown, P. R.; Bulović, V.; Bawendi, M. M. G. *Nat. Mater.* **2014**, *13*, 796.
- (17) Marshall, A. R.; Young, M. R.; Nozik, A. J.; Beard, M. C.; Luther, J. M. *J. Phys. Chem. Lett.* **2015**, 2892–2899.
- (18) McDonald, S. A.; Konstantatos, G.; Zhang, S.; Cyr, P. W.; Klem, E. J. D.; Levina, L.; Sargent, E. H. *Nat. Mater.* **2005**, *4*, 138–142.
- (19) Semonin, O. E.; Luther, J. M.; Choi, S.; Chen, H.-Y.; Gao, J.; Nozik, A. J.; Beard, M. C. *Science* **2011**, *334*, 1530–1533.
- (20) Zhao, T.; Goodwin, E. D.; Guo, J.; Wang, H.; Diroll, B. T.; Murray, C. B.; Kagan, C. R. *ACS Nano* **2016**, *10*, 9267–9273.
- (21) Konstantatos, G.; Howard, I.; Fischer, A.; Hoogland, S.; Clifford, J.; Klem, E.; Levina, L.; Sargent, E. H. *Nature* **2006**, *442*, 180–3.
- (22) Oertel, D. C.; Bawendi, M. G.; Arango, A. C.; Bulović, V. *Appl. Phys. Lett.* **2005**, *87*, 213505.
- (23) Stiff-Roberts, A. D.; Lantz, K. R.; Pate, R. *J. Phys. D. Appl. Phys.* **2009**, *42*, 234004.
- (24) Coe, S.; Woo, W.-K.; Bawendi, M.; Bulović, V. *Nature* **2002**, *420*, 800–3.

- (25) Kim, B. H. et al. *Nano Lett.* **2015**, *15*, 969–973.
- (26) Alivisatos, A. P. *Science* **1996**, *271*, 933–937.
- (27) Choi, J.-H.; Fafarman, A. T.; Oh, S. J.; Ko, D.-K.; Kim, D. K.; Diroll, B. T.; Muramoto, S.; Gillen, J. G.; Murray, C. B.; Kagan, C. R. *Nano Lett.* **2012**, *12*, 2631–8.
- (28) Boles, M. A.; Ling, D.; Hyeon, T.; Talapin, D. V. *Nat. Mater.* **2016**, *15*, 141–153.
- (29) Koleilat, G. I.; Levina, L.; Shukla, H.; Myrskog, S. H.; Hinds, S.; Pattantyus-Abraham, A. G.; Sargent, E. H. *ACS Nano* **2008**, *2*, 833–840.
- (30) Kovalenko, M. V.; Scheele, M.; Talapin, D. V. *Science* **2009**, *324*, 1417–20.
- (31) Nag, A.; Kovalenko, M. V.; Lee, J.-S.; Liu, W.; Spokoyny, B.; Talapin, D. V. *J. Am. Chem. Soc.* **2011**, *133*, 10612–10620.
- (32) Goodwin, E. D.; Diroll, B. T.; Oh, S. J.; Paik, T.; Murray, C. B.; Kagan, C. R. *J. Phys. Chem. C* **2014**, *118*, 27097–27105.
- (33) Talgorn, E.; Moysidou, E.; Abellon, R. D.; Savenije, T. J.; Goossens, A.; Houtepen, A. J.; Siebbeles, L. D. A. *J. Phys. Chem. C* **2010**, *114*, 3441–3447.
- (34) Gao, Y.; Aerts, M.; Sandeep, C. S. S.; Talgorn, E.; Savenije, T. J.; Kinge, S.; Siebbeles, L. D. A.; Houtepen, A. J. *ACS Nano* **2012**, *6*, 9606–9614.
- (35) Guglietta, G. W.; Diroll, B. T.; Gauding, E. A.; Fordham, J. L.; Li, S.; Murray, C. B.; Baxter, J. B. *ACS Nano* **2015**, *9*, 1820–1828.
- (36) Ip, A. H. et al. *Nat. Nanotechnol.* **2012**, *7*, 577–82.
- (37) Grinolds, D. D. W.; Brown, P. R.; Harris, D. K.; Bulovic, V.; Bawendi, M. G. *Nano Lett.* **2015**, *15*, 21–26.
- (38) Keldysh, L. V. *JETP Lett.* **1979**, *29*, 658–661.

Chapter 2

Theory of Time-Resolved Microwave Conductivity

2.1 Introduction

Semiconductors occupy a unique position that allow them to be used in electronic devices such as transistors, solar cells, and photodetectors. The carrier concentration is larger than in insulators but less than in metals, and the carrier concentration can be modulated from insulating to conducting through doping or applying an external field. Two of the figures of merit in semiconductors are the charge carrier's mobility and lifetime. The mobility represents how quickly a carrier moves in a semiconductor under an applied electric field, and materials with larger mobilities can be switched faster and operate in higher performance electronic devices. The lifetime indicates how long an excess carrier lives before recombining and returning the material to its equilibrium carrier concentration. In light-harvesting semiconductors the mobility-lifetime product must be large enough to allow carriers to be extracted before recombining.

Most techniques used to study the mobility and lifetime in semiconductors require

the application of ohmic electrical contacts to apply electric fields and/or inject and extract carriers. Electrical contacts can influence the measured values through added resistance, Schottky barrier formation, or Fermi level pinning. Time-resolved Microwave Conductivity (TRMC) is a technique to contactlessly probe the mobility and lifetime in semiconductors.^{1,2} TRMC is also used to study photoinduced intramolecular charge separation in organic molecules.³ In a TRMC measurement, a semiconductor sample is placed in a microwave cavity, and free electrons and holes absorb microwave radiation. A pulsed laser is used to excite excess photogenerated carriers, which absorb additional microwave radiation. The change in reflected microwave power is monitored, and the microwave transient can be fit to determine the lifetime. The change in reflected microwave power is proportional to the change in conductivity, and the mobility-quantum yield product can be determined from the change in conductivity and known photoexcitation density.

2.2 Theory

2.2.1 Microwave Absorption in Semiconductors

Microwaves are on the order of a μeV to a meV , but semiconductor band-gaps are many orders of magnitude larger. Therefore, microwaves do not directly change the carrier density, though heating effects like in a microwave oven are possible at very high powers. We will consider how free carriers absorb microwaves.

In an ideal undoped semiconductor, the only free carriers present are those generated thermally. Let n be the concentration of electrons, p the concentration of holes, and n_i the intrinsic carrier concentration such that $np = n_i^2$. In silicon $n_i \approx 10^{10} \text{ cm}^{-3}$ at 300 K. Typically, in a doped semiconductor, doping levels are many orders of

magnitude greater than the intrinsic carrier concentration, and at room temperature, the energy required to ionize typical dopants is much less than kT . To good approximation, the concentration of free carriers is equal to the concentration of dopants in a non-degenerate semiconductor.⁴ For example, if the concentration of donor dopants $N_D = 10^{15} \text{ cm}^{-3}$, then $n = 10^{15} \text{ cm}^{-3}$. However, $np = n_i^2$, so $p = 10^5 \text{ cm}^{-3}$ and is negligible compared to the concentration of electrons. Thus, an n -type semiconductor is one in which the majority carrier is electrons, and a p -type semiconductor is dominated by holes.

Valid results for the absorption of microwaves can be derived using the classical Drude-Lorentz model.⁵ In this model, the resonant frequency ω_0 in the Lorentz model (where absorbers are treated as dipole oscillators) is set to zero.

Under the Drude-Lorentz model, the equation of motion for the charge carrier is

$$m \frac{d^2x}{dt^2} + m\gamma \frac{dx}{dt} = -qE_0 e^{-i\omega t} \quad (2.1)$$

This equation is of the same form as a damped harmonic oscillator equation with the electromagnetic wave as the driving force.

The solution to this equation is $x = x_0 e^{-i\omega t}$, and then algebra gives

$$x(t) = \frac{qE(t)}{m\omega^2 + im\gamma\omega} \quad (2.2)$$

where $E(t) = E_0 e^{-i\omega t}$.

The electric displacement $\vec{D} = \epsilon_0 \epsilon_r(\omega) \vec{E} = \epsilon_0 \vec{E} + \vec{P}$ in isotropic media, and the polarization $P = -qNx(t)$ where N is the concentration of free carriers. However, free carriers are not the only contributors to the polarization in semiconductors. The main other contributor is bound carriers in the semiconductor. This can be taken into account by letting $D = \epsilon_0 E + P_{\text{other}} + P_{\text{free carrier}}$,⁵ and we let $\epsilon_0 E + P_{\text{other}} = \epsilon_s \epsilon_0 E$

where ϵ_s is the low frequency (i.e., static) dielectric constant. Additionally, since the free carriers are moving in the conduction and valence band, the mass m must be replaced with the effective mass m^* . Thus,

$$D = \epsilon_s \epsilon_0 E - \frac{Nq^2 E}{m^* \omega^2 + im\gamma\omega} \quad (2.3)$$

Since $D = \epsilon_0 \epsilon_r(\omega) E$, then

$$\epsilon_r(\omega) = \epsilon_s - \frac{Nq^2}{\epsilon_0 m^* (\omega^2 + i\gamma\omega)} \quad (2.4)$$

The damping coefficient $\gamma = 1/\tau$, where τ is the scattering time. In semiconductors, the DC conductivity $\sigma = \frac{q^2 N \tau}{m^*}$.⁵ Rearranging, $\frac{1}{\tau} = \frac{q^2 N}{\sigma m^*}$. From Equation 2.4, the dielectric constant is

$$\epsilon_r(\omega) = \epsilon_s \left(1 - \frac{Nq^2}{\epsilon_s \epsilon_0 m^* (\omega^2 + i\omega \frac{q^2 N}{\sigma m^*})} \right). \quad (2.5)$$

Even for high mobility crystalline semiconductors, $\omega \ll \gamma = \tau^{-1}$,

$$\epsilon_r(\omega) \approx \epsilon_s \left(1 - \frac{Nq^2}{i\omega \epsilon_s \epsilon_0 \frac{q^2 N}{\sigma}} \right) = \epsilon_s \left(1 + \frac{i\sigma}{\epsilon_s \epsilon_0 \omega} \right). \quad (2.6)$$

This is the dielectric constant at microwave frequencies.

Assuming $\left| \frac{i\sigma}{\epsilon_s \epsilon_0 \omega} \right| \ll 1$, then $\sqrt{\epsilon_r(\omega)} \approx \sqrt{\epsilon_s} \left(1 + \frac{i\sigma}{2\epsilon_s \epsilon_0 \omega} \right)$, and since $k = \frac{\sqrt{\epsilon_r(\omega)} \omega}{c_0}$ where c_0 is the speed of light in vacuum, then

$$I(x) \propto |E(x)|^2 = E_0^2 \exp \left(-\frac{\sigma}{c_0 \sqrt{\epsilon_s} \epsilon_0} x \right) \quad (2.7)$$

and the absorption constant

$$\alpha = \frac{\sigma}{c_0 \sqrt{\epsilon_s \epsilon_0}}. \quad (2.8)$$

Therefore, the absorption of microwaves is proportional to the semiconductors' conductivity ($\sigma = q\mu_e n_e + q\mu_h n_h$).⁶

Photoexcitation creates additional electrons Δn_e and holes Δn_h , causing a change in conductivity and microwave absorption. By monitoring the reflected power and measuring the the photoexcitation density, the change in mobility can be measured. If photogenerated carriers recombine before being measured (*e.g.*, through Auger recombination),⁷ then the mobility determined from TRMC will be artificially low. Thus, the mobility measured by TRMC is a lower bound on the true mobility. Formally, TRMC determines the mobility quantum-yield product. Photoexcitation may also change the carrier mobility because trap states can be passivated or created by photoexcitation.⁸

2.2.2 Waveguide Modes

Consider a rectangular waveguide with dimensions a in width (x) and b in height (y), but extending infinitely in length (z). Because the waveguide is assumed to be a perfect electrical conductor, the tangential component of the electric field must be zero adjacent to the surface of the waveguide. We consider the transverse electric (TE; no field in the direction of propagation z) modes, since for TRMC we are interested in the electric field. Let $\beta_i = 2\pi/\lambda_i$ for $i = x, y$ where λ_i is the wavelength and must be an integer multiple of two times the waveguide dimension a or b . β is identical to k in Section 2.2.1.

⁶We recommend Balanis, *Advanced Engineering Electromagnetics 2nd ed.* (Wiley 2012) for more detailed explanations and derivations of the waveguide equations.

The solution for the electric field modes is

$$E_x(x, y, z) = \frac{\beta_y}{\epsilon} A_{mn} \cos \beta_x x \sin \beta_y y \exp -i\beta_z z \quad (2.9)$$

$$E_y(x, y, z) = \frac{\beta_x}{\epsilon} A_{mn} \sin \beta_x x \cos \beta_y y \exp -i\beta_z z \quad (2.10)$$

$$E_z(x, y, z) = 0 \quad (2.11)$$

with

$$\beta_x^2 + \beta_y^2 = \left(\frac{m\pi}{a}\right)^2 + \left(\frac{n\pi}{b}\right)^2 = \beta^2 = \omega^2 \mu \epsilon. \quad (2.12)$$

where A_{mn} is a constant $m, n = 0, 1, 2, \dots$ with m and n not simultaneously zero.

The cutoff frequency is the frequency below which a wave cannot propagate through the waveguide. For mode m, n the cutoff frequency

$$(\omega_c)_{m,n} = \frac{1}{\sqrt{\mu\epsilon}} \sqrt{\left(\frac{m\pi}{a}\right)^2 + \left(\frac{n\pi}{b}\right)^2}. \quad (2.13)$$

Here, μ is the permeability, not the sample mobility.

2.2.3 Resonant Cavity

Because we are studying thin films with low-to-moderate mobilities, a resonant cavity is necessary to improve the signal-to-noise ratio. The selection of a resonant cavity significantly increases the measurable signal at the expense of an increased instrumental response time resulting from cavity ringdown.⁹

The microwave resonant cavity we use is a section of WR90 waveguide that is confined in the z direction, with length L (Figure 2.1). The TE solutions for the electric field must then be:

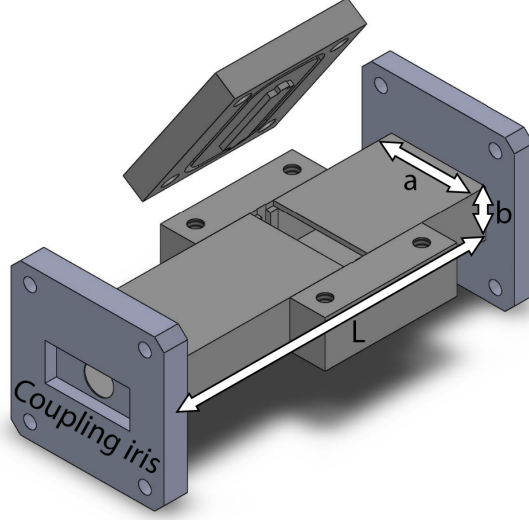


Figure 2.1: Rendering of the TRMC resonant cavity.

$$E_x(x, y, z) = \frac{\beta_y}{\epsilon} A_{mnp} \cos \beta_x x \sin \beta_y y \sin \beta_z z \quad (2.14)$$

$$E_y(x, y, z) = \frac{\beta_x}{\epsilon} A_{mnp} \sin \beta_x x \cos \beta_y y \sin \beta_z z \quad (2.15)$$

$$E_z(x, y, z) = 0 \quad (2.16)$$

with

$$\beta_x^2 + \beta_y^2 + \beta_z^2 = \left(\frac{m\pi}{a}\right)^2 + \left(\frac{n\pi}{b}\right)^2 + \left(\frac{p\pi}{L}\right)^2 = \beta^2 = \omega^2 \mu \epsilon \quad (2.17)$$

since the tangential component of the electric field must be zero at the walls. Solving (2.17) for the resonant frequency ($\nu = 2\pi\omega$) gives:

$$\nu_{mnp}^{\text{TE}} = \frac{1}{2\pi\sqrt{\mu\epsilon}} \sqrt{\left(\frac{m\pi}{a}\right)^2 + \left(\frac{n\pi}{b}\right)^2 + \left(\frac{p\pi}{L}\right)^2} \quad (2.18)$$

where $m, n, p = 0, 1, 2, 3, \dots$, but m and n cannot both be zero and $p \neq 0$. Here, μ is the permeability, not the sample mobility.

2.2.4 Complex Propagation Constant

The above derivation is only valid assuming that the waveguide is filled with a single lossless medium. When carrying out TRMC on thin-film samples, the waveguide is partially filled with lossy media. Similar to our use of the Drude-Lorentz model to study microwave absorption in semiconductors in Section 2.2.1, we consider a lossy medium filling the waveguide. For lossy media, the propagation constant

$$\gamma = \sqrt{i\omega\mu(\sigma + i\omega\epsilon)} = \pm\alpha \pm i\beta \quad (2.19)$$

where β is the phase constant and is identical to β in Section 2.2.2. α is the attenuation constant.

Equation 2.19 can be solved by separating and equating the real and imaginary parts. One finds:

$$\alpha = \omega\sqrt{\mu\epsilon} \left(\frac{1}{2} \left[\sqrt{1 + \left(\frac{\sigma}{\omega\epsilon}\right)^2} - 1 \right] \right)^{1/2} \quad (2.20)$$

$$\beta = \omega\sqrt{\mu\epsilon} \left(\frac{1}{2} \left[\sqrt{1 + \left(\frac{\sigma}{\omega\epsilon}\right)^2} + 1 \right] \right)^{1/2}. \quad (2.21)$$

In TRMC on semiconductors, we generally probe low conductivity materials (good dielectrics), where $(\sigma/\omega\epsilon)^2 \ll 1$. α can be approximated by expanding Equation 2.20 to second order:

$$\begin{aligned} \alpha &= \omega\sqrt{\mu\epsilon} \left(\frac{1}{2} \left[\left\{ 1 + \frac{1}{2} \left(\frac{\sigma}{\omega\epsilon}\right)^2 + \dots \right\} - 1 \right] \right)^{1/2} \\ &\approx \frac{\sigma}{2} \sqrt{\frac{\mu}{\epsilon}} \end{aligned} \quad (2.22)$$

and similarly, if β is only kept to first order it can be approximated as:

$$\begin{aligned}\beta &= \omega\sqrt{\mu\epsilon}\left(\frac{1}{2}[\{1 + \dots\} + 1]\right)^{1/2} \\ &\approx \omega\sqrt{\mu\epsilon}\end{aligned}\tag{2.23}$$

Like we found in Section 2.2.1, α is proportional to the conductivity of the semiconductor.

2.3 Experimental

Many publications describe TRMC apparatuses.^{1,9-11}

Our resonant cavity is shown in Figure 2.1. It is fabricated out of out of commercially-purchased copper WR90 waveguide, with end plates and a top plate machined from silicon bronze. One of the silicon bronze plates is machined to a thickness of 0.001” with an 8 mm hole drilled through the center that serves as a coupling iris. The iris is a below-cutoff waveguide, so evanescent microwaves traverse the iris and couple into the cavity. We seal the iris with Corning Eagle XG glass and Torr-Seal epoxy. The other plate has a 1/4” hole drilled through the center which is also sealed with Corning Eagle XG glass and Torr-Seal epoxy. Light is focused through the hole and expanded to a ~9 mm spot on the sample.

A schematic of our TRMC apparatus is shown in Figure 2.2. X-band (~9 GHz) microwaves are generated either using a voltage-controlled oscillator in which the microwave frequency is tuned by a programmable power supply, or by a synthesized CW generator (HP 83712A or 8671B). A circulator directs microwaves from the source into a microwave antenna, transferring microwaves from coaxial cabling to a WR90

Adapted in part with permission from Elsevier from Goodwin, E. D.; Straus, D. B.; Gaulding, E. A.; Murray, C. B.; Kagan, C. R. *Chem. Phys.* **2016**, *471*, 81-88.

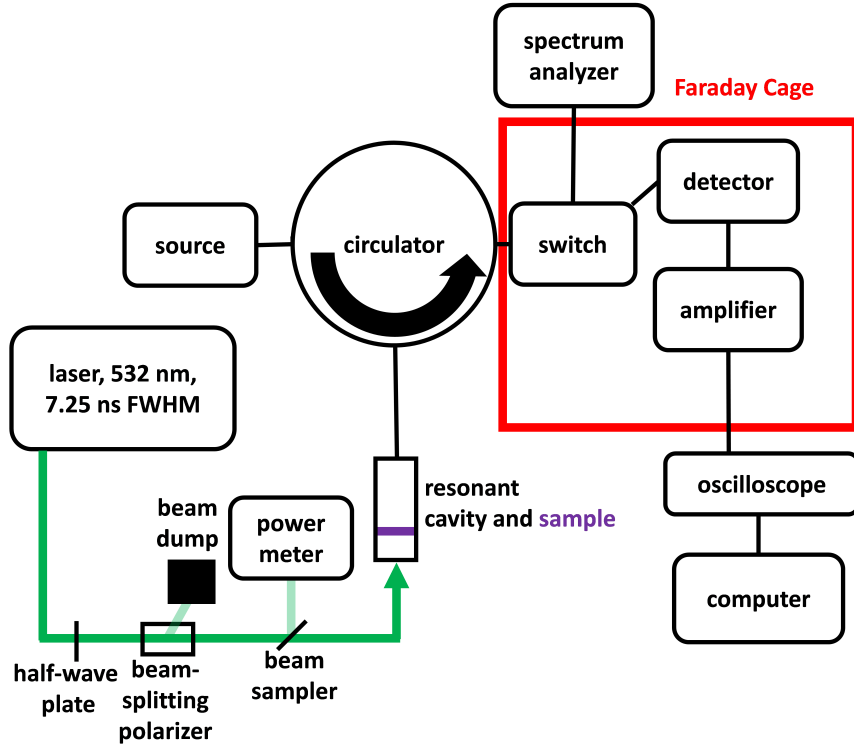


Figure 2.2: Schematic of the TRMC experiment.

waveguide connected to a home-built, sealed, resonant microwave cavity (Figure 2.1).

We load samples into the cavity in a nitrogen-filled glovebox to prevent sample oxidation. ~ 5 ns, 532 nm laser pulses are generated by a Continuum MiniLite II or Quantel Ultra Nd:YAG laser and focused through the aperture into the resonant cavity. The circulator directs reflected microwaves into a microwave switch that allows us to visualize the resonance peak on an HP 8566B spectrum analyzer (Figure 2.3), or to convert microwave power to voltage on a microwave detector (Keysight 8472B or Herotek DTM180AA). Detected microwave power is amplified and microwave transients are digitized using a Tektronix TDS3054B or Keysight DSO S054A oscilloscope. To measure the incident microwave power on resonance in the absence of light, the voltage output by the microwave detector is recorded on the oscilloscope.

Because a Schottky diode is used to detect microwave power, it needs to be

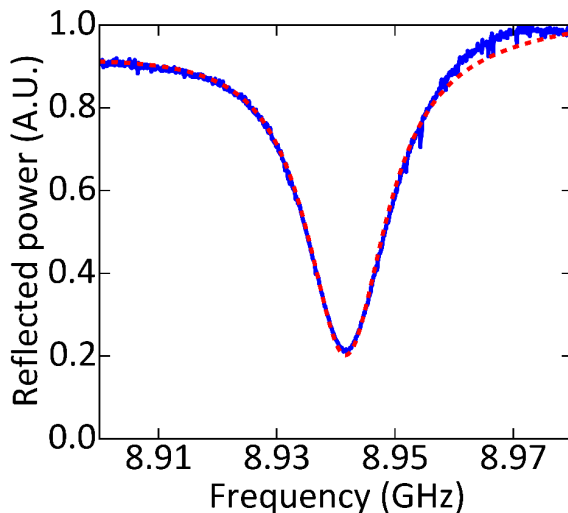


Figure 2.3: Resonant microwave peak for the cavity loaded with a sample. The data are shown in blue, and the Lorentzian fit in red.

calibrated to ensure the output voltage V accurately measures the reflected microwave power, using the equation $P = V^n$ where P is the reflected microwave power. For the Keysight 8472B diode, $n = 1.42$, and for the Herotek DTM180AA, $n = 1.31$. Because the photoinduced change in voltage ΔV is small compared to V , then $\frac{\Delta P}{P_0} = n \frac{\Delta V}{V_0}$.

2.4 The Sensitivity Constant

2.4.1 The Analytical Method

To relate the change in reflected microwave power ΔP to the change in conductivity ΔG and mobility μ , the sample-dependent sensitivity factor for the microwave cavity K must be determined.

The traditional method of determining the sensitivity factor uses an analytical method originally employed for resonant cavities uniformly filled with a liquid and irradiated as described by Infelta *et al.*⁹ and briefly summarized here.

The resonance peak of a loaded microwave cavity (*e.g.*, Figure 2.3) is fit to a Lorentzian function:

$$R(f) = \frac{R_0 + \left(\frac{2(f-f_0)}{\Delta W}\right)^2}{1 + \left(\frac{2(f-f_0)}{\Delta W}\right)^2} \quad (2.24)$$

where f_0 is the resonant frequency (in Hz), ΔW is the full width at half-maximum of the resonance peak, and R_0 is the depth of the normalized peak. In Figure 2.3, a linear term is also used to correct for the frequency-dependent output characteristics of the source. The quality factor $Q = \frac{f_0}{\Delta W}$, and the cavity's response time $\tau_m = \frac{Q}{\pi f_0}$. In our microwave cavity loaded with a low conductivity thin film sample deposited on a 25.2 x 9.4 x 1.1 mm Corning Eagle XG glass substrate, $f_0 \approx 8.92$ GHz, $Q \approx 500$, $R_0 \approx 0.25$, and $\tau_m \approx 20$ ns.

Pulsed photoexcitation or irradiation of the sample in the resonant cavity causes a change in the reflected microwave power ΔP . The normalized change in microwave power $\frac{\Delta P}{P_0} = K \Delta G = K' \Delta \sigma$ where K and K' are sensitivity factors, G the conductance, σ the conductivity, and P_0 the reflected microwave power in the absence of light. $\Delta G = \Delta \sigma \frac{a}{b} l$ where l is the sample thickness.¹²

For a cavity uniformly filled (*e.g.*, with a dielectric liquid), the sensitivity factor K' is:

$$K' = \mp \frac{Q \left(\frac{1}{\sqrt{R_0}} \pm 1 \right)}{\pi f_0 \epsilon_0 \epsilon_r} f(L_1, L_2) \quad (2.25)$$

where ϵ_r is the permittivity of the liquid and $f(L_1, L_2)$ is a correction to allow for incomplete irradiation of the waveguide. If a length of the cavity from $0 \leq z = L_1$ to a distance $z = L_2 \leq L$ is irradiated, then

$$f(L_1, L_2) = \frac{\int_{L_1}^{L_2} \sin^2\left(\frac{n\pi}{L} z\right) dz}{\int_0^L \sin^2\left(\frac{n\pi}{L} z\right) dz} \quad (2.26)$$

where n is the integer number of microwave half-wavelengths that fit in the cavity.

Although an increase in conductivity will cause additional microwaves to be absorbed, the change in conductivity also changes the admittance of the resonance cavity. In some cases, the increase in sample conductivity causes a decrease in the microwaves reflected from the cavity. The upper sign in Equation 2.25 corresponds to an absorption of microwaves from the cavity, and the lower the emission.⁹

Thin film samples are routinely deposited on non-conductive glass or fused silica substrates. Equation 2.25 is routinely modified for the use of thin-film samples¹² using the partial illumination correction (Equation 2.26). We assume the the film is located at an electric field maximum and its thickness l is small compared to the wavelength of microwaves. We find by calculating $f(L_1, L_2)$ and converting $\Delta\sigma$ to ΔG that

$$K = \mp \frac{2Q\left(\frac{1}{\sqrt{R_0}} \pm 1\right)}{\pi f_0 \epsilon_0 \epsilon_r L \frac{a}{b}}. \quad (2.27)$$

where $a = 22.86$ mm and $b = 10.16$ mm are the dimension of the WR90 waveguide, and $L = 9.00$ cm is the length of the resonance cavity.

Until recently,¹³ little discussion of the appropriate value of ϵ_r appears in the literature. Naively, ϵ_r can be three things: 1 because the cavity is filled with air, ~ 4 based on the dielectric constant of glass, or the dielectric constant of the thin film (based on Equations 2.8 or 2.22). A length-weighted average is also naively possible, though this would be ~ 1 . The correct value of ϵ_r will be addressed in Section 2.4.2.

Regardless of how K is determined for thin film samples, the change in conductance

$$\Delta G = -\left(\frac{\Delta P}{P_0}\right)\left(\frac{F_I}{K}\right) \quad (2.28)$$

where F_I is a correction for the laser spot not illuminating the entire area of the sample that takes the electric field cross-section in the microwave cavity into account.¹⁴

Assuming a top-hat beam profile, F_I can be analytically determined:

$$F_I = \frac{\int_0^a \int_0^b \sin^2\left(\frac{\pi x}{a}\right) dy dx}{4 \int_0^r \sqrt{r^2 - x^2} \cos^2\left(\frac{\pi x}{a}\right) dx} \quad (2.29)$$

For a 9 mm diameter top-hat beam, $F_I = 2.00$.

If the beam has a Gaussian profile with irradiance $I(r) = I_0 \exp\left(-\frac{2r^2}{w_0^2}\right)$, then

$$F_I = \frac{\int_0^a \int_0^b \sin^2\left(\frac{\pi x}{a}\right) dy dx}{4 \int_0^{\frac{a}{2}} \int_0^{\frac{b}{2}} \exp\left(-2\left(\frac{x^2}{w_0^2} + \frac{y^2}{w_0^2}\right)\right) \cos^2\left(\frac{\pi x}{a}\right) dy dx} \quad (2.30)$$

The expanded Gaussian beam of our Minilite laser has $w_0 = 3.61$ mm, resulting in $F_I = 6.05$.

The quantum yield-mobility product is:

$$\phi \Sigma \mu = \phi(\mu_e + \mu_h) = \frac{\Delta G_{max}}{\frac{a}{b} q I_0 F_A} \quad (2.31)$$

where q is the fundamental charge, I_0 the photon fluence, and F_A the fraction of absorbed light.

The spot size used to compute F_I does not need to be exact and in fact does not significantly affect the measured conductivity value if the laser hits the center of the sample and the spot is round with diameter less than a (10.16 mm). As the spot area goes down, I_0 becomes proportionally larger. For a top-hat beam, the fluence $I_0 = \frac{p}{\pi x^2}$ for a beam containing p photons. If $p = 1$, then for our 9 mm top-hat beam $I_0 = 0.0157/\text{mm}^2$. For a given beam profile we must compare F_I/I_0 because

$$\phi \Sigma \mu \propto \frac{F_I \frac{\Delta P}{P_0}}{I_0 F_A}. \quad (2.32)$$

For the 9 mm top-hat beam, $F_I/I_0 = 127.4 \text{ mm}^2$. If instead we assumed we had a

7 mm top-hat beam, then $F_I = 3.12$ and $I_0 = 0.0259/\text{mm}^2$, so $F_I/I_0 = 120.5 \text{ mm}^2$, which 5.5% smaller than for the 9 mm top-hat beam. For the more accurate Gaussian beam profile, if $p = 1$, then $I_0 = 0.0491/\text{mm}^2$ so therefore $F_I/I_0 = 123.2\text{mm}^2$ and is 2.5% smaller than for the 9 mm top-hat beam.

Measuring an accurate beam spot size is important for reporting the photoexcitation density I_0 , so it should not be neglected.

If the entire waveguide cross-section is illuminated with uniform light intensity, $F_I = 1$. We can find that for $p = 1$, $I_0 = 0.00430/\text{mm}^2$, so $F_I/I_0 = 232.6\text{mm}^2$, much larger than the other values of F_I/F .

2.4.2 The Computational Method

Recently, we and others¹³ have used computational modeling to more accurately determine K . We use CST Microwave Studio to numerically simulate the TRMC resonant cavity. Frequency domain simulations in CST require explicit meshing of all elements including the thin film, so mesh adaptation must be disabled or else the small simulated changes in conductivity may affect the mesh, making the simulation results inaccurate.

Figure 2.4 shows an example of the simulated electric field distribution in the TRMC cavity showing the standing wave pattern of the TE(1,0,4) mode.

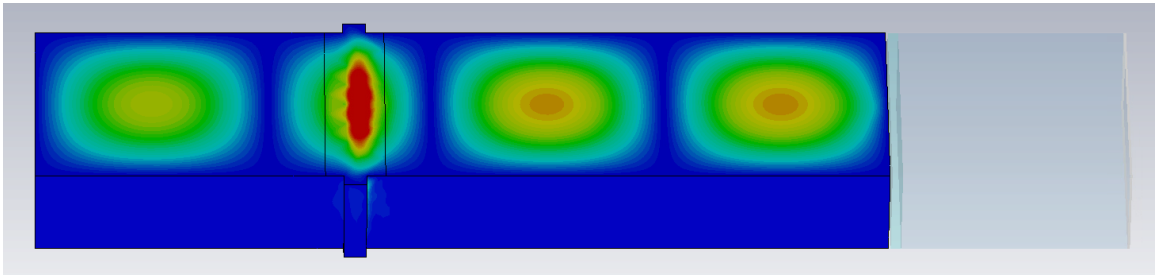


Figure 2.4: Simulated electric field distribution in TRMC resonant cavity.

In the simulations, the dimensions of the simulated microwave cavity match those of the experimental cavity. The material parameters are first adjusted so that the simulated resonance peak matches the resonance peak of the unloaded cavity. The conductivity of the copper WR90 waveguide is simulated as 5.8×10^7 S/m, and the conductivity of silicon bronze is simulated as 4.6×10^6 S/m.

The sensitivity factor is very sensitive to the dimensions of the substrate. We cut the 1.1 mm thick Eagle XG glass on a dicing saw to a size of 25.2 x 9.4 mm. We then simulate the cavity loaded with a blank Eagle XG substrate and set the conductivity and dielectric constant of the glass so the simulated and experimental resonance curves match. We find $\epsilon_{\text{glass}} = 5.3$ and $\sigma_{\text{glass}} = 0.012$ S/m. Eagle XG is reported to have a dielectric constant of 5.27 (at 1 KHz), matching our simulation and indicating that the dielectric constant is not frequency-sensitive between DC and ~ 10 GHz.

To determine the sensitivity constant through simulations, we model a thin film with dielectric (ϵ_r) and dark conductivity σ_0 . We then simulate a small increase $\Delta\sigma_{\text{sim}} = 0.01$ S/m in the film's conductivity. Then,

$$K = \frac{\frac{P_1 - P_0}{P_0}}{\Delta G_{\text{sim}}} \quad (2.33)$$

where $\Delta G_{\text{sim}} = \Delta\sigma_{\text{sim}} \frac{a}{b} l$

When our cavity is loaded with low conductivity thin films deposited on Corning Eagle XG glass, $K = -33800(1400) \Omega$, similar to the simulations by Reid *et al.*¹³ We note that our cavity should have a higher Q than the cavity used by Reid *et al.* because other than the top plate through which the sample is loaded, we do not have low conductivity joints in our cavity; our cavity is soldered together with silver solder. We also use Eagle XG glass instead of fused silica or quartz, and Eagle XG glass has a higher dielectric than fused silica (5.3 compared to ~ 3.8), which will lower K .

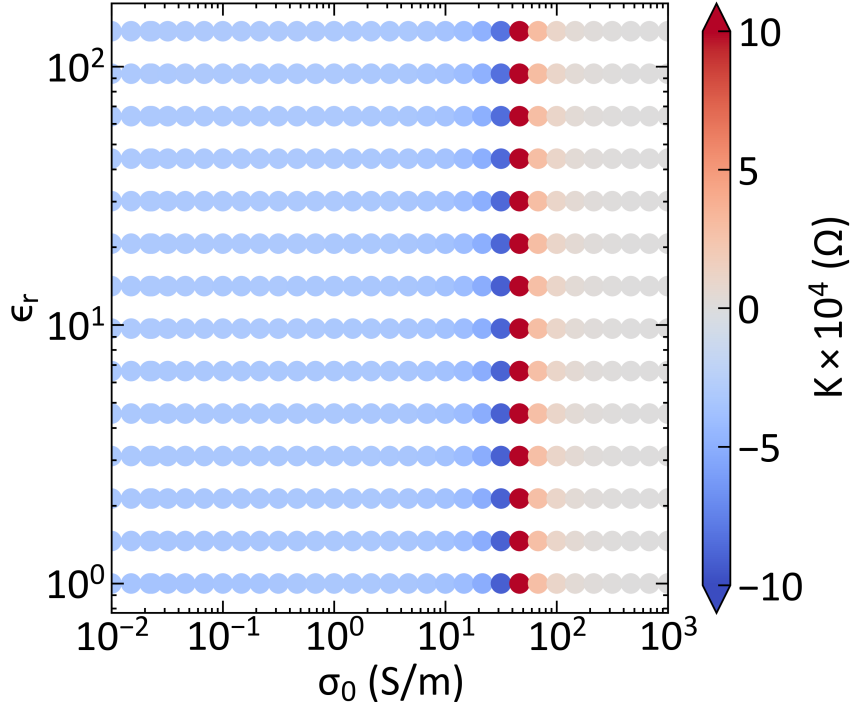


Figure 2.5: Sensitivity constant K for a 1000 nm thick film with varying dielectric (ϵ_r) and σ_0 calculated by simulating $\Delta\sigma_{\text{sim}} = 0.01$ S/m.

Comparing the simulated K to values from the analytical model in Equation 2.27, we find that the effective $\epsilon_r = 1.66 - 1.85$, indicating that neither ϵ_r for air, glass, or the thin film sample are appropriate.

Simulations allow us to explore the effect of varying the conductivity, dielectric, and thickness of the thin film. Figure 2.5 shows the effect of varying the conductivity σ_0 and dielectric ϵ_r of a 1000 nm thin film deposited on Eagle XG glass. We notice several things. First, K is independent of ϵ_r , indicating that the dielectric constant of the thin film does not affect the sensitivity factor. Second, for a 500 nm (1000 nm) thick film, K is relatively constant until $\sigma_0 \approx 40$ S/m (10 S/m) at which point there is a pole: K becomes extremely negative, and then extremely positive, and then settles in at a value slightly greater than zero. The change in sign results from the conductive thin film changing the resonant properties of the cavity such that small

increases in the film's conductivity result in an increase in reflected microwave power. This phenomenon is also present in the analytical model in Equations 2.25 and 2.27, where the upper sign represents the absorption and lower sign represents the emission of microwaves induced by the change in sample conductivity.⁹ K is also insensitive to thickness changes in the sample if σ_0 is small.

To conclude, for thin samples of low conductivity, f_0 , R_0 , and ΔW of the resonance peak for the loaded cavity should not significantly change compared to the parameters extracted from the resonance peak for the cavity loaded with blank glass. Under these conditions, $K = -33800(1400) \Omega$. Otherwise, K must be simulated for the sample. To do the simulations accurately, the thickness of the sample must be measured and explicitly simulated, and the simulated conductivity of the film should be iteratively changed until the simulated and experimental resonance curves match. Then, a small $\Delta\sigma$ should be simulated, and K calculated using Equation 2.33.

2.5 Other Types of Samples

The advantage of simulating the sensitivity constant is that we can study samples other than uniform thin films.^{13,15,16} The actual sample geometry must be simulated, and the dielectric constant and conductivity of the sample must be known or measured. It may be possible to model these by matching the simulated and experimental resonance curve, though a good reference value is needed.

To measure non-standard samples such as single crystals of low-conductivity semiconductors, we attach the crystal to a Eagle XG substrate with Scotch double-

Adapted with permission from Elbaz, G. A.; Straus, D. B.; Semonin, O. E.; Hull, T. D.; Paley, D. W.; Kim, P.; Owen, J. S.; Kagan, C. R.; Roy, X. *Nano Lett.* **2017**, *17*, 1727–1732 and Semonin, O. E.; Elbaz, G. A.; Straus, D. B.; Hull, T. D.; Paley, D. W.; Van der Zande, A. M.; Hone, J. C.; Kymissis, I.; Kagan, C. R.; Roy, X.; Owen, J. S. *J. Phys. Chem. Lett.* **2017**, *8*, 6092–6093. Copyright 2017 American Chemical Society.



Figure 2.6: A crystal of the perovskite methylammonium lead iodide attached to a glass substrate using double-sided Scotch tape. The width of the substrate is 25.2 mm.

sided tape (Figure 2.6). We confirm by taking resonance curves of glass with and without tape attached that the tape does not affect the resonance characteristics of the cavity and we pulse 532 nm light on the tape to confirm it is not responsible for the TRMC signal.

We use image analysis to map the dimensions of the crystal, and use calipers to measure its thickness. We simulate the crystal with two thicknesses: at its thinnest part and at its thickest, and report the average value with the range as the uncertainty. The simulated electric field strength around the crystal in Figure 2.6 loaded in the microwave cavity is shown in Figure 2.7.

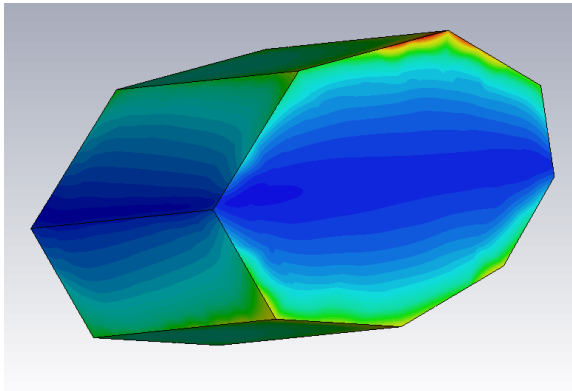


Figure 2.7: Simulated electric field distribution for the crystal in Figure 2.6.

We redefine the sensitivity constant

$$K = \frac{P_1 - P_0}{l \Delta\sigma_{sim}} \quad (2.34)$$

where l is the thickness of the crystal in which conductivity is simulated to increase. $l\Delta\sigma_{sim} \propto \Delta G_{sim}$, so this is an equivalent formalism to Equation 2.33.

Experimentally,

$$l\Delta\sigma = \frac{\Delta P}{P_0} \left(\frac{F_I}{K} \right) \quad (2.35)$$

where F_I is a correction for Gaussian illumination. If I_0 is taken to be the maximum fluence at the center of the Gaussian beam, then F_I is computed using a modified form of Equation 2.30 with integration performed only over the area of the waveguide that the crystal occupies:

$$F_I = \frac{\iint_S \sin^2 \left(\frac{\pi x}{a} \right) dS}{\iint_S \exp \left(-2 \left(\frac{(x-\frac{a}{2})^2}{w_0^2} + \frac{(y-\frac{b}{2})^2}{w_0^2} \right) \right) \sin^2 \left(\frac{\pi x}{a} \right) dS} \quad (2.36)$$

The mobility-quantum yield product is thus

$$\phi\Sigma\mu = \phi(\mu_e + \mu_h) = \frac{l\Delta\sigma_{max}}{qI_0F_A} \quad (2.37)$$

Accounting for Gaussian illumination using Equation 2.30 may introduce some error. In CST, we cannot simulate a Gaussian profile for the conductivity change, so we assume that the photoinduced conductivity change is uniform over the face of the crystal. If the crystal(s) is(are) small and centrally located in the waveguide, Equation 2.36 should not introduce significant error. If the crystal is very large, different optics can be used to achieve a smaller spot size on the crystal so this approximation can be used. Read et al. use this approach, in which the beam is focused to a small ($< 1 \text{ mm}^2$) area and simulate K using this spot size.¹³ This will minimize error from a nonuniform beam profile at the expense of a much higher photoexcitation density, which may lower the yield of free carriers through Auger recombination and at sufficiently high densities may even damage the sample.

Sensitivity factors for crystals are orders of magnitude lower than for thin films. For the perovskite crystal shown in Figures 2.6 and 2.7, we model $\epsilon_r = 60$ and $\sigma = 0.167$ S/m.^{17,18} We assume the conductivity change from illumination only occurs in the top 50 μm of the crystal based on the absorption coefficient of methylammonium lead iodide.¹⁶ Setting $\Delta\sigma = 0.01$ S/m, we find $K = -22.6 \Omega$, which is three orders of magnitude lower than we find for thin films but in line with what Reid et al. find for single crystals.¹³ We note that the simulated sensitivity constants only weakly depend on the dark conductivity of the crystal and change by $<1\%$ if the conductivity is varied from 0 to 1 S/m. However, changes in the crystal dielectric constant greatly affect K .

2.6 References

- (1) Kunst, M.; Beck, G. *J. Appl. Phys.* **1986**, *60*, 3558–3566.
- (2) Kroeze, J. E.; Savenije, T. J.; Vermeulen, M. J. W.; Warman, J. M. *J. Phys. Chem. B* **2003**, *107*, 7696–7705.
- (3) Warman, J. J. M.; De Haas, M. P.; Verhoeven, J. W.; Paddon-Row, M. N.; Verhoeven, J. W. In *Adv. Chem. Phys. Electron Transf. - from Isol. Mol. to Biomol. Part 1*, Jortner, J., Bixler, M., Eds.; Wiley: New York, 1999; Vol. 106, pp 571–601.
- (4) Pierret, R. F., *Advanced semiconductor fundamentals*, 2nd; Prentice Hall: Upper Saddle River, 2003.
- (5) Fox, M., *Optical Properties of Solids*; Oxford University Press: New York, 2001.
- (6) Gibson, A. *Proc. Phys. Soc. Sect. B* **1956**, *488*.

- (7) Klimov, V. I. V.; Mikhailovsky, A. A.; McBranch, D. W.; Leatherdale, C. A.; Bawendi, M. G. *Science* **2000**, *287*, 1011–1013.
- (8) Kroeze, J. E.; Savenije, T. J.; Warman, J. M. *J. Am. Chem. Soc.* **2004**, *126*, 7608–18.
- (9) Infelta, P. P.; de Haas, M. P.; Warman, J. M. *Radiat. Phys. Chem.* **1977**, *10*, 353–365.
- (10) Warman, J. M.; De Haas, M. P.; Hummel, A. *Chem. Phys. Lett.* **1973**, *22*, 480–483.
- (11) Warman, J. M.; Infelta, P. P.; De Haas, M. P.; Hummel, A. *Can. J. Chem.* **1977**, *55*, 2249–2257.
- (12) Savenije, T. J.; Ferguson, A. J.; Kopidakis, N.; Rumbles, G. *J. Phys. Chem. C* **2013**, *117*, 24085–24103.
- (13) Reid, O. G.; Moore, D. T.; Li, Z.; Zhao, D.; Yan, Y.; Zhu, K.; Rumbles, G. *J. Phys. D. Appl. Phys.* **2017**, *50*, 493002.
- (14) Kunst, M.; Beck, G. *J. Appl. Phys.* **1988**, *63*, 1093–1098.
- (15) Elbaz, G. A.; Straus, D. B.; Semonin, O. E.; Hull, T. D.; Paley, D. W.; Kim, P.; Owen, J. S.; Kagan, C. R.; Roy, X. *Nano Lett.* **2017**, *17*, 1727–1732.
- (16) Semonin, O. E.; Elbaz, G. A.; Straus, D. B.; Hull, T. D.; Paley, D. W.; van der Zande, A. M.; Hone, J. C.; Kymissis, I.; Kagan, C. R.; Roy, X.; Owen, J. S. *J. Phys. Chem. Lett.* **2016**, *7*, 3510–3518.
- (17) Onoda-Yamamuro, N.; Matsuo, T.; Suga, H. *J. Phys. Chem. Solids* **1992**, *53*, 935–939.
- (18) Stoumpos, C. C.; Malliakas, C. D.; Kanatzidis, M. G. *Inorg. Chem.* **2013**, *52*, 9019–9038.

Chapter 3

The Effects of Inorganic Surface Treatments on Photogenerated Carrier Mobility and Lifetime in PbSe Quantum Dot Thin Films

Abstract

We use flash-photolysis, time-resolved microwave conductivity (TRMC) to probe the carrier mobility and lifetime in PbSe quantum dot (QD) thin films treated with solutions of the metal salts of Na₂Se and PbCl₂. The metal salt treatments tune the Pb:Se stoichiometry and sweep the Fermi energy throughout the QD thin film bandgap. A stoichiometric imbalance favoring excess Se heavily *p*-dopes the QD thin film, shifts the Fermi energy toward the valence band, and yields the highest TRMC

Reprinted with permission from Elsevier from Goodwin, E. D.; Straus, D. B.; Gauling, E. A.; Murray, C. B.; Kagan, C. R. *Chem. Phys.* **2016**, *471*, 81-88.

mobility and lifetime. Introducing Pb first compensates the p -doping and shifts the Fermi level through mid-gap, decreasing the TRMC mobility. Further Pb addition creates an excess of Pb, n -dopes the QD thin film, moves the Fermi level to near the conduction band, and again increases the TRMC mobility. The increase in TRMC mobility as the Fermi energy is shifted toward the band edges by non-stoichiometry is consistent with the QD thin film density of states.

3.1 Introduction

Colloidal semiconductor quantum dots (QDs) are of current interest for their size, shape, and compositionally tunable electronic, optical, and thermal properties¹⁻⁴ as well as the simple and low-cost, solution-based methods available to synthesize QDs and assemble QD thin films. For example, QD thin films have been incorporated as the semiconductor active layer in electronic transistors and circuits;⁵⁻⁹ optoelectronic solar photovoltaics,¹⁰⁻¹⁵ photodetectors,¹⁶⁻¹⁹ and light-emitting diodes;^{20,21} and thermoelectric devices.²² To design QDs and QD thin films for integration into devices, the electronic structure and the charge carrier dynamics, namely the carrier mobility and lifetime, of the QDs and QD thin films must be tailored.

The physical and electronic structure of colloidal QD thin films differ from those of bulk semiconductors, presenting both challenges and opportunities. Wet-chemical synthetic methods are typically used to prepare colloidal QDs capped with long, insulating, organic ligands. Solvents are used to isolate the QDs from the growth medium and to assemble thin films of closely-packed QDs separated by these long ligands. To reduce the interparticle spacing and design QD materials for electronic applications, the insulating ligands are replaced with short organic ligands, such as 3-mercaptopropionic acid (MPA),^{23,24} or compact inorganic ligands, such as chalcogenides,²⁵ halides,¹³ or

the pseudohalide thiocyanate.²⁶ The solvents used in post-synthesis purification and in thin film deposition and the ligand exchange process can strip surface atoms,^{27–29} creating vacancies at the QD surface. Unlike bulk semiconductors with well-defined conduction and valence bands separated by a forbidden energy gap, the density of electronic states for QD thin films is constructed from a high density of quantized conduction and valence band states (or LUMO and HOMO) and localized mid-gap and tail states introduced by vacancies at the QD surface and by interfacial states introduced in electronic devices used to probe carrier transport. These mid-gap electronic states are undesirable and act as traps which inhibit charge carrier transport⁵ and limit carrier lifetime.¹¹ Infilling the QD thin film with an inorganic matrix by atomic layer deposition has been shown to passivate the QD surface and increase the carrier mobility and lifetime.^{30,31} Recent introduction of surface chemical modifications have been reported to enrich the QD surface in metal and/or chalcogen or halide ions^{28,32–36} that serve to dope the QD thin films and passivate surface traps, controlling the charge carrier type, concentration, mobility, and lifetime. For example, PbSe QD thin films surface-enriched with Se were doped p-type, but the surfaces were unstable and susceptible to oxidation and structural transformation. Subsequent Pb enrichment of the QD surface passivated the unstable Se surface and n-doped the QD films.³⁷ Similar structural transformations in PbS QD thin films have been reported for S-enriched surfaces³⁸ or through solvent stripping of surface ligands and atoms.^{39,40} Surface passivation has been shown to increase the lifetime of photogenerated carriers^{28,41} and doping shifts the Fermi level closer to the conduction or valence band, allowing carriers to populate these higher densities of states, and leads to the higher carrier mobilities reported in field-effect transistor (FET) measurements.^{5,37}

PbSe QDs are particularly attractive as solar cell materials because of their broad absorption that spans the solar spectrum and the promise of increased power conver-

sion efficiencies through multiple-exciton generation.^{42,43} However, the photogenerated charge carrier lifetime is equally as important as mobility to device performance.⁴⁴ Flash-photolysis time-resolved microwave conductivity (TRMC) is a technique by which the lifetime and mobility of photogenerated charge carriers can be measured independently of each other and it has been used previously to study the optoelectronic properties of QD thin films.^{45,46} Unlike more traditional methods used to determine carrier mobilities, such as FET and time-of-flight (TOF) photoconductivity measurements, TRMC is a contactless measurement. TRMC is therefore not influenced by the properties of metal-semiconductor junctions which may introduce Fermi level pinning, electron-hole recombination, and contact resistance, which have been shown to affect the measured charge carrier dynamics in QD thin films.^{12,47} TRMC also differs from these traditional methods because it measures conductivity at zero DC electric field, without a gate field which is applied in FET measurements, and probes a length scale of tens to hundreds of nanometers, so larger scale features like grain boundaries and cracks found across the channel length of FETs or through thick layers needed for TOF measurements have little effect on the results.⁴⁸

In this work, we study the influences of commonly and recently introduced small-organic and compact, inorganic ligand exchange treatments on the photogenerated charge carrier mobility and lifetime of PbSe QD thin films by TRMC. Electron microscopy, optical absorption, and FET measurements are used to characterize the structural, optical, and electronic properties of the QD films for each ligand treatment. We show that the photogenerated charge carrier mobility depends on the position of the Fermi energy in the semiconductor bandgap and is largest near the band edges, consistent with the trend in FET measurements and with the QD thin film density of states.

3.2 Experimental Methods

3.2.1 Synthesis

6 nm PbSe QDs with a first absorption peak at 1725 nm are synthesized using a previously published method⁴⁹ modified to increase yield.⁵⁰ In short, 1.78 g of PbO (99.999%), 40 mL of 1-octadecene (90%), and 6 mL of oleic acid (OA) (90%) are heated in a 125 mL 3 neck flask under vacuum on a Schlenk line for 1.5 h to form a lead oleate complex. The flask is then switched to nitrogen and the solution heated to 180 °C. At 180 °C, a solution of 16 mL of 1 M Se (99.999%) in tri-n-octylphosphine (90%) (previously prepared) and 138 μ L of diphenylphosphine (98%) (added just beforehand) are rapidly injected into the lead oleate solution. The temperature is then dropped to \sim 150 °C, held at this temperature for 10 min, and removed from heat to cool. Once cooled to room temperature, the solution is transferred into a Schlenk tube using a cannula and brought into a nitrogen glovebox for purification. The solution is purified by 3 repeated steps of precipitating the QDs with a 2:1 anhydrous butanol:ethanol mixture, centrifugation, and redispersion in anhydrous toluene. The QDs are redispersed in 20 mL of anhydrous hexane for storage. The anhydrous solvents and reagents used in synthesis are all purchased from Sigma-Aldrich.

Before depositing thin films from the QD dispersions, the particles are precipitated with anhydrous isopropanol (Acros) in a 1:3 ratio and centrifuged. The supernatant is discarded and the remaining solvent evaporated. The QDs are re-dispersed at 10 mg/mL in anhydrous octane (Sigma-Aldrich).

3.2.2 PbSe QD Thin Film Deposition

PbSe QD thin film deposition for optical characterization and FET and TRMC measurements is carried out in a nitrogen-filled glovebox and followed the procedure of Oh et al.³⁷ QD thin films for FETs are assembled on n++ silicon wafers (Silicon Inc.) with a 250 nm thermal oxide layer. 20 nm of Al₂O₃ is deposited by atomic layer deposition (ALD). The oxidized wafers are then cleaned by sonication in ethanol for 5 min and then UV-ozone treated in the nitrogen glovebox for 20-30 min. QD thin films for optical characterization and TRMC measurements are assembled on aluminosilicate float glass (Delta Technologies) that were cleaned by sonication in Hellmanex detergent in water, de-ionized water (3x), 0.1-1.0 M HCl (Fisher), de-ionized water (3x), and ethanol (3x). The aluminosilicate glass surface is coated with a (3-mercaptopropyl)-trimethoxysilane (MPTS, Sigma-Aldrich, 95%) self-assembled monolayer according to modified literature procedures.⁵¹ The MPTS layer prevents delamination of the QDs during subsequent surface treatment.⁵² The PbSe QDs dispersed in octane are spin-cast in the nitrogen glovebox at 800 rpm for 20 s followed by 4000 rpm for 5 s.

We exchange the long oleic acid ligands used to synthesize and disperse the PbSe QDs for short organic and compact inorganic ligands, namely by treatment with 3-mercaptopropionic acid (MPA), Na₂Se, and Na₂Se followed by PbCl₂. For MPA treatment, a 1% MPA (Sigma-Aldrich, 99%) solution in anhydrous methanol (Acros) is deposited on the QD film on the spinner, held for 3 s, dried by spinning at 4000 rpm, and rinsed twice with methanol. For Na₂Se treatment, a 1 mM Na₂Se (Alfa Aesar, 99.8%) solution in methanol is deposited on the QD film on the spinner, held for 10 s, dried by spinning at 4000 rpm, and rinsed twice with methanol. The sequence of QD spin-casting and ligand exchange is carried out an additional two times to form uniform, crack-free QD thin films approximately 50 nm in thickness. The thickness is measured using an atomic force microscope (Asylum). For subsequent

PbCl₂ treatment, the three-layer, Na₂Se-treated QD thin films are immersed in 15 mM PbCl₂ (Sigma-Aldrich, 99.999%) in oleylamine on a hotplate at 80 °C for either 1 min, 15 min, 1 h, or 24 h. The QD films are then washed with anhydrous hexane to remove excess oleylamine, and then washed three times with anhydrous isopropanol.

3.2.3 Structural, Optical, and Electrical Characterization

Thinner PbSe QD thin films for TEM characterization are prepared as described above, but by diluting the QD dispersion in octane to ~1 mg/mL and by depositing only a single layer. TEM is performed on a JEOL 2100 microscope operating at 200 keV.

Fourier-transform infrared (FTIR) spectra are taken on a Thermo-Fisher Nicolet 6700 spectrophotometer in transmission mode. The FTIR absorption spectra are normalized using the height of the first excitonic peak from the near-infrared (NIR) absorption spectra of the same QD films. NIR spectra are taken on an Agilent Cary 5000 spectrophotometer at 2 nm spectral bandwidth in transmission mode. NIR measurements reported herein are taken on QD thin films that were encapsulated in the nitrogen glovebox using cover glass and epoxy.²⁸

Cr (20 nm) and Au (30 nm) top contacts are deposited by thermal evaporation through a shadow mask onto the PbSe QD thin films deposited on Si wafers to make top-contact, bottom-gate FETs. Channel lengths (L) range from 50-200 μm and channel widths (W) range from 750-3000 μm with a constant W/L of 15 for all channels. FET measurements are performed in a Karl Suss PM5 probestation mounted in a nitrogen glovebox and measured on an Agilent 4156C semiconductor parameter analyzer.

3.2.4 Flash-Photolysis Time-Resolved Microwave Conductivity

Flash-photolysis, time-resolved microwave conductivity (TRMC) measurements are used to perform contactless carrier mobility and lifetime measurements.⁵³⁻⁵⁶ The theory of TRMC and our experimental setup are described in detail in Chapter 2. Briefly, X-band (9 GHz) microwaves are generated using a voltage-controlled oscillator (SilversIMA) with the frequency controlled by a Keithley 2220-30-1 power supply. Microwaves are passed through an isolator (Pasternack) to prevent back reflection and then through a variable attenuator set to 10 dB (Keysight). A circulator (Pasternack) directs microwaves from the source into a microwave antenna (Penn Engineering), transferring microwaves from coaxial cable to a WR90 waveguide connected to a home-built, sealed, resonant microwave cavity (Figure 2.1). The resonant microwave cavity is loaded with each sample in the nitrogen-filled glovebox to prevent sample oxidation. 3-5 ns, 532 nm laser pulses are generated by a Continuum MiniLite II Nd:YAG laser and focused through an aperture into the resonant cavity, expanding to a ~7 mm spot diameter at the sample. The circulator directs reflected microwaves into a microwave switch that allows us to visualize the resonance peak on an HP 8566B spectrum analyzer, or to convert microwave power to voltage on a Keysight 8472B microwave detector. Detected microwave power is amplified through an impedance-matching 25x amplifier (Comlinear CLC-221) and microwave transients are digitized using a Tektronix TDS3054B oscilloscope. To measure the incident microwave power on resonance in the absence of light, the voltage from the microwave detector is recorded on the oscilloscope, and to measure photoinduced microwave transients, a high pass filter with a cutoff frequency of 0.16 Hz is used to cancel the DC offset.

The selection of a resonant cavity significantly increases the measurable signal at the expense of an increased instrumental response time.⁵³ However, because the

cavity response time is determined from the resonance peak, the mobility is calculated by deconvolving the cavity response time from the measured signal.⁵⁷ Let h be the experimentally measured TRMC signal, f the sample response, g the cavity response, $*$ the convolution operator, and \mathcal{F} denote a Fourier transformation. Then, $f * g = h$ such that

$$\begin{aligned}\mathcal{F}(h) &= \mathcal{F}(f * g) \\ &= \mathcal{F}(f) \cdot \mathcal{F}(g), \\ \mathcal{F}(f) &= \frac{\mathcal{F}(h)}{\mathcal{F}(g)},\end{aligned}$$

and

$$f = \mathcal{F}^{-1}\left(\frac{\mathcal{F}(h)}{\mathcal{F}(g)}\right).$$

Because of noise introduced by the deconvolution process, fifty deconvolved data points are binned and averaged for mobility calculations. Figure 3.1 shows the experimental TRMC data (h) in blue, and the binned sample's response (f) in red.

3.3 Results and Discussion

We deposit thin films of 6 nm diameter oleic acid (OA)-capped PbSe QDs by spin-coating and by subsequently treating the QD thin films in solutions of MPA, Na₂Se, and Na₂Se followed by PbCl₂. The MPA ligand is chosen for comparison because it is commonly used in lead chalcogenide QD solar cells.^{24,58} Na₂Se and PbCl₂ treatments are chosen because they have been shown to dope PbSe QD thin films p- or n-type, respectively.³⁷ TEM, FTIR and NIR spectroscopy, and FET measurements are used to structurally, chemically and electronically characterize the thin films studied here.

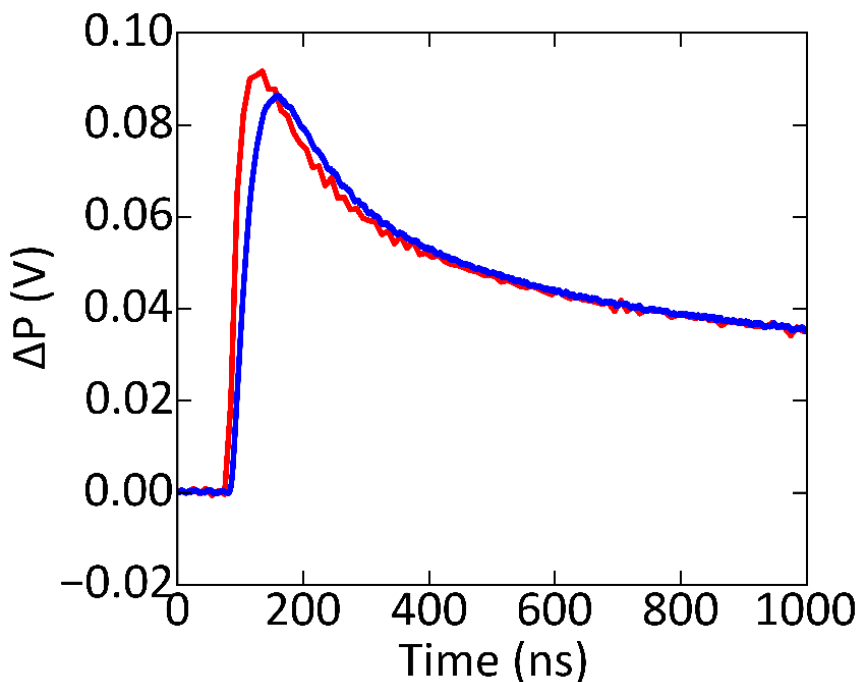


Figure 3.1: Deconvolution. The original TRMC trace is in blue, and the deconvolved sample response is in red.

3.3.1 Structural and Optical Characterization of PbSe QD Thin Films

To characterize the interparticle spacing and nanoscale structure, TEM images are taken of OA-capped and MPA, Na_2Se , and Na_2Se and then 1 h PbCl_2 -treated PbSe QD thin films (Figure 3.2a-d). A decrease in interparticle spacing is observed upon ligand treatment, as desired to transform the QD films into electronically active materials. QD thin films treated with MPA (Figure 3.2b) retain their single particle character and partially transform from hexagonal to square packing, as reported previously.⁴⁷ In contrast, QD films treated with Na_2Se , show the onset of epitaxial, oriented attachment of QDs, as has also been previously reported.³⁷ We note that the degree of oriented attachment increases over time, even as the QD film remains at room temperature in the nitrogen-filled glovebox, representative of the TEM image shown in Figure 3.2c. QD thin films treated with Na_2Se and then immediately with

PbCl₂ (Figure 3.2d), as exemplified for a 1 h treatment, display a small interparticle spacing, without significant epitaxial, oriented attachment, as the Pb and Cl ions passivate surface Se sites and arrest QD fusion.³⁷ We also note that the added surface Pb sites are passivated by oleylamine and/or Cl atoms during the PbCl₂ treatment, further protecting the QDs from fusion and oxidation.

FTIR measurements are performed on the OA and ligand treated PbSe QD thin films to characterize the removal of the organic capping layer as shown in Figure 3.2e, highlighting the C-H stretching region. The FTIR absorption spectrum of an OA-capped PbSe QD thin film is included in the inset of Figure 3.2e. The FTIR spectra before and after ligand treatment show 86-93% removal of OA ligands by all treatments, as expected and reported previously^{24,37} and consistent with the observed decrease in interparticle spacing presented above in TEM images.

NIR absorption measurements are performed on OA-capped and ligand treated PbSe QD thin films, as shown in Figure 3.2f. The QD films are allowed to sit for 6 h in the nitrogen atmosphere of the glovebox before measurement to more closely reflect the films measured in TEM above and described below in FET and TRMC measurements. OA-capped PbSe QD thin films display a first exciton peak at 1728 nm. The absorption spectrum of Na₂Se-treated QD films show a 31 meV red shift, caused by QD fusion during the 6 h wait time and the addition of a Se layer to the QD surface. Spectra of QD films treated with PbCl₂ for 1 min, 15 min, 1 h, or 24 h immediately after Na₂Se treatment show red shifts of 26-29 meV. We note the longer PbCl₂ treatment times are observed to result in a smaller red shift in the QD film absorption resonance, as the PbCl₂ treatment arrests QD fusion caused by the unstable, Se rich surfaces, consistent with the TEM images. The absorption spectrum of PbSe QD thin films treated with MPA show a red shift of 23 meV compared to that for OA-capped QD films, consistent with the reduced interparticle spacing, noting

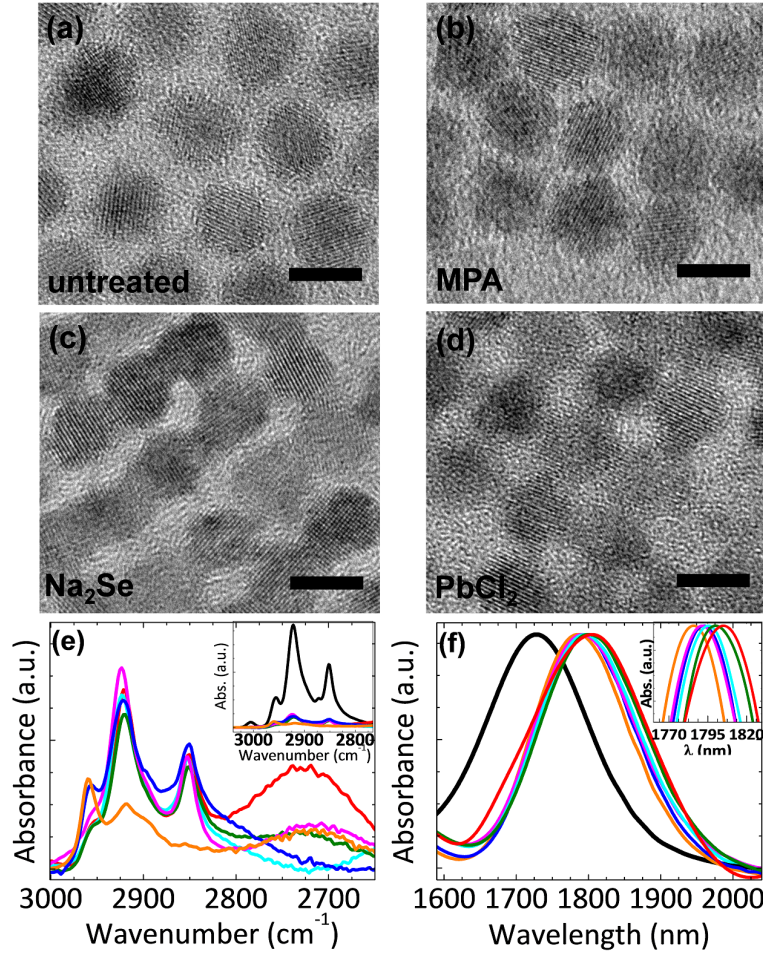


Figure 3.2: (a-d) TEM images and normalized (e) FTIR and (f) NIR absorption spectra of (a) an OA-capped PbSe QD thin film (black) and of PbSe QD thin films treated with (b) MPA (orange), (c) Na₂Se (red), and Na₂Se immediately followed by PbCl₂ for 1 min (green), 15 min (cyan), 1 h (blue), and 24 h (pink). The PbSe QD film shown in (d) is treated for 1 h in PbCl₂ immediately after Na₂Se treatment. Scale bars are 6 nm. (e) Inset: FTIR spectra highlighting the OA-capped PbSe QD thin film (black). Fourier-transform filtering is applied to the NIR absorption spectra to remove the interference pattern caused by the cover glass-QD film-glass stack.

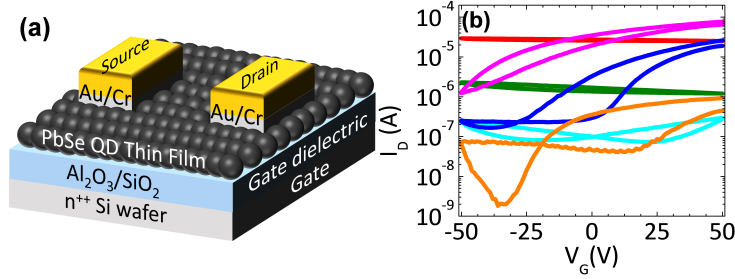


Figure 3.3: (a) Diagram of a bottom-gate, top-contact FET fabricated from PbSe QD thin films. (b) Transfer curves of PbSe QD thin films treated with MPA (orange), Na_2Se (red), and Na_2Se followed by PbCl_2 for 1 min (green), 15 min (cyan), 1 h (blue), and 24 h (pink). $V_{DS} = -50$ V for QD thin films treated with Na_2Se and Na_2Se followed by PbCl_2 for 1 min and 15 min. $V_{DS} = +50$ V for QD thin films treated with MPA and Na_2Se followed by PbCl_2 for 1 h and 24 h.

little to no QD fusion is observed and no ionic layer is added in the MPA treatment.

3.3.2 Electrical Transport Measurements in PbSe QD Field-Effect Transistors

To confirm the charge carrier type and relative carrier concentration of ligand treated PbSe QD thin films, thin films are integrated into FETs to form the semiconducting channel layer (Figure 3.3a). Transfer curves of the devices are shown in Figure 3.3b. Na_2Se -treated QD films become degenerately p-doped by the introduction of excess Se, consistent with the Fermi level shifting towards the valence band. Successive PbCl_2 treatment after Na_2Se treatment adds Pb ions to the QD surface, shifts the stoichiometric imbalance towards excess Pb, and moves the Fermi level towards the conduction band. Pb addition first compensates the Se p-doping at short 1 min and 15 min treatment times and then increasingly n-dopes the devices with longer 1 h and 24 h treatment times. In contrast, MPA-treated PbSe QD thin films are highly resistive and show ambipolar, predominantly n-type transport. These FET characteristics reproduce reports of similarly treated PbSe QD thin films.^{37,47}

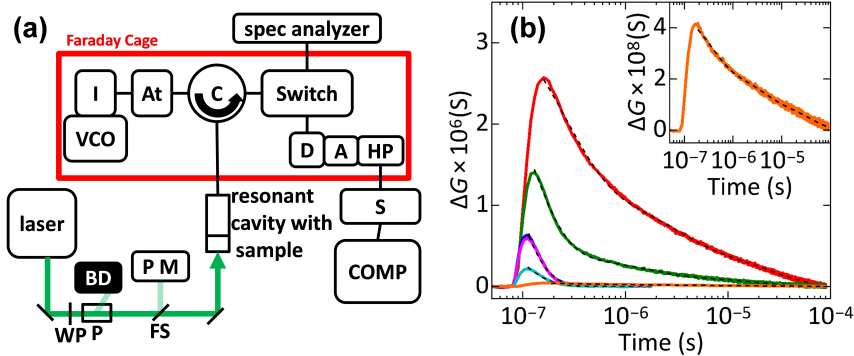


Figure 3.4: (a) Diagram of the home-built, TRMC setup showing the VCO: voltage controlled oscillator (microwave source), I: isolator, At: 10dB attenuator, C: microwave circulator, microwave switch, spectrum analyzer, D: microwave power detector, A: amplifier, HP: high pass filter, S: oscilloscope, and computer. Also shown is the laser (532 nm) and optics for controlling and delivering the light to the sample. WP: rotating half wave plate, P: polarizer, BD: beam dump, FS: UV-fused silica window, and P M: power meter. (b) Example photoconductance transients of PbSe QD thin films treated with Na₂Se (red) and Na₂Se followed by PbCl₂ for 1 min (green), 15 min (cyan), 1 h (blue), and 24 h (pink). Inset: Photoconductance transient of MPA (orange) treated PbSe QD thin film. Dashed lines show fits (see text for details).

3.3.3 Flash-Photolysis Time-Resolved Microwave Conductivity

To characterize the photogenerated charge carrier mobility and lifetime, the treated QD films are probed in a home-built, flash-photolysis, time-resolved microwave conductivity (TRMC) measurement apparatus (Figure 3.4a). Example photoconductance (ΔG) transients of the treated QD films are shown in Figure 3.4b for the largest excitation intensity, as this data shows the best signal-to-noise ratio. The Na₂Se-treated QD film show the largest ΔG , noting the sample is allowed to fuse in the nitrogen atmosphere of the glovebox prior to measurement. The impact of QD fusion on the TRMC measurements will be discussed below. As Pb is added by successive PbCl₂ treatments for times of 1 min and 15 min, ΔG decreases. For longer 1 h and 24 h PbCl₂ treatment times, an increase in ΔG is observed. MPA-treated QD thin films display the smallest ΔG and are highlighted in the inset of Figure 3.4b.

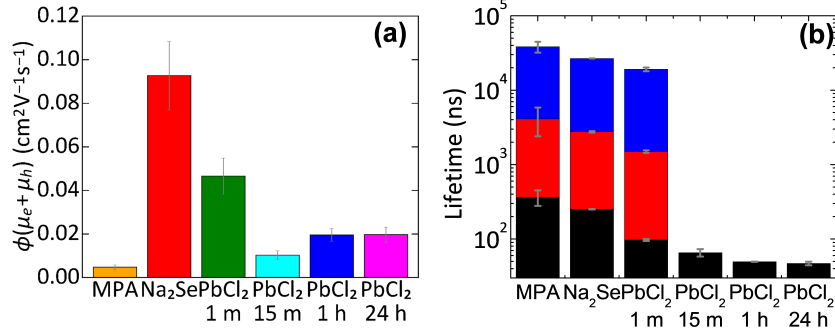


Figure 3.5: (a) $\phi\Sigma\mu$ product at the lowest photoexcitation density in PbSe QD thin films treated with MPA (orange), Na_2Se (red), Na_2Se followed by PbCl_2 for 1 min (green), 15 min (cyan), 1 h (blue), and 24 h (pink). (b) Photogenerated charge carrier lifetimes from nonlinear least-squares fits of the photoconductance transient data to: the sum of three exponential decay functions for MPA, Na_2Se , and Na_2Se followed by 1 min PbCl_2 -treated (black, red, and blue showing lifetimes on the order of 100 ns, 1 μs , and 10 μs , respectively) and single exponential decay functions for Na_2Se followed by 15 min, 1 h and 24 h PbCl_2 -treated PbSe QD thin films. Error bars are one standard deviation.

Figure 3.5a shows the product of the quantum yield for charge generation and the sum of the electron and hole mobilities, $\phi\Sigma\mu$, for the treated PbSe QD thin films as measured by TRMC. Since the quantum yield for carrier generation has a maximum value of unity, the data presents a lower bound for charge carrier mobility, in convention with previous reports.^{46,59} We note and will discuss below that as shown in Figure 3.6, $\phi\Sigma\mu$ does not saturate even at the lowest photoexcitation density used in this work (~ 0.5 photoexcitations/QD), consistent with a quantum yield that is less than unity and with true carrier mobilities that are greater than what are reported here. The decrease in $\phi\Sigma\mu$ with increasing photoexcitation density is consistent with higher order recombination that occurs on timescales faster than the 14-27 ns response time of the microwave resonance cavity,^{45,46} as discussed in further detail below.

Table 3.1 reports the maximum $\phi\Sigma\mu$ for the differently treated PbSe QD thin films, calculated at the lowest photoexcitation density. MPA-treated QD films exhibit the lowest mobility of the QD films presented in this work and consistent with the

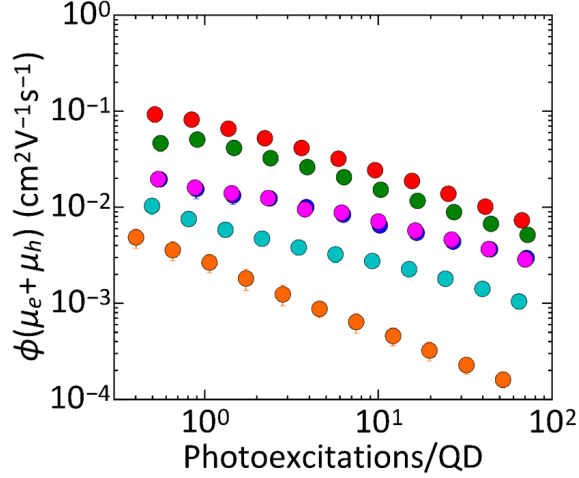


Figure 3.6: $\phi\Sigma\mu$ product vs photoexcitation density in PbSe QD thin films treated with MPA (orange), Na_2Se (red), Na_2Se followed by PbCl_2 for 1 min (green), 15 min (cyan), 1 h (blue), and 24 h (pink).

greater interparticle spacing and the lack of intentional doping. Ligand exchange with the inorganic Na_2Se salt increases the carrier mobility, consistent with the observed QD fusion and heavy p -doping introduced by excess Se. As the Se-rich QD thin films are treated with PbCl_2 , a lower mobility is observed after 1 min and further after 15 min. PbCl_2 treatment arrests QD fusion and the addition of surface Pb compensates the p -doping, shifting the Fermi level from the valence band toward mid-gap. Further PbCl_2 treatment for 1 h n -dopes the QD thin films and increases the carrier mobility. No further increase in mobility is seen upon longer PbCl_2 treatment times of 24 h. As greater amounts of Pb^{2+} is added to the surface, the Fermi level is swept through the QD thin film density of states, from the valence band, through mid-gap, toward the conduction band.

The ΔG transients in Figure 3.4b show that the lifetimes for MPA, Na_2Se , and Na_2Se followed by 1 min PbCl_2 -treated QD films persist for tens of μs through multi-exponential decay processes and the transients are fit to a sum of three exponential decays. The QD films treated with PbCl_2 for 15 min, 1 h, and 24 h show ΔG transients

Ligand Treatment	$\phi\Sigma\mu$ (cm ² V ⁻¹ s ⁻¹)	f_1	τ_1 (ns)	f_2	τ_2 (μ s)	f_3	τ_3 (μ s)
MPA	0.005 \pm 0.001	0.54 \pm 0.03	365 \pm 86	0.22 \pm 0.02	4.1 \pm 1.7	0.23 \pm 0.01	38.5 \pm 6.4
Na ₂ Se	0.09 \pm 0.02	0.674 \pm 0.005	252 \pm 2	0.137 \pm 0.003	2.76 \pm 0.07	0.190 \pm 0.003	26.68 \pm 0.03
Na ₂ Se + PbCl ₂ 1 min	0.047 \pm 0.08	0.908 \pm .004	97 \pm 3	0.061 \pm 0.003	1.50 \pm 0.06	0.030 \pm 0.001	19.1 \pm 1.1
Na ₂ Se + PbCl ₂ 15 min	0.010 \pm 0.002	–	66 \pm 8	–	–	–	–
Na ₂ Se + PbCl ₂ 1 h	0.020 \pm 0.002	–	50 \pm 1	–	–	–	–
Na ₂ Se + PbCl ₂ 24 h	0.020 \pm 0.003	–	47 \pm 3	–	–	–	–

Table 3.1: Summary of the quantum yield-mobility products ($\phi\Sigma\mu$) and the carrier lifetimes (s) extracted from TRMC transients of ligand exchanged PbSe QD thin films. $\phi\Sigma\mu$ shown is calculated at the lowest photoexcitation density.

that decay by a single exponential process on faster hundreds of ns timescales and are fit to a single exponential decay. Figure 3.5b and Table 3.1 summarize the charge carrier lifetimes extracted from the TRMC data shown in Figure 3.4b. The normalized fit amplitudes f_i corresponding to the lifetimes τ_i in Table 3.1 show the decrease in f_2 and f_3 in the Na₂Se followed by 1 min PbCl₂ treated films in comparison to the Na₂Se treated films, showing the progression from multi-exponential to single exponential decay processes.

The long tens of μ s lifetimes in MPA, Na₂Se, and Na₂Se followed by 1 min PbCl₂-treated films are consistent with reported spectroscopic measurements of carrier lifetime in PbSe QD thin films. A TRMC study by Gao et al.⁴⁵ reports a half-amplitude lifetime of tens of ns for 6 nm ethanedithiol (EDT) treated PbSe QD thin films with a long-lived component in the transient that extended to μ s.⁴⁵ Transient absorption measurements of MPA-treated PbS QD thin films report carrier lifetimes of 31 μ s and even longer 93 μ s lifetimes for EDT treated particles.²⁴

Figure 3.7 shows the dependence of carrier lifetime on photoexcitation density. For Na₂Se-treated QD films the lifetime increases at larger photoexcitation densities for all calculated lifetimes. We hypothesize that this increase in lifetime arises from greater trap filling at larger photoexcitation densities and therefore the charge carrier decay in the Na₂Se-treated PbSe QD films is dominated by trap-assisted recombination on the timescales probed by TRMC. No change in lifetime is observed for the 1

min PbCl₂-treated QD films with increasing photoexcitation density. In contrast, the lifetime for Na₂Se followed by 15 min, 1 h, and 24 h PbCl₂ treatments of the QD films decreases with increasing photoexcitation density. This decrease suggests that the charge carrier decays are largely dominated by bimolecular or higher-order recombination processes such as Auger recombination, and lifetimes are reported for excitation densities greater than a few per quantum dot to study the influence of these processes. In addition, the photoinduced change in conductivity $\Delta\sigma = q(\mu_e + \mu_h)\Delta N$, assuming unimolecular charge carrier kinetics, should scale linearly with the number of photoexcitations/QD. $\phi\Sigma\mu$, however, decreases with increasing photoexcitation density (Figure 3.6), consistent with higher order recombination processes that reduce the quantum yield for charges measured in TRMC.⁶⁰⁻⁶² The lifetimes for MPA-treated QD films do not show a clear trend with increasing photoexcitation density because of the large error in the low signal-to-noise data of these highly resistive thin films (Figure 3.8).

We note that the TRMC signals are convolved with the 3-5 ns laser pulse width, the ns response of the electronic circuitry, and the cavity response time of 14 to 27 ns (Figure 3.1). We deconvolve the cavity response time from the measured signal because it has the largest impact. Dynamics occurring on timescales shorter than several nanoseconds cannot be detected using the TRMC apparatus. The low TRMC mobilities measured for Na₂Se followed by 1 h and 24 h PbCl₂-treated QD films may be limited by charge trapping or decay within the TRMC instrument response time. Notably, the TRMC mobilities are smaller than the 25 cm² V⁻¹ s⁻¹ mobilities reported for Na₂S exchanged PbSe QD thin films studied by time-resolved terahertz spectroscopy (TRTS).⁶³ The same study also reports carrier lifetimes for Na₂S exchanged PbSe QD thin films of 1 ns or less, much shorter than the 200-27,000 ns lifetimes we report here for Na₂Se exchanged PbSe QD thin films. TRTS offers a complementary technique

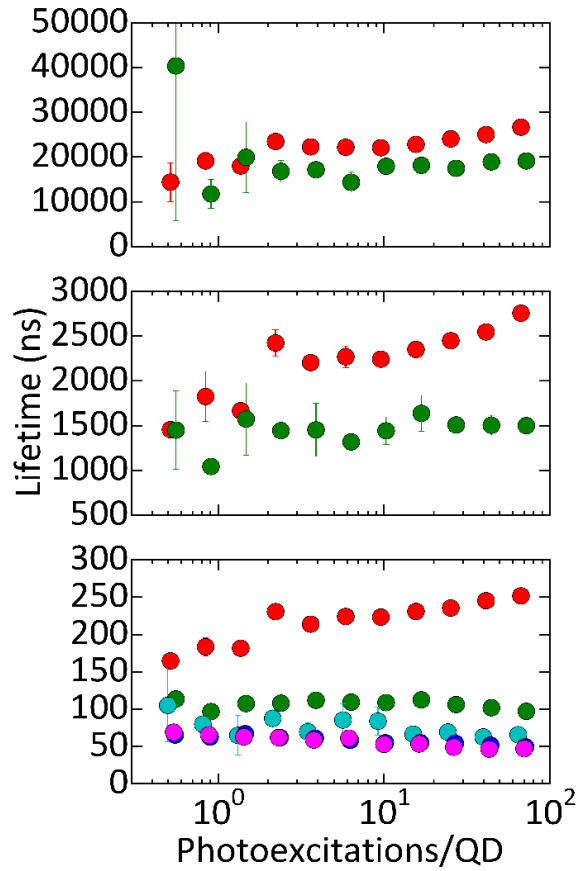


Figure 3.7: Photogenerated charge carrier lifetimes from nonlinear least-squares fits of photoconductance transient data to the sum of three exponential decay functions for Na₂Se (red), and Na₂Se followed by 1 min PbCl₂ (green) treatments and to a single exponential decay function for Na₂Se followed by PbCl₂ treatment for 15 min (cyan), 1 h (blue) and 24 h (pink) of PbSe QD thin films. Lifetimes on the order of 100 ns are shown in (a), 1 μ s in (b), and 10 μ s in (c). Error bars are one standard deviation.

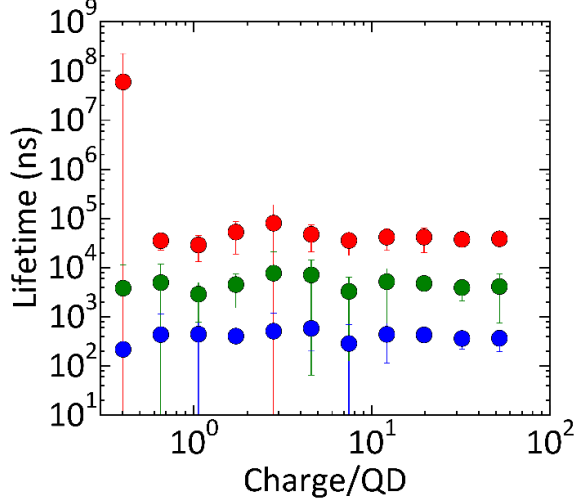


Figure 3.8: Photogenerated charge carrier lifetimes from nonlinear least-squares fits of photoconductance transient data to the sum of three exponential decay functions for MPA treated PbSe QD films. The shortest lifetime is shown in blue, the intermediate in green, and long in red. Error bars are one standard deviation.

that detects mobility and lifetime on a ps timescale; however, it does not reach the several ns- to- μ s timescale that is probed in TRMC measurements. We attribute the discrepancy in lifetimes to the fact that the two measurements probe different carrier dynamics occurring on different timescales. We note that the timescales measured in TRMC are of particular interest to photovoltaic applications as it is on those timescales that charge transport and collection occurs.²⁴

The degree of epitaxial, oriented attachment between PbSe QDs in thin films affects the red shift observed in NIR absorption measurements (Figure 3.9) and the measured TRMC carrier mobility (Figure 3.10), regardless of whether the QD thin film is enriched in Se or Pb. For example, PbSe QD thin films treated with Na₂Se and measured within 30 min of fabrication show a TRMC mobility of 0.04 cm² V⁻¹ s⁻¹. However, films stored in a nitrogen glovebox and measured 2-6 h after fabrication have a mobility of 0.09 cm² V⁻¹ s⁻¹ that is consistent over this storage time. To see how fusion would affect the mobility of subsequently PbCl₂- treated films, Na₂Se-treated

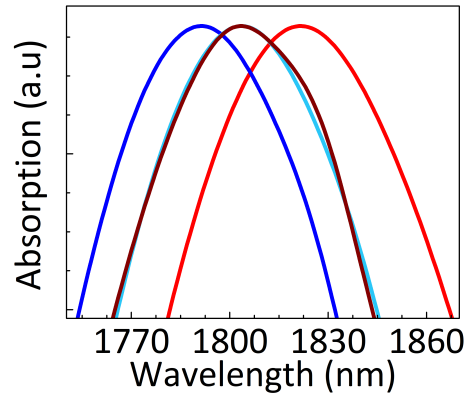


Figure 3.9: NIR absorption measurements of PbSe QD films immediately after Na_2Se treatment (maroon), after Na_2Se treatment and storage in a nitrogen glovebox for 6 h (red), after Na_2Se treatment followed by immediate PbCl_2 treatment for 1 h (blue), and after Na_2Se treatment and storage in a nitrogen glovebox for 24 h followed by 1 h PbCl_2 treatment (light blue).

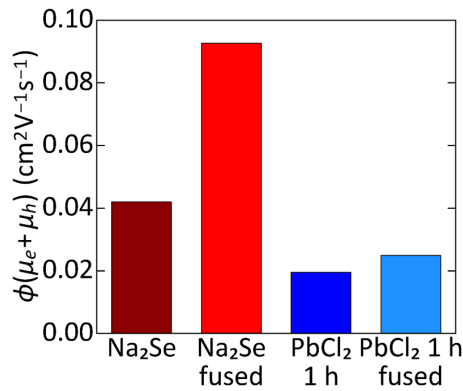


Figure 3.10: Quantum yield-mobility product for samples shown in Figure 3.9.

PbSe QD thin films are left to sit for 24 h in the nitrogen glovebox to allow for epitaxially oriented attachment prior to a 1 h PbCl_2 treatment. These films show an increase in TRMC mobility to $0.25 \text{ cm}^2 \text{ V}^{-1} \text{ s}^{-1}$ compared to $0.20 \text{ cm}^2 \text{ V}^{-1} \text{ s}^{-1}$ for films that are immediately treated with PbCl_2 for 1 h after Na_2Se treatment.

3.4 Conclusion

We use TRMC measurements to study the evolution in carrier dynamics in PbSe QD thin films as we enrich the QD surface in Se and Pb through treatments with inorganic Na₂Se and PbCl₂ salts and sweep the Fermi energy through the QD thin film density of states. Se-rich films are highly *p*-doped and demonstrated high carrier mobility and long lifetime. As increasing amounts of Pb are added to the surface of the QDs, the mobility first decreases as the Fermi level moves near mid-gap, and then increases again as QD films are *n*-doped and the Fermi level approaches the conduction band. Future experiments will explore the origin of the recombination processes leading to the long lifetimes seen for Se-enriched in comparison to the shorter lifetimes of Pb-enriched QD thin films.

3.5 References

- (1) Manna, L.; Milliron, D. J.; Meisel, A.; Scher, E. C.; Alivisatos, A. P. *Nat. Mater.* **2003**, *2*, 382–5.
- (2) Murray, C. B.; Norris, D. J.; Bawendi, M. G. *J. Am. Chem. Soc.* **1993**, *115*, 8706–8715.
- (3) Murray, C. B.; Kagan, C. R.; Bawendi, M. G. *Annu. Rev. Mater. Sci.* **2000**, *30*, 545–610.
- (4) Yu, D.; Wang, C.; Guyot-Sionnest, P. *Science* **2003**, *300*, 1277–80.
- (5) Choi, J.-H.; Fafarman, A. T.; Oh, S. J.; Ko, D.-K.; Kim, D. K.; Diroll, B. T.; Muramoto, S.; Gillen, J. G.; Murray, C. B.; Kagan, C. R. *Nano Lett.* **2012**, *12*, 2631–8.

- (6) Kim, D. K.; Lai, Y.; Diroll, B. T.; Murray, C. B.; Kagan, C. R. *Nat. Commun.* **2012**, *3*, 1216.
- (7) Lee, J.-S.; Kovalenko, M. V.; Huang, J.; Chung, D. S.; Talapin, D. V. *Nat. Nanotechnol.* **2011**, *6*, 348–52.
- (8) Oh, S. J.; Berry, N. E.; Choi, J.-H.; Gaulding, E. A.; Paik, T.; Hong, S.-H.; Murray, C. B.; Kagan, C. R. *ACS Nano* **2013**, *7*, 2413–2421.
- (9) Talapin, D. V.; Murray, C. B. *Science* **2005**, *310*, 86–9.
- (10) Gur, I.; Fromer, N. A.; Geier, M. L.; Alivisatos, A. P. *Science* **2005**, *310*, 462–5.
- (11) Ip, A. H. et al. *Nat. Nanotechnol.* **2012**, *7*, 577–82.
- (12) Luther, J. M.; Law, M.; Beard, M. C.; Song, Q.; Reese, M. O.; Ellingson, R. J.; Nozik, A. J. *Nano Lett.* **2008**, *8*, 3488–92.
- (13) Tang, J.; Kemp, K. W.; Hoogland, S.; Jeong, K. S.; Liu, H.; Levina, L.; Furukawa, M.; Wang, X.; Debnath, R.; Cha, D.; Chou, K. W.; Fischer, A.; Amassian, A.; Asbury, J. B.; Sargent, E. H. *Nat. Mater.* **2011**, *10*, 765–771.
- (14) Tang, J.; Liu, H.; Zhitomirsky, D.; Hoogland, S.; Wang, X.; Furukawa, M.; Levina, L.; Sargent, E. H. *Nano Lett.* **2012**, *12*, 4889–4894.
- (15) Zhitomirsky, D.; Furukawa, M.; Tang, J.; Stadler, P.; Hoogland, S.; Voznyy, O.; Liu, H.; Sargent, E. H. *Adv. Mater.* **2012**, *24*, 6181–5.
- (16) Geyer, S.; Porter, V. J.; Halpert, J. E.; Mentzel, T. S.; Kastner, M. A.; Bawendi, M. G. *Phys. Rev. B* **2010**, *82*, 155201.
- (17) Konstantatos, G.; Howard, I.; Fischer, A.; Hoogland, S.; Clifford, J.; Klem, E.; Levina, L.; Sargent, E. H. *Nature* **2006**, *442*, 180–3.
- (18) McDonald, S. A.; Konstantatos, G.; Zhang, S.; Cyr, P. W.; Klem, E. J. D.; Levina, L.; Sargent, E. H. *Nat. Mater.* **2005**, *4*, 138–142.

- (19) Oertel, D. C.; Bawendi, M. G.; Arango, A. C.; Bulović, V. *Appl. Phys. Lett.* **2005**, *87*, 213505.
- (20) Coe, S.; Woo, W.-K.; Bawendi, M.; Bulović, V. *Nature* **2002**, *420*, 800–3.
- (21) Colvin, V. L.; Schlamp, M. C.; Alivisatos, A. P. *Nature* **1994**, *370*, 354–357.
- (22) Wang, R. Y.; Feser, J. P.; Lee, J. S.; Talapin, D. V.; Segalman, R.; Majumdar, A. *Nano Lett.* **2008**, *8*, 2283–2288.
- (23) Barkhouse, D. A. R.; Debnath, R.; Kramer, I. J.; Zhitomirsky, D.; Pattantyus-Abraham, A. G.; Levina, L.; Etgar, L.; Grätzel, M.; Sargent, E. H. *Adv. Mater.* **2011**, *23*, 3134–3138.
- (24) Jeong, K. S.; Tang, J.; Liu, H.; Kim, J.; Schaefer, A. W.; Kemp, K.; Levina, L.; Wang, X.; Hoogland, S.; Debnath, R.; Brzozowski, L.; Sargent, E. H.; Asbury, J. B. *ACS Nano* **2012**, *6*, 89–99.
- (25) Kovalenko, M. V.; Scheele, M.; Talapin, D. V. *Science* **2009**, *324*, 1417–20.
- (26) Fafarman, A. T.; Koh, W.-k.; Diroll, B. T.; Kim, D. K.; Ko, D.-K.; Oh, S. J.; Ye, X.; Doan-Nguyen, V.; Crump, M. R.; Reifsnnyder, D. C.; Murray, C. B.; Kagan, C. R. *J. Am. Chem. Soc.* **2011**, *133*, 15753–61.
- (27) Anderson, N. C.; Hendricks, M. P.; Choi, J. J.; Owen, J. S. *J. Am. Chem. Soc.* **2013**, *135*, 18536–48.
- (28) Goodwin, E. D.; Diroll, B. T.; Oh, S. J.; Paik, T.; Murray, C. B.; Kagan, C. R. *J. Phys. Chem. C* **2014**, *118*, 27097–27105.
- (29) Hassinen, A.; Moreels, I.; De Nolf, K.; Smet, P. F.; Martins, J. C.; Hens, Z. *J. Am. Chem. Soc.* **2012**, *134*, 20705–12.
- (30) Liu, Y.; Tolentino, J.; Gibbs, M.; Ihly, R.; Perkins, C. L.; Liu, Y.; Crawford, N.; Hemminger, J. C.; Law, M. *Nano Lett.* **2013**, *13*, 1578–1587.

- (31) Moroz, P.; Kholmicheva, N.; Mellott, B.; Liyanage, G.; Rijal, U.; Bastola, E.; Huband, K.; Khon, E.; McBride, K.; Zamkov, M. *ACS Nano* **2013**, *7*, 6964–6977.
- (32) Bae, W. K.; Joo, J.; Padilha, L. A.; Won, J.; Lee, D. C.; Lin, Q.; Koh, W. K.; Luo, H.; Klimov, V. I.; Pietryga, J. M. *J. Am. Chem. Soc.* **2012**, *134*, 20160–20168.
- (33) Choi, J.-H.; Oh, S. J.; Lai, Y.; Kim, D. K.; Zhao, T.; Fafarman, A. T.; Diroll, B. T.; Murray, C. B.; Kagan, C. R. *ACS Nano* **2013**, *7*, 8275–83.
- (34) Greaney, M. J.; Couderc, E.; Zhao, J.; Nail, B. A.; Mecklenburg, M.; Thornbury, W.; Osterloh, F. E.; Bradforth, S. E.; Brutchey, R. L. *Chem. Mater.* **2015**, *27*, 744–756.
- (35) Kim, D. K.; Fafarman, A. T.; Diroll, B. T.; Chan, S. H.; Gordon, T. R.; Murray, C. B.; Kagan, C. R. *ACS Nano* **2013**, *7*, 8760–70.
- (36) Thon, S. M.; Ip, A. H.; Voznyy, O.; Levina, L.; Kemp, K. W.; Carey, G. H.; Masala, S.; Sargent, E. H. *ACS Nano* **2013**, *7*, 7680–7688.
- (37) Oh, S. J.; Berry, N. E.; Choi, J.-H.; Gauldin, E. A.; Lin, H.; Paik, T.; Diroll, B. T.; Muramoto, S.; Murray, C. B.; Kagan, C. R. *Nano Lett.* **2014**, *14*, 1559–1566.
- (38) Zhang, H.; Hu, B.; Sun, L.; Hovden, R.; Wise, F. W.; Muller, D. a.; Robinson, R. D. *Nano Lett.* **2011**, *11*, 5356–5361.
- (39) Baumgardner, W. J.; Whitham, K.; Hanrath, T. *Nano Lett.* **2013**, *13*, 3225–31.
- (40) Boneschanscher, M. P.; Evers, W. H.; Geuchies, J. J.; Altantzis, T.; Goris, B.; Rabouw, F. T.; van Rossum, S. A. P.; van der Zant, H. S. J.; Siebbeles,

- L. D. A.; Van Tendeloo, G.; Swart, I.; Hilhorst, J.; Petukhov, A. V.; Bals, S.; Vanmaekelbergh, D. *Science* **2014**, *344*, 1377–1380.
- (41) Nag, A.; Chung, D. S.; Dolzhenkov, D. S.; Dimitrijevic, N. M.; Chattopadhyay, S.; Shibata, T.; Talapin, D. V. *J. Am. Chem. Soc.* **2012**, *134*, 13604–13615.
- (42) Ellingson, R. J.; Beard, M. C.; Johnson, J. C.; Yu, P.; Micic, O. I.; Nozik, A. J.; Shabaev, A.; Efros, A. L. *Nano Lett.* **2005**, *5*, 865–871.
- (43) Schaller, R. D.; Klimov, V. I. *Phys. Rev. Lett.* **2004**, *92*, 186601–1.
- (44) Tang, J.; Sargent, E. H. *Adv. Mater.* **2011**, *23*, 12–29.
- (45) Gao, Y.; Aerts, M.; Sandeep, C. S. S.; Talgorn, E.; Savenije, T. J.; Kinge, S.; Siebbeles, L. D. A.; Houtepen, A. J. *ACS Nano* **2012**, *6*, 9606–9614.
- (46) Talgorn, E.; Moysidou, E.; Abellon, R. D.; Savenije, T. J.; Goossens, A.; Houtepen, A. J.; Siebbeles, L. D. A. *J. Phys. Chem. C* **2010**, *114*, 3441–3447.
- (47) Oh, S. J.; Wang, Z.; Berry, N. E.; Choi, J.-h.; Zhao, T.; Gaubing, E. A.; Paik, T.; Lai, Y.; Murray, C. B.; Kagan, C. R. *Nano Lett.* **2014**, *14*, 6210–6216.
- (48) Aerts, M.; Suchand Sandeep, C. S.; Gao, Y.; Savenije, T. J.; Schins, J. M.; Houtepen, A. J.; Kinge, S.; Siebbeles, L. D. A. *Nano Lett.* **2011**, *11*, 4485–4489.
- (49) Yu, W. W.; Falkner, J. C.; Shih, B. S.; Colvin, V. L. *ChemInform* **2004**, *35*, 3318–3322.
- (50) Steckel, J. S.; Yen, B. K. H.; Oertel, D. C.; Bawendi, M. G. *J. Am. Chem. Soc.* **2006**, *128*, 13032–3.
- (51) Pallavicini, P.; Dacarro, G.; Galli, M.; Patrini, M. *J. Colloid Interface Sci.* **2009**, *332*, 432–438.
- (52) Katari, J. E. B.; Colvin, V. L.; Alivisatos, A. P. *J. Phys. Chem.* **1994**, *98*, 4109–4117.

- (53) Infelta, P. P.; de Haas, M. P.; Warman, J. M. *Radiat. Phys. Chem.* **1977**, *10*, 353–365.
- (54) Kunst, M.; Beck, G. *J. Appl. Phys.* **1986**, *60*, 3558–3566.
- (55) Warman, J. M.; De Haas, M. P.; Hummel, A. *Chem. Phys. Lett.* **1973**, *22*, 480–483.
- (56) Warman, J. M.; Infelta, P. P.; De Haas, M. P.; Hummel, A. *Can. J. Chem.* **1977**, *55*, 2249–2257.
- (57) Ten Cate, S.; Liu, Y.; Suchand Sandeep, C. S.; Kinge, S.; Houtepen, A. J.; Savenije, T. J.; Schins, J. M.; Law, M.; Siebbeles, L. D. A. *J. Phys. Chem. Lett.* **2013**, *4*, 1766–1770.
- (58) Pattantyus-Abraham, A. G.; Kramer, I. J.; Barkhouse, A. R.; Wang, X.; Konstantatos, G.; Debnath, R.; Levina, L.; Raabe, I.; Nazeeruddin, M. K.; Grätzel, M.; Sargent, E. H. *ACS Nano* **2010**, *4*, 3374–3380.
- (59) Sandeep, C. S. S.; Ten Cate, S.; Schins, J. M.; Savenije, T. J.; Liu, Y.; Law, M.; Kinge, S.; Houtepen, A. J.; Siebbeles, L. D. A. *Nat. Commun.* **2013**, *4*, 2360.
- (60) Martin, S. T.; Herrmann, H.; Hoffmann, M. R. *J. Chem. Soc., Faraday Trans.* **1994**, *90*, 3323–3330.
- (61) Schins, J. M.; Prins, P.; Grozema, F. C.; Abellón, R. D.; De Haas, M. P.; Siebbeles, L. D. A. *Rev. Sci. Instrum.* **2005**, *76*, 084703.
- (62) Talgorn, E.; de Vries, M. A.; Siebbeles, L. D. A.; Houtepen, A. J. *ACS Nano* **2011**, *5*, 3552–8.
- (63) Guglietta, G. W.; Diroll, B. T.; Gauding, E. A.; Fordham, J. L.; Li, S.; Murray, C. B.; Baxter, J. B. *ACS Nano* **2015**, *9*, 1820–1828.

Chapter 4

Increased Carrier Mobility and Lifetime in CdSe Quantum Dot Thin Films Through Surface Trap Passivation and Doping

Abstract

Passivating surface defects and controlling the carrier concentration and mobility in quantum dot (QD) thin films is prerequisite to designing electronic and optoelectronic devices. We investigate the effect of introducing indium in CdSe QD thin films on the dark mobility and the photogenerated carrier mobility and lifetime using field-effect transistor (FET) and time-resolved microwave conductivity (TRMC) measurements. We evaporate indium films ranging from 1 nm to 11 nm in thickness on top of

Reproduced with permission from Straus, D. B.; Goodwin, E. D.; Gauding, E. A.; Muramoto, S.; Murray, C. B.; Kagan, C. R. *J. Phys. Chem. Lett.* **2015**, *6*, 4605–4609. Copyright 2015 American Chemical Society.

approximately 40 nm thick, thiocyanate-capped, CdSe QD thin films and anneal the QD films at 300°C to densify and drive diffusion of indium through the films. As the amount of indium increases, the FET and TRMC mobilities and the TRMC lifetime increase. The increase in mobility and lifetime is consistent with increased indium passivating mid-gap and band-tail trap states and doping the films, shifting the Fermi energy closer to and into the conduction band.

4.1 Introduction

Colloidal semiconductor quantum dots (QDs) are an attractive materials class for next-generation electronic,¹⁻⁴ optoelectronic,⁵⁻¹² and thermoelectric¹³ devices because of their size, shape, and compositionally tunable electronic and optical properties¹⁴⁻¹⁹ as well as the low-cost, solution-based methods available for their synthesis, assembly, and processing into QD thin film solids. Colloidal QDs are synthesized with long insulating organic ligands to mediate their size and shape and to stabilize their dispersion.^{14,17} To assemble QDs into electronically coupled solids, these long ligands are removed and/or replaced with short organic ligands, such as 1,2-ethanedithiol^{20,21} or 3-mercaptopropionic acid,^{10,22} or compact inorganic ligands, such as metal chalcogenides ($\text{Sn}_2\text{S}_6^{4-}$, etc.),²³ chalcogenides (S^{2-} , Se^{2-} , etc.),^{24,25} halides (Cl^- , Br^- , I^-),²⁶ or pseudohalides (N_3^- , SCN^-).²⁷⁻³¹ Unlike most bulk semiconductors, defects and dangling bonds at the QD surfaces in thin films introduce a large density of mid-gap and band-tail trap states.^{5,32} These defects lead to poor carrier mobility and lifetime, even in strongly, electronically-coupled QD thin films.³³⁻³⁶ Recently, ligands and atoms have been introduced at the QD surface that serve to passivate defect states and dope QD thin films, allowing the carrier statistics and Fermi energy to be tailored and the design of higher performance QD thin film devices, such as field-effect transis-

tors, photovoltaics, photodetectors, and light-emitting diodes.^{5,25,37} While previous reports^{1,25} have shown that increased surface trap passivation and doping increase the carrier mobility in QD thin films by introducing more carriers in higher energy, higher densities of states, studies are lacking that directly relate the effects of trap passivation and doping on carrier lifetime.³⁸ In this work, we combine field-effect transistor (FET) and flash-photolysis, time-resolved microwave conductivity (TRMC) measurements to directly probe the relationship between the carrier mobility and lifetime and the degree of surface passivation and doping in strongly-coupled, thiocyanate (SCN)-capped, CdSe QD thin films as a function of varying amounts of thermally-evaporated indium. We find that both the mobility and lifetime of charge carriers increase as a function of doping, even for degenerately-doped QD thin films, which is significant because it is in contrast to bulk systems, where carrier lifetime tends to decrease as a function of increased doping.³⁹

4.2 Experimental Methods

4.2.1 Synthetic Methods

Cadmium stearate is prepared by combining 10 g CdO (99%, Strem), 55 g stearic acid (97%, Acros), and 50 mL octadecene (90%, Aldrich). The reaction is heated to 280 °C under nitrogen until the solution stops bubbling. The solution is cooled, precipitated with acetone (ACS, Fisher), vigorously mixed, and centrifuged. The supernatant is discarded. The cadmium stearate is an off-white powder. Again the cadmium stearate is washed with acetone and then dried in a vacuum oven. The dried cadmium stearate is milled in a mortar and pestle. The cadmium stearate is then washed twice with methanol (ACS, Fisher), dried, and milled; washed twice with

methanol again, dried, and milled; and lastly washed twice with acetone, dried, and milled.

CdSe quantum dots (QDs) are synthesized according to modified literature procedures.⁴⁰ 40 g of trioctylphosphine oxide (TOPO) (90%, Aldrich), 40 g octadecylamine (90%, Acros), and 4.2 g of cadmium stearate are added to a flask connected to a Schlenk line. The mixture is degassed at 135 °C under vacuum and then heated to 320 °C under nitrogen. Once at temperature, 20 mL of 1.25 M tributylphosphine selenide (prepared by mixing tributylphosphine, Aldrich 97%, and selenium shot, Strem 99.99%, and stirring overnight) is quickly injected. The reaction is kept at 290 °C for 15 min and then quenched by injecting 50 mL of anhydrous toluene (Acros). The solution is transferred to a Schlenk flask and precipitated in a nitrogen glove box with anhydrous ethanol (distilled in-house) and centrifuged. The supernatant is discarded. The precipitate is dissolved in anhydrous hexanes (Aldrich), centrifuged, and the supernatant is kept. The CdSe QDs are then precipitated with anhydrous ethanol, anhydrous acetone (Acros), and anhydrous isopropanol (Acros), and after each precipitation step, the QDs are centrifuged and then the supernatant is discarded and the precipitate is redispersed in hexanes. Purified QDs are stored in a nitrogen glove box. Energy dispersive X-ray measurements give a Cd:Se ratio for the as-synthesized QDs as 1.47 ± 0.04 .

After synthesis, the native organic ligands on the CdSe QDs are exchanged with ammonium thiocyanate in solution and are redispersed in dimethylformamide (DMF).²⁸ CdSe QDs are diluted in anhydrous hexanes in a nitrogen glove box to an optical density of 5 (measured at the first absorption maximum with a path length of 1 cm) to a total volume of 2.4 mL. 1.2 mL of 10 mg/mL recrystallized ammonium thiocyanate (Acros) in anhydrous acetone is added to the QD dispersion, vortexed for 2 min, and centrifuged, discarding the supernatant. The exchanged QDs are washed with 2.4

mL of anhydrous tetrahydrofuran (Acros, inhibitor free), vortexed for 2 min, and centrifuged, discarding the supernatant. The QDs are then washed with 2.4 mL of anhydrous toluene, vortexed for 1 min, centrifuged, and the supernatant is discarded. The QDs are then redispersed in 0.17 mL of anhydrous dimethylformamide (Acros, over molecular sieves).

After ligand exchange, the QDs are spin cast from DMF to form approximately 40 nm thick films in a nitrogen glove box on 1) aluminosilicate glass for TRMC, visible absorbance, spectroscopic ellipsometry, secondary ion mass spectrometry (SIMS), and X-ray photoelectron spectroscopy (XPS) measurements; 2) double-polished silicon for Fourier-transform infrared spectroscopy measurements; and 3) n++ silicon with 300 nm of thermal oxide and 20 nm of alumina deposited by atomic layer deposition for FET measurements.¹ 0, 1, 3, 5, 7, 9, or 11 nm of indium is thermally deposited uniformly over the surface of the QD thin films by thermal evaporation, which are then annealed in a nitrogen glove box at 300 °C for 20 min to decompose the SCN, which leaves surface sulfide and densifies the QD thin films,²⁸ and to drive indium diffusion, which passivates traps and dopes the QD thin films.¹ 80 nm of indium and 40 nm of Au are deposited by thermal evaporation as top contacts for FETs. Note that FETs are not annealed after deposition of In and Au contacts.

4.2.2 Time-Resolved Microwave Conductivity

TRMC measurements are described in detail in Chapter 2. To process TRMC transients, we filter them using a Butterworth filter of the fifth order (Figure 4.1) and the cavity response is deconvolved from the traces (Figure 4.2).

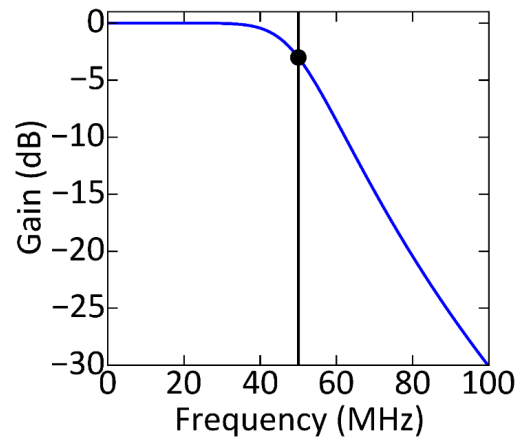


Figure 4.1: Frequency response (blue) of the fifth order Butterworth filter. A 40 MHz to 50 MHz cutoff frequency is used to filter the data. The cutoff frequency (here, 50 MHz) is shown in black.

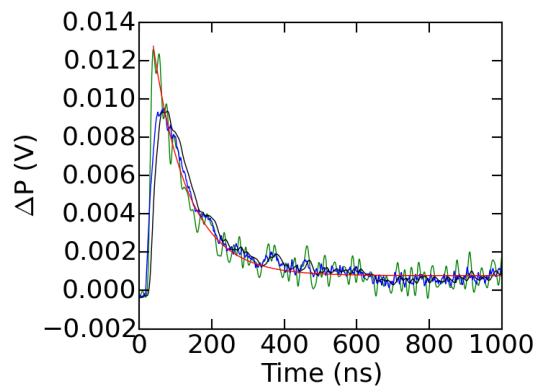


Figure 4.2: Reflected microwave power transients as measured in TRMC showing the as-measured transient (blue), the transient after application of a Butterworth filter (black), and the sample response transient determined by deconvolution of the resonant cavity response from the filtered transient (green). Fit by non-linear least squares regression to a single exponential decay function of the deconvolved sample response transient (red).

4.3 Results and Discussion

Fourier transform infrared absorption spectroscopy is used to determine the degree of completion of the ligand exchange reaction. Figure 4.3 shows the IR absorption spectra of CdSe QD thin films of as-synthesized, organic-capped QDs (light grey) and SCN-capped QDs (dark grey). The spectra are normalized to the first excitonic resonance in the UV-Vis absorption. 92% of the native organic ligands are removed, as quantified by integrating the C-H stretch region in Figure 4.3. The integrated peak area ratio between the C-N and C-H stretch in the SCN-capped CdSe QD film is 3.6:1.

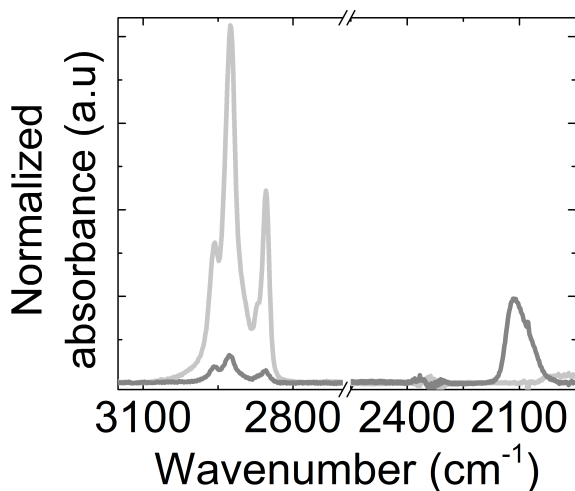


Figure 4.3: Fourier transform infrared absorption spectra of as-synthesized, organic-capped CdSe QD film (light grey) and SCN-capped CdSe QD film (dark grey).

A schematic of the indium doping and annealing process is shown in Figure 4.4a. Figures 4.4b and c show the effect of annealing at 300 °C on the structural and spectroscopic properties of the CdSe QD thin films. When annealed in the absence of indium, neighboring CdSe QDs fuse together forming larger crystallites (Figure 4.4b(i)). When annealed in the presence of indium, such fusing is not seen (Figure 4.4b(ii)). The optical absorption spectra (Figure 4.4c) show that compared to the discrete electronic resonances characteristic of the as-synthesized and SCN-capped,

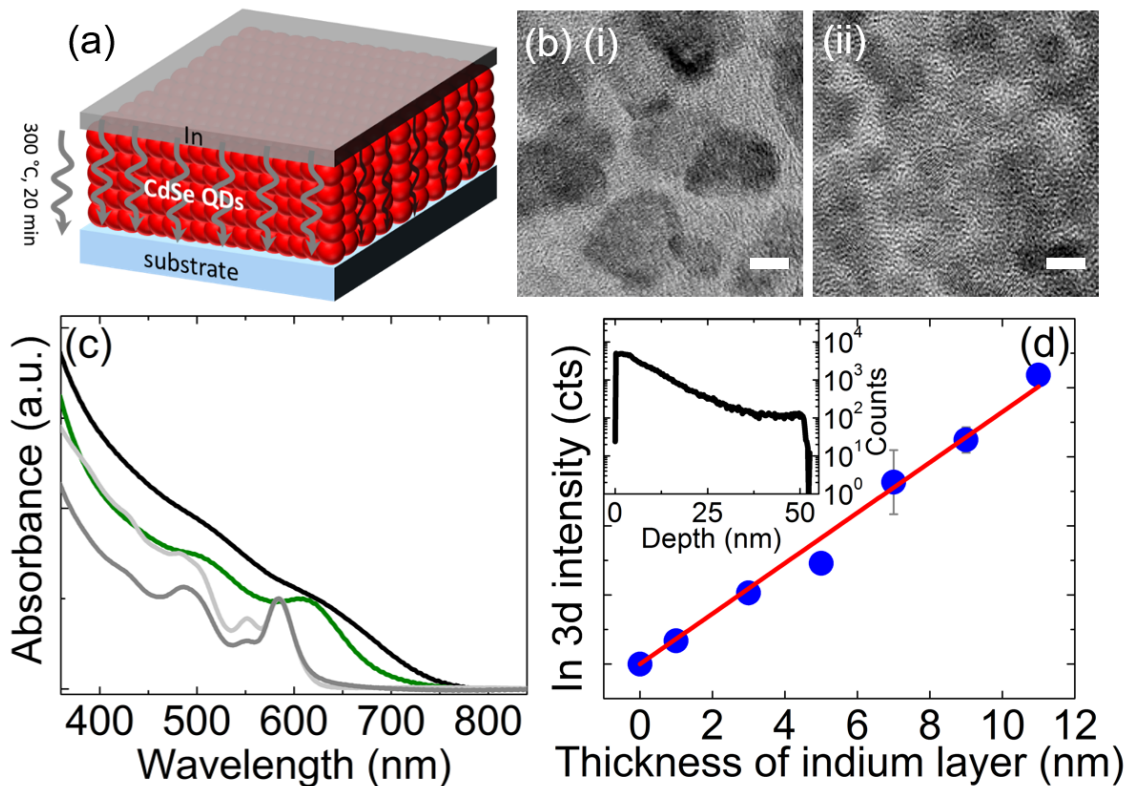


Figure 4.4: (a) Schematic of thermally-driven doping of evaporated indium onto SCN-capped, CdSe QD thin films. (b) Transmission electron micrographs of SCN-capped, CdSe QD assemblies that are annealed at 300 °C for 20 min in the absence (i) and presence (ii) of indium. Scale bars are 5 nm. (c) UV-Vis absorption spectra of CdSe QD thin films that are organic-capped (light grey), SCN-capped (dark grey) and SCN-capped and annealed at 300 °C for 20 min with 0 nm (black) and 5 nm (green) of evaporated indium. (d) XPS measurements monitoring the intensity of the indium 3d signal in SCN-capped, CdSe QD thin films doped with 0 nm to 11 nm of indium and annealed at 300 °C for 20 min. A linear fit to the XPS thickness is shown in red. Uncertainties represent standard deviations of three measurements. Inset: SIMS depth profile showing the intensity of the InO^{2-} ion as a function of depth into the CdSe QD thin film doped with 11 nm of indium and annealed at 300 °C for 20 min. The QD films are exposed to air for several days before SIMS measurements, and the InO^{2-} intensity represents that the indium has oxidized.

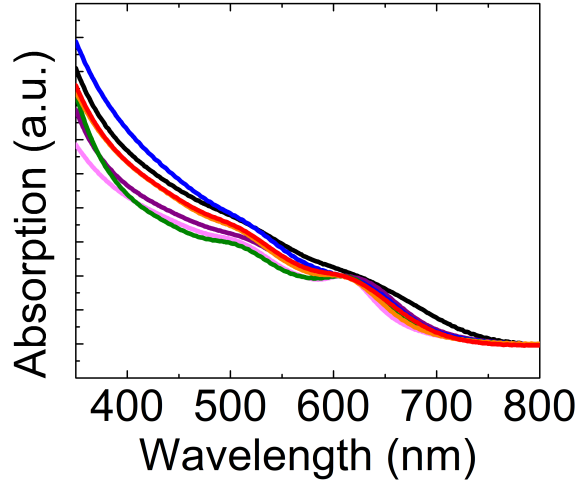


Figure 4.5: UV-Vis-NIR absorption spectra of SCN-capped CdSe QD films with a nominal thickness of 0 nm (black), 1 nm (red), 3 nm (orange), 5 nm (green), 7 nm (blue), 9 nm (purple), and 11 nm (pink) of indium after being annealed at 300 °C for 20 min.

QD films (light and dark grey curves, respectively), annealing of the QD films in the absence of indium causes almost complete loss of quantum-confinement (black curve), as seen previously with annealing at 300 °C.¹ However, annealing in the presence of even 1 nm of indium preserves discrete resonances which are red-shifted, consistent with increased electronic coupling between QDs (green curve and Figure 4.5). Verification of indium deposition is accomplished using X-ray photoelectron spectroscopy (XPS) measurements of the top 20 nm – 30 nm of the QD film (Figure 4.4d), where the intensity of the indium 3d peak is used to quantitatively correlate the thickness-dependent indium content in CdSe QD films. As the thickness of the thermally evaporated indium increases, the incorporated indium content increases linearly. The inset of Figure 4.4d shows the depth profile of indium in the QD films as measured by secondary ion mass spectrometry (SIMS), demonstrating that indium diffuses throughout the films.

Charge transport in indium-doped, CdSe QD thin films is probed in the platform of the field-effect transistor under the control of an external gate-field (Figure 4.6

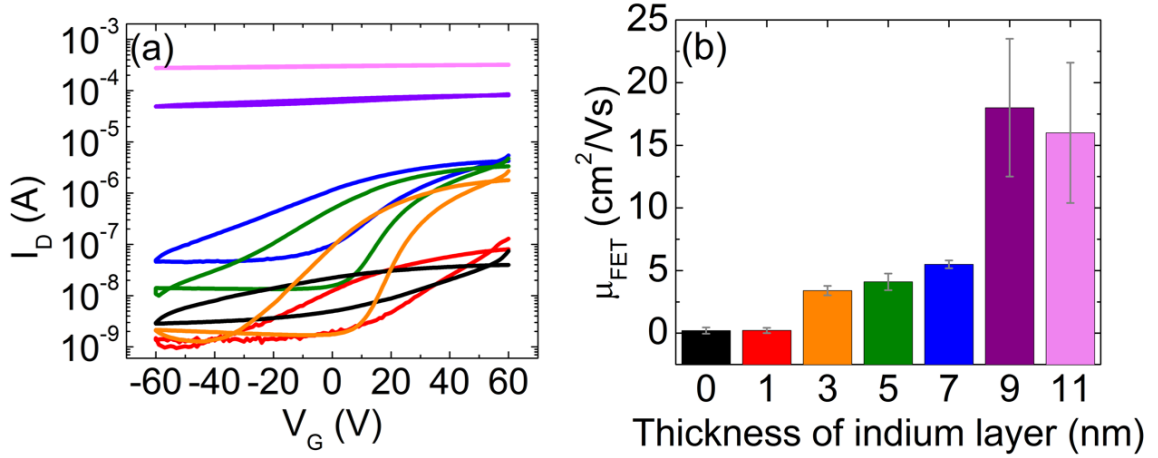


Figure 4.6: (a) Transfer characteristics ($I_D - V_G$) and (b) FET mobilities of SCN-capped, CdSe QD thin films annealed at 300 °C for 20 min with nominal thicknesses of 0 nm (black), 1 nm (red), 3 nm (orange), 5 nm (green), 7 nm (blue), 9 nm (purple), and 11 nm (pink) of deposited indium. Uncertainties represent standard deviations of at least three measurements.

nm In	FET μ ($\text{cm}^2\text{V}^{-1}\text{s}^{-1}$)	$I_{\text{on}}/I_{\text{off}}$	TRMC μ ($\text{cm}^2\text{V}^{-1}\text{s}^{-1}$)	τ (ns)
0	0.2 ± 0.3	40 ± 30	0.004 ± 0.001	37 ± 4
1	0.2 ± 0.2	200 ± 300	0.0014 ± 0.0002	36 ± 2
3	3.4 ± 0.4	2000 ± 1000	0.011 ± 0.002	49 ± 5
5	4.1 ± 0.7	200 ± 100	0.021 ± 0.004	90 ± 10
7	5.5 ± 0.3	90 ± 20	0.011 ± 0.005	90 ± 10
9	18 ± 6	1.5 ± 3	0.5 ± 0.1	5000 ± 1000
11	16 ± 6	1.14 ± 0.04	0.20 ± 0.06	2000 ± 1000

Table 4.1: Summary of FET and TRMC results. Uncertainties represent standard deviations of at least three measurements.

and Table 4.1). Representative transfer characteristics measured in the linear regime ($V_{DS} = 0.1 \text{ V}$) are shown in Figure 4.6a. Field-effect mobility presented in Figure 4.6b and Table 4.1 is the average of the mobilities calculated from the forward and the reverse sweep of the transfer curves and is used as a guide to understand the doping level in CdSe QD thin films. FETs with no indium and 1 nm of indium added to the CdSe QD thin film display low field-effect mobilities of $(0.2 \pm 0.3) \text{ cm}^2 \text{ V}^{-1} \text{ s}^{-1}$ and $(0.2 \pm 0.2) \text{ cm}^2 \text{ V}^{-1} \text{ s}^{-1}$, respectively. The large error in these mobility values demonstrates the inconsistency of these devices, similar to previous reports of low-performance NC FETs.⁴¹ The off current for the FET with 1 nm indium is lower by an order of magnitude compared to that of the FET with 0 nm indium, consistent with the added indium preventing the fusion of neighboring QDs in the film. As the indium doping increases, the mobility increases to $(3.4 \pm 0.4) \text{ cm}^2 \text{ V}^{-1} \text{ s}^{-1}$ for 3 nm of indium, $(4.1 \pm 0.7) \text{ cm}^2 \text{ V}^{-1} \text{ s}^{-1}$ for 5 nm of indium, and $(5.5 \pm 0.3) \text{ cm}^2 \text{ V}^{-1} \text{ s}^{-1}$ for 7 nm of indium. However, the on/off ratio increases from 300 for 1 nm of indium to 2000 for 3 nm of indium as the on-current increases, but subsequently decreases to 200 for 5 nm of indium and 90 for 7 nm of indium as the off-current increases more significantly (Figure 4.7).

CdSe QD films doped with 9 nm and 11 nm of indium are degenerate with high mobilities of $(18 \pm 6) \text{ cm}^2 \text{ V}^{-1} \text{ s}^{-1}$ and $(16 \pm 6) \text{ cm}^2 \text{ V}^{-1} \text{ s}^{-1}$, respectively, and on/off ratios near unity (Figure 4.7), reflecting a shift of the Fermi level into the conduction band in the density of electronic states. We note that small changes in the slope of the transfer characteristics for these high current, degenerately-doped devices give rise to the large observed variation in FET mobility (Figure 4.8).

The mobility and lifetime of photogenerated charge carriers in the absence of a gate-field are explored in indium-doped, CdSe QD thin films by TRMC measurements (Figure 4.9 and Table 4.1). Representative transients are shown in Figure 4.10. The

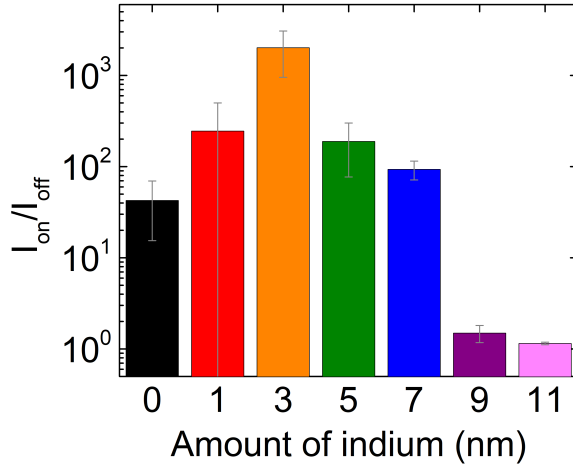


Figure 4.7: On/off ratio for CdSe QD thin film field effect transistors doped with a nominal thickness of 0 nm (black), 1 nm (red), 3 nm (orange), 5 nm (green), 7 nm (blue), 9 nm (purple), and 11 nm (pink) of indium after being annealed at 300 °C for 20 min. Uncertainties represent standard deviations of at least three measurements.

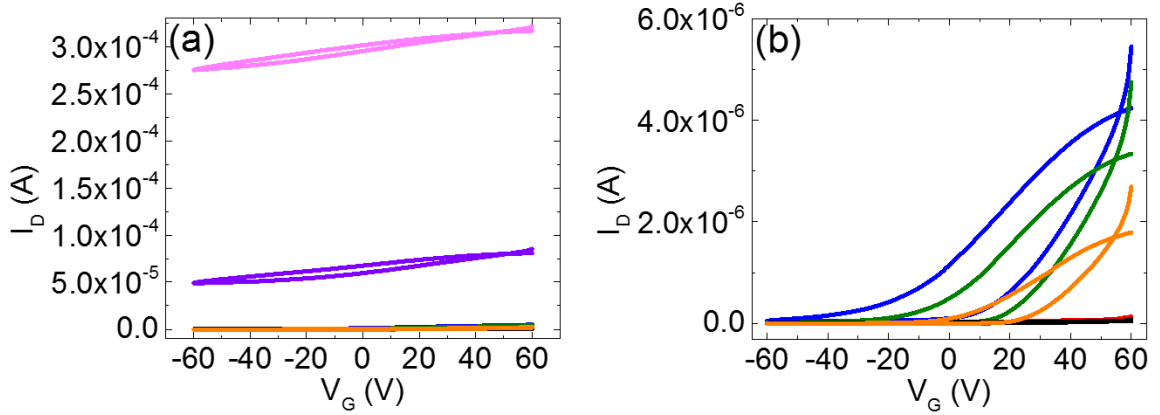


Figure 4.8: (a, b) Transfer characteristics (I_D - V_G) from Figure 4.6, reproduced on a linear scale, for SCN-capped, CdSe QD thin films annealed at 300 °C for 20 min with 0 nm (black), 1 nm (red), 3 nm (orange), 5 nm (green), 7 nm (blue), 9 nm (purple), and 11 nm (pink) of deposited indium.

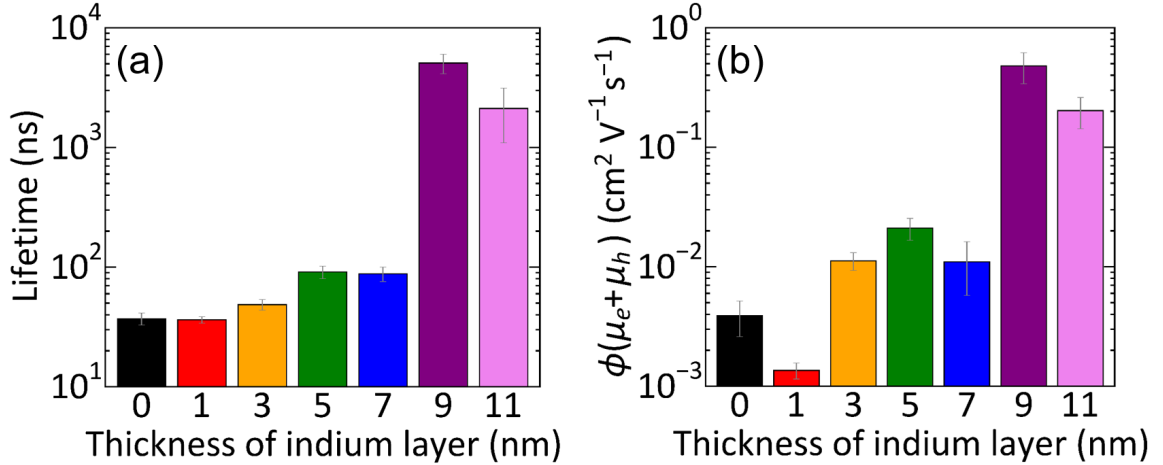


Figure 4.9: TRMC (a) lifetime and (b) mobility for SCN-capped, CdSe QD thin films annealed at 300 °C for 20 min with nominal thicknesses of 0 nm (black), 1 nm (red), 3 nm (orange), 5 nm (green), 7 nm (blue), 9 nm (purple), and 11 nm (pink) of deposited indium. Uncertainties represent standard deviations of at least three measurements.

experimental setup is described in Chapter 2. Photogenerated charge carrier lifetimes (Figure 4.9a and Table 4.1) are the lowest for CdSe QD films with no doping and doping with 1 nm of deposited indium, consistent with surface chalcogenide sites introducing mid-gap trap states⁴² and reducing photogenerated charge carrier lifetimes. As the doping is increased by depositing 3 nm and 5 nm of indium, the carrier lifetime increases, in agreement with the reported mechanism of indium binding to surface chalcogenide sites¹⁵ and passivating mid-gap trap states.⁴² Upon further doping with 7 nm of indium, the carrier lifetime remains constant. We hypothesize that the constant lifetime for CdSe QD films doped with 5 nm and 7 nm of indium arises as the dominant trap states are passivated beyond 5 nm of deposited indium. Doping with 9 and 11 nm of indium leads to an increase in carrier lifetime by more than an order of magnitude, consistent with observations by Thon *et al.* and Katsiev *et al.* that correlate a reduction in band tail states with improved photovoltaic performance.^{35,36}

TRMC measurements probe the product of the carrier quantum yield (ϕ) and the sum of the electron and hole mobility ($\mu_e + \mu_h$). For low photoexcitation densities,

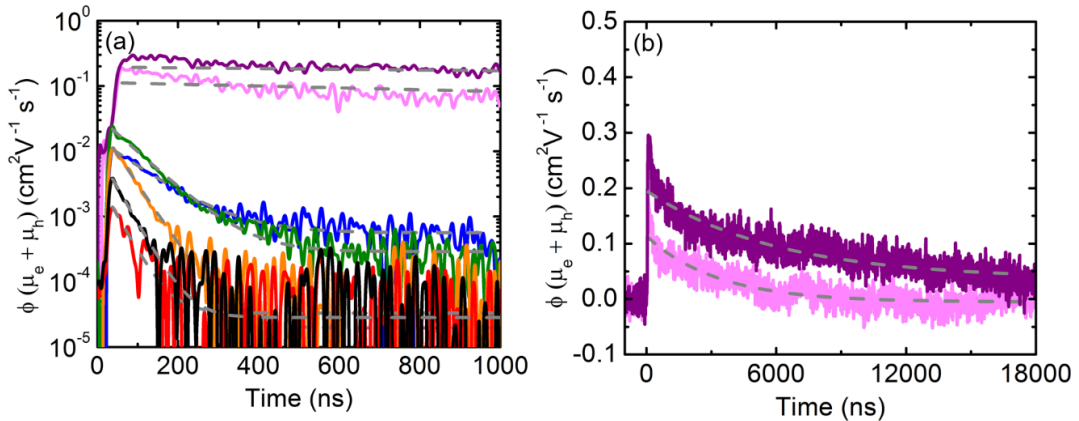


Figure 4.10: (a, b) Representative, deconvolved TRMC transients for CdSe QD thin films doped with 0 (black), 1 (red), 3 (orange), 5 (green), 7 (blue), 9 (purple), and 11 nm (pink) of indium. Single exponential fits are shown in gray.

the quantum yield-mobility product ($\phi(\mu_e + \mu_h)$) of the CdSe QD films is constant with excitation density for QD films doped with 0 nm to 7 nm of indium (Figure 4.11), indicating the absence of higher order recombination processes.⁴³ Still, quantum yield-mobility products determined by TRMC may be less than FET mobilities as first order recombination processes, such as geminate recombination, cause the free carrier quantum yield to be less than unity. The influence of first order processes on the quantum yield does not change with excitation density. Therefore we interpret trends in quantum yield-mobility product to represent trends in mobility and to give a lower bound on carrier mobility. For these films, we average the constant $\phi(\mu_e + \mu_h)$ regime, shown in Figure 4.9b, to characterize the doping dependence of the carrier mobility. Figure 4.11a shows the TRMC quantum yield-mobility product for CdSe QD thin films doped with indium. For all except the QD thin films doped with 9 nm and 11 nm of indium, the average of the first three points shown in Figure 4.11a are used to calculate the mobility presented in Figure 4.9, because these points approach a constant mobility-quantum yield product.

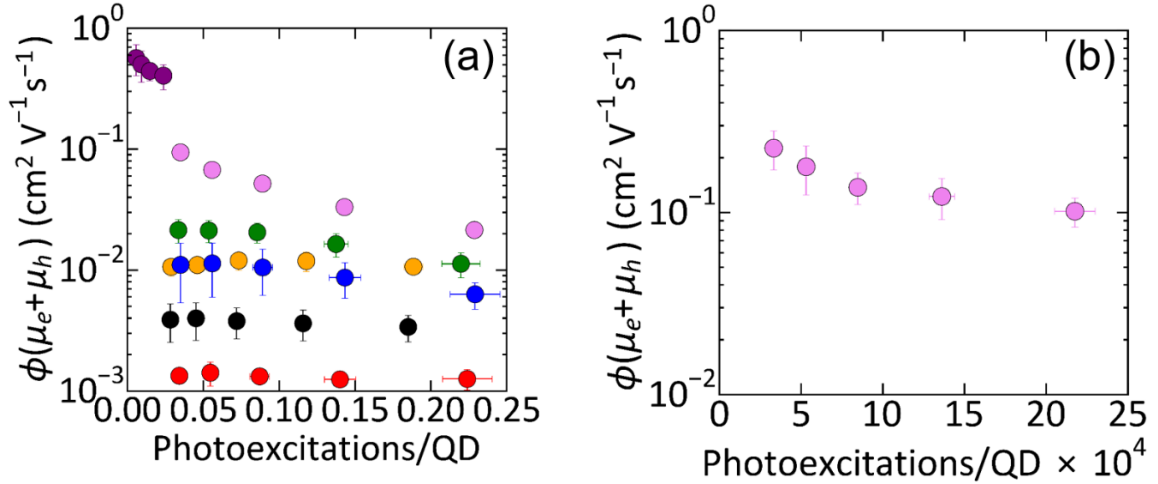


Figure 4.11: (a) TRMC mobility-quantum yield product as a function of photoexcitation density product for CdSe QD thin films doped with 0 (black), 1 (red), 3 (orange), 5 (green), 7 (blue), 9 (purple) nm of indium, and 11 nm (pink) of indium at higher fluence, and (b) 11 nm at lower fluence. Uncertainties represent standard deviations of at least three measurements.

CdSe QD films doped with 1 nm of indium exhibit the lowest mobility as indium prevents the fusion of nearest-neighbor QDs, unlike undoped QD films, and the small amount of indium-doping is insufficient to passivate mid-gap trap states and shift the Fermi level for high-mobility transport. This is consistent with the low mobilities and the trend in the FET off-currents for 0 nm and 1 nm indium doping. The mobility increases and then remains constant with 3, 5, and 7 nm of indium doping, consistent with indium passivation and doping shifting the Fermi level closer to the conduction band and increasing the population of electrons in higher density, higher mobility electronic states, as reported previously.^{1,25,37} The TRMC mobilities presented here for CdSe QD films doped with 3 nm to 7 nm of indium are greater than those previously reported for CdSe QD thin films²¹ by almost an order of magnitude, consistent with increased electronic coupling through the SCN ligand exchange and with surface trap passivation and doping by indium. As the indium doping is increased to 9 nm and 11 nm, the mobility increases by more than an order of magnitude, consistent with the large increase seen in TRMC lifetime and the degenerate behavior shown in FETs

above.

We note that the TRMC quantum yield-mobility product is smaller than the FET mobility for all CdSe QD films, and we hypothesize that the lower TRMC quantum yield-mobility product is consistent with a low free carrier yield in CdSe QD thin films.^{44,45} Figure 4.11 also shows that the high mobility, high conductivity films doped with 9 nm and 11 nm of indium allow TRMC measurements at lower photoexcitation density than the more lightly doped QD films. However even at lower excitation densities, $\phi(\mu_e + \mu_h)$ in the 9 nm and 11 nm indium doped QD thin films is not constant with fluence, suggesting a lower threshold for higher-order recombination processes, such as Auger recombination, consistent with the high carrier concentrations seen in FET measurements. The mobility value reported for the QD film doped with 9 nm of indium is an average of the four points shown in Figure 4.11a, and the mobility value for the QD film doped with 11 nm of indium is the average of the first two points in Figure 4.11b. The 9 nm and 11 nm doped QD films do not exhibit constant mobility-quantum yield products.

4.4 Conclusion

We show that surface trap passivation and doping of QD thin films results in an increase in both photogenerated charge carrier mobility and lifetime. The photogenerated carrier mobility determined by TRMC measurements follows the same trend as the field-effect mobility with increasing passivation and doping, further confirming that the contactless TRMC method is an effective screening tool for semiconductor device performance. These results suggest that surface passivation and doping can be used as a general strategy to improve performance in QD optoelectronic devices.

4.5 References

- (1) Choi, J.-H.; Fafarman, A. T.; Oh, S. J.; Ko, D.-K.; Kim, D. K.; Diroll, B. T.; Muramoto, S.; Gillen, J. G.; Murray, C. B.; Kagan, C. R. *Nano Lett.* **2012**, *12*, 2631–8.
- (2) Kim, D. K.; Lai, Y.; Diroll, B. T.; Murray, C. B.; Kagan, C. R. *Nat. Commun.* **2012**, *3*, 1216.
- (3) Lee, J.-S.; Kovalenko, M. V.; Huang, J.; Chung, D. S.; Talapin, D. V. *Nat. Nanotechnol.* **2011**, *6*, 348–52.
- (4) Talapin, D. V.; Murray, C. B. *Science* **2005**, *310*, 86–9.
- (5) Ip, A. H. et al. *Nat. Nanotechnol.* **2012**, *7*, 577–82.
- (6) Konstantatos, G.; Howard, I.; Fischer, A.; Hoogland, S.; Clifford, J.; Klem, E.; Levina, L.; Sargent, E. H. *Nature* **2006**, *442*, 180–3.
- (7) Lobež, J. M.; Andrew, T. L.; Bulovic, V.; Swager, T. M. *ACS Nano* **2012**, *6*, 3044–3056.
- (8) Luther, J. M.; Law, M.; Beard, M. C.; Song, Q.; Reese, M. O.; Ellingson, R. J.; Nozik, A. J. *Nano Lett.* **2008**, *8*, 3488–92.
- (9) Oertel, D. C.; Bawendi, M. G.; Arango, A. C.; Bulović, V. *Appl. Phys. Lett.* **2005**, *87*, 213505.
- (10) Pattantyus-Abraham, A. G.; Kramer, I. J.; Barkhouse, A. R.; Wang, X.; Konstantatos, G.; Debnath, R.; Levina, L.; Raabe, I.; Nazeeruddin, M. K.; Grätzel, M.; Sargent, E. H. *ACS Nano* **2010**, *4*, 3374–3380.
- (11) Schornbaum, J.; Zakharko, Y.; Held, M.; Thiemann, S.; Gannott, F.; Zaumseil, J. *Nano Lett.* **2015**, *15*, 1822–1828.

- (12) Stiff-Roberts, A. D.; Lantz, K. R.; Pate, R. *J. Phys. D. Appl. Phys.* **2009**, *42*, 234004.
- (13) Wang, R. Y.; Feser, J. P.; Lee, J. S.; Talapin, D. V.; Segalman, R.; Majumdar, A. *Nano Lett.* **2008**, *8*, 2283–2288.
- (14) Alivisatos, A. P. *Science* **1996**, *271*, 933–937.
- (15) Kim, D. K.; Fafarman, A. T.; Diroll, B. T.; Chan, S. H.; Gordon, T. R.; Murray, C. B.; Kagan, C. R. *ACS Nano* **2013**, *7*, 8760–70.
- (16) Murray, C. B.; Norris, D. J.; Bawendi, M. G. *J. Am. Chem. Soc.* **1993**, *115*, 8706–8715.
- (17) Murray, C. B.; Kagan, C. R.; Bawendi, M. G. *Annu. Rev. Mater. Sci.* **2000**, *30*, 545–610.
- (18) Oh, S. J.; Berry, N. E.; Choi, J.-H.; Gaulding, E. A.; Paik, T.; Hong, S.-H.; Murray, C. B.; Kagan, C. R. *ACS Nano* **2013**, *7*, 2413–2421.
- (19) Peng, H.; Song, J.-H.; Kanatzidis, M. G.; Freeman, A. J. *Phys. Rev. B* **2011**, *84*, 1–13.
- (20) Luther, J. M.; Law, M.; Song, Q.; Perkins, C. L.; Beard, M. C.; Nozik, A. J. *ACS Nano* **2008**, *2*, 271–80.
- (21) Talgorn, E.; Moysidou, E.; Abellon, R. D.; Savenije, T. J.; Goossens, A.; Houtepen, A. J.; Siebbeles, L. D. A. *J. Phys. Chem. C* **2010**, *114*, 3441–3447.
- (22) Jeong, K. S.; Tang, J.; Liu, H.; Kim, J.; Schaefer, A. W.; Kemp, K.; Levina, L.; Wang, X.; Hoogland, S.; Debnath, R.; Brzozowski, L.; Sargent, E. H.; Asbury, J. B. *ACS Nano* **2012**, *6*, 89–99.
- (23) Kovalenko, M. V.; Scheele, M.; Talapin, D. V. *Science* **2009**, *324*, 1417–20.

- (24) Nag, A.; Kovalenko, M. V.; Lee, J.-S.; Liu, W.; Spokoyny, B.; Talapin, D. V. *J. Am. Chem. Soc.* **2011**, *133*, 10612–10620.
- (25) Oh, S. J.; Berry, N. E.; Choi, J.-H.; Gauldin, E. A.; Lin, H.; Paik, T.; Diroll, B. T.; Muramoto, S.; Murray, C. B.; Kagan, C. R. *Nano Lett.* **2014**, *14*, 1559–1566.
- (26) Tang, J.; Kemp, K. W.; Hoogland, S.; Jeong, K. S.; Liu, H.; Levina, L.; Furukawa, M.; Wang, X.; Debnath, R.; Cha, D.; Chou, K. W.; Fischer, A.; Amassian, A.; Asbury, J. B.; Sargent, E. H. *Nat. Mater.* **2011**, *10*, 765–771.
- (27) Dolzhenkov, D. S.; Zhang, H.; Jang, J.; Son, J. S.; Panthani, M. G.; Shibata, T.; Chattopadhyay, S.; Talapin, D. V. *Science* **2015**, *347*, 425–428.
- (28) Fafarman, A. T.; Koh, W.-k.; Diroll, B. T.; Kim, D. K.; Ko, D.-K.; Oh, S. J.; Ye, X.; Doan-Nguyen, V.; Crump, M. R.; Reifsnyder, D. C.; Murray, C. B.; Kagan, C. R. *J. Am. Chem. Soc.* **2011**, *133*, 15753–61.
- (29) Gao, Y.; Aerts, M.; Sandeep, C. S. S.; Talgorn, E.; Savenije, T. J.; Kinge, S.; Siebbeles, L. D. A.; Houtepen, A. J. *ACS Nano* **2012**, *6*, 9606–9614.
- (30) Oh, S. J.; Wang, Z.; Berry, N. E.; Choi, J.-h.; Zhao, T.; Gauldin, E. A.; Paik, T.; Lai, Y.; Murray, C. B.; Kagan, C. R. *Nano Lett.* **2014**, *14*, 6210–6216.
- (31) Zhang, H.; Jang, J.; Liu, W.; Talapin, D. V. *ACS Nano* **2014**, *8*, 7359–7369.
- (32) Kim, D.; Kim, D.-H.; Lee, J.-H.; Grossman, J. C. *Phys. Rev. Lett.* **2013**, *110*, 196802.
- (33) Bakulin, A. A.; Neutzner, S.; Bakker, H. J.; Ottaviani, L.; Barakel, D.; Chen, Z. *ACS Nano* **2013**, *7*, 8771–9.
- (34) Goodwin, E. D.; Diroll, B. T.; Oh, S. J.; Paik, T.; Murray, C. B.; Kagan, C. R. *J. Phys. Chem. C* **2014**, *118*, 27097–27105.

- (35) Katsiev, K. et al. *Adv. Mater.* **2014**, *26*, 937–942.
- (36) Thon, S. M.; Ip, A. H.; Voznyy, O.; Levina, L.; Kemp, K. W.; Carey, G. H.; Masala, S.; Sargent, E. H. *ACS Nano* **2013**, *7*, 7680–7688.
- (37) Goodwin, E.; Straus, D. B.; Gauding, E. A.; Murray, C. B.; Kagan, C. R. *Chem. Phys.* **2016**, *471*, 81–88.
- (38) Zhitomirsky, D.; Voznyy, O.; Hoogland, S.; Sargent, E. H. *ACS Nano* **2013**, *7*, 5282–5290.
- (39) Gaubas, E.; Vanhellefont, J. *J. Electrochem. Soc.* **2007**, *154*, H231.
- (40) Qu, L.; Peng, X. *J. Am. Chem. Soc.* **2002**, *124*, 2049–2055.
- (41) Jang, J.; Dolzhenkov, D. S.; Liu, W.; Nam, S.; Shim, M.; Talapin, D. V. *Nano Lett.* **2015**, *15*, 6309–6317.
- (42) Choi, J.-H.; Oh, S. J.; Lai, Y.; Kim, D. K.; Zhao, T.; Fafarman, A. T.; Diroll, B. T.; Murray, C. B.; Kagan, C. R. *ACS Nano* **2013**, *7*, 8275–83.
- (43) Talgorn, E.; de Vries, M. A.; Siebbeles, L. D. A.; Houtepen, A. J. *ACS Nano* **2011**, *5*, 3552–8.
- (44) Gao, J.; Zhang, J.; van de Lagemaat, J.; Johnson, J. C.; Beard, M. C. *ACS Nano* **2014**, *8*, 12814–12825.
- (45) Leatherdale, C. A.; Kagan, C. R.; Morgan, N. Y.; Empedocles, S. A.; Kastner, M. A.; Bawendi, M. G. *Phys. Rev. B* **2000**, *62*, 2669–2680.

Part II

Optical Spectroscopy of Two-Dimensional Hybrid Perovskites

Chapter 5

Introduction to Two-Dimensional Hybrid Perovskites

5.1 Introduction

Organic-inorganic hybrid perovskites have been heavily investigated recently¹⁻⁷ for their use in solar cells because in just a few years, the efficiency of perovskite-based solar cells has risen to rival commercial silicon solar cells.⁸ Hybrid perovskites comprise a metal (in recent work, typically Pb or Sn) atom in a corner-sharing octahedral halide cage, with a properly-sized⁹⁻¹² positively charged organic (or cesium)¹³ cation occupying the interstitial space. Most solar cells are fabricated from three-dimensional (3D) perovskites that have a uniform structure throughout the material (Figure 5.1A). In these materials, the Goldschmidt tolerance parameter formalizes the restriction on overall size of the cation: if the cation is too large, a 3D perovskite lattice cannot

Reproduced with permission from Straus, D. B.; Kagan, C. R. *J. Phys. Chem. Lett.* **2018**, *9*, 1434–1447. Copyright 2018 American Chemical Society.

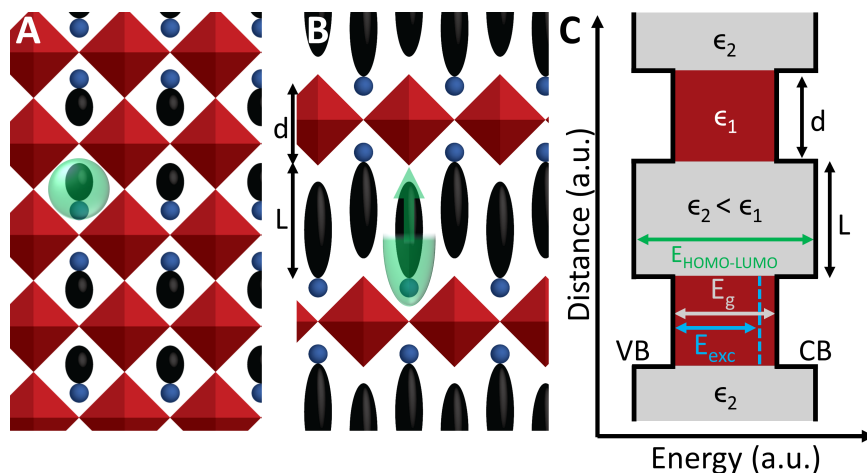


Figure 5.1: A) Schematic of a projection of the 3D hybrid perovskite, showing an inorganic network of corner sharing metal halide octahedra (red) with interstitial organic cations (blue, black). (green) Highlighting the restriction on cation size. B) Schematic of a projection down the c -axis of the 2D hybrid perovskite, showing the alternation of organic (blue, black) and corner-sharing inorganic (red) layers for $n = 1$ with inorganic layer thickness d and organic layer thickness L . (green) Highlighting the restriction solely on the cross-sectional area, but not the length of the organic cation. C) Energy diagram corresponding to the 2D structure in B). Labeling of the valence band VB, conduction band CB, electronic band gap E_g (grey) and the optical band gap E_{exc} (blue) of the inorganic framework, and the larger HOMO-LUMO gap of the organic cations (green). The organic framework (grey regions) has a dielectric constant ϵ_2 , which is smaller than the dielectric constant ϵ_1 of the inorganic framework (red regions).

crystallize.^{9,10} This restriction limits the degree of tunability that can be provided through cation modifications.¹⁴

Perovskite frenzy has brought renewed attention to two-dimensional (2D) analogues that were heavily studied in the 1990s-early 2000s. 2D hybrid perovskites spontaneously form if the length of the organic cation is increased (Figure 5.1B).^{11,12,15-17} 2D perovskites are typically described as “perfect” quantum well superlattices because these materials have alternating organic and inorganic layers and are stoichiometric compounds that do not have the interfacial roughness common to molecular-beam epitaxially (MBE) grown quantum wells.^{18,19} Many 2D perovskites have a Type I band alignment of the organic and inorganic frameworks,^{12,20,21} with a few reports of Type II heterostructures realized through the introduction of conjugated organic cations.^{22,23}

In addition, 2D perovskites show increased moisture stability compared to 3D analogues because of the inclusion of hydrophobic organic cations.^{24,25} The relaxation of the restriction on the length of the cation allows the properties of 2D perovskites to be tailored to a much greater degree because in addition to stoichiometric changes in metal and halide composition, there is a much wider range of acceptable organic cations^{11,23,26–29} and the thickness of the inorganic layers can be varied by controlling the number of inorganic layers n for each organic layer.^{6,24,30} Here we correlate the unique structural and optoelectronic properties in semiconducting 2D perovskites and discuss current and future applications for this diverse class of materials.

5.2 Quantum and Dielectric Confinement

Quantum and dielectric confinement effects in 2D perovskites increase the effective bandgap and the exciton binding energy (red, Figures 5.1B and C) compared to the 3D perovskites.^{31–34} For example, the exciton binding energy in 2D perovskites increases by more than an order of magnitude from ~ 10 meV in 3D perovskites^{35,36} to >150 meV in 2D perovskites with $n = 1$ (Figure 5.1C, dashed blue).^{31,32,34} Quantum confinement in one dimension shifts the conduction and valence bands by $\frac{\hbar^2\pi^2}{2m_{e,h}d^2}$, where m_e and m_h are the mass of the electron and hole and d is the well thickness, and thereby increases the effective bandgap. It also increases the exciton binding energy such that the exciton binding energy of the $1s$ exciton is

$$E_B = \left(\frac{2}{\alpha - 1}\right)^2 E_{B,3D} \quad (5.1)$$

where $E_{B,3D} = \left(\frac{1}{\epsilon_1}\right)^2 \left(\frac{m_{ex}}{m_0}\right) R_H$ is the bulk exciton binding energy, ϵ_1 is the dielectric constant (i.e., relative permittivity) of the inorganic framework, $m_{ex} = \left(\frac{1}{m_e} + \frac{1}{m_h}\right)^{-1}$

is the reduced exciton mass, m_0 is the free electron mass, and R_H is the hydrogen Rydberg constant.^{37,38} α is the dimensionality of the system: in a bulk, non-confined material $\alpha = 3$, and in a perfect 2D system $\alpha = 2$, with a corresponding exciton binding energy $E_{B,2D} = 4E_{B,3D}$. As the thickness d of the quantum well increases, α increases from 2 and begins to approach 3.

Dielectric confinement is an electrostatic phenomenon that results when a thin layer of material with dielectric constant ϵ_1 is sandwiched between a material with dielectric constant $\epsilon_2 < \epsilon_1$. The electrostatic force between charges in the high dielectric constant (ϵ_1) material increases because the electric field generated by a charge extends into the lower dielectric constant (ϵ_2) medium where it is screened less effectively.^{33,39,40} This phenomenon is also called the image-charge effect. The change in Coulomb forces in the high dielectric constant material renormalizes the energy levels, increasing both the electronic band gap as well as the exciton binding energy.⁴¹ Using first-order perturbation theory and an approximate model that assumes charge carriers are confined to the inorganic framework by an infinite barrier and assumes a two-band model with separable wavefunctions, the change in exciton binding energy

$$\Delta E_B \approx 2 \left(\frac{\epsilon_1 - \epsilon_2}{\epsilon_1 + \epsilon_2} \right) \left(\frac{q^2}{\epsilon_1 \epsilon_0 d} \right) I \quad (5.2)$$

where q is the fundamental charge, ϵ_0 the vacuum permittivity, and I is a factor that is approximately unity.^{37,38,42} These equations provide a simple framework to model confinement effects in 2D perovskites. However, they are inexact as it is not possible to define parent 3D organic and inorganic components from which to extrapolate their properties, as commonly done for MBE-grown semiconductor quantum well superlattices.⁴³ To account for Coulomb interactions between the organic and inorganic constituents as well as spin-orbit coupling effects, detailed calculations of the band

structure for 2D perovskites are needed.⁴³

5.3 Band Structure

In conventional semiconductors, the valence band is made up of p-orbitals and the conduction band is made up of s-orbitals. This structure creates complexity in the valence band (e.g., heavy and light hole and spin-orbit bands), but not in the conduction band.⁴⁴ In contrast, 3D and 2D hybrid perovskites have a valence band made up predominantly of halide p-orbitals hybridized with some metal s-orbital character, and a conduction band predominantly made of metal p-orbitals; in lead iodide hybrid perovskites, the relevant orbitals are I 5p, and Pb 6s and 6p.^{20,45,46} For a comprehensive discussion of the electronic structure of 3D and 2D perovskites, we refer the reader to Ref. [43], as the band structure depends on the details of the crystal structure of the perovskite. The band structure and density-of-states for the 2D hybrid perovskite 4-fluorophenethylammonium lead iodide ((4-FPEA)₂PbI₄, PEA = C₆H₅C₂H₄NH₃⁺) notably shows complexity in the conduction band.⁴⁵ The combination of this complex band structure and the incorporation of heavy Pb atoms (and to a lesser degree Sn atoms in analogous tin halide perovskites) generates significant spin-orbit coupling in the conduction band,²⁰ with a calculated spin-orbit splitting Δ_{SO} between the first two conduction band states of 1.2 eV in (4-FPEA)₂PbI₄.^{43,45,47} The large spin-orbit coupling and non-centrosymmetric structure of hybrid perovskites sets up the necessary condition for spin-dependent properties and the possibility of exotic Rashba and Dresselhaus effects.^{45–49} In the Rashba or Dresselhaus effect, charge carriers experience an effective magnetic field, and the non-centrosymmetric potential can cause one spin orientation to be stabilized.⁴⁸ Recently, a “giant” Rashba splitting was claimed to be observed in phenethylammonium lead iodide ((PEA)₂PbI₄),

indicating the potential for 2D perovskites in spintronics applications.⁵⁰

5.4 Length of the Organic Cation

2D perovskites can be synthesized with different chain length L alkylammonium cations. The length L of typical alkylammonium cations $C_m H_{2m+1} NH_3^+$ where $m \geq 4$ has a negligible effect on the optical properties of the perovskite.¹⁶ For example, 1.6 K optical absorption spectra of cleaved single crystals of $(C_m H_{2m+1} NH_3)_2 PbI_4$ with $m = 4, 8, 9, 10, 12$, in which the interlayer Pb-Pb distance ($L + d$, Figures 5.1B and C) varies from 15.17 Å to 24.51 Å, show a similar 320 ± 30 meV exciton binding energy.¹⁶ Temperature-dependent photoluminescence (PL) measurements show thermally-activated quenching of the free-exciton luminescence intensity with an activation energy near room temperature of 370 ± 50 meV in single crystals of the same materials.¹⁶ This higher temperature activation energy has been compared with the low temperature exciton binding energy in support of the insensitivity of the optical properties to alkyl chain length; however, these values may vary as these 2D perovskites undergo a structural phase transition (discussed later in this perspective) between temperatures of 250 K and 310 K that depends on m and correlates with melting of the amine (e.g., $m = 4, 8, 9, 10$ are in the low temperature phase and $m = 12$ is in the high temperature phase) and as the crystals can degrade under illumination during measurements.¹⁶

5.5 Dielectric Constant of the Organic Cation (ϵ_2)

While simply changing the length L of the organic cation has little effect on the electronic and optical properties, changing the dielectric constant of the organic cation

ϵ_2 , e.g., by choosing aromatic instead of aliphatic amines, significantly decreases the exciton binding energy in $n = 1$ 2D perovskites. For instance 10 K absorption spectra of single crystals show a decrease in exciton binding energy from 320 meV in $(\text{C}_{10}\text{H}_{21}\text{NH}_3)_2\text{PbI}_4$ to 220 meV in $(\text{PEA})_2\text{PbI}_4$, consistent with PEA^+ having a higher dielectric constant ϵ_2 than alkyl amines including $\text{C}_{10}\text{H}_{21}\text{NH}_3^+$.³¹ The activation energy for PL quenching in $(\text{PEA})_2\text{PbI}_4$ single crystals is found to be 220 ± 30 meV. The electronic band gap also decreases,³¹ in accord with dielectric confinement.⁴¹ The local environment of the perovskite sample also affects the exciton binding energy. A recent study on butylammonium lead iodide BA_2PbI_4 , $\text{BA}=\text{C}_4\text{H}_9\text{NH}_3^+$ single crystals found an exciton binding energy of 370 meV that is enhanced substantially to 490 meV upon exfoliation and transfer such that the perovskite layer is bounded by silica ($\epsilon = 2.13$) on one side and air ($\epsilon = 1$) on the other.⁵¹ The increase in dielectric confinement created by the sample environment should also increase the band gap of the exfoliated layer compared to that of the crystal, though this is hard to directly compare at low temperatures because substrate interactions suppress the phase transition.⁵¹

5.6 Cross-sectional Area of the Organic Cation

2D perovskites form if the length of the organic cation is increased, however there is a restriction on their cross-sectional area such that they fit within the interstitial space between the inorganic octahedra (Figure 5.1B, green). For example, in 2D lead iodide perovskites, the maximum cross-sectional area is on the order of 40 \AA^2 .¹² The limited cross-sectional area available to host the organic cation can also be harnessed to tailor the optical properties of the perovskite by straining the inorganic framework. Increasing the cross-sectional area of the organic cation will change the orientation of the cations in the organic framework, and for the perovskite to crystallize, the inter-

octahedral metal-halide-metal bond angle must change to accommodate the larger cation (Figure 5.2A), though it is possible for the cation to be too large for a perovskite structure to form.¹¹ Reduction of the metal-halide-metal bond angle from the ideal 180° alters the band structure and increases the band gap of the perovskite.²⁷ This effect has been seen experimentally in 2D tin-halide perovskites.²⁷⁻²⁹ Experimental exciton resonances in SnI_4 -based 2D perovskites with functionalized aromatic moieties and ethylammonium tethers are plotted against the Sn-I-Sn bond angle in Figure 5.2B.²⁷ Strain effects are also reported in 2D lead halide perovskites. A recent study found that in 2D lead halide perovskites containing aromatic cations, the length of the alkyl tether connecting the ammonium cation to the aromatic moiety has a much larger effect on the band gap than the number of aromatic rings on the cation.¹⁸ A methyl tether results in more strain and a smaller Pb-X-Pb (X=Cl, Br, I) bond angle than an ethyl tether.¹⁸ We are not aware of any studies quantitatively probing the effect of strain on the exciton binding energy. However, akin to strain engineering in conventional Si electronics⁵² and in 3D perovskites⁵³ which warps the light and heavy hole bands, we expect strain in 2D perovskites will modify the band structure, changing the carrier effective masses and therefore the exciton binding energy.

5.7 Cationic Phase Transitions

We already described examples above where, in addition to tuning the length and dielectric constant, for some organic cations the perovskite undergoes a phase transition upon cooling.^{16,54,55} We highlight these phase transitions here as they drive changes in band structure that complicate the evaluation of temperature-dependent optical properties.⁴³ The influence of the structural phase transition on band gap is readily seen by eye at temperatures between 235 and 310 K in alkylammonium lead

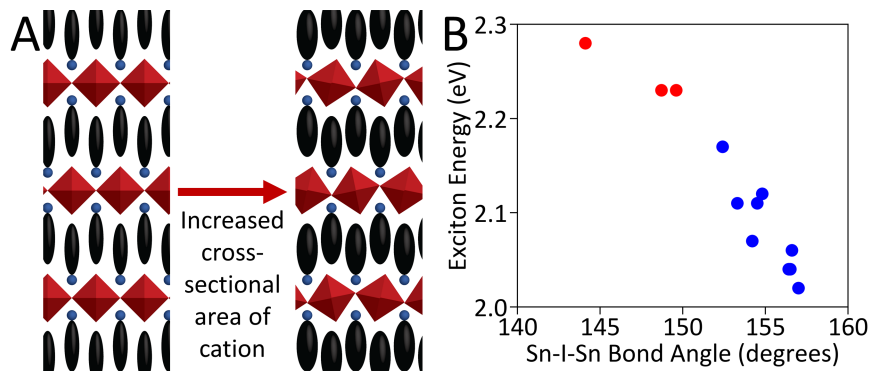


Figure 5.2: A) Schematic showing distortion in the metal-halide framework to accommodate an organic cation with a larger cross-sectional area. B) Experimental energies of the excitonic absorption in $(\text{PEA})_2\text{SnI}_4$ -based 2D perovskites with functionalized cations that exhibit solely in-plane distortion (blue) and a combination of in- and out-of-plane distortion (red). Data from Ref. [27].

halide perovskites $[(\text{C}_m\text{H}_{2m+1}\text{NH}_3)_2\text{PbI}_4, m = 4, 8, 9, 10, 12]$ as a change in color from orange at high temperature to yellow at low temperature.¹⁶ Notably, this phase transition is absent for $(\text{C}_6\text{H}_{13}\text{NH}_3)_2\text{PbI}_4$.¹⁶ In addition, no phase transition is observed in $(\text{PEA})_2\text{PbI}_4$,³¹ demonstrating the influence of the cation on the thermodynamic properties of 2D hybrid perovskites. Interactions between 2D perovskites and the surrounding environment also affect phase transitions. The interaction of an exfoliated sheet with a silica substrate suppresses the freezing/melting phase transition in BA_2PbI_4 ,⁵¹ and this distinction must be taken into account when comparing the temperature-dependent optical properties of exfoliated sheets and larger single crystals.

5.8 Halide and Metal Substitutions

The band gap of 2D perovskites can be tuned through halide substitution. Replacing iodide with bromide or chloride results in an increase in the band gap,^{11,18,56,57} as it does in 3D hybrid perovskites, and is consistent with lowering of the valence band maximum that has predominantly halide p -character.⁵⁸ Mixed halide systems can also

be used to further tailor the optical and electronic properties. By using two halides in PEA-based 2D perovskites and varying the proportion z in $((\text{PEA})_2\text{PbX}_{4(1-z)}\text{Y}_{4z})$, $X, Y = \text{Cl, Br, I}$), the band gap can be continuously tuned.⁵⁹ We are not aware of quantitative studies of the halide-dependent exciton binding energy in 2D perovskites. As $E_{B,2D} = 4E_{B,3D} = 4\left(\frac{1}{\epsilon_1}\right)^2\left(\frac{m_{ex}}{m_0}\right)R_H$, the exciton binding energy will change in proportion to the exciton effective mass and in inverse proportion to the square of the dielectric constant. Although studies of effective mass do not conclusively show a difference between lead iodide and lead bromide perovskites,^{35,60,61} as iodide is replaced by bromide and then chloride and the band gap increases, m_e and m_h and therefore E_B are anticipated to increase for perovskites with similar crystal and band structures.⁶² Increases in the carrier effective masses will also reduce the carrier mobility.

In the 3D perovskites, the dielectric constants trend as $\epsilon_{\text{MAPbCl}_3} < \epsilon_{\text{MAPbBr}_3} < \epsilon_{\text{MAPbI}_3}$ ($\text{MA} = \text{methylammonium, CH}_3\text{NH}_3^+$),⁶³ consistent with a larger binding energy for excitons in MAPbBr_3 than in MAPbI_3 .^{61,64} As ϵ_1 decreases for lower- z halides, dielectric confinement (Equation 5.2) in 2D perovskites is further expect to increase E_B as $\Delta E_B \propto \epsilon_1^{-1}$ for $\epsilon_1 \gg \epsilon_2$. Structural changes including any changes in well thickness from halide substitution may also affect the band structure and exciton binding energy.

The properties of 2D perovskites can be further tuned through metal substitutions. Sn-based 2D perovskites have a smaller band gap than Pb-based 2D perovskites for the same organic cation (e.g., 2.19 eV for $(\text{PEA})_2\text{SnI}_4$ versus 2.62 eV for $(\text{PEA})_2\text{PbI}_4$).⁶⁵ This trend can be rationalized by the larger Pauling electronegativity of Sn (1.96) compared to that for Pb (1.87) (and 2.66 for I), making, e.g., Pb-I bonds more ionic than Sn-I bonds.⁵⁷ Replacing Pb with Sn also slightly reduces the exciton binding energy from 220 to 190 meV.⁶⁵ The smaller band gap of 2D Sn-based perovskites is expected to result in a larger mobility, which is seen in the 3D perovskites MAPbI_3 ($E_g = 1.54$ eV

and $\mu_e = 66 \text{ cm}^2\text{V}^{-1}\text{s}^{-1}$) and MASnI_3 ($E_g = 1.20 \text{ eV}$ and $\mu_e = 2320 \text{ cm}^2\text{V}^{-1}\text{s}^{-1}$).⁶⁶

5.9 Length Scale of Excitons

There is debate in the literature as to whether excitons in the inorganic framework of 2D perovskites are Wannier (extended over multiple unit cells) or Frenkel (localized to a single unit cell) in character, with most reports settling on the existence of Wannier excitons in the inorganic framework. The Bohr exciton radius in $n = 1$ 2D perovskites varies with the particular 2D perovskite, with measurements ranging from approximately one to several lattice constants.^{16,31,32,57,59,60,67-73} In addition, even in a single 2D perovskite system (e.g., $m = 6$ and 10 ($\text{C}_m \text{H}_{2m+1} \text{NH}_3$)₂ PbI_4), the Bohr exciton radius varies and both Wannier^{16,31,72,74} and Frenkel^{67,69} excitons have been reported. Typically, Wannier excitons have small binding energies $<100 \text{ meV}$ and are seen in inorganic semiconductors, whereas Frenkel excitons have large ($\sim 500+$ meV) binding energies and are typical for organic materials.⁵⁷ In addition to excitons localized in the inorganic framework, there are also Frenkel excitons localized on the organic framework.⁷⁵ It is possible that excitons in 2D perovskites fall between the Wannier and Frenkel regimes and exhibit properties of both types of excitons because even the largest measured Bohr exciton radius in 2D perovskites is on the order of several unit cells.⁵⁷ Given the softness of the hybrid perovskite lattice, we hypothesize that dynamic modulation of the structure may give rise to temperature and time-dependent localization effects that alter the character of the exciton.^{19,76}

5.10 Anisotropic Optical Properties

The band structure and optical properties of 2D hybrid perovskites are highly anisotropic. Ishihara et al. collected 1.6 K reflection spectra of single crystals of the $n = 1$ species $(\text{C}_{10}\text{H}_{21}\text{NH}_3)_2\text{PbI}_4$ and found that when light propagated perpendicular to the \vec{c} -axis ($\vec{k} \perp \vec{c}$, i.e. parallel to the inorganic framework), the excitonic absorption varied greatly with the polarization.¹⁶ When the electric vector $\vec{E} \perp \vec{c}$ (parallel to the inorganic framework), there is a strong excitonic resonance at 2.55 eV with a large oscillator strength of 0.7 ± 0.1 per formula unit, which is consistent with a dipole-allowed, direct excitonic transition.¹⁶ In contrast, when $\vec{E} \parallel \vec{c}$ (perpendicular to the inorganic framework), the excitonic resonance is extremely weak with an oscillator strength of 0.03 ± 0.01 per formula unit.¹⁶ These results indicate that the transition dipole moment is oriented along the inorganic framework in $n = 1$ (and likely in higher order) 2D perovskites. When light propagates parallel to the \vec{c} -axis ($\vec{k} \parallel \vec{c}$, perpendicular to the inorganic framework), $\vec{E} \perp \vec{c}$ always, resulting in a strong excitonic transition. However, there is still a polarization dependence in the higher energy excitations, especially around 3.2 eV, indicating that the \vec{a} and \vec{b} axes of the crystal have somewhat different electronic properties.¹⁶

5.11 Conclusion

The tunable composition and thickness of the inorganic framework and the tailorable geometry and chemistry of the organic cation interlayers make 2D hybrid perovskites an intriguing materials class to study. While these materials were explored in the 1990s-2000s, renewed interest in 2D perovskites, driven by the success of the 3D perovskites as the active layer in emerging photovoltaic devices, has led to an

expansion in the size of the community and the number of studies that are uncovering new structures and fascinating physics.

5.12 References

- (1) Ahn, N.; Son, D.-Y.; Jang, I.-H.; Kang, S. M.; Choi, M.; Park, N.-G. *J. Am. Chem. Soc.* **2015**, *137*, 8696–8699.
- (2) Dong, Q.; Fang, Y.; Shao, Y.; Mulligan, P.; Qiu, J.; Cao, L.; Huang, J. *Science* **2015**, *347*, 967–970.
- (3) Elbaz, G. A.; Straus, D. B.; Semonin, O. E.; Hull, T. D.; Paley, D. W.; Kim, P.; Owen, J. S.; Kagan, C. R.; Roy, X. *Nano Lett.* **2017**, *17*, 1727–1732.
- (4) Nie, W.; Tsai, H.; Asadpour, R.; Blancon, J.-C.; Neukirch, A. J.; Gupta, G.; Crochet, J. J.; Chhowalla, M.; Tretiak, S.; Alam, M. a.; Wang, H.-L.; Mohite, A. D. *Science* **2015**, *347*, 522–525.
- (5) Semonin, O. E.; Elbaz, G. A.; Straus, D. B.; Hull, T. D.; Paley, D. W.; van der Zande, A. M.; Hone, J. C.; Kymissis, I.; Kagan, C. R.; Roy, X.; Owen, J. S. *J. Phys. Chem. Lett.* **2016**, *7*, 3510–3518.
- (6) Tsai, H. et al. *Nature* **2016**, *536*, 312–316.
- (7) Zhu, H.; Miyata, K.; Fu, Y.; Wang, J.; Joshi, P. P.; Niesner, D.; Williams, K. W.; Jin, S.; Zhu, X.-Y. *Science* **2016**, *353*, 1409–1413.
- (8) NREL Best Research-Cell Efficiencies. <http://www.nrel.gov/pv/assets/images/efficiency-chart.png> (accessed 01/16/2018).
- (9) Goldschmidt, V. M. *Naturwissenschaften* **1926**, *14*, 477–485.
- (10) Kieslich, G.; Sun, S.; Cheetham, A. K. *Chem. Sci.* **2015**, *6*, 3430–3433.

- (11) Mitzi, D. B. *Prog. Inorg. Chem.* **1999**, *48*, 1–121.
- (12) Mitzi, D. B.; Chondroudis, K.; Kagan, C. R. *IBM J. Res. Dev.* **2001**, *45*, 29–45.
- (13) Møller, C. *Nature* **1958**, *182*, 1436–1436.
- (14) Grote, C.; Berger, R. F. *J. Phys. Chem. C* **2015**, *119*, 22832–22837.
- (15) Arend, H.; Huber, W.; Mischgofsky, F.; Richter-Van Leeuwen, G. *J. Cryst. Growth* **1978**, *43*, 213–223.
- (16) Ishihara, T.; Takahashi, J.; Goto, T. *Phys. Rev. B* **1990**, *42*, 11099–11107.
- (17) Mitzi, D. B.; Feild, C. A.; Harrison, W. T. A.; Guloy, A. M. *Nature* **1994**, *369*, 467–469.
- (18) Du, K.-Z.; Tu, Q.; Zhang, X.; Han, Q.; Liu, J.; Zauscher, S.; Mitzi, D. B. *Inorg. Chem.* **2017**, *56*, 9291–9302.
- (19) Straus, D. B.; Hurtado Parra, S.; Iotov, N.; Gebhardt, J.; Rappe, A. M.; Subotnik, J. E.; Kikkawa, J. M.; Kagan, C. R. *J. Am. Chem. Soc.* **2016**, *138*, 13798–13801.
- (20) Gebhardt, J.; Kim, Y.; Rappe, A. M. *J. Phys. Chem. C* **2017**, *121*, 6569–6574.
- (21) Mao, L.; Tsai, H.; Nie, W.; Ma, L.; Im, J.; Stoumpos, C. C.; Malliakas, C. D.; Hao, F.; Wasielewski, M. R.; Mohite, A. D.; Kanatzidis, M. G. *Chem. Mater.* **2016**, *28*, 7781–7792.
- (22) Braun, M.; Tuffentsammer, W.; Wachtel, H.; Wolf, H. *Chem. Phys. Lett.* **1999**, *303*, 157–164.
- (23) Mitzi, D. B.; Chondroudis, K.; Kagan, C. R. *Inorg. Chem.* **1999**, *38*, 6246–6256.
- (24) Milot, R. L.; Sutton, R. J.; Eperon, G. E.; Haghighirad, A. A.; Martinez Hardigree, J.; Miranda, L.; Snaith, H. J.; Johnston, M. B.; Herz, L. M. *Nano Lett.* **2016**, *16*, 7001–7007.

- (25) Smith, I. C.; Hoke, E. T.; Solis-Ibarra, D.; McGehee, M. D.; Karunadasa, H. I. *Angew. Chemie - Int. Ed.* **2014**, *53*, 11232–11235.
- (26) Dohner, E. R.; Jaffe, A.; Bradshaw, L. R.; Karunadasa, H. I. *J. Am. Chem. Soc.* **2014**, *136*, 13154–13157.
- (27) Knutson, J. L.; Martin, J. D.; Mitzi, D. B. *Inorg. Chem.* **2005**, *44*, 4699–4705.
- (28) Mitzi, D. B.; Dimitrakopoulos, C. D.; Kosbar, L. L. *Chem. Mater.* **2001**, *13*, 3728–3740.
- (29) Xu, Z.; Mitzi, D. B.; Dimitrakopoulos, C. D.; Maxcy, K. R. *Inorg. Chem.* **2003**, *42*, 2031–2039.
- (30) Wu, X.; Trinh, M. T.; Niesner, D.; Zhu, H.; Norman, Z.; Owen, J. S.; Yaffe, O.; Kudisch, B. J.; Zhu, X.-Y. *J. Am. Chem. Soc.* **2015**, *137*, 2089–2096.
- (31) Hong, X.; Ishihara, T.; Nurmikko, A. V. *Phys. Rev. B* **1992**, *45*, 6961–6964.
- (32) Ishihara, T.; Hong, X.; Ding, J.; Nurmikko, A. *Surf. Sci.* **1992**, *267*, 323–326.
- (33) Keldysh, L. V. *JETP Lett.* **1979**, *29*, 658–661.
- (34) Kumagai, M.; Takagahara, T. *Phys. Rev. B* **1989**, *40*, 12359–12381.
- (35) Miyata, A.; Mitioglu, A.; Plochocka, P.; Portugall, O.; Wang, J. T.-W.; Stranks, S. D.; Snaith, H. J.; Nicholas, R. J. *Nat. Phys.* **2015**, *11*, 582–587.
- (36) Yang, Y.; Ostrowski, D. P.; France, R. M.; Zhu, K.; van de Lagemaat, J.; Luther, J. M.; Beard, M. C. *Nat. Photonics* **2015**, *10*, 53–59.
- (37) He, X.-F. *Phys. Rev. B* **1991**, *43*, 2063–2069.
- (38) Mathieu, H.; Lefebvre, P.; Christol, P. *Phys. Rev. B* **1992**, *46*, 4092–4101.
- (39) Hanamura, E.; Nagaosa, N.; Kumagai, M.; Takagahara, T. *Mater. Sci. Eng. B* **1988**, *1*, 255–258.

- (40) Ishihara, T. In *Opt. Prop. Low-Dimensional Mater.* World Scientific: 1996, pp 288–339.
- (41) Raja, A. et al. *Nat. Commun.* **2017**, *8*, 15251.
- (42) Andreani, L. C.; Pasquarello, A. *Phys. Rev. B* **1990**, *42*, 8928–8938.
- (43) Even, J.; Pedesseau, L.; Katan, C.; Kepenekian, M.; Lauret, J.-S.; Saponi, D.; Deleporte, E. *J. Phys. Chem. C* **2015**, *119*, 10161–10177.
- (44) Sze, S. M.; Ng, K. K., *Physics of Semiconductor Devices*, 3rd ed., Hoboken, NJ, 2007.
- (45) Even, J.; Pedesseau, L.; Dupertuis, M.-A.; Jancu, J.-M.; Katan, C. *Phys. Rev. B* **2012**, *86*, 205301.
- (46) Even, J.; Pedesseau, L.; Jancu, J. M.; Katan, C. *J. Phys. Chem. Lett.* **2013**, *4*, 2999–3005.
- (47) Pedesseau, L.; Saponi, D.; Traore, B.; Robles, R.; Fang, H.-H. H.; Loi, M. A.; Tsai, H.; Nie, W.; Blancon, J.-C. C.; Neukirch, A.; Tretiak, S.; Mohite, A. D.; Katan, C.; Even, J.; Kepenekian, M. *ACS Nano* **2016**, *10*, 9776–9786.
- (48) Kepenekian, M.; Even, J. *J. Phys. Chem. Lett.* **2017**, *8*, 3362–3370.
- (49) Kepenekian, M.; Robles, R.; Katan, C.; Saponi, D.; Pedesseau, L.; Even, J. *ACS Nano* **2015**, *9*, 11557–11567.
- (50) Zhai, Y.; Baniya, S.; Zhang, C.; Li, J.; Haney, P.; Sheng, C.-X.; Ehrenfreund, E.; Vardeny, Z. V. *Sci. Adv.* **2017**, *3*, e1700704.
- (51) Yaffe, O.; Chernikov, A.; Norman, Z. M.; Zhong, Y.; Velauthapillai, A.; van der Zande, A.; Owen, J. S.; Heinz, T. F. *Phys. Rev. B* **2015**, *92*, 045414.
- (52) Chidambaram, P. R.; Bowen, C.; Chakravarthi, S.; Machala, C.; Wise, R. *IEEE Trans. Electron Devices* **2006**, *53*, 944–964.

- (53) Amat, A.; Mosconi, E.; Ronca, E.; Quarti, C.; Umari, P.; Nazeeruddin, M. K.; Grätzel, M.; De Angelis, F. *Nano Lett.* **2014**, *14*, 3608–3616.
- (54) Barman, S.; Venkataraman, N. V.; Vasudevan, S.; Seshadri, R. *J. Phys. Chem. B* **2003**, *107*, 1875–1883.
- (55) Naik, V. V.; Vasudevan, S. *J. Phys. Chem. C* **2010**, *114*, 4536–4543.
- (56) Ishihara, T.; Hirasawa, M.; Goto, T. *Jpn. J. Appl. Phys.* **1995**, *34*, 71.
- (57) Saparov, B.; Mitzi, D. B. *Chem. Rev.* **2016**, *116*, 4558–4596.
- (58) Butler, K. T.; Frost, J. M.; Walsh, A. *Mater. Horizons* **2015**, *2*, 228–231.
- (59) Lanty, G.; Jemli, K.; Wei, Y.; Leymarie, J.; Even, J.; Lauret, J.-S.; Deleporte, E. *J. Phys. Chem. Lett.* **2014**, *5*, 3958–3963.
- (60) Koutselas, I. B.; Ducasse, L.; Papavassiliou, G. C. *J. Phys. Condens. Matter* **1996**, *8*, 1217–1227.
- (61) Tanaka, K.; Takahashi, T.; Ban, T.; Kondo, T.; Uchida, K.; Miura, N. *Solid State Commun.* **2003**, *127*, 619–623.
- (62) Kittel, C., *Introduction to Solid State Physics*, 8th ed.; Wiley: Hoboken, NJ, 2005.
- (63) Onoda-Yamamuro, N.; Matsuo, T.; Suga, H. *J. Phys. Chem. Solids* **1992**, *53*, 935–939.
- (64) Galkowski, K.; Mitioglu, A.; Miyata, A.; Plochocka, P.; Portugall, O.; Eperon, G. E.; Wang, J. T.-W.; Stergiopoulos, T.; Stranks, S. D.; Snaith, H. J.; Nicholas, R. J. *Energy Environ. Sci.* **2016**, *9*, 962–970.
- (65) Papavassiliou, G.; Koutselas, I.; Terzis, A.; Whangbo, M.-H. *Solid State Commun.* **1994**, *91*, 695–698.

- (66) Stoumpos, C. C.; Malliakas, C. D.; Kanatzidis, M. G. *Inorg. Chem.* **2013**, *52*, 9019–9038.
- (67) Hirasawa, M.; Ishihara, T.; Goto, T. *J. Phys. Soc. Japan* **1994**, *63*, 3870–3879.
- (68) Hong, X.; Ishihara, T.; Nurmikko, A. *Solid State Commun.* **1992**, *84*, 657–661.
- (69) Kataoka, T.; Kondo, T.; Ito, R.; Sasaki, S.; Uchida, K.; Miura, N. *Phys. B Phys. Condens. Matter* **1993**, *184*, 132–136.
- (70) Tanaka, K.; Takahashi, T.; Kondo, T.; Umebayashi, T.; Asai, K.; Ema, K. *Phys. Rev. B* **2005**, *71*, 045312.
- (71) Tanaka, K.; Takahashi, T.; Kondo, T.; Umeda, K.; Ema, K.; Umebayashi, T.; Asai, K.; Uchida, K.; Miura, N. *Jpn. J. Appl. Phys.* **2005**, *44*, 5923–5932.
- (72) Tanaka, K.; Sano, F.; Takahashi, T.; Kondo, T.; Ito, R.; Ema, K. *Solid State Commun.* **2002**, *122*, 249–252.
- (73) Xu, C.-Q.; Sakakura, H.; Kondo, T.; Takeyama, S.; Miura, N.; Takahashi, Y.; Kumata, K.; Ito, R. *Solid State Commun.* **1991**, *79*, 249–253.
- (74) Xu, C.-Q.; Fukuta, S.; Sakakura, H.; Kondo, T.; Ito, R.; Takahashi, Y.; Kumata, K. *Solid State Commun.* **1991**, *77*, 923–926.
- (75) Ema, K.; Inomata, M.; Kato, Y.; Kunugita, H.; Era, M. *Phys. Rev. Lett.* **2008**, *100*, 1–4.
- (76) Neukirch, A. J.; Nie, W.; Blancon, J.-C.; Appavoo, K.; Tsai, H.; Sfeir, M. Y.; Katan, C.; Pedesseau, L.; Even, J.; Crochet, J. J.; Gupta, G.; Mohite, A. D.; Tretiak, S. *Nano Lett.* **2016**, *16*, 3809–3816.

Chapter 6

Direct Observation of Electron-Phonon Coupling and Slow Vibrational Relaxation in Organic-Inorganic Hybrid Perovskites

Abstract

Quantum and dielectric confinement effects in 2D hybrid perovskites create excitons with a binding energy exceeding 150 meV. We exploit the large exciton binding energy to study exciton and carrier dynamics as well as electron-phonon coupling in hybrid perovskites using absorption and photoluminescence (PL) spectroscopies. At

Reproduced with permission from Straus, D. B.; Hurtado Parra, S.; Iotov, N.; Gebhardt, J.; Rappe, A. M.; Subotnik, J. E.; Kikkawa, J. M.; Kagan, C. R. *J. Am. Chem. Soc.* **2016**, *138*, 13798–13801. Copyright 2016 American Chemical Society.

temperatures less than 75 K, we resolve splitting of the excitonic absorption and PL into multiple regularly-spaced resonances every 40-46 meV, consistent with electron-phonon coupling to phonons located on the organic cation. We also resolve resonances with a 14 meV spacing, in accord with coupling to phonons with mixed organic and inorganic character. These assignments are supported by density-functional theory calculations. Hot exciton PL and time-resolved PL measurements show that vibrational relaxation occurs on a picosecond timescale competitive with that for PL. At temperatures greater than 75 K, excitonic absorption and PL exhibit homogeneous broadening. While absorption remains homogeneous, PL becomes inhomogeneous at temperatures less than 75K, which we speculate is caused by the formation and subsequent dynamics of a polaronic exciton.

6.1 Introduction

The three-dimensional (3D) hybrid organic-inorganic perovskite methylammonium lead iodide (MAPbI_3) has attracted tremendous interest as the active layer in solution-processed solar cells with $>20\%$ power conversion efficiency.¹ This high efficiency arises from a moderately high carrier mobility and a notably long carrier lifetime.²⁻⁴ The structure and optoelectronic properties of hybrid perovskites can be tuned by selection of the metal, halogen, and organic components.⁵ Replacing the methylammonium cation with a longer organic ammonium cation allows the preparation of two-dimensional (2D) hybrid perovskites with alternating organic and inorganic metal halide sheets that are structurally and functionally akin to quantum well superlattices.⁵⁻⁷ The 2D and 3D hybrid perovskites share a number of common characteristics. Excitons in hybrid perovskites are Wannier in character and delocalized in the metal-halide framework.⁸⁻¹¹ Dimensionality does not significantly affect

electron-phonon coupling (EPC),¹² and carriers and excitons experience EPC in both 2D and 3D perovskites.^{8,11,13,14} However, quantum and dielectric confinement effects in 2D hybrid perovskites give rise to unique properties such as large, >150 meV exciton binding energies and anisotropic charge transport,^{8,9,15-18} which have been used to create white-light emitters,¹³ solar cells,¹⁹ and thin-film transistors.²⁰

Here we exploit the increased binding energy in 2D perovskites to observe exciton and carrier dynamics that are hidden by the low, 13-16 meV binding energy in analogous 3D perovskites.^{21,22} We study spectroscopically exciton and carrier dynamics in thin films of the 2D perovskite phenethylammonium lead iodide ((PEA)₂PbI₄, PEA=C₆H₅C₂H₄NH₃) and supplement our experimental results with density-functional theory (DFT) calculations. We find the rate of vibrational relaxation is competitive with the rate of excitonic photoluminescence (PL). Slow vibrational relaxation combined with EPC to a mode located on the organic cation gives rise at temperatures <75 K to hot PL from higher energy vibrational states that exists for picoseconds and directly corresponds to phonon sidebands in the optical absorption spectrum. While the Lorentzian lineshape of the excitonic absorption persists from room to low temperature, the corresponding room temperature Lorentzian PL lines become Gaussian at temperatures <75 K. The change in lineshape is consistent with the formation of a polaronic exciton that changes the dynamics of carrier and exciton interaction with the inorganic lattice. The direct observation of slow exciton cooling and EPC supports the conclusion that polarons influence charge carrier dynamics in hybrid perovskites.²³

6.2 Experimental Methods

Phenethylammonium iodide is synthesized by adding 6 mL of 2-phenethylamine (Aldrich, 99.5%) to 12 mL ethanol (Decon, 190 proof) and then cooling the solution in an ice bath. 10 mL of hydriodic acid (57% w/w in water, Sigma-Aldrich, with hypophosphorous acid as stabilizer) is added dropwise over several minutes. Phenethylammonium iodide precipitates from the solution and is vacuum filtered, recrystallized twice using isopropanol (ACS grade, Fisher), and subsequently dried under vacuum.

(PEA)₂PbI₄ crystals are synthesized by first performing a liquid-liquid extraction of 9 mL of hydriodic acid (57% w/w in water, unstabilized, Sigma-Aldrich) with a 10% v/v solution of tributyl phosphate (99+%, Acros Organics) in chloroform (Fisher, ACS grade) until the aqueous phase is clear. The HI is placed in a round bottom flask containing 0.498 g phenethylammonium iodide and 0.461 g lead(II) iodide (99.999%, Sigma-Aldrich). The flask is heated under nitrogen in a boiling water bath until the solids dissolve. The solution is slowly cooled over 3 h to room temperature and then placed in a refrigerator overnight. The reaction mixture is vacuum filtered and the (PEA)₂PbI₄ crystals are washed with hydriodic acid purified by extraction and then dried under vacuum.

(PEA)₂PbI₄ thin films are cast by dissolving the synthesized perovskite crystals in anhydrous acetonitrile (Acros Organics) at a concentration of 15 mg/mL in a nitrogen glove box. The mixture is sonicated until the crystals dissolve. The solution is filtered through a 0.2 μm PTFE syringe filter (Pall Corporation) and spun in a nitrogen glove box by ramping the spin rate over 2 s to 2500 rpm and spinning for 10 s. The (PEA)₂PbI₄ thin films are deposited on sapphire substrates (Rayotek Scientific) that are cleaned using Hellmanex detergent, rinsed 3x with deionized water and 3x with ethanol (190 proof, Decon Labs), and then treated with UV-Ozone for 30 min,

rendering the surface hydrophilic. After spin-casting, the films are annealed for 10 min at 80 °C in the glove box.²⁰

(PEA)₂PbI₄ thin films cast without first synthesizing crystals are fabricated by dissolving 31 mg phenethylammonium iodide with an excess (85 mg) of PbI₂ (Alfa-Aesar, 99.9985%) in 6 mL of anhydrous acetonitrile. The solution is filtered through a 0.2 μm PTFE syringe filter (Pall Life Sciences) to remove excess lead iodide before deposition. This solution is deposited following the same procedure used to deposit the (PEA)₂PbI₄ thin films made by dissolving synthesized perovskite crystals in acetonitrile.

X-ray diffraction measurements are taken on a Rigaku Smartlab diffractometer using Cu-k α radiation in θ -2 θ geometry. UV-Vis absorption measurements are performed on an Agilent Cary 5000 spectrophotometer. Continuous-wave and nano-to-microsecond time-resolved photoluminescence (PL) measurements are collected on a Horiba Jobin Yvon Fluorolog FL-3 equipped with a Hamamatsu R928 photomultiplier tube and time-correlated single photon counting (TCSPC) electronics. A Picoquant 405 nm diode laser or a Ushio UXL450SO xenon arc lamp in the FL3 is used as the excitation source. Samples are measured in air or in an evacuated Advanced Research Systems cryostat. Samples spend at most thirty minutes in air before being loaded into the vacuum cryostat.

An optical Kerr gate is used for picosecond time-resolved photoluminescence (TRPL) measurements.^{24,25} The output from a 1 kHz, 800 nm, 120 fs regenerative amplifier (Spectra-Physics Spitfire) is frequency doubled using a beta-barium borate (BBO) crystal and subsequently split into a 400 nm excitation beam and an 800 nm gate beam. The excitation beam is attenuated to 4 μW and is focused to a 300 μm spot diameter at normal incidence to the sample. PL is passed through a linear polarizer and focused onto a glass cuvette filled with a CS₂ optical Kerr gate medium,

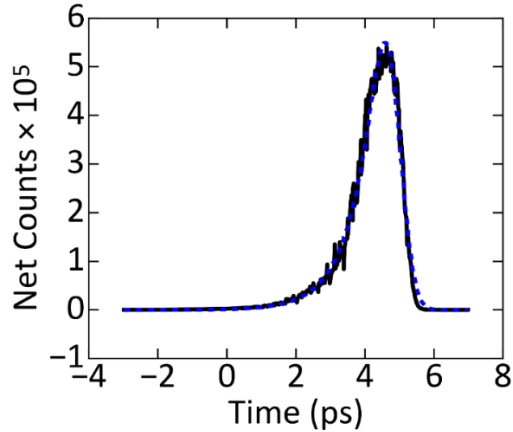


Figure 6.1: Measured instrument response function (black) for the Kerr-gate TRPL. The response is modeled as and fit to the convolution of a Gaussian with an exponential rise (blue).

which sits between crossed polarizers. The gate beam is also focused onto the gate medium and briefly induces a birefringent response that rotates the PL polarization, allowing it to partially transmit through a subsequent polarization analyzer. This PL signal is then guided into a 0.55 m spectrometer (Jobin-Yvon Triax) and detected with a thermoelectrically-cooled CCD camera (Princeton Instruments Spec-10). The delay between the gate beam and PL is controlled by a mechanical delay line on the excitation beam. To collect time-integrated PL measurements, the polarizers are uncrossed and the gate beam is blocked. In order to prevent degradation, the sample is rastered during excitation. The instrument response function for TRPL is shown in Figure 6.1.

6.3 Computational Methods

The electronic and geometric structure of $(\text{PEA})_2\text{PbI}_4$ are obtained from first-principles calculations based on non-collinear density-functional theory (DFT). We

use the Perdew-Burke-Ernzerhof-type generalized gradient approximation²⁶ as implemented in the Quantum Espresso package²⁷ supplemented by the D2 method²⁸ in order to account for dispersive interactions. Core electrons are treated by norm-conserving, optimized, designed nonlocal pseudopotentials generated with OPIUM.^{29,30} Wave functions are expanded in a plane-wave basis with an energy cutoff of 680 eV. Total energies and atomic structures are fully relaxed to 3×10^{-8} eV/cell and until forces acting on ions are below 5×10^{-3} eV/Å. The Brillouin zone is sampled by a 4x4x4 Monkhorst-Pack k-point grid.³¹

Phonon calculations were carried out at the γ point for a minimal unit cell with only one formula unit and a reduced 4x4x1 k-point grid employing tighter energy and force thresholds of 3×10^{-10} eV/cell and 5×10^{-5} eV/Å, respectively. Mode contributions for the two species $\alpha = (\text{Pb-I, phenethylammonium})$ are evaluated from the norm of mass weighted, normalized atomic displacements $u_{(\alpha,\nu)}$ by summing the contributions of all atoms for the Pb-I and the phenethylammonium subsystems, respectively, for every mode ν . Electron-phonon couplings (EPCs) were evaluated taking into account the conduction and the valence bands, assuming that the edge states dominate the investigated excitation/emission processes. Couplings were computed as perturbations of the Kohn-Sham potential by phononic atom displacements from the ground state wave functions using the standard perturbation theory approach.³² We compute the reported dimensionless EPC constants $\lambda_\nu = \sum_{ij} \int dk \frac{1}{\Omega} |M_{ij,kq,\nu}|^2 / \omega_{q\nu}^2$ from the frequency dependent coupling matrix elements $M_{ij,kq,\nu}$ between states i and j at $q = \gamma$. For visualization we broadened λ_ν by a Gaussian function.

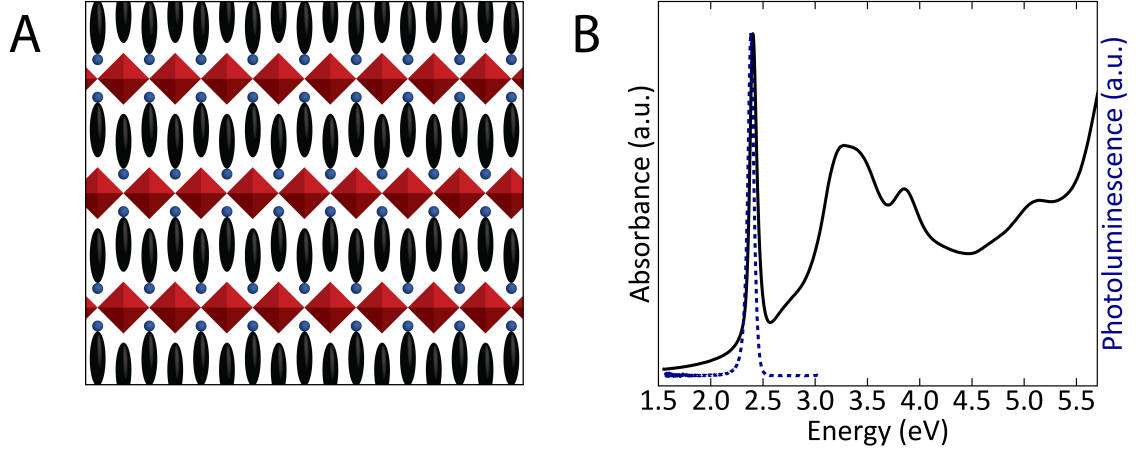


Figure 6.2: (A) Schematic projection of the layered $(\text{PEA})_2\text{PbI}_4$ structure composed of lead iodide corner sharing octahedra (red) separated by phenethyl- (black) ammonium (blue) cations. Room temperature (B) absorption (black) and PL (blue) spectra.

6.4 Results and Discussion

Figure 6.2A shows a schematic of the $(\text{PEA})_2\text{PbI}_4$ layered structure. X-ray diffraction patterns (Figure 6.3) of $(\text{PEA})_2\text{PbI}_4$ thin films confirm deposition of a single phase 2D material with an interlayer spacing of 1.64 nm. Room temperature absorption and PL (excited at 3.10 eV) spectra (Figure 6.2B) show the excitonic transition centered at 2.407 eV in absorption and 2.383 eV in PL. The excitonic resonances have a Lorentzian lineshape in absorption and PL (Figure 6.4), consistent with homogeneous broadening and similar to that found in the 3D perovskite MAPbI_3 attributed to effects of EPC.¹¹ 300 K time-resolved photoluminescence (TRPL) decays are single exponential with a lifetime of 24.1 ± 0.1 ps (Figure 6.5).

As the $(\text{PEA})_2\text{PbI}_4$ thin film is cooled from room temperature (Figure 6.2B) to 15 K (Figure 6.6A-B), the absorption and PL spectra (excited at 3.10 eV) change dramatically (Figure 6.7). The excitonic absorption spectrum splits into three obvious transitions: resonance α at 2.438 eV, β at 2.398 eV, and γ at 2.355 eV, in addition to a shoulder ζ_1 to the γ peak that is centered at 2.368 eV (Figure 6.6B-C). Each resonance

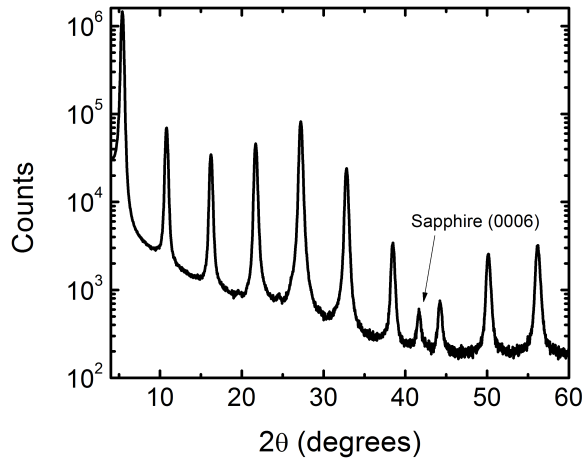


Figure 6.3: X-ray diffraction pattern in $\theta - 2\theta$ geometry using Cu- α radiation of a $(\text{PEA})_2\text{PbI}_4$ thin film deposited on a sapphire substrate. Bragg analysis yields an interlayer spacing of 1.64 nm, consistent with previous measurements for $(\text{PEA})_2\text{PbI}_4$.^{5,33,34}

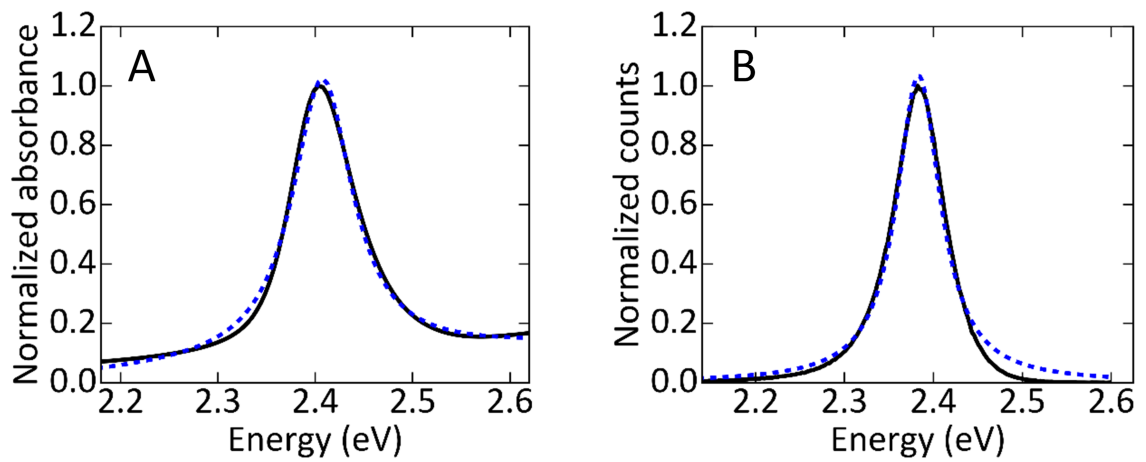


Figure 6.4: Room temperature (A) absorption (black) and (B) PL spectra of $(\text{PEA})_2\text{PbI}_4$ thin films. Spectra are fit to a Lorentzian (blue, dashed), and a linear background is used to fit absorption.

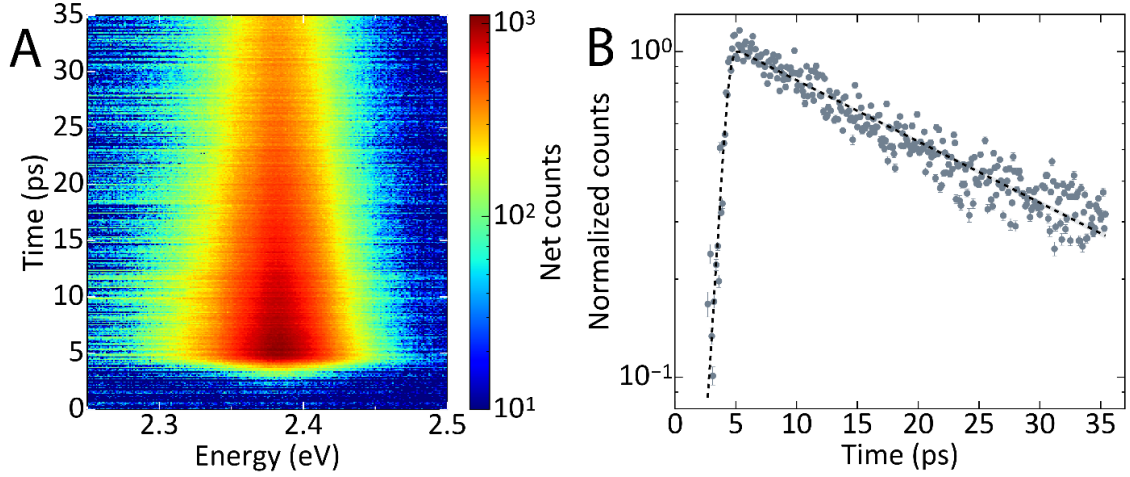


Figure 6.5: (A) Room temperature TRPL spectrum. Each time bin is fit to a single Lorentzian. (B) Integral of Lorentzian fit at each time (grey) fit to single exponential convolved with the instrument response (Figure 6.1) (black).

is fit to a Lorentzian lineshape (Table 6.1). The regular 40-43 meV spacing between α , β , and γ indicates that the splitting arises from EPC. Phononic sidebands have previously been observed in low temperature absorption spectra of 2D perovskites.^{8,9,18} Linear fitting of the band-edge absorption (Figure 6.6A, green) yields an onset of 2.54 ± 0.07 eV and therefore an exciton binding energy of 190 ± 70 meV, in agreement with reported values.^{8,15}

The low temperature excitonic PL spectrum splits into two clear peaks (Figure 6.6B): γ at 2.351 eV, which shows a Stokes shift of 4 meV compared to γ in absorption, and δ at 2.311 eV, which mirrors β in absorption. There is also a hidden peak ζ_2 centered at 2.339 eV, which is found by fitting the resonances to Gaussian lineshapes (Figure 6.6D, Table 6.1). Although we cannot resolve ζ_2 directly in PL collected using 3.10 eV excitation, by exciting at 2.40 eV, three peaks are independently resolved in PL (6.8). While γ and δ do not shift energy, ζ_2 red shifts 2 meV to 2.337 eV. The mirror symmetry of ζ_1 and ζ_2 , separated by 12-14 meV from γ , suggests that these peaks are the result of coupling to a phonon mode⁸ and is consistent with a reported 14 meV

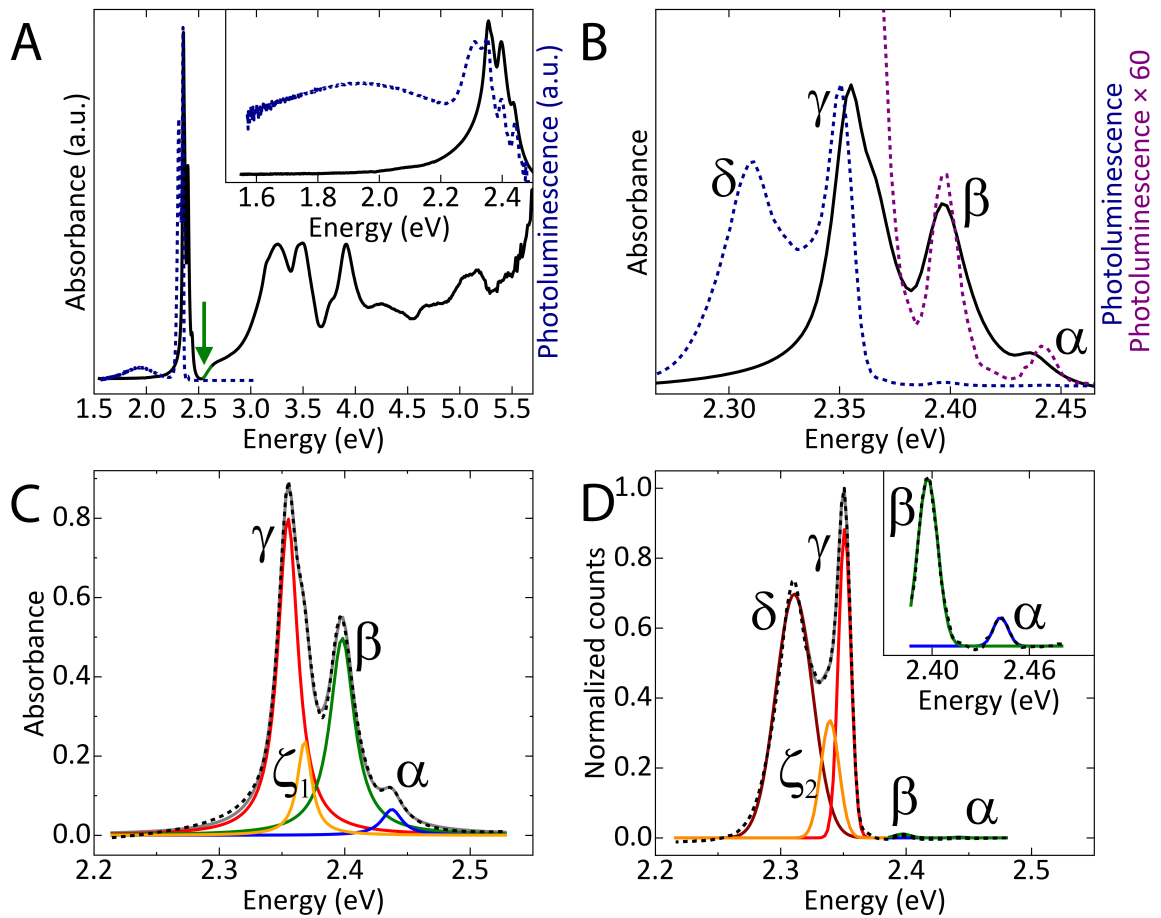


Figure 6.6: (A) 15K absorption (black) and PL (blue) spectra plotted on a linear and (inset) logarithmic scale to highlight the broad PL centered at 1.93 eV. (B) Excitonic absorption (black) and PL (blue) and PL $\times 60$ (purple) to highlight high energy structure. (C) The absorption spectrum in (B) fit to the sum of four Lorentzians with a linear baseline. (D) The PL spectrum in (B) fit to the sum of five Gaussians in addition to a linear term to correct for the slow rise of the broad feature at 1.93 eV. Inset resonances are fit separately from the three central peaks because of the large discrepancy in peak heights. The linear baseline is subtracted from the data in (C) and (D).

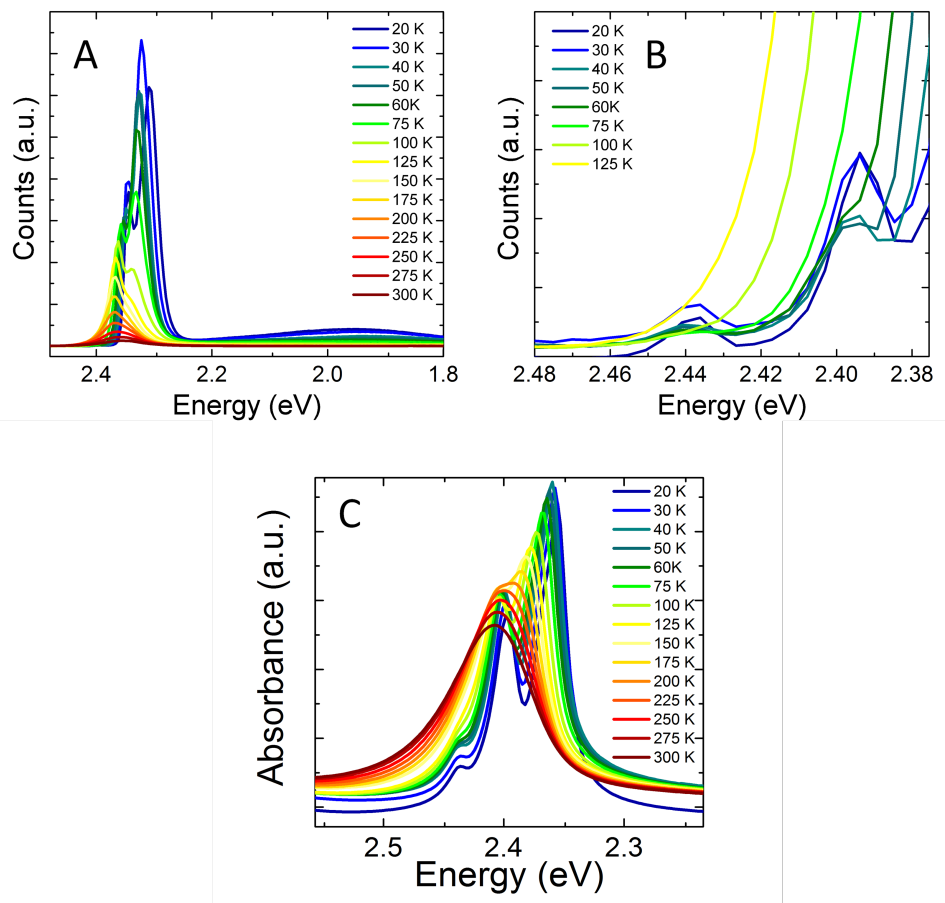


Figure 6.7: (A) PL spectra of a (PEA)₂PbI₄ thin film at temperatures between 20 K and 300 K excited at 400 nm, using the Xe arc lamp in combination with the monochromator of the Fluorolog FL-3. (B) Highlight of the hot excitonic PL peaks. (C) Absorption spectra at temperatures between 20 K and 300 K.

Absorption			
Transition	Center (eV)	FWHM (meV)	Absorbance
α	2.438	20 ± 5	0.065 ± 0.009
β	2.398	23.7 ± 0.8	0.497 ± 0.008
ζ_2	2.368	14 ± 2	0.24 ± 0.02
γ	2.355	19.6 ± 0.6	0.80 ± 0.02
Emission			
Transition	Center (eV)	FWHM (meV)	Normalized counts
α	2.442	11 ± 2	0.0021 ± 0.0003
β	2.397	14.5 ± 0.5	0.0122 ± 0.0003
γ	2.351	11.7 ± 0.6	1.0 ± 0.1
ζ_2	2.339 ± 0.002	17 ± 4	0.38 ± 0.05
δ	2.311	34 ± 1	0.79 ± 0.01

Table 6.1: Parameters for 15 K absorption and PL lineshape fits for $(\text{PEA})_2\text{PbI}_4$ thin films. Uncertainties are 95% confidence intervals of the regressions, although transition centers are given to meV precision because regression uncertainty is smaller than calibration precision (0.5-1 meV).

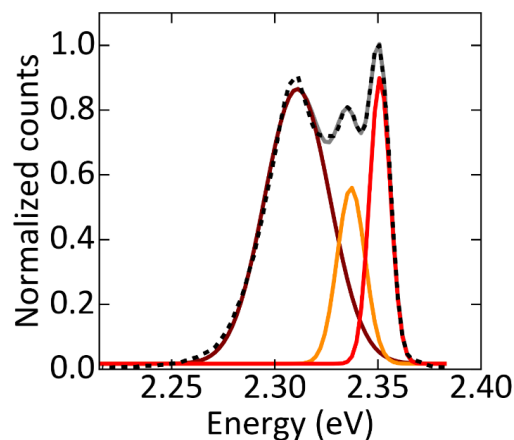


Figure 6.8: 15 K PL spectrum of a $(\text{PEA})_2\text{PbI}_4$ thin film excited at 2.40 eV (dashed black). The emission spectrum is fit (grey) to the sum of three Gaussians. The peaks are centered at 2.351 eV (red), 2.337 eV (orange), and 2.311 eV (maroon).

LO phonon in lead (II) iodide.³⁵ DFT calculations show the phonons at 11.9-14.3 meV have Pb-I character, but also involve the organic cation (Figure 6.9). Strong EPC is predicted for these modes, in accordance with the observed ζ resonances.

A very broad feature centered at 1.93 eV appears in the PL spectrum (Figure 6.6A) that does not have a corresponding absorption. Comparison of photoluminescence excitation (PLE) spectra collected monitoring the emission at the excitonic transitions and at 2.00 eV (Figure 6.10) shows the broad feature is more strongly coupled to band-to-band than excitonic transitions and supports reports that the broad PL results from trap-assisted recombination.^{36,37} The amount of trap PL can be tailored by varying the film quality or excitation wavelength (Figure 6.11).

There are also two previously unreported resonances in PL directly corresponding to absorption sidebands: β at 2.397 eV and α at 2.442 eV (Figure 6.6B and 6.6D, inset). The existence of these features indicates that a small fraction of hot excitons in higher energy vibrational states radiatively recombines before relaxing to the lowest lying excited state. These PL features are spaced 40-46 meV apart, matching the energy

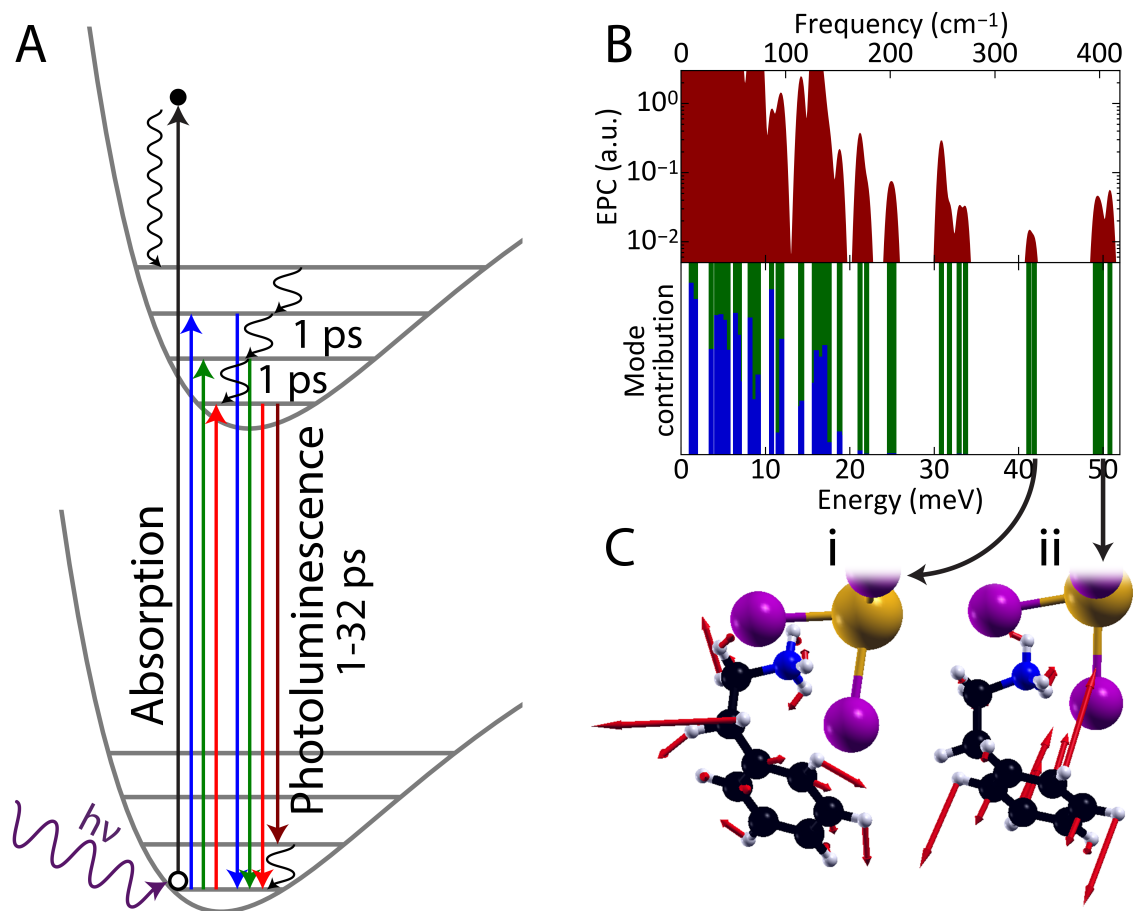


Figure 6.9: (A) Schematic detailing low temperature absorption and PL processes α (blue arrows), β (green arrows), γ (red arrows), and δ (maroon arrow) in (PEA)₂PbI₄. δ is only shown in PL because there is no corresponding absorption. Nonradiative relaxation between vibrational states is shown by black curved arrows. (B) Computed phonon modes below 50 meV, with contributions from the Pb-I cage (blue) and the organic cations (green). EPC is shown in red. (C)(i) 41 meV phonon modes are rotation of NH₃⁺ and phenyl moieties. (ii) 49 meV phonons are out-of-plane bending of phenyl groups.

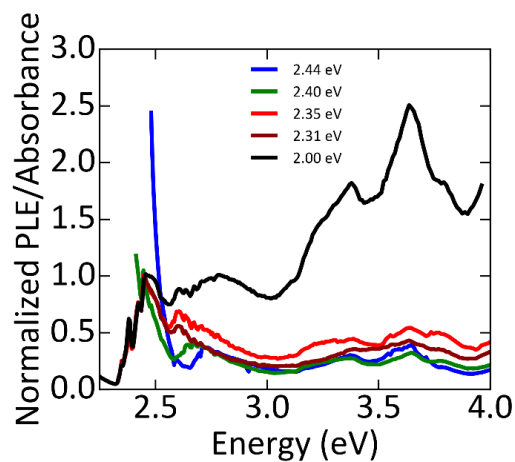


Figure 6.10: PLE spectra divided by absorbance of a $(\text{PEA})_2\text{PbI}_4$ thin film collected at 2.44 (blue), 2.40 (green), 2.35 (red), 2.31 (maroon), and 2.00 (black) eV. All are normalized to the number of counts at 2.45 eV except for the spectrum collected at 2.44 eV which is normalized such that its value at 2.59 eV is the same as that for the PLE spectrum collected at 2.40 eV.

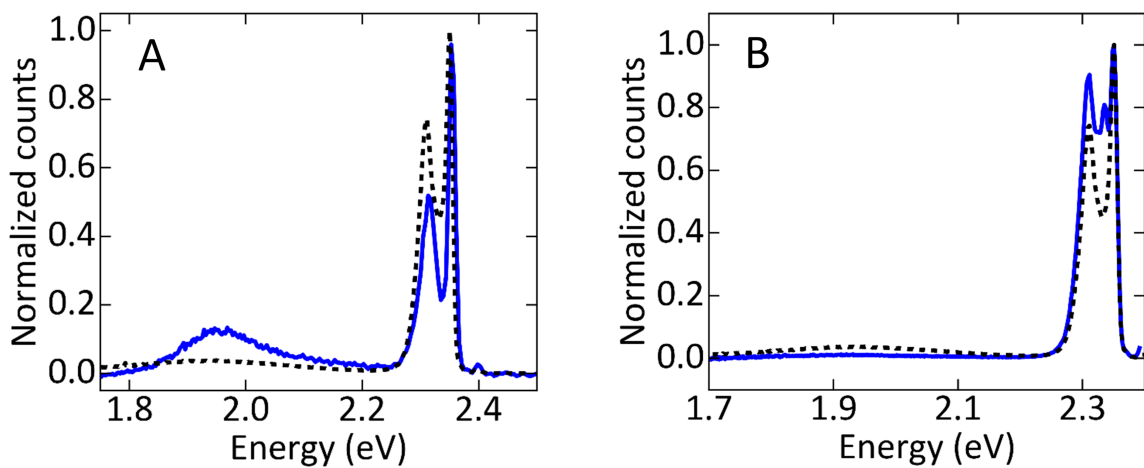


Figure 6.11: PL spectrum of a $(\text{PEA})_2\text{PbI}_4$ thin film spun by dissolving synthesized crystals in acetonitrile (black) and by mixing phenethylammonium iodide with an excess of lead iodide in acetonitrile (blue). (B) 15 K PL spectra of a $(\text{PEA})_2\text{PbI}_4$ thin film spun by dissolving synthesized crystals in acetonitrile excited at 3.10 eV (black) and 2.40 eV (blue).

separation between absorption resonances and supporting the conclusion that EPC manifests as phononic sidebands both in absorption and in PL.

The regularity of the absorption and PL peaks allows us to assign each peak to a specific transition (Figure 6.9A). γ corresponds to the central transition between states ($S_{i,j}$) $S_{0,0} \leftrightarrow S_{1,0}$, where i refers to the electronic state and j refers to vibrational level, because of the symmetry in the resonances surrounding it. β is assigned to the $S_{0,0} \leftrightarrow S_{1,1}$ transition, and α to the $S_{0,0} \leftrightarrow S_{1,2}$ transition. δ is the $S_{1,0} \rightarrow S_{0,1}$ transition because of its comparable intensity to the central peak in addition to the lack of a corresponding absorption; at 15 K only the lowest vibrational level in the ground state of a mode with 20 meV zero-point energy is populated.

To investigate the phonon spectrum of $(\text{PEA})_2\text{PbI}_4$, we perform DFT calculations. At zone center, we find two sets of nearly degenerate vibrational modes with energies of 41 and 49 meV. These phonons are localized on phenethylammonium cations, and all phonons with energies larger than 19 meV show no significant Pb-I contribution (Figure 6.9B). A similar phonon at 49.8 meV was calculated for MAPbI_3 .³⁸ In $(\text{PEA})_2\text{PbI}_4$, we compute an NH_3 rotation accompanied by a rotation within the phenyl moieties (Figure 6.9C(i)). A second degenerate set arises at 49 meV that are predominantly out-of-plane bending modes of the phenyl units (Figure 6.9C(ii)) and thus should be absent in MAPbI_3 . Figure 6.9B also shows that both sets of phonons exhibit nonzero EPC. However, many modes are predicted to exhibit EPC, yet only 14 and 40-46 meV phonon replica are observed in optical spectra. This discrepancy may be related to contributions of q points other than the γ point phonons, dynamic changes in electronic states, or differences in carrier and exciton coupling to phonons that are excluded in our current model. Previously the existence of multiple excitonic resonances in $(\text{PEA})_2\text{PbI}_4$ and other 2D alkylammonium lead iodide perovskites have been attributed to free and bound excitons^{39,40} in addition to phononic sidebands.^{9,15}

We believe that phononic sidebands are the most likely explanation because of the existence of the previously unreported α and β hot PL resonances. In addition PLE spectra of α , β , γ , and δ appear similar (Figure 6.10), indicating that these resonances have the same origin.⁸

15K TRPL (Figure 6.12A) is used to understand the timescale of vibrational relaxation. The PL spectrum at each time step is fit to the sum of 5 Gaussians, and their integrals are plotted in Figure 6.12B. There is a shoulder ζ_3 9 meV higher in energy than γ that merges with γ within the first six ps, so the integrals of γ and ζ_3 are summed (Figure 6.12B); we do not know the origin of this feature. The integrals as a function of time are fit to a single or double exponential (Table 6.2) convolved with the instrument response. α ($\tau = 1.2 \pm 0.5$ ps) and β ($\tau_1 = 1.1 \pm 0.5$ ps and $\tau_2 = 7 \pm 3$ ps) have lifetimes an order of magnitude shorter than $\gamma + \zeta_3$ ($\tau = 12.5 \pm 0.9$ ps) and δ ($\tau = 32.4 \pm 0.4$ ps). α and β decay while $\gamma + \zeta_3$ and δ still rise (grey line, Figure 6.9B) indicating that vibrational relaxation on the ~ 1 ps timescale is competitive with hot PL emission at α and β , i.e. a small fraction of the excited vibrational population radiatively transitions to the ground state before it can relax into lower energy vibrational states. The dynamics of absorption and PL are depicted in Figure 6.9A.

Transition	A₁	t₁ (ps)	A₂	t₂ (ps)
α	0.14 ± 0.07	1.2 ± 0.5		
β	0.5 ± 0.3	1.1 ± 0.5	0.08 ± 0.03	7 ± 3
$\gamma + \zeta_3$	1.00 ± 0.08	12.5 ± 0.9		
δ	0.572 ± 0.003	32.4 ± 0.4		

Table 6.2: Tabulated fit parameters for lifetime fits shown in Figure 6.9B. Picosecond time-resolved photoluminescence is fit to the function $(\sum_i A_i \exp(t/t_i)) * \text{IRF}$ where $*$ represents convolution and IRF is the instrument response function (Figure 6.1). Amplitudes are normalized to the $\gamma + \zeta_3$ amplitude. Uncertainties are 95% confidence interval of the regressions.

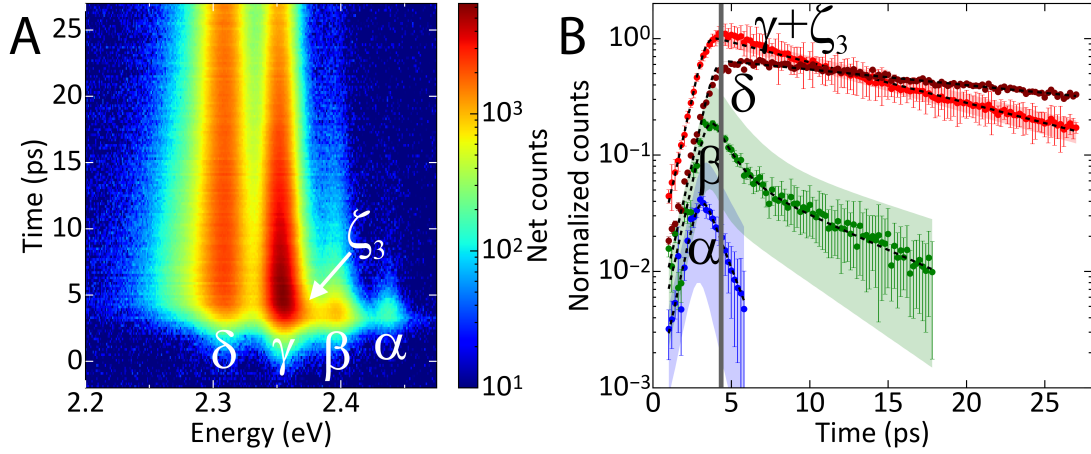


Figure 6.12: (A) Pseudocolor plot of 15K TRPL. Each time bin is fit to the sum of Gaussians. (B) Integral of each peak plotted at each time and fit (black) to a single or double exponential. Shaded area is 95% confidence interval of fit.

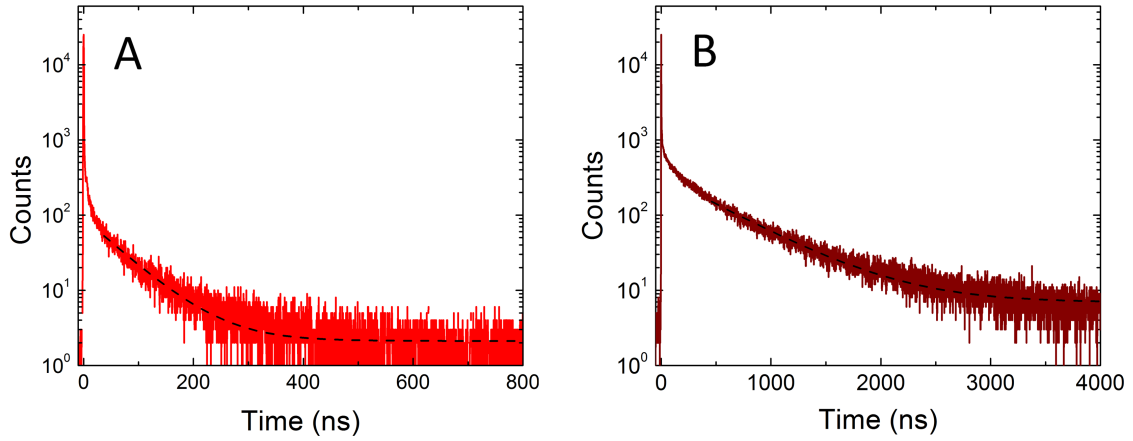


Figure 6.13: 15K TRPL of (A) γ (2.35 eV resonance) and (B) δ (2.31 eV resonance) emissions.

While most of the PL of γ and δ decays within tens of picoseconds, there is a long tail in the TRPL of γ and δ that warrants further study (Figure 6.13). For γ the tail has a lifetime of 67 ± 1 ns and for δ it is 462 ± 5 ns. Figure 6.14 shows TRPL of the broad PL peak centered at 1.93 eV, and the triple exponential fit has an amplitude weighted lifetime of 17.9 ± 0.1 ns (Table 6.3). No PL occurs from this peak within the timeframe of the ps TRPL measurement, supporting the assignment to trap-assisted recombination.

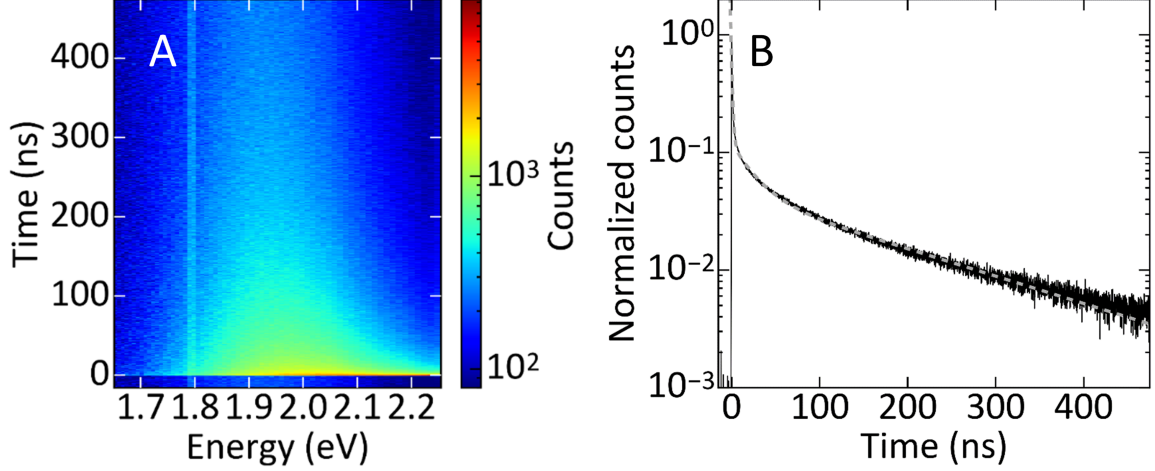


Figure 6.14: (A) 20K TRPL of the broad emission centered at 1.93 eV. The increased counts at 1.79 eV are Cr_2^+ impurities in the sapphire substrate. Each time bin is fit to a single Gaussian. (B) The integral of the Gaussian is plotted versus time and fit to a triple exponential decay (Table 6.3).

A_1	t_1 (ns)	A_2	t_2 (ns)	A_3	t_3 (ns)
0.8 ± 0.1	1.3 ± 0.1	0.125 ± 0.006	24 ± 2	0.074 ± 0.003	187 ± 7

Table 6.3: Tabulated fit parameters for TRPL of the broad feature at 1.93 eV. The integrated amplitude is fit to the function $A(t) = A_1 \exp\left(-\frac{t}{t_1}\right) + A_2 \exp\left(-\frac{t}{t_2}\right) + A_3 \exp\left(-\frac{t}{t_3}\right)$. Uncertainties are 95% confidence interval of the regression.

The timescale for relaxation of the vibrational bending mode of the organic cation in MAPbI₃ at 300K was reported to be ~ 3 ps,⁴¹ which is similar to the PL lifetimes for the hot PL resonances measured here and indicates that the timescale for vibrational relaxation is not significantly temperature dependent. Similarly slow vibrational relaxation (a hot phonon bottleneck) has also been found for free carriers at room temperature in MAPbI₃ thin films,²² indicating that slow vibrational relaxation is a common trait to this materials class which we can directly observe in (PEA)₂PbI₄ because of the large exciton binding energy.

As indicated above, the absorption spectra are homogeneously broadened from room temperature to 15 K. Unexpectedly, the PL lineshape changes from homogeneous (Lorentzian) to inhomogeneous (Gaussian) broadening at temperatures below 75 K ($kT \sim 7$ meV). At present, we cannot give a firm explanation of all the phenomena observed here. According to a straightforward interpretation of Kubo theory, the lineshapes for absorption and emission would be symmetric: when the optical gap fluctuates quickly one finds a Lorentzian, when the optical gap fluctuates slowly one finds a Gaussian. To break this symmetry, one must appeal to excited state motion and/or some other decay process.

Given the vibronic structure in Figure 6.6, we hypothesize that EPC and polaronic motion are responsible for such effects. In particular, the most plausible explanation is the formation of a large polaron coupling the exciton⁴² to the ~ 14 meV phonon (labeled ζ). We must further stipulate that this phonon couples reasonably strongly to the exciton (with ~ 10 meV barriers between minima) and weakly to the ground state (with very small barriers between minima). As such, an exciton at low temperature exhibits inhomogeneous broadening in emission and homogeneous broadening in absorption. At temperatures > 75 K ($kT > 7$ meV) where thermal energy exceeds all barriers, the excitons are not as strongly coupled to the inorganic lattice and experience an

averaged electronic environment, which results in homogeneous broadening in all cases. Theoretical studies are underway to confirm this hypothesis.

6.5 Conclusion

We demonstrate the existence of slow vibrational relaxation and EPC to phonons located in both the organic and inorganic components of hybrid perovskites. Vibrational relaxation occurs on a ps timescale and is competitive with PL, which in combination with EPC and a small Stokes shift between the ground and excited state potential energy surfaces gives rise to hot excitonic PL peaks. Absorption exhibits homogeneous broadening at all temperatures, but polaronic exciton formation and subsequent dynamics likely cause inhomogeneously broadened PL below 75 K. The formation of the polaronic exciton, EPC, and slow vibrational relaxation support the conclusion that polarons are important to exciton and carrier dynamics in perovskites and that in the future, slow vibrational relaxation may be harnessed and controlled to allow for hot carrier extraction in perovskite solar cells.

6.6 References

- (1) NREL Best Research-Cell Efficiencies. <http://www.nrel.gov/pv/assets/images/efficiency-chart.png> (accessed 01/16/2018).
- (2) Boix, P. P.; Agarwala, S.; Koh, T. M.; Mathews, N.; Mhaisalkar, S. G. *J. Phys. Chem. Lett.* **2015**, *6*, 898–907.
- (3) Dong, Q.; Fang, Y.; Shao, Y.; Mulligan, P.; Qiu, J.; Cao, L.; Huang, J. *Science* **2015**, *347*, 967–970.

- (4) Ponseca, C. S.; Savenije, T. J.; Abdellah, M.; Zheng, K.; Yartsev, A.; Pascher, T.; Harlang, T.; Chabera, P.; Pullerits, T.; Stepanov, A.; Wolf, J.-p. P.; Sundström, V. *J. Am. Chem. Soc.* **2014**, *136*, 5189–5192.
- (5) Mitzi, D. B. *Prog. Inorg. Chem.* **1999**, *48*, 1–121.
- (6) Mitzi, D. B. *Chem. Mater.* **1996**, *8*, 791–800.
- (7) Tabuchi, Y.; Asai, K.; Rikukawa, M.; Sanui, K.; Ishigure, K. *J. Phys. Chem. Solids* **2000**, *61*, 837–845.
- (8) Gauthron, K.; Lauret, J.-S.; Doyennette, L.; Lanty, G.; Al Choueiry, A.; Zhang, S. J.; Brehier, A.; Largeau, L.; Mauguin, O.; Bloch, J.; Deleporte, E. *Opt. Express* **2010**, *18*, 5912.
- (9) Tanaka, K.; Sano, F.; Takahashi, T.; Kondo, T.; Ito, R.; Ema, K. *Solid State Commun.* **2002**, *122*, 249–252.
- (10) Tilchin, J.; Dirin, D. N.; Maikov, G. I.; Sashchiuk, A.; Kovalenko, M. V.; Lifshitz, E. *ACS Nano* **2016**, *10*, 6363–6371.
- (11) Wehrenfennig, C.; Liu, M.; Snaith, H. J.; Johnston, M. B.; Herz, L. M. *J. Phys. Chem. Lett.* **2014**, *5*, 1300–1306.
- (12) Chemla, D.; Miller, D.; Schmitt-Rink, S. In *Opt. Nonlinearities Instab. Semicond.* Haug, H., Ed.; Academic Press: San Diego, 1988, pp 83–120.
- (13) Dohner, E. R.; Jaffe, A.; Bradshaw, L. R.; Karunadasa, H. I. *J. Am. Chem. Soc.* **2014**, *136*, 13154–13157.
- (14) Wright, A. D.; Verdi, C.; Milot, R. L.; Eperon, G. E.; Pérez-Osorio, M. A.; Snaith, H. J.; Giustino, F.; Johnston, M. B.; Herz, L. M. *Nat. Commun.* **2016**, *7*, 11755.
- (15) Hong, X.; Ishihara, T.; Nurmikko, A. V. *Phys. Rev. B* **1992**, *45*, 6961–6964.

- (16) Koutselas, I. B.; Ducasse, L.; Papavassiliou, G. C. *J. Phys. Condens. Matter* **1996**, *8*, 1217–1227.
- (17) Mitzi, D. B.; Chondroudis, K.; Kagan, C. R. *IBM J. Res. Dev.* **2001**, *45*, 29–45.
- (18) Tanaka, K.; Takahashi, T.; Kondo, T.; Umebayashi, T.; Asai, K.; Ema, K. *Phys. Rev. B* **2005**, *71*, 045312.
- (19) Tsai, H. et al. *Nature* **2016**, *536*, 312–316.
- (20) Kagan, C. R.; Mitzi, D. B.; Dimitrakopoulos, C. D. *Science* **1999**, *286*, 945–947.
- (21) Miyata, A.; Mitioglu, A.; Plochocka, P.; Portugall, O.; Wang, J. T.-W.; Stranks, S. D.; Snaith, H. J.; Nicholas, R. J. *Nat. Phys.* **2015**, *11*, 582–587.
- (22) Yang, Y.; Ostrowski, D. P.; France, R. M.; Zhu, K.; van de Lagemaat, J.; Luther, J. M.; Beard, M. C. *Nat. Photonics* **2015**, *10*, 53–59.
- (23) Zhu, X.-Y.; Podzorov, V. *J. Phys. Chem. Lett.* **2015**, *6*, 4758–4761.
- (24) Diroll, B. T.; Turk, M. E.; Gogotsi, N.; Murray, C. B.; Kikkawa, J. M. *ChemPhysChem* **2016**, *17*, 759–765.
- (25) Turk, M. E.; Vora, P. M.; Fafarman, A. T.; Benjamin, T.; Murray, C. B.; Kagan, C. R.; Kikkawa, J. M. *ACS Nano* **2015**, *9*, 1440–1447.
- (26) Perdew, J. P.; Burke, K.; Ernzerhof, M. *Phys. Rev. Lett.* **1996**, *77*, 3865–3868.
- (27) Giannozzi, P. et al. *J. Phys. Condens. Matter* **2009**, *21*, 395502.
- (28) Grimme, S. *J. Comput. Chem.* **2006**, *27*, 1787–1799.
- (29) Ramer, N. J.; Rappe, A. M. *Phys. Rev. B* **1999**, *59*, 12471–12478.
- (30) Rappe, A. M.; Rabe, K. M.; Kaxiras, E.; Joannopoulos, J. D. *Phys. Rev. B* **1990**, *41*, 1227–1230.
- (31) Monkhorst, H. J.; Pack, J. D. *Phys. Rev. B* **1976**, *13*, 5188–5192.

- (32) Baroni, S.; de Gironcoli, S.; Dal Corso, A.; Giannozzi, P. *Rev. Mod. Phys.* **2001**, *73*, 515–562.
- (33) Era, M.; Hattori, T.; Taira, T.; Tsutsui, T. *Chem. Mater.* **1997**, *9*, 8–10.
- (34) Liang, K.; Mitzi, D. B.; Prikas, M. T. *Chem. Mater.* **1998**, *10*, 403–411.
- (35) Goto, T.; Nishina, Y. *Solid State Commun.* **1979**, *31*, 369–372.
- (36) Wu, X.; Trinh, M. T.; Niesner, D.; Zhu, H.; Norman, Z.; Owen, J. S.; Yaffe, O.; Kudisch, B. J.; Zhu, X.-Y. *J. Am. Chem. Soc.* **2015**, *137*, 2089–2096.
- (37) Wu, X.; Trinh, M. T.; Zhu, X.-Y. *J. Phys. Chem. C* **2015**, *119*, 14714–14721.
- (38) Pérez-Osorio, M. A.; Milot, R. L.; Filip, M. R.; Patel, J. B.; Herz, L. M.; Johnston, M. B.; Giustino, F. *J. Phys. Chem. C* **2015**, *119*, 25703–25718.
- (39) Fujisawa, J.-I.; Ishihara, T. *Phys. Rev. B* **2004**, *70*, 205330.
- (40) Ishihara, T.; Takahashi, J.; Goto, T. *Phys. Rev. B* **1990**, *42*, 11099–11107.
- (41) Bakulin, A. A.; Selig, O.; Bakker, H. J.; Rezus, Y. L.; Müller, C.; Glaser, T.; Lovrincic, R.; Sun, Z.; Chen, Z.; Walsh, A.; Frost, J. M.; Jansen, T. L. C. *J. Phys. Chem. Lett.* **2015**, *6*, 3663–3669.
- (42) Soufiani, A. M.; Huang, F.; Reece, P.; Sheng, R.; Ho-Baillie, A.; Green, M. A. *Appl. Phys. Lett.* **2015**, *107*, 231902.

Chapter 7

Tailoring the Organic Framework and Energetic Disorder in Excitonic 2D Hybrid Perovskites

Abstract

We synthesize and characterize derivatives of the two-dimensional hybrid perovskite (2DHP) phenethylammonium lead iodide ((PEA)₂PbI₄) in which the H para to the ethylammonium group on the aromatic moiety of the cation is replaced with F, Cl, CH₃, or Br. These single atom substitutions increase the length of the cation but leave the cross-sectional area unchanged, resulting in structurally similar PbI₄²⁻ frameworks with increasing interlayer spacing that allow us to explore the role of the cation on the structural and optical properties of 2DHPs. We find that the organic framework

Reproduced with permission from *The Journal of the American Chemical Society*, submitted for publication. Unpublished work copyright 2018 American Chemical Society.

superstructure can be controlled by tuning intermolecular interactions between adjacent cations, with H- and CH₃-substituted (PEA)₂PbI₄ adopting a herringbone packing while F-, Cl-, and Br-substituted (PEA)₂PbI₄ adopt a face-on packing. The length, but not the packing or the mass, of the cation changes the energy landscape of the 2DHP. Longer cations result in broader blue-shifted excitonic absorption spectra with reduced or eliminated fine structure, indicative of greater energetic disorder. Photoluminescence spectra are largely invariant and insensitive to the greater disorder, suggesting polaron formation stabilizes a structural and electronic minimum. Analyzing temperature-dependent absorption and photoluminescence linewidths reveals that excitons couple to a phonon located on the organic framework that is weakly sensitive to these cation substitutions. Our results demonstrate that single atom substitutions on the organic cation can be used to tune the structural, optical, and electronic properties of 2DHPs despite carriers being confined to the inorganic framework.

7.1 Introduction

Two-dimensional (2D) organic-inorganic hybrid perovskites (2DHPs) are stoichiometric compounds that crystallize into structures of alternating inorganic monolayers and organic mono- or bilayers.¹⁻³ 2DHPs with organic bilayers have the formula A₂MX₄ and consist of stacks of octahedral metal-halide (M-X) monolayers where M is typically a divalent metal,¹⁻⁴ each separated by organoammonium cations (A) to maintain charge balance. A wide variety of A cations can be incorporated into 2DHPs.¹⁻³ Varying the metal is known to affect the conformation and superstructure of compositionally identical organic frameworks,⁵ and varying the organic cation can alter bond lengths and angles in the inorganic framework.¹⁻⁷

Electronically, 2DHPs are akin to quantum well superlattices.³ However, they do

not exhibit the interfacial roughness common to molecular beam epitaxially-grown materials^{1,5,8,9} and are more like monolayer transition-metal dichalcogenides.¹⁰ Pb-based 2DHPs have band gaps tunable from approximately 2-4 eV and can form both Type I and Type II heterojunctions depending on the choice of metal, halide, and cation,^{1,3,11} allowing their optical and electronic properties to be tailored for specific applications. In the Type I heterojunctions discussed herein, strong quantum and dielectric confinement effects¹²⁻¹⁶ create stable room temperature excitons with binding energies >150 meV in the Pb-X layers.³ The broad tunability, solution processability, and existence of stable excitons make 2DHPs an ideal platform both for exploring the structure-function relation in 2D materials and for designing excitonic and electronic devices.^{4,17-24}

While charge carriers and excitons are confined to the M-X layers in Type I 2DHPs, the choice of organic cation has been shown to significantly affect the band gap and exciton binding energy. Cations with large cross-sectional area strain the inorganic framework, distorting the metal-halide octahedra and decreasing the M-X-M bond angle away from the ideal 180°, and increase the band gap.⁶ This property is akin to strain-engineering in conventional semiconductors,²⁵ but here strain is provided through the choice of cation rather than through epitaxy or ion-implantation techniques.⁶ Aromatic in comparison to aliphatic ammonium cations increase the dielectric constant of the organic interlayer and therefore decrease the dielectric contrast with the inorganic framework responsible for confinement, lowering exciton binding energies.^{1,3,5,13,26,27} At cryogenic temperatures, fine structure is observed in the excitonic absorption and photoluminescence (PL) in some 2DHPs.^{13,28,29} Previously, we reported that at temperatures < 75 K in the 2DHP phenethylammonium lead iodide ((PEA)₂PbI₄, PEA = C₆H₅C₂H₄NH₃⁺), referred to as 4-H herein, the excitonic fine structure in absorption consists of three regularly-spaced resonances separated by

40-43 meV.²⁹ PL is observed out of all three absorption resonances indicating that hot excitons recombine radiatively before relaxing to the lowest excited state.³⁰ We hypothesized that the fine structure is caused by coupling of excitons in the inorganic framework with phonons in the organic cations. Subsequent works both support^{31,32} and question^{28,33} our hypothesis. A similar debate is ongoing in regard to the role of electron-phonon coupling and the origin of fine structure in 3D perovskites.^{32,34,35} Regardless of the origin, published spectra^{28,31} indicate that the cation plays a large role in modulating the fine structure of excitonic absorption and PL resonances.

Here, we investigate how the size and functionalization of the cation dictate the structure and energy landscape of 2DHPs. We synthesize, structurally characterize, and optically study a family of 4-H derivatives $(XC_6H_4C_2H_4NH_3)_2PbI_4$ in which the 4-position hydrogen (para to the ethylammonium group) is substituted for $X = F$ (referred to as 4-F), Cl (4-Cl), methyl (4-Me), and Br (4-Br). Importantly, these substitutions increase the interlayer spacing without changing the cross-sectional area of the cation, leaving the PbI_4^{2-} framework and therefore the band edges³⁶ largely unchanged,³ and do not significantly alter the dielectric constant of the organic interlayer, allowing us to isolate the effect of the cationic substitutions with few complicating factors. We discover that functionalizing the organic cation changes the superstructure of the organic framework. 4-H and 4-Me adopt herringbone whereas 4-F, 4-Cl, and 4-Br adopt face-on packings of the organic cations, highlighting that intermolecular forces can be exploited to template the cations in 2DHPs without modifying the inorganic framework. While 4-H^{37,38} and 4-F³⁹⁻⁴¹ have been previously structurally characterized, no comment has been made on the change in packing induced by fluorination. Previous reports involve modifying the inorganic M-X framework to control the orientation of the organic cations^{1,5} rather than tailoring the cation directly.

We show the length and not the packing or mass of the organic cation dominates differences seen in the excitonic properties of the PbI_4^{2-} framework. Over a broad temperature range (10-300 K) the excitonic absorption maxima blue-shifts and linewidth broadens as the 4-position substituent increases the interlayer spacing between the PbI_4^{2-} layers, consistent with longer cations producing greater dynamic energetic disorder⁴²⁻⁴⁵ in the ground state of 2DHPs. Increasing the length of the cation also results in reduced or eliminated excitonic fine structure in 10 K absorption spectra for 4-F, 4-Cl, 4-Me, and 4-Br compared to 4-H. PL spectra for the different 4-substituted organic cations are similarly structured with largely invariant maxima and linewidths, consistent with polaron formation^{28,29,33,43,44,46-49} in the excited state stabilizing a structural and electronic minimum. Temperature-dependent linewidths in absorption and PL support the existence of strong exciton-phonon coupling to a phonon with energy 27-45 meV, depending on the 4-position substituent. Our results highlight how single atom substitutions on the cation change the structure of the organic framework and tune the degree of energetic disorder, providing additional parameters that can be harnessed to tailor the structure and energy landscape of 2DHPs for excitonic^{4,17-20,24} and other²¹⁻²³ device applications.

7.2 Methods

4-H, 4-F, 4-Cl, 4-Me, and 4-Br are synthesized using a modified version of previously published procedures.^{29,50,51} First, a liquid-liquid extraction of 7 mL of unstabilized hydroiodic acid (Sigma Aldrich, 57% w/w) is performed with a 10% v/v solution of tributylphosphate (Acros Organics, 99+%) in chloroform (Fisher, HPLC grade) until the aqueous phase is clear.⁵² The hydroiodic acid is placed in a round bottom flask containing 0.231 g lead(II) iodide (Strem, 99.999+%) and is heated under

nitrogen at 100° C until the lead iodide is dissolved. A stoichiometric amount of 0.13 mL phenethylamine (Sigma-Aldrich, >99.5%) or 4-fluorophenethylamine (Acros Organics, 99%); 0.14 mL 4-chlorophenethylamine (Acros Organics, 98%) or 4-bromophenethylamine (Acros Organics, 98%); or 0.15 mL 4-methylphenethylamine (Acros Organics, 97%) is added to the flask under flowing nitrogen.

The reaction for 4-H is then cooled to room temperature at a rate of 2 °C/h, at which point orange crystals are visible. The mixture is cooled in a 4 °C refrigerator for 30 min, vacuum filtered, washed copiously with diethyl ether (Fisher, ACS grade, anhydrous, stabilized with BHT), and dried overnight under vacuum at 50 °C.

Upon addition of 4-fluorophenethylamine, 4-chlorophenethylamine, 4-methylphenethylamine, or 4-bromophenethylamine, small orange crystals (for 4-F) or an orange powder (for 4-Cl, 4-Me, and 4-Br) quickly form. The hot solution is vacuum filtered, and the product is washed copiously with diethyl ether and dried overnight under vacuum at 50 °C.

The syntheses of 4-H and 4-F yielded crystals suitable for single-crystal X-ray diffraction (SCXRD). The syntheses of 4-Cl, 4-Me, and 4-Br yield powders not suitable for SCXRD.

Crystals of 4-Cl suitable for SCXRD are grown by dissolving 50 mg of 4-Cl powder in 0.5 mL anhydrous dimethylformamide (DMF) (Acros Organics) in a vial and chilling the solution to -23 °C. 8 mL of room temperature toluene (Fisher, ACS grade) is carefully layered on top. The solution is left for 4 days, at which point crystals suitable for SCXRD are removed, washed with toluene and diethyl ether, and dried under flowing nitrogen.

Crystals of 4-Me suitable for SCXRD are grown by dissolving 50 mg of 4-Me powder in 0.3 mL anhydrous DMF and placing the solution in an NMR tube. 2 mL of diethyl ether is carefully layered on top. The tube is sealed and left for 2 weeks, at

which point the crystals are removed and washed with diethyl ether.

Crystals of 4-Br suitable for SCXRD are grown by vapor diffusion.⁵³ 4-Br powder is dissolved in anhydrous DMF and placed in an open-top 20 mL vial. The vial is placed in a larger sealed container containing diethyl ether, where it is left for 2 weeks. The DMF-ether mixture is then decanted, and the crystals are washed with diethyl ether and dried under vacuum for 1 h.

SCXRD data are collected on a Bruker Kappa APEX II DUO diffractometer with a CCD area detector employing graphite-monochromated Mo-K α radiation ($\lambda=0.71073\text{\AA}$). Crystals measured at 100 K are cooled by an Oxford Cryostream. The data collection strategy is determined by COSMO (Bruker AXS) and collected in φ/ω scans. Integration is performed with SAINT (Bruker AXS), and scaling and absorption corrections are applied using SADABS (Bruker AXS) and TWINABS (Bruker AXS) for 4-Cl. Structure solution and refinement is performed using the SHELX suite⁵⁴ using OLEX2 as a graphical viewer for atom assignment and GUI.⁵⁵ OLEX2 is also used to generate crystallographic data tables.⁵⁵

Additional structural characterization and all optical studies are performed on thin films of 4-H, 4-F, 4-Cl, 4-Me, and 4-Br. To deposit thin films, 2DHP crystals (4-H and 4-F) or powders (4-Cl, 4-Me, and 4-Br) are dissolved in anhydrous DMF at a concentration of 15 mg/mL and spin-cast in a nitrogen glove box on sapphire rounds at 800 rpm for 60 s followed by 4000 rpm for 20 s. The films are then annealed in a nitrogen glove box at 80 °C for 10 min.

Powder diffraction patterns are taken on thin films using a Rigaku SmartLab diffractometer operating at 40 kV and 30 mA using Cu-K α radiation in $\theta - 2\theta$ geometry.

For all absorption and PL measurements, samples are placed in an evacuated Advanced Research Systems DE202 cryostat. An Agilent Cary 5000 spectrometer is used to collect absorption spectra. PL spectra of 4-H and 4-F are acquired in

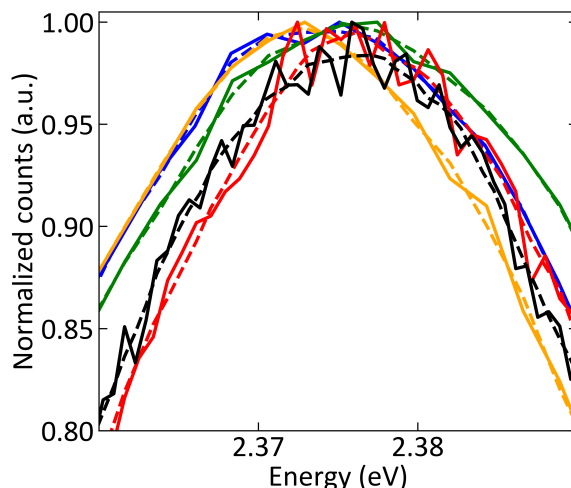


Figure 7.1: Unsmoothed (solid) and smoothed (dashed) 300 K PL spectra for 4-H (black), 4-F (red), 4-Cl orange), 4-Me (green), and 4-Br (blue).

an Edinburgh Instruments FLS1000 fluorescence spectrometer using a Hamamatsu R13456 photomultiplier tube detector. PL spectra of 4-Cl, 4-Me, and 4-Br are acquired in a Horiba Fluorolog FL3 using a Hamamatsu R928 photomultiplier tube detector. Excitation is provided by a monochromated Xe arc lamp for all PL measurements. Room temperature PL spectra exhibit noise that makes extracting the maxima difficult. We use a second order Savitzky-Golay smoothing filter with a window size of 3 nm for 4-H and 4-F and 2.5 nm for 4-Cl, 4-Me, and 4-Br to extract the room temperature PL maxima, FWHM, and Stokes shifts. Smoothed spectra are shown in Figure 7.1.

Raman scattering measurements are collected on as-synthesized crystals or powders of 4-H, 4-F, 4-Cl, 4-Me, and 4-Br using a Horiba LabRam HR confocal Raman scattering microscope with a HeNe laser.

Electronic structure calculations are performed using Q-Chem 5.0⁵⁶ with the 6-311G* basis set and B3LYP functional.^{57,58} We extract the coordinates of a cation from the SCXRD structure, perform a geometry optimization, and then calculate the vibrational modes and their Raman activities.

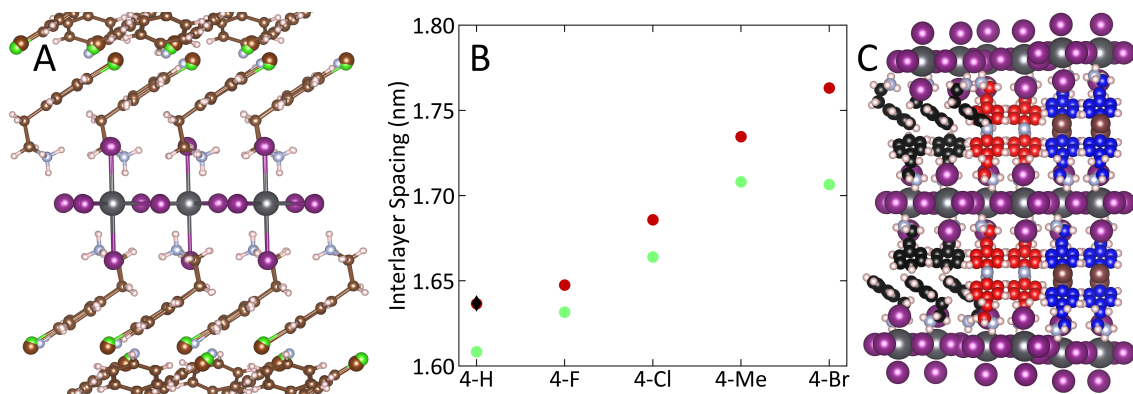


Figure 7.2: (A) Overlaid 100 K crystal structures of 4-H, 4-F, 4-Cl, and 4-Br. Disorder in iodine not shown for 4-H. (B) Interlayer spacings at 100 K from SCXRD structures (green circles), at room temperature from powder diffraction patterns (red circles), and at 300 K from SCXRD structure for 4-H (black diamond). (C) Comparison of organic framework packing and thickness in 4-H (black), 4-F (red) and 4-Br (blue). Disorder in iodine not shown for 4-H. Structures in (A, C) visualized using VESTA.[59]

7.3 Results and Discussion

7.3.1 Structural Characterization

To characterize the 2DHPs, SCXRD measurements are performed at 100 K (Figure 7.2A). 4-H, 4-F, 4-Cl, 4-Me, and 4-Br form planar octahedral PbI_4^{2-} layers separated by the 4-substituted PEA cations. The 100 K 4-H structure resolves to the $P\bar{1}$ space group, matching previous reports.^{37,38} Our a and b lattice parameters are within four standard deviations of a previously published 100 K structure,³⁸ and unlike this structure but like a recent room temperature structure,³⁷ we resolve the cation orientation without disorder. Several structures of 4-F have been reported,^{39–41} and our cell parameters match those reported in Ref. [41] to within 0.02 Å. To the best of our knowledge, 4-Cl, 4-Me, and 4-Br have not been previously synthesized and no structures have been reported, though Sn-based 4-Cl has been synthesized.⁶ Select parameters of the SCXRD structures are tabulated in Table 7.1, with full parameter sets tabulated in Table A.1. 50% thermal ellipsoids are shown in Figure 7.3, and

depictions of the possible cation conformations in 4-Me are shown in Figure 7.4.

Compound		Edge lengths (Å)	Angles (deg)	Avg. Pb-I-Pb angle (deg)	Avg. Pb-I bond length (Å)	
					Equatorial	Axial
4-H (100 K)	P $\bar{1}$	$a = 8.6863(2)$	$\alpha = 85.2360(10)$	152.198(15)	3.1631(3)	3.2068(4)
	$Z = 4$	$b = 8.6856(2)$	$\beta = 85.2760(10)$			
	$V/Z=606.69(3) \text{ \AA}^3$	$c = 32.3872(8)$	$\gamma = 89.4460(10)$			
4-H (300 K)	P $\bar{1}$	$a = 8.7437(2)$	$\alpha = 84.6160(9)$	153.26(2)	3.1761(5)	3.2151(7)
	$Z = 4$	$b = 8.7437(2)$	$\beta = 84.6307(9)$			
	$V/Z=625.67(2) \text{ \AA}^3$	$c = 33.0253(6)$	$\gamma = 89.6320(9)$			
4-F (100 K)	P2 $_1/c$	$a = 16.548(2)$	$\beta = 99.606(6)$	151.405(10)	3.1571(3)	3.2197(5)
	$Z = 2$	$b = 8.5712(10)$				
	$V/Z=610.7(1) \text{ \AA}^3$	$c = 8.7339(10)$				
4-Cl (100 K)	C2/c	$a = 33.3256(17)$	$\beta = 93.002(2)$	152.479(16)	3.1602(3)	3.2085(5)
	$Z = 4$	$b = 8.6453(4)$				
	$V/Z=627.08(5) \text{ \AA}^3$	$c = 8.7179(4)$				
4-Me (100 K)	P $\bar{1}$	$a = 6.1306(2)$	$\alpha = 81.582(2)$	152.21(2)	3.1536(4)	3.2116(5)
	$Z = 1$	$b = 6.1143(2)$	$\beta = 79.945(2)$			
	$V/Z=640.26(4) \text{ \AA}^3$	$c = 17.5420(5)$	$\gamma = 89.980(2)$			
4-Br (100 K)	C2/c	$a = 34.1474(13)$	$\beta = 91.890(2)$	152.145(8)	3.1553(2)	3.2157(3)
	$Z = 4$	$b = 8.6378(4)$				
	$V/Z=640.17(5) \text{ \AA}^3$	$c = 8.6862(4)$				

Table 7.1: Select crystallographic parameters from SCXRD structures.

The Pb-I framework in the 100 K crystal structures of 4-H, 4-F, 4-Cl, and 4-Br (Figure 7.2A, 4-Me is shown in Figure 7.5) overlay well. While within a compound the in-plane and out-of-plane Pb-I bond lengths differ, they are consistent between compounds to within 0.02 Å. The average Pb-I-Pb bond angles do not trend with cation size and range from 152.145(16)° to 152.479(16)° for all but 4-F, which differs more and is 151.405(10)°. Introducing larger cations increases the interlayer spacing (green circles, Figure 1B) and therefore the available volume (Figure 7.2C) in the interstitial space; the normalized unit cell volume V/Z scales with the interlayer spacing (Table 7.1).

The orientation of the phenyl moiety undergoes a rotation between adjacent layers in 4-H (black, Figure 7.2C), forming a herringbone structure that is commonly seen in polycyclic aromatic organic compounds such as pentacene.^{60,61} 4-Me exhibits the cation orientations that are present in 4-H but we are unable to resolve the superstructure. The existence of 4-H structures that both resolve³⁷ and do not resolve³⁸ the herringbone

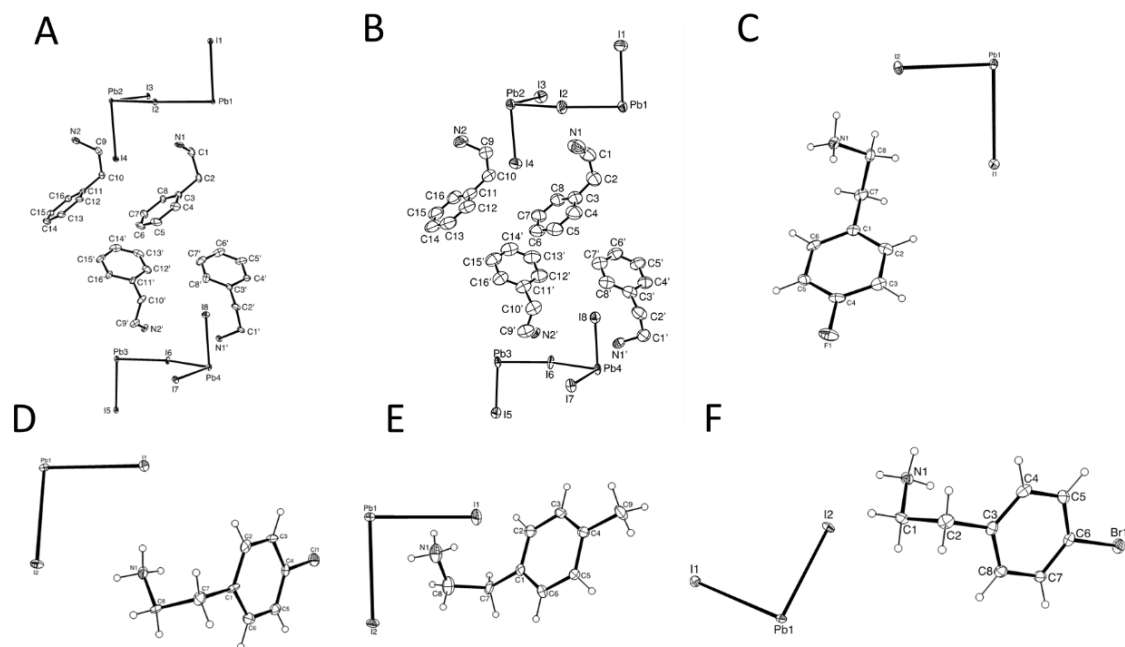


Figure 7.3: Drawings of SCXRD structure or asymmetric unit with 50% thermal ellipsoids for (A) 4-H (100 K), (B) 4-H (300 K), (C) 4-F, (D) 4-Cl, (E) 4-Me, and (F) 4-Br.

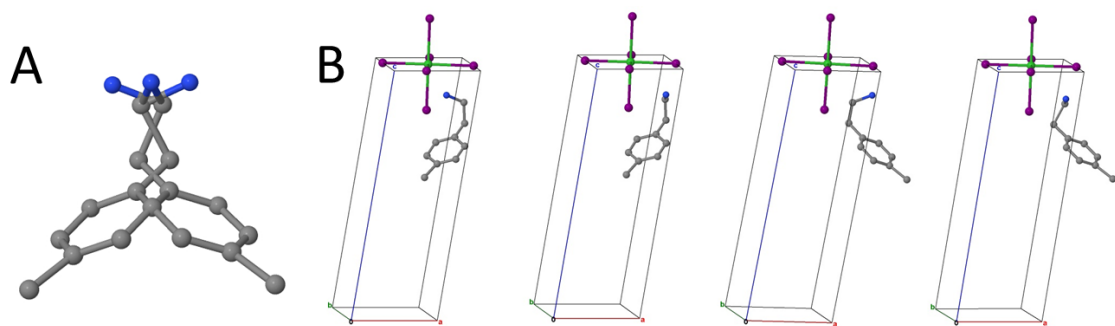


Figure 7.4: (A) Disordered cation in 4-Me, with (B) the four conformers shown individually.

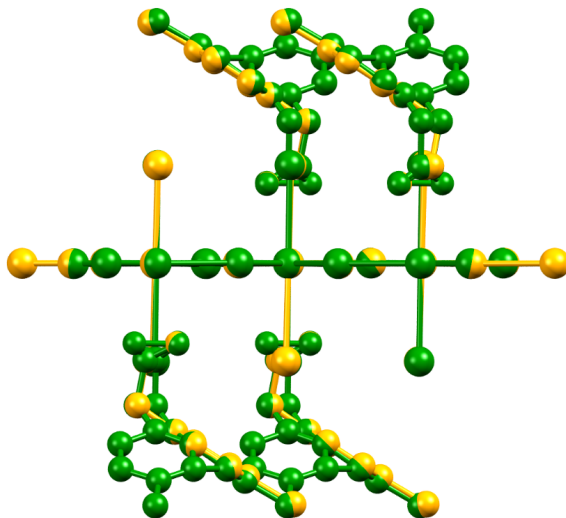


Figure 7.5: Overlaid SCXRD structures of 4-Cl (orange) and 4-Me (green).

superstructure makes the herringbone orientation in 4-Me likely.

Unlike 4-H and 4-Me, the cations in 4-F (red, Figure 1C), 4-Cl, and 4-Br (blue, Figure 7.2C) resolve without disorder in a face-on orientation in which the aromatic rings are linearly offset. We hypothesize that a known π - σ electrostatic attraction between the halogenated phenyl rings promotes face-on offset stacking⁶² because the halogen substituents both inductively withdraw electron density from the σ framework and are π donors.⁶³ The face-on orientation cannot result from steric effects because the cation in 4-Me is larger than the cation in 4-F and 4-Cl. Halogen bonding also cannot stabilize the face-on orientation as adjacent halogens in 4-F, 4-Cl, and 4-Br exhibit a symmetric Type I orientation in which electrophilic regions interact,⁶⁴ and halogen-aryl interactions cannot be stabilizing here because the halogen sides and the aryl π systems are both nucleophilic.⁶⁴

Room-temperature powder X-ray diffraction patterns of the corresponding thin films show a similar increase in interlayer spacing with cation size (red circles, Figure 7.2B; Figure 7.6A). The interlayer spacing increases with temperature, consistent with thermal expansion of the perovskite lattice.⁶⁵ We also performed 300 K SCXRD on 4-H

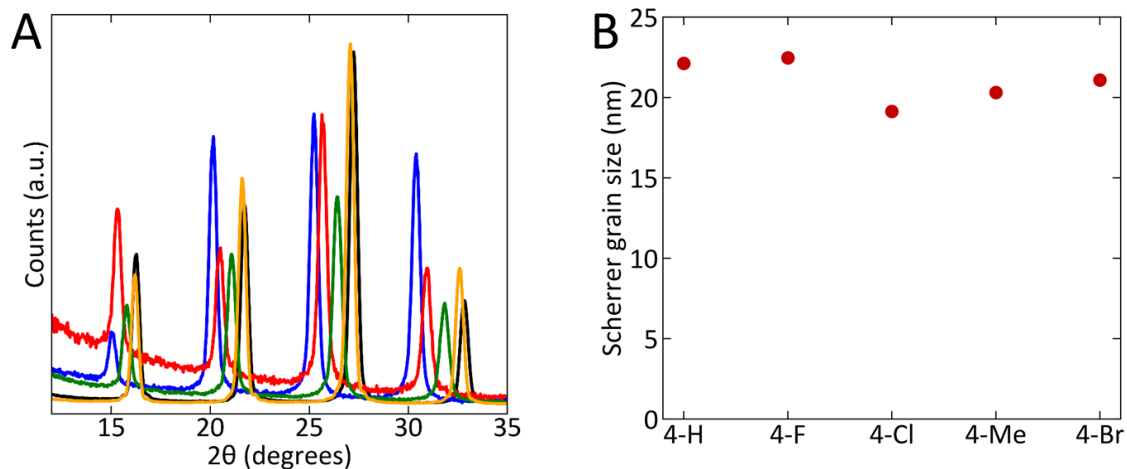


Figure 7.6: (A) Room temperature powder XRD patterns of thin films of 4-H (black), 4-F (red), 4-Cl (orange), 4-Me (green), and 4-Br (blue) deposited on sapphire. (B) Scherrer grain sizes determined from patterns in (A).

(Table 7.1). The interlayer spacing from this structure is shown in the black diamond in Figure 7.2B and is identical within error to the interlayer spacing determined from the room temperature powder diffraction pattern, indicating that dissolving crystals in DMF and spin-casting does not change the interlayer spacing in the resultant perovskite structure. Interestingly, while 4-Br has a greater interlayer spacing than 4-Me at room temperature, the reverse is true at 100 K. The Scherrer grain size (Figure 7.6B) in the films is between 19.1(1) and 22.5(1) nm for all species, which is over an order of magnitude larger than the unit cell length and Bohr radius.³ The degree of quantum confinement should therefore be unchanged in thin films compared to single crystals.

7.3.2 Optical Characterization

Figure 7.7 shows 300 K (A-C) and 10 K (D-F) excitonic absorption and PL spectra of 4-H (black), 4-F (red), 4-Cl (orange), 4-Me (green), and 4-Br (blue). Figure 7.8A,B summarizes the energies of the maxima and full-width at half-maxima (FWHM) for

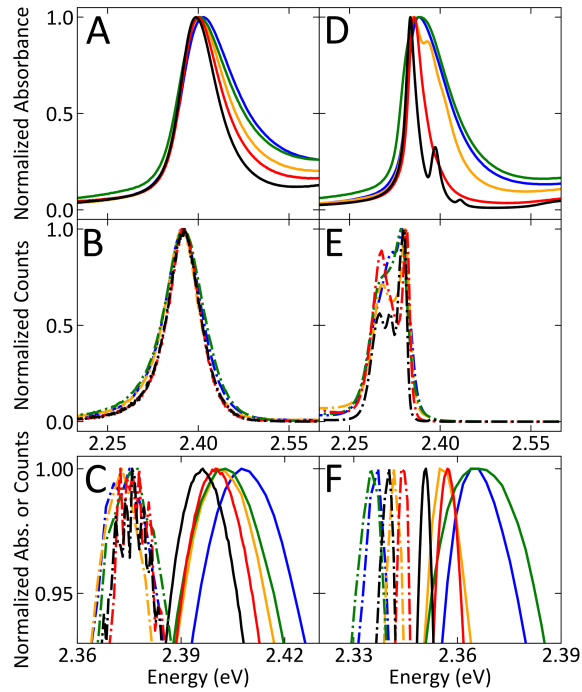


Figure 7.7: 300 K excitonic absorption (A) and PL (B) spectra and (C) their overlay, highlighting resonance maxima, and 10K excitonic absorption (D) and PL (E) spectra and (F) their overlay, highlighting resonance maxima, for 4-H (black), 4-F (red), 4-Cl (orange), 4-Me (green), and 4-Br (blue). All PL spectra use 3.10 eV excitation.

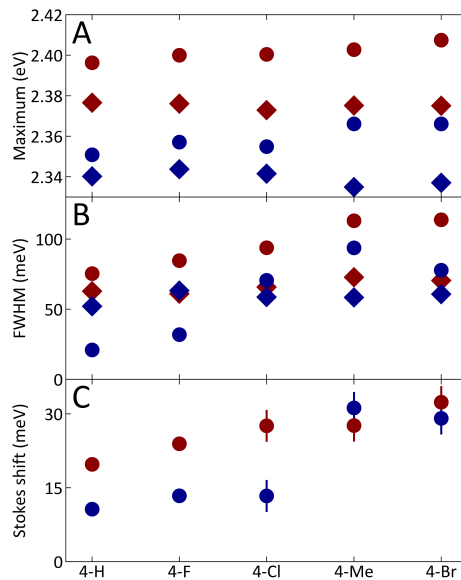


Figure 7.8: Summary of (A) maximum, (B) FWHM, and (C) Stokes shift of excitonic absorption (circles) and PL (diamonds) spectra from Figure 2 at 300 K (red) and 10 K (blue). Error represents instrumental uncertainty.

the 300 K (red) and 10 K (blue) excitonic absorption (circles) and PL (diamonds) spectra. At both 300 K and 10 K, the absorption maxima correlate with cation size, increasing by 11(2) meV from 4-H to 4-Br at 300 K and by 15(2) meV from 4-H to 4-Me at 10 K. The absorption FWHM strongly correlates with cation size both at 300 K, where it grows from 75.4(7) meV for 4-H to 113(3) meV for 4-Br, and at 10 K, where it increases from 21.0(7) meV for 4-H to 94(3) meV for 4-Me. At 300 K, the absorption FWHM of 4-Br is wider than that of 4-Me, while the reverse is true at 10 K, which is consistent with the temperature-dependent interlayer spacing (Figure 7.2B). The PL maxima and FWHM are largely independent of cation size, so the Stokes shift (Figure 7.8C) follows the trend of the absorption maxima and therefore the cation size at both 300 K, where it increases from 20(1) meV for 4-H to 32(3) meV for 4-Br, and at 10 K, where it increases from 11(1) meV for 4-H to 31(3) meV for 4-Me. 10 K excitonic absorption and PL spectra for all species are plotted on the same axes in Figure 7.9.

At 10 K, the excitonic absorption spectrum of 4-H (Figure 7.7D, black) shows three Lorentzian fine structure resonances which are separated by 41(1) meV (Figure 7.10A), which we²⁹ and others^{28,66} have previously observed. In contrast, 4-F (red) is missing the discrete resonances, showing only a single wider absorption resonance with a similar envelope to the 4-H absorption. Like 4-H, we fit 4-F to the sum of three Lorentzians (Figure 7.10B). The Lorentzian lineshapes indicate that 4-H and 4-F are homogeneously broadened.^{29,67} 4-Cl (orange) is broader still, but unlike 4-F shows two discrete absorption peaks. Still wider are 4-Br and 4-Me, which like 4-F only appear to have a single absorption resonance. The broader linewidths coincide with the need to fit 4-Cl, 4-Br, and 4-Me to the sum of three Gaussians (Figure 7.10C-E) instead of Lorentzians, and the switch to Gaussian lineshapes indicates that inhomogeneous broadening dominates.⁶⁷ The centers and widths of the lineshapes used

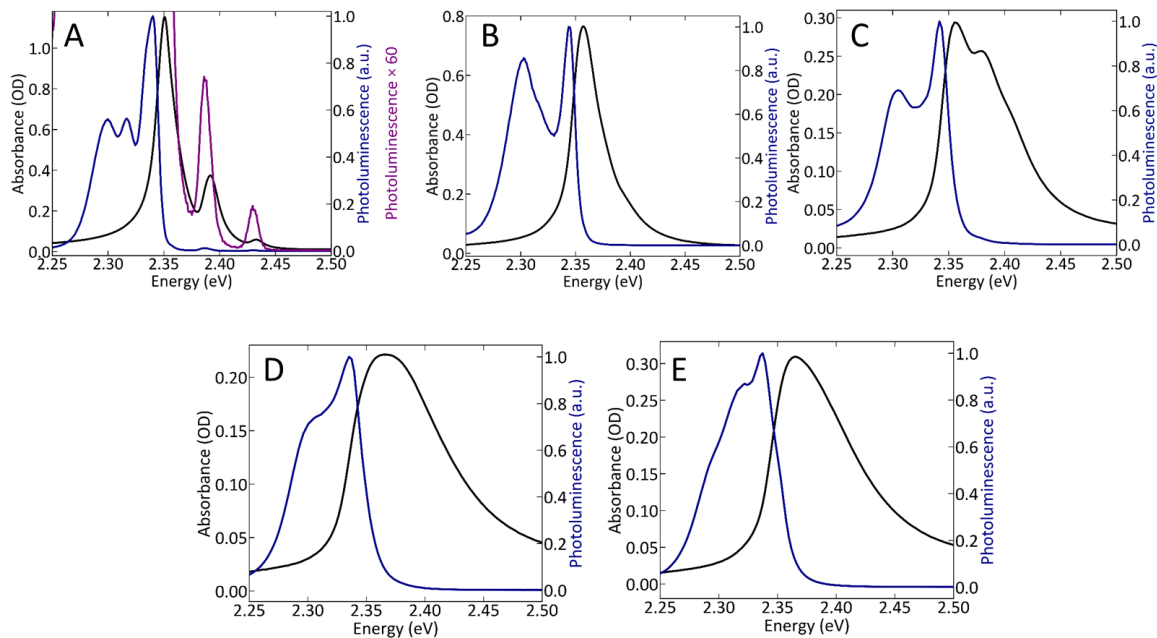


Figure 7.9: 10K absorption (black) and PL (blue, $\times 60$ in purple) spectra of (A) 4-H, (B) 4-F, (C) 4-Cl, (D) 4-Me, and (E) 4-Br.

to fit the absorption spectra are shown in circles in Figure 7.11A-B. Given the lack of well-defined, discrete resonances, we note the ambiguity in fitting the absorption spectra of 4-F, 4-Cl, 4-Me, and 4-Br.

All species exhibit fine structure in 10 K PL spectra, though only 4-H has discrete higher energy hot excitonic PL resonances (Figure 7.9A).²⁹ To further analyze the 10 K PL spectra, we fit the PL spectra using the sum of Gaussian functions like in our previous work.²⁹ Fits of 10 K PL spectra are shown in Figure 7.10, and fit parameters are tabulated in Table A.2. The energy and FWHM of the central (red) resonance and lower-energy sideband (dark red) are shown in diamonds in Figure 7.11A-B, with the Stokes shift (Figure 7.11C) determined from fits as the difference in energy between the red resonances in absorption and PL shown in Figure 7.10. An important feature from the fits is that the 37-42 meV difference between the red and dark red PL resonances appears in all PL spectra, though it is harder to pick out discrete resonances for 4-Br

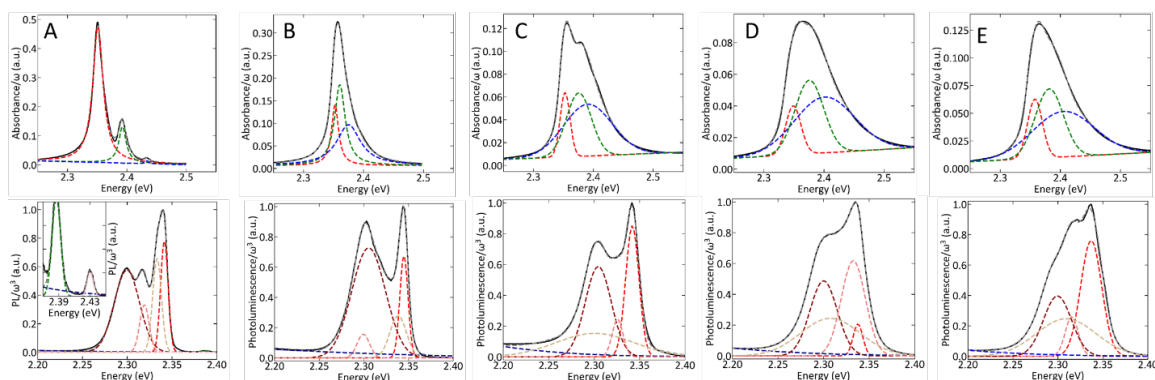


Figure 7.10: Fits of 10K absorption (top) and PL (bottom) spectra of (A) 4-H, (B) 4-F, (C) 4-Cl, (D) 4-Me, and (E) 4-Br. Absorption spectra are fit to the sum of 3 Lorentzian (4-H and 4-F) or Gaussian (4-Cl, 4-Br, and 4-Me) functions. PL spectra are fit to the sum of 5 Gaussian functions (7 for 4-H to account for the hot excitonic PL resonances).

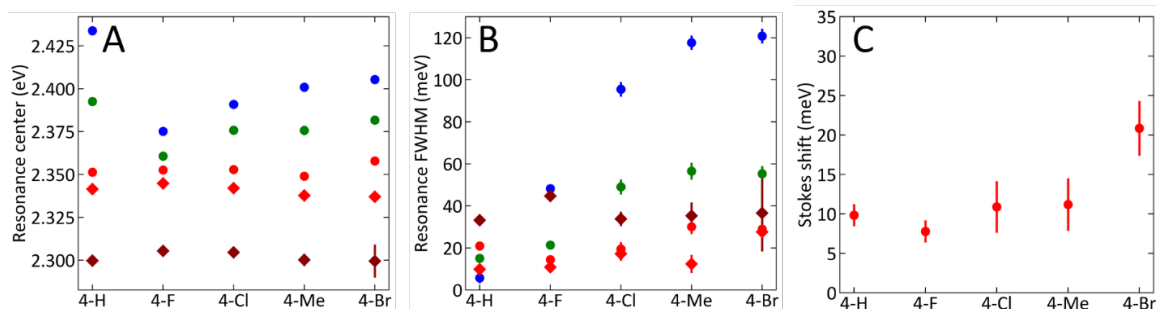


Figure 7.11: Summary of 10 K absorption (circles) and PL (diamonds) fits, with (A) selected resonance centers, (B) FWHM, and (C) Stokes shift.

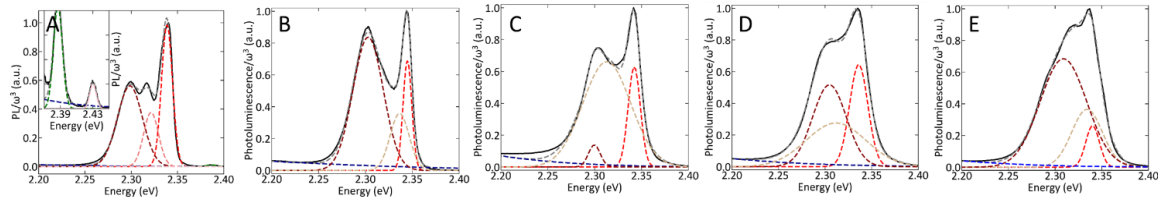


Figure 7.12: Fits of 10 K PL spectra of (A) 4-H, (B) 4-F, (C) 4-Cl, (D) 4-Me, and (E) 4-Br to the sum of 4 Gaussian functions (6 for 4-H to account for the hot excitonic PL resonances), one fewer than in Figure 7.10.

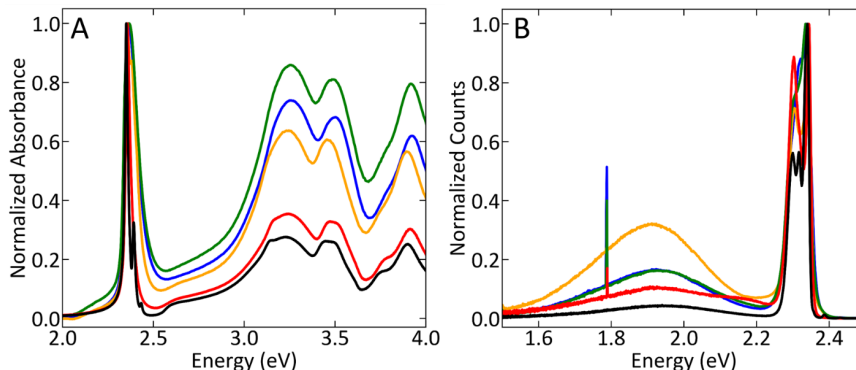


Figure 7.13: Full 10 K (A) absorption and (B) PL spectra of 4-H (black), 4-F (red), 4-Cl (orange), 4-Me (green), and 4-Br (blue).

and 4-Me. The energetic similarity of the lower-energy sideband indicates either that introducing substituents onto the 4-position of the cation does not greatly perturb the phonon responsible for the fine structure, or the low-energy fine structure in PL does not originate from exciton-phonon coupling. We note the ambiguity in fitting the PL spectra of 4-F, 4-Cl, 4-Br, and 4-Me due to a lack of clear structure, so alternate fits using one fewer Gaussian function are presented in Figure 7.12 and Table A.3. In all PL fits, one Gaussian function is used to fit the broad PL feature centered at 1.9 eV that has been attributed to self-trapped exciton recombination.^{4,7,17,18,68} Full 10K absorption and PL spectra are shown in Figure 7.13.

We explore the temperature dependence of the absorption and PL spectra (Figure 7.14) and analyze their maxima and FWHM for the different 4-substituted cations. We assume that trends in the excitonic absorption and PL maxima are a proxy for those of

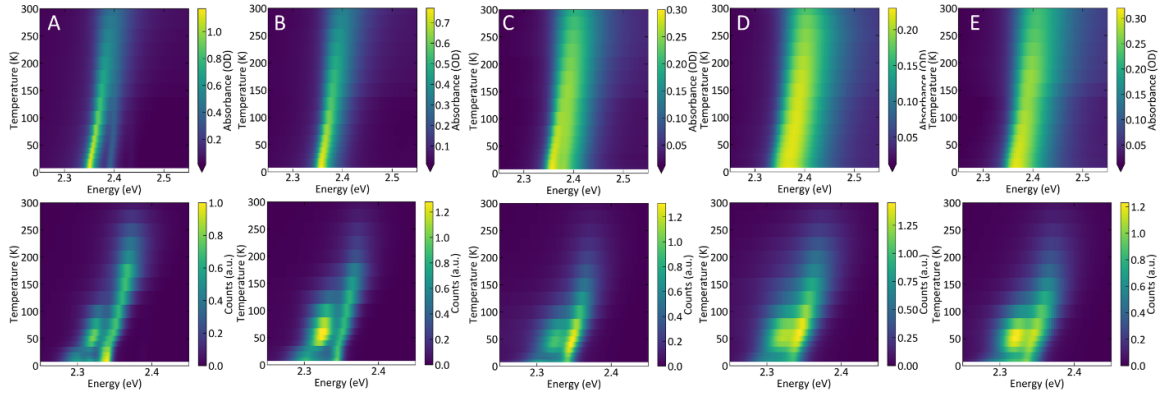


Figure 7.14: Absorption (top) and PL (bottom) spectra from 10 K to 300 K for (A) 4-H, (B) 4-F, (C) 4-Cl, (D) 4-Me, and (E) 4-Br.

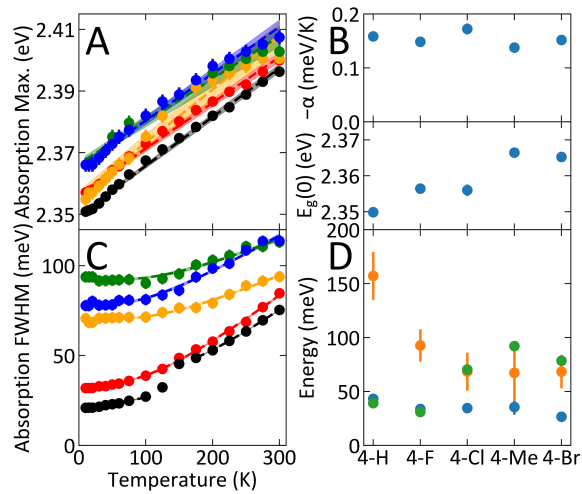


Figure 7.15: Excitonic absorption maxima for 4-H (black), 4-F (red), 4-Cl (orange), 4-Me (green), and 4-Br (blue) (circles; error indicates instrumental uncertainty), with linear fit (dashed lines with one-sigma uncertainties shaded). (B) Results of fits shown in (A). Error indicates one-sigma confidence intervals from the linear regressions. (C) Excitonic absorption FWHM (circles) of 4-H (black), 4-F (red), 4-Cl (orange), 4-Me (green), and 4-Br (blue). Error indicates instrumental uncertainty. Fits to model are indicated by the dashed lines with one-sigma uncertainties shaded. (D) Extracted fit parameters E_{LO} (blue circles), γ_{LO} (orange circles), and Γ_0 (green circles) from absorption for 4-H (≥ 175 K), 4-F, 4-Cl, 4-Me, and 4-Br. Error indicates one-sigma confidence intervals from the nonlinear regressions.

the band gap because the layers in 2DHPs are not electronically coupled and expansion of the cation should not significantly affect the degree of quantum or dielectric confinement.³ This is seen in alkylammonium ($C_n H_{2n+1} NH_3^+$)-based PbI_4^{2-} 2DHPs, where the exciton binding energy is invariant for $n \geq 4$.^{3,8} The phenethylammonium-based cations we use are longer than $C_4H_9NH_3^+$.⁸ As the temperature increases from 10 K to 300 K, the absorption maxima versus temperature is well-fit to a linear model (Figure 7.15A) where $E_g(T) = E_g(0) - \alpha T$. For 4-H, 4-F, 4-Cl, 4-Me, and 4-Br, α varies slightly from -0.14 to -0.16 meV/K (Figure 7.15B) and shows no correlation with cation size. Fitting the temperature dependence of the highest energy excitonic resonance in PL (Figure 7.16A) yields similar α , varying from -0.12 to -0.15 meV/K, again showing no correlation with cation size (Figure 7.16B). The independence of α on the choice of cation suggests it depends only on the PbI_4^{2-} framework. The linear trend and negative α match that found in lead chalcogenides,^{69–71} and a negative α is also seen in most Pb-based 2D and 3D hybrid perovskites.^{13,35,72} $E_g(0)$ values from absorption spectra (Figure 7.15B) increase with increased interlayer spacing from 2.3499(5) eV for 4-H to 2.366(1) eV for 4-Me, while $E_g(0)$ values from PL spectra do not show a correlation with the size of the cation (Figure 7.16C) and range from 2.335(1) for 4-Me to 2.346(2) for 4-F. A previous report on 4-H thin films found a slightly smaller α (-0.11 meV/K) and a much greater $E_g(0)$ (2.372 eV).⁶⁵ However, we note that the work used glass, instead of thermally-conductive sapphire substrates as used here, and therefore the sample temperatures may be higher than anticipated.

Absorption FWHM (Figure 7.15C) are fit using a model originally developed for the temperature-dependent excitonic absorption linewidth in 2D transition-metal dichalcogenides^{73,74} and more recently applied to 3D³⁵ hybrid perovskites and

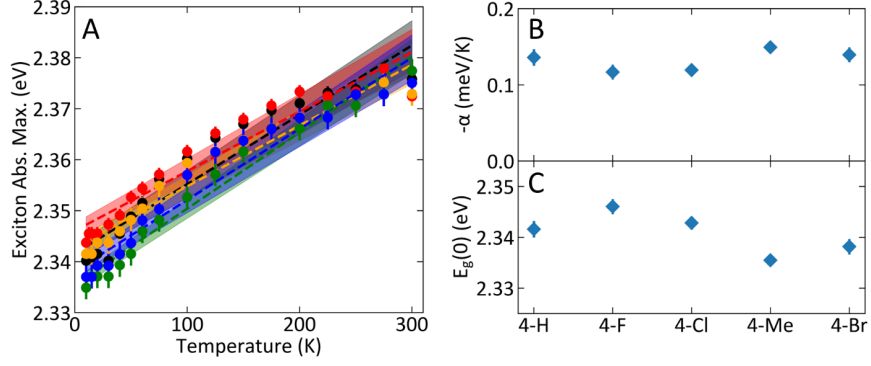


Figure 7.16: (A) Temperature-dependent PL maxima for 4-H (black), 4-F (red), 4-Cl (orange), 4-Me (green), and 4-Br (blue). Error bars represent instrumental uncertainty. (B, C) Results from linear fits of data in (A). Error bars represent one-sigma confidence interval from the linear regressions.

2DHPs.^{28,39} The FWHM varies with temperature as:

$$\Gamma(T) = \Gamma_0 + \gamma_{ac}T + \frac{\gamma_{LO}}{\exp(E_{LO}/k_B T) - 1} + \gamma_{imp} \exp(-E_b/k_B T) \quad (7.1)$$

where Γ_0 is the zero-temperature FWHM from intrinsic effects such as disorder,⁷⁵ γ_{ac} (γ_{LO}) are the acoustic (LO) phonon coupling strengths, and γ_{imp} is the strength of impurity scattering.³⁵ Like in 3D lead iodide-based hybrid perovskites, contributions of acoustic and impurity scattering components do not match the data and are considered small, so we fix $\gamma_{ac} = \gamma_{imp} = 0$.³⁵ We find that 4-F, 4-Cl, 4-Me, and 4-Br are well-fit by this model across the 10 K to 300 K temperature range with the parameters shown in Figure 7.15D and Table 7.2. 4-F, 4-Cl, and 4-Me are broadened by an LO phonon with $E_{LO} = 34$ -36 meV, while for 4-Br $E_{LO} = 27(4)$ meV. 4-H exhibits a discontinuity in the FWHM at temperatures of 100-150 K (Figure 7.15C). We fit the FWHM for temperatures spanning 175 K to 300 K, and 4-H exhibits broadening by a phonon with $E_{LO} = 43(4)$ meV. In addition, γ_{LO} is the largest for 4-H at 160(20) meV, consistent with our previous hypothesis of strong exciton-phonon coupling,²⁹ and γ_{LO} decreases as the interlayer spacing in the 2DHP increases (Figure 7.15D). The zero-temperature

FWHM Γ_0 also increases with interlayer spacing for the 4-substituted cations with $\Gamma_0 = 39(1)$ meV for 4-H and 30.9(6) meV for 4-F to 92.2(6) for 4-Me. We cannot explain the 30% smaller Γ_0 for 4-F than 4-H (≥ 175 K) given the larger interlayer spacing in 4-F and consider that F's extremely large electronegativity may change the electron density in the phenyl moiety and therefore give rise to the smaller Pb-I-Pb bond angle seen structurally and Γ_0 found optically. Our results imply that a more constrained organic framework strengthens exciton-phonon coupling and reduces energetic disorder. The dependence of the LO phonon coupling strength on the rigidity of the organic framework also supports our previous finding that the phonon responsible for the excitonic fine structure in 4-H is located on the organic cation.²⁹ Unlike in conventional semiconductors where γ_{LO} is largely unchanged with the reduction in dimensionality from 3D to 2D,⁷⁶ E_{LO} is ~ 3 x greater and γ_{LO} is 1.7-4.5x greater in these 2DHPs compared to 3D lead iodide perovskites (where $\gamma_{LO} = 40$ meV and $E_{LO} = 11-15$ meV),³⁵ which is again consistent with strong exciton-phonon coupling and excitonic fine structure originating from phonons on the organic cation in 2DHPs.

	4-H (≥ 175 K)	4-F	4-Cl	4-Me	4-Br
E_{LO} (meV)	43(4)	34(5)	35(5)	36(7)	27(4)
γ_{LO} (meV)	160(20)	92(15)	68(18)	67(26)	68(15)
Γ_0 (meV)	39(1)	30.9(6)	70.3(4)	92.2(6)	78.5(6)

Table 7.2: Extracted parameters from broadening model applied to absorption spectra. The FWHM of 4-F, 4-Cl, 4-Me, and 4-Br are fit from 10 K to 300 K. The temperature-dependent FWHM of 4-H is discontinuous between 100 and 150 K, so we fit the FWHM from 175 K to 300 K.

The 10 K absorption spectrum of 4-H shows discrete fine structure resonances separated by 41(1) meV (Figure 7.10A), with the discrete resonances persisting to 100 K (Figure 7.14A).²⁹ This separation is similar to the 43(4) meV phonon that broadens 4-H at temperatures ≥ 175 K, once the fine structure is no longer observable. These

similar energies and the large γ_{LO} for 4-H lead us to hypothesize that the phonon that causes discrete fine structure at low temperature is the same phonon that broadens the linewidth at temperatures ≥ 175 K. Given the small number of data points, the 4-H absorption spectra FWHM at temperatures ≤ 100 K when the discrete fine structure resonances are present are consistent with either weak coupling to a low energy LO phonon or coupling to acoustic phonons.^{47,77,78}

The instantaneous absorption process samples the ground state energy landscape and reflects a snapshot of the instantaneous structure. The increase in FWHM and changeover from homogeneous to inhomogeneous broadening in absorption spectra for larger cations are consistent with a greater available volume in the organic framework (Figure 7.2C) increasing the dynamic energetic disorder.^{42,44,45} The absorption maxima and FWHM are unrelated to cation mass because methyl (15.0 amu) is much lighter than chlorine (35.4 amu), but methyl exhibits a larger width and Stokes shift, and they are also unrelated to the organic framework’s packing motif. The increased energetic disorder for larger cations acts to increase the effective temperature of the 4-substituted perovskites. Compared to 4-H ($\Gamma_0 = 39(1)$ meV), we find that the effective temperature at 0 K is 279(2) K for 4-Cl ($\Gamma_0 = 70.3(4)$ meV), 364(3) K for 4-Me ($\Gamma_0 = 92.2(6)$ meV), and 312(3) K for 4-Br ($\Gamma_0 = 78.5(6)$ meV). Γ_0 is smaller for 4-F than for 4-H (≥ 175 K) but larger than that of 4-H (≤ 100 K). Cation-induced dynamic disorder has been previously observed in 3D^{42,43,45,79,80} and 2D⁶⁵ lead halide hybrid perovskites.

We perform a similar FWHM analysis on PL spectra for 4-H, 4-F, and 4-Cl from 125 K to 300 K (Figure 7.17, Table 7.3). We restrict the analysis to higher temperatures at which a single resonance dominates the PL spectra so the low-energy sidebands in the fine structure do not artificially increase the FWHM (Figure 7.17A; spectra in Figure 7.14). The low energy fine structure is significant until 175 K for 4-Me and 4-Br, at

which point the temperature-dependent FWHM appears linear with temperature, so we cannot reliably extract an LO phonon energy and exclude these compounds from this analysis. In PL, 4-H, 4-F, and 4-Cl are broadened by phonons with similar E_{LO} (45(2) meV for 4-H, 40(4) meV for 4-F, and 38(8) meV for 4-Cl) to one another and to the E_{LO} we find in absorption. γ_{LO} is 20% larger in PL (190(20) meV) than in absorption (160(20) meV) for 4-H and is considerably larger in PL for 4-F (130(20) meV) and 4-Cl (130(50) meV) than in absorption, while Γ_0 in PL is much smaller and closer in energy than in absorption for 4-H (20.0(5) meV), 4-F (24(1) meV), and 4-Cl (27(2) meV). Polaron formation^{28,29,33,43,44,46–49} likely creates one structural and energetic minimum in the excited state on the picosecond timescale of PL,²⁹ resulting in similar Γ_0 and γ_{LO} in PL for 4-H, 4-F, and 4-Cl. The larger γ_{LO} and smaller Γ_0 in PL compared to absorption support this hypothesis.

	4-H	4-F	4-Cl
E_{LO} (meV)	45(2)	40(4)	38(8)
γ_{LO} (meV)	190(20)	130(20)	130(50)
Γ_0	21.0(6)	24(1)	27(2)

Table 7.3: Extracted parameters from broadening model applied to PL spectra. The FWHM are fit for temperatures from 125 K and 300 K.

In these compounds, vibrations with energy $> 200 \text{ cm}^{-1}$ (25 meV) should be located exclusively on the organic cation because the heavy Pb and I atoms result in low energy vibrations.²⁹ In addition, the similarity of the organic and inorganic frameworks combined with the consistent energies of the LO phonons responsible for linewidth broadening in 4-H, 4-F, 4-Cl, 4-Me, and 4-Br indicate that 4-substitution does not greatly change the responsible mode. Therefore, we hypothesize that a torsional mode about the longitudinal axis of the phenyl moiety couples to excitons, as the addition of on-axis mass ($r = 0$) will not significantly change the moment of inertia ($I = \sum_i m_i r_i^2$)

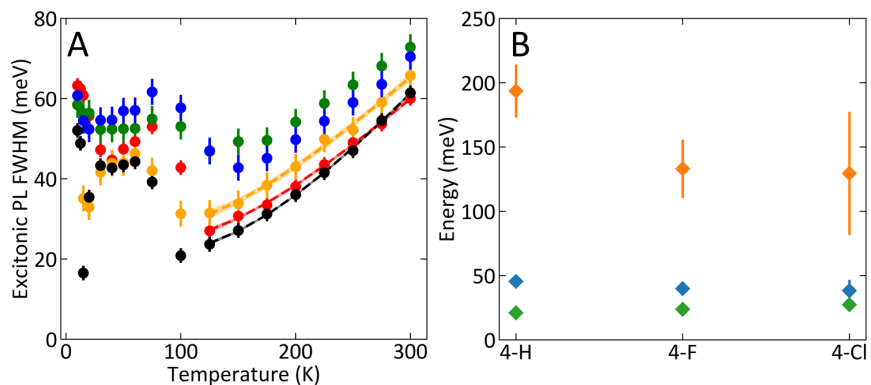


Figure 7.17: (A) Temperature-dependent PL FWHM of 4-H (black), 4-F (red), 4-Cl (orange), 4-Me (green), and 4-Br (blue). Error bars represent instrumental uncertainty. (B) Γ_0 (green), γ_{LO} (orange), and E_{LO} from fits of data in (A) for 4-H, 4-F, and 4-Cl from 125 K to 300 K. Error bars represent one-sigma confidence interval from the nonlinear regressions.

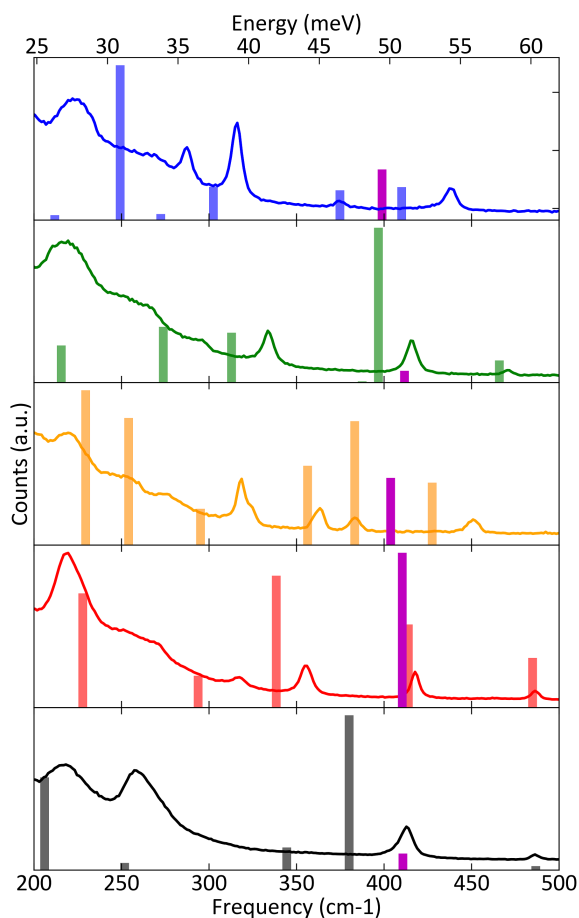


Figure 7.18: Room temperature Raman scattering spectra (lines) of single crystals or powders of 4-H (black), 4-F (red), 4-Cl (orange), 4-Me (green), and 4-Br (blue), with computed Raman spectra of cation (bars). Pink bar indicates mode shown in Figure 7.19.

of a torsional oscillator. To investigate the vibrational modes that may be coupling to the exciton, we collect Raman spectra for 4-H, 4-F, 4-Cl, 4-Me, and 4-Br (Figure 7.18). 4-H shows Raman active modes at 260 and 410 cm^{-1} (32 and 51 meV) with broad scattering in between, in contrast to a previous report that claimed no clear vibrations in 4-H in this energy range but which did not show Raman spectra at energies greater than 200 cm^{-1} (25 meV).⁶⁵ It is possible that the Raman activity of some vibrational modes is symmetry disallowed.^{81,82} Several distinct Raman modes are seen in 4-F, 4-Cl, 4-Me, and 4-Br between 200 and 400 cm^{-1} (25 and 50 meV). The additional modes in these species compared to 4-H are likely the result of the heavier substituents reducing the energy of higher energy vibrations or the substitutions causing additional vibrations to become Raman active. To investigate further, we use electronic structure calculations to compute the vibrational modes of the 4-substituted PEA cations. We extract the coordinates of the cation from the 100 K crystal structures, perform a geometry optimization, and determine the normal modes along with their infrared and Raman activities. We find 10 vibrational modes with energy < 600 cm^{-1} (74 meV) in 4-H and 12-13 modes with energy < 600 cm^{-1} in 4-F, 4-Cl, 4-Me, and 4-Br, indicating that 4-substitution lowers the energy of some higher energy vibrational modes. Simulated Raman spectra for the cations from 200-500 cm^{-1} (25-62 meV) are shown as bars in Figure 7.18. In accord with our hypothesis, we find a twisting mode (Figure 7.19; pink bars in Figure 7.18) of the phenyl ring at $\sim 410 \text{ cm}^{-1}$ (51 meV) in 4-H, 4-F, and 4-Me, at 403 cm^{-1} (50 meV) in 4-Cl, and at 398 cm^{-1} (49 meV) in 4-Br. The slight lowering in energy is consistent with E_{LO} in 4-Br being smaller than in the other species. This mode is identical in 4-H, 4-Cl, 4-Br, and 4-Me, while in 4-F, this mode uniquely contains additional motion of the ethylammonium tether and the F atom perhaps because of F's large electronegativity changing the electron density in the phenyl moiety. This difference may explain why fine structure is absent in

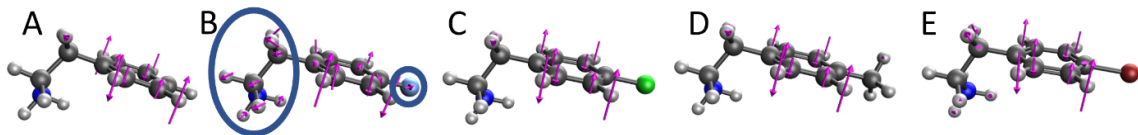


Figure 7.19: Ring twisting vibrational mode in (A) 4-H, (B) 4-F, (C) 4-Cl, (D) 4-Me, and (E) 4-Br cations. Circles in (B) highlight differences in 4-F vibrational mode.

absorption for 4-F but present for 4-H and 4-Cl, while increased disorder in 4-Me and 4-Br washes out the fine structure. The difference in energy between this computed mode and experimental E_{LO} values as well as discrepancies between simulated and experimental spectra are not surprising. A calculated vibrational spectrum of the 3D hybrid perovskite methylammonium lead iodide finds higher vibrational energies than are observed experimentally.⁸² Additionally, cationic vibrational modes tend to be sensitive to the local environment of the perovskite.⁸² While not conclusive, our simulations support the existence of a similar vibrational mode on the cation in all species that is consistent with our experimental observations.

7.4 Conclusion

Using 4-H as a template, we introduce single atom substitutions in the 4-position of the phenyl moiety that do not greatly affect the inorganic framework of the 2DHPs. Despite the similarity in the organic cation, different intermolecular interactions alter its packing from a herringbone orientation in 4-H and 4-Me to a face-on orientation in 4-F, 4-Cl, and 4-Br. This transformation is realized without structurally or chemically modifying the inorganic framework, as has been employed previously.⁵ Cd-based 2DHPs have been used to polymerize organic cations,⁸³ and the ability to use the organic cation itself to control the superstructure in the organic framework may allow for advanced devices incorporating polymerized organic compounds to be created,

such as bulk heterojunction solar cells or organic-inorganic p - n junctions.^{1,3}

Despite carriers being confined to the PbI_4^{2-} framework, we provide further evidence that the cation is not inert and can be used to tailor the optoelectronic properties of 2DHPs without perturbing the structure of the inorganic lattice. Larger cations, independent of packing motif or mass, result in increased energetic disorder in the ground state, which is seen in absorption spectra. Temperature-dependent absorption and PL linewidth analysis supports the existence of exciton-phonon coupling to LO phonons with energies of 27-45 meV in 4-H and its derivatives, supporting our earlier conclusion that the fine structure in 4-H is caused by exciton-phonon coupling to phonons on the cation.²⁹ The similar maxima and FWHM in PL spectra indicate that excitons in 4-H, 4-F, 4-Cl, 4-Me, and 4-Br find a similar state before recombining, which we attribute to the slower timescale for PL allowing for polaron formation.^{28,29,44,47,48} Our findings suggest that stiffening or constraining the organic lattice by reducing the available volume of the cation enhances excitonic fine structure, increases exciton-phonon coupling, and reduces energetic disorder in 2DHPs, which are important design rules when considering 2DHPs for optical and electronic applications.

7.5 References

- (1) Mitzi, D. B. *Prog. Inorg. Chem.* **1999**, *48*, 1–121.
- (2) Saparov, B.; Mitzi, D. B. *Chem. Rev.* **2016**, *116*, 4558–4596.
- (3) Straus, D. B.; Kagan, C. R. *J. Phys. Chem. Lett.* **2018**, *9*, 1434–1447.
- (4) Smith, M. D.; Karunadasa, H. I. *Acc. Chem. Res.* **2018**, *51*, 619–627.
- (5) Mitzi, D. B.; Chondroudis, K.; Kagan, C. R. *IBM J. Res. Dev.* **2001**, *45*, 29–45.
- (6) Knutson, J. L.; Martin, J. D.; Mitzi, D. B. *Inorg. Chem.* **2005**, *44*, 4699–4705.

- (7) Smith, M. D.; Pedesseau, L.; Kepenekian, M.; Smith, I. C.; Katan, C.; Even, J.; Karunadasa, H. I. *Chem. Sci.* **2017**, *8*, 1960–1968.
- (8) Ishihara, T.; Takahashi, J.; Goto, T. *Phys. Rev. B* **1990**, *42*, 11099–11107.
- (9) Papavassiliou, G. *Prog. Solid State Chem.* **1997**, *25*, 125–270.
- (10) Duan, X.; Wang, C.; Pan, A.; Yu, R.; Duan, X. *Chem. Soc. Rev.* **2015**, *44*, 8859–8876.
- (11) Braun, M.; Tuffentsammer, W.; Wachtel, H.; Wolf, H. *Chem. Phys. Lett.* **1999**, *303*, 157–164.
- (12) Hanamura, E.; Nagaosa, N.; Kumagai, M.; Takagahara, T. *Mater. Sci. Eng. B* **1988**, *1*, 255–258.
- (13) Hong, X.; Ishihara, T.; Nurmikko, A. V. *Phys. Rev. B* **1992**, *45*, 6961–6964.
- (14) Ishihara, T. In *Opt. Prop. Low-Dimensional Mater.* World Scientific: 1996, pp 288–339.
- (15) Keldysh, L. V. *JETP Lett.* **1979**, *29*, 658–661.
- (16) Mathieu, H.; Lefebvre, P.; Christol, P. *Phys. Rev. B* **1992**, *46*, 4092–4101.
- (17) Dohner, E. R.; Hoke, E. T.; Karunadasa, H. I. *J. Am. Chem. Soc.* **2014**, *136*, 1718–1721.
- (18) Dohner, E. R.; Jaffe, A.; Bradshaw, L. R.; Karunadasa, H. I. *J. Am. Chem. Soc.* **2014**, *136*, 13154–13157.
- (19) Fujita, T.; Sato, Y.; Kuitani, T.; Ishihara, T. *Phys. Rev. B* **1998**, *57*, 12428–12434.
- (20) Han, Z.; Nguyen, H.-S.; Boitier, F.; Wei, Y.; Abdel-Baki, K.; Lauret, J.-S.; Bloch, J.; Bouchoule, S.; Deleporte, E. *Opt. Lett.* **2012**, *37*, 5061–3.

- (21) Kagan, C. R.; Mitzi, D. B.; Dimitrakopoulos, C. D. *Science* **1999**, *286*, 945–947.
- (22) Matsushima, T.; Hwang, S.; Sandanayaka, A. S. D.; Qin, C.; Terakawa, S.; Fujihara, T.; Yahiro, M.; Adachi, C. *Adv. Mater.* **2016**, *28*, 10275–10281.
- (23) Matsushima, T.; Hwang, S.; Terakawa, S.; Fujihara, T.; Sandanayaka, A. S. D.; Qin, C.; Adachi, C. *Appl. Phys. Express* **2017**, *10*, 024103.
- (24) Wei, Y.; Lauret, J. S.; Galmiche, L.; Audebert, P.; Deleporte, E. *Opt. Express* **2012**, *20*, 10399.
- (25) Chidambaram, P. R.; Bowen, C.; Chakravarthi, S.; Machala, C.; Wise, R. *IEEE Trans. Electron Devices* **2006**, *53*, 944–964.
- (26) Ishihara, T.; Hong, X.; Ding, J.; Nurmikko, A. *Surf. Sci.* **1992**, *267*, 323–326.
- (27) Kumagai, M.; Takagahara, T. *Phys. Rev. B* **1989**, *40*, 12359–12381.
- (28) Neutzner, S.; Thouin, F.; Cortecchia, D.; Petrozza, A.; Silva, C.; Srimath Kandada, A. R. *Phys. Rev. Mater.* **2018**, *2*, 064605.
- (29) Straus, D. B.; Hurtado Parra, S.; Iotov, N.; Gebhardt, J.; Rappe, A. M.; Subotnik, J. E.; Kikkawa, J. M.; Kagan, C. R. *J. Am. Chem. Soc.* **2016**, *138*, 13798–13801.
- (30) Permogorov, S. *Phys. status solidi* **1975**, *68*, 9–42.
- (31) Cortecchia, D.; Neutzner, S.; Srimath Kandada, A. R.; Mosconi, E.; Meggiolaro, D.; De Angelis, F.; Soci, C.; Petrozza, A. *J. Am. Chem. Soc.* **2017**, *139*, 39–42.
- (32) Iaru, C. M.; Geuchies, J. J.; Koenraad, P. M.; Vanmaekelbergh, D.; Silov, A. Y. *ACS Nano* **2017**, *11*, 11024–11030.
- (33) Thouin, F.; Chávez, D. A. V.; Quarti, C.; Cortecchia, D.; Bargigia, I.; Beljonne, D.; Petrozza, A.; Silva, C.; Kandada, A. R. S. *Arxiv* **2018**.
- (34) Becker, M. A. et al. *Nature* **2018**, *553*, 189–193.

- (35) Wright, A. D.; Verdi, C.; Milot, R. L.; Eperon, G. E.; Pérez-Osorio, M. A.; Snaith, H. J.; Giustino, F.; Johnston, M. B.; Herz, L. M. *Nat. Commun.* **2016**, *7*, 11755.
- (36) Gebhardt, J.; Kim, Y.; Rappe, A. M. *J. Phys. Chem. C* **2017**, *121*, 6569–6574.
- (37) Du, K.-Z.; Tu, Q.; Zhang, X.; Han, Q.; Liu, J.; Zauscher, S.; Mitzi, D. B. *Inorg. Chem.* **2017**, *56*, 9291–9302.
- (38) Ma, D.; Fu, Y.; Dang, L.; Zhai, J.; Guzei, I. A.; Jin, S. *Nano Res.* **2017**, *10*, 2117–2129.
- (39) Dammak, T.; Koubaa, M.; Boukheddaden, K.; Bougzhala, H.; Mlayah, A.; Abid, Y. *J. Phys. Chem. C* **2009**, *113*, 19305–19309.
- (40) Kikuchi, K.; Takeoka, Y.; Rikukawa, M.; Sanui, K. *Curr. Appl. Phys.* **2004**, *4*, 599–602.
- (41) Slavney, A. H.; Smaha, R. W.; Smith, I. C.; Jaffe, A.; Umeyama, D.; Karunadasa, H. I. *Inorg. Chem.* **2017**, *56*, 46–55.
- (42) Motta, C.; El-Mellouhi, F.; Kais, S.; Tabet, N.; Alharbi, F.; Sanvito, S. *Nat. Commun.* **2015**, *6*, 7026.
- (43) Munson, K. T.; Kennehan, E. R.; Doucette, G. S.; Asbury, J. B. *Chem* **2018**, 1–18.
- (44) Nishida, J.; Breen, J. P.; Lindquist, K. P.; Umeyama, D.; Karunadasa, H. I.; Fayer, M. D. *J. Am. Chem. Soc.* **2018**, *140*, 9882–9890.
- (45) Yaffe, O.; Guo, Y.; Tan, L. Z.; Egger, D. A.; Hull, T.; Stoumpos, C. C.; Zheng, F.; Heinz, T. F.; Kronik, L.; Kanatzidis, M. G.; Owen, J. S.; Rappe, A. M.; Pimenta, M. A.; Brus, L. E. *Phys. Rev. Lett.* **2017**, *118*, 136001.

- (46) Neukirch, A. J.; Nie, W.; Blancon, J.-C.; Appavoo, K.; Tsai, H.; Sfeir, M. Y.; Katan, C.; Pedesseau, L.; Even, J.; Crochet, J. J.; Gupta, G.; Mohite, A. D.; Tretiak, S. *Nano Lett.* **2016**, *16*, 3809–3816.
- (47) Ni, L.; Huynh, U.; Cheminal, A.; Thomas, T. H.; Shivanna, R.; Hinrichsen, T. F.; Ahmad, S.; Sadhanala, A.; Rao, A. *ACS Nano* **2017**, *11*, 10834–10843.
- (48) Soufiani, A. M.; Huang, F.; Reece, P.; Sheng, R.; Ho-Baillie, A.; Green, M. A. *Appl. Phys. Lett.* **2015**, *107*, 231902.
- (49) Zhu, H.; Miyata, K.; Fu, Y.; Wang, J.; Joshi, P. P.; Niesner, D.; Williams, K. W.; Jin, S.; Zhu, X.-Y. *Science* **2016**, *353*, 1409–1413.
- (50) Mitzi, D. B.; Feild, C. A.; Harrison, W. T. A.; Guloy, A. M. *Nature* **1994**, *369*, 467–469.
- (51) Mitzi, D. B. *Chem. Mater.* **1996**, *8*, 791–800.
- (52) Smith, I. C.; Hoke, E. T.; Solis-Ibarra, D.; McGehee, M. D.; Karunadasa, H. I. *Angew. Chemie - Int. Ed.* **2014**, *53*, 11232–11235.
- (53) Elbaz, G. A.; Straus, D. B.; Semonin, O. E.; Hull, T. D.; Paley, D. W.; Kim, P.; Owen, J. S.; Kagan, C. R.; Roy, X. *Nano Lett.* **2017**, *17*, 1727–1732.
- (54) Sheldrick, G. M. *Acta Crystallogr. Sect. A Found. Adv.* **2015**, *71*, 3–8.
- (55) Dolomanov, O. V.; Bourhis, L. J.; Gildea, R. J.; Howard, J. A. K.; Puschmann, H. *J. Appl. Crystallogr.* **2009**, *42*, 339–341.
- (56) Shao, Y. et al. *Mol. Phys.* **2015**, *113*, 184–215.
- (57) Becke, A. D. *J. Chem. Phys.* **1993**, *98*, 5648–5652.
- (58) Stephens, P. J.; Devlin, F. J.; Chabalowski, C. F.; Frisch, M. J. *J. Phys. Chem.* **1994**, *98*, 11623–11627.
- (59) Momma, K.; Izumi, F. *J. Appl. Crystallogr.* **2011**, *44*, 1272–1276.

- (60) Curtis, M. D.; Cao, J.; Kampf, J. W. *J. Am. Chem. Soc.* **2004**, *126*, 4318–4328.
- (61) Nabok, D.; Puschnig, P.; Ambrosch-Draxl, C.; Werzer, O.; Resel, R.; Smilgies, D.-M. *Phys. Rev. B* **2007**, *76*, 235322.
- (62) Hunter, C. A.; Sanders, J. K. *J. Am. Chem. Soc.* **1990**, *112*, 5525–5534.
- (63) Rosenthal, J.; Schuster, D. I. *J. Chem. Educ.* **2003**, *80*, 679.
- (64) Cavallo, G.; Metrangolo, P.; Milani, R.; Pilati, T.; Priimagi, A.; Resnati, G.; Terraneo, G. *Chem. Rev.* **2016**, *116*, 2478–2601.
- (65) Thouin, F.; Neutzner, S.; Cortecchia, D.; Dragomir, V. A.; Soci, C.; Salim, T.; Lam, Y. M.; Leonelli, R.; Petrozza, A.; Ram, A.; Kandada, S.; Silva, C.; Kandada, A. R. S.; Silva, C. *Phys. Rev. Mater.* **2018**, *2*, 034001.
- (66) Gauthron, K.; Lauret, J.-S.; Doyennette, L.; Lanty, G.; Al Choueiry, A.; Zhang, S. J.; Brehier, A.; Largeau, L.; Mauguin, O.; Bloch, J.; Deleporte, E. *Opt. Express* **2010**, *18*, 5912.
- (67) Nitzan, A., *Chemical Dynamics in Condensed Phases*; Oxford University Press: New York, 2006.
- (68) Song, K. S.; Williams, R. T., *Self-Trapped Excitons*; Moriya, T., Ed.; Springer Series in Solid-State Sciences, Vol. 105; Springer Berlin Heidelberg: Berlin, Heidelberg, 1993.
- (69) Gibbs, Z. M.; Kim, H.; Wang, H.; White, R. L.; Drymiotis, F.; Kaviany, M.; Jeffrey Snyder, G. *Appl. Phys. Lett.* **2013**, *103*, DOI: 10.1063/1.4858195.
- (70) Piccioli, N.; Besson, J.; Balkanski, M. *J. Phys. Chem. Solids* **1974**, *35*, 971–977.
- (71) Ravindra, N. M.; Auluck, S.; Srivastava, V. K. *Phys. Status Solidi* **1979**, *52*, K151–K155.

- (72) Dittrich, T.; Awino, C.; Prajongtat, P.; Rech, B.; Lux-Steiner, M. C. *J. Phys. Chem. C* **2015**, *119*, 23968–23972.
- (73) Chemla, D.; Miller, D.; Smith, P.; Gossard, A.; Wiegmann, W. *IEEE J. Quantum Electron.* **1984**, *20*, 265–275.
- (74) Rudin, S.; Reinecke, T. L.; Segall, B. *Phys. Rev. B* **1990**, *42*, 11218–11231.
- (75) Malikova, L.; Krystek, W.; Pollak, F. H.; Dai, N.; Cavus, A.; Tamargo, M. C. *Phys. Rev. B* **1996**, *54*, 1819–1824.
- (76) Chemla, D.; Miller, D.; Schmitt-Rink, S. In *Opt. Nonlinearities Instab. Semicond.* Haug, H., Ed.; Academic Press: San Diego, 1988, pp 83–120.
- (77) Elbaz, G. A.; Ong, W. L.; Doud, E. A.; Kim, P.; Paley, D. W.; Roy, X.; Malen, J. A. *Nano Lett.* **2017**, *17*, 5734–5739.
- (78) Guo, Z.; Wu, X.; Zhu, T.; Zhu, X.; Huang, L. *ACS Nano* **2016**, *10*, 9992–9998.
- (79) Even, J.; Pedesseau, L.; Katan, C. *J. Phys. Chem. C* **2014**, *118*, 11566–11572.
- (80) Poglitsch, A.; Weber, D. *J. Chem. Phys.* **1987**, *87*, 6373–6378.
- (81) Caretta, A.; Miranti, R.; Havenith, R. W. A.; Rampi, E.; Donker, M. C.; Blake, G. R.; Montagnese, M.; Polyakov, A. O.; Broer, R.; Palstra, T. T. M.; van Loosdrecht, P. H. M. *Phys. Rev. B* **2014**, *89*, 024301.
- (82) Quarti, C.; Grancini, G.; Mosconi, E.; Bruno, P.; Ball, J. M.; Lee, M. M.; Snaith, H. J.; Petrozza, A.; Angelis, F. D. *J. Phys. Chem. Lett.* **2014**, *5*, 279–284.
- (83) Tieke, B.; Chapuis, G. *J. Polym. Sci. Polym. Chem. Ed.* **1984**, *22*, 2895–2921.

Chapter 8

Controlling Exciton Dynamics, Fine Structure, and Hot Photoluminescence Through Cation Modification in 2D Hybrid Perovskites

8.1 Introduction

Conventional two-dimensional (2D) materials typically consist of epitaxially grown inorganic layers.¹ In a Type I band alignment, electrons and holes are funneled into a single material layer, with the surrounding environment providing quantum and dielectric confinement effects. Interfacial roughness between layers can scatter carriers, but otherwise the surrounding environment does not directly interact with carriers other than providing quantum and dielectric confinement effects.¹

An emerging class of 2D materials are 2D organic-inorganic hybrid perovskites.²⁻⁴ 2D perovskites are solution-processable semiconductors that spontaneously crystallize

out of solution. They consist of sheets of corner-sharing metal-halide octahedra separated by organoammonium cations, and their stoichiometric nature allows them to be considered “perfect” quantum well superlattices that are free from interfacial roughness and defects typical of epitaxially-grown 2D materials.⁴ The properties of 2D perovskites are widely tunable: the choice of metal, halide, and cation affect the optical and electronic properties. For lead halide 2D perovskites, the band gaps are tunable between 2 and 4 eV with both Type I and Type II band alignments possible.⁴ The lead iodide-based 2D perovskites discussed herein are all Type I heterojunctions in which carriers are confined to the lead iodide framework, and the band gaps are around 2 eV.

Kasha’s rule states that in most molecules and materials, carriers relax to the lowest-lying excited state before fluorescing.⁵ In our previous work, we found that in the 2D perovskite phenethylammonium lead iodide ((PEA)₂PbI₄; PEA = C₆H₅C₂H₄NH₃⁺), 99.5% of the excitonic photoluminescence (PL) is emitted out of the lowest-lying excited state at 15 K. However, 0.5% of the PL is emitted out of discrete higher energy resonances, separated by ~40 meV from the lowest-lying resonance and from one another.⁶ These discrete resonances also appear in the absorption spectrum. Using time-resolved PL measurements, we previously demonstrated that PL from these higher energy resonances competes with relaxation to the lowest-lying excited state, and the kinetics combined with the regular spacing of these resonances led us to hypothesize that we observed a phonon progression. Importantly, theoretical calculations demonstrated that phonons with energy near 40 meV are located exclusively on the organic cation. Therefore, unlike conventional 2D materials, the surrounding environment directly interacts with the confined charge carriers, though our hypothesis that electron-phonon coupling causes the fine structure resonances has been contested by the Silva group.^{7,8} Subsequently, electron-phonon coupling to phonons on the organic

and inorganic frameworks was optically observed in other 2D hybrid perovskites^{9–11} and exciton-phonon coupling was optically visualized in 3D perovskite nanocrystals.¹²

Here, we demonstrate in addition to tuning the energetic disorder (Chapter 7), that the dynamics of the exciton can be modified by tuning the organic cation, even though the band edges are formed by Pb and I orbitals.¹³ We modify the cation by introducing a halogen atom in the 2-position of the phenyl group (*ortho* to ethylammonium) in the PEA cation, forming the perovskites 2-fluorophenethylammonium lead iodide (2-F), 2-chlorophenethylammonium lead iodide (2-Cl), and 2-bromophenethylammonium lead iodide (2-Br). Unlike what we observed in 4-substituted phenethylammonium lead iodide perovskites in Chapter 7, 2-substitution more substantially changes the phonon modes that couple to the exciton. 2-substitution enhances the violation of Kasha’s rule by increasing hot exciton PL by an order of magnitude compared to (PEA)₂PbI₄ (referred to as 2-H herein). Our findings have profound effects in the design and application of 2D perovskites because the cation can be used to tune the properties and dynamics of the confined charge carriers without the need to directly alter the inorganic framework.

8.2 Methods

2-H, 2-F, 2-Cl, and 2-Br are synthesized following the method used to synthesize 2-H in Section 7.2. All syntheses directly yielded crystals suitable for single crystal X-ray diffraction.

Single-crystal X-ray diffraction data are collected on a Bruker APEX II CCD area detector using graphite-monochromated Mo-K α radiation ($\lambda=0.71073\text{\AA}$) at 100 K.

Thin films are fabricated by dissolving crystals of the perovskites in anhydrous acetonitrile (Sigma-Aldrich) at a concentration of 15 mg/mL and spin-cast on sapphire

at 2500 rpm for 20 s in a nitrogen-filled glove box. The films are subsequently annealed at 80 °C for 10 min in a nitrogen-filled glove box. Powder diffraction patterns are taken on thin films using a Rigaku SmartLab X-ray diffractometer using Cu- $k\alpha$ radiation operating at 40 kV and 30 mA in $\theta - 2\theta$ geometry.

Absorption and photoluminescence measurements are taken on thin films of the perovskites in an evacuated Advanced Research Systems DE202 cryostat. Absorption spectra are collected in an Agilent Cary 5000 spectrometer. Steady state photoluminescence (PL) and nanosecond time-resolved photoluminescence (TRPL) spectra are collected in an Edinburgh Instruments FLS1000 fluorescence spectrometer using a Hamamatsu R13456 photomultiplier tube detector. Steady state spectra are excited using a monochromated Xe arc lamp, and nanosecond TRPL spectra are excited using a 378 nm Picoquant diode laser. Picosecond TRPL measurements are taken using an optical Kerr-gate setup described previously.⁶

8.3 Results and Discussion

8.3.1 Structural Characterization

2-H has been previously characterized by us and others.^{11,14,15}

2-F crystallizes in the monoclinic space group C2/m (systematic absences hkl : $h+k = \text{odd}$) with $a = 32.8889(14)$ Å, $b = 6.1790(3)$ Å, $c = 6.0988(3)$ Å, $\beta = 89.989(2)^\circ$, $V = 1239.40(10)$ Å³, $Z = 2$, and $d_{\text{calc}} = 2.667$ g/cm³ at 100 K. The interlayer spacing is 16.445 Å compared to 16.084 Å in 2-H. The equatorial iodine atoms exhibit 50/50 disorder and the organic cations exhibit four-fold disordered carbon atoms. The disorder may be indicative of an unresolved superstructure.¹⁶ The Pb-I-Pb bond angles are asymmetric with angles of $151.48(5)^\circ$ and $148.73(6)^\circ$. The smaller bond angle is

indicative of greater strain¹⁷ in the inorganic framework than in 2-H (with an average Pb-I-Pb bond angle of 152.198(15)°).

2-Cl crystallizes in the monoclinic space group C2/m (systematic absences hkl : $h+k = \text{odd}$) with $a = 33.2779(18)$ Å, $b = 6.1691(3)$ Å, $c = 6.1839(3)$ Å, $\beta = 90.255(3)^\circ$, $V = 1269.51(11)$ Å³, $Z = 2$, and $d_{\text{calc}} = 2.689$ g/cm³ at 100 K. The spacing between inorganic layers is 16.639 Å, and is larger than in 2-F, consistent with Cl having a larger atomic radius than F. Like 2-F, 2-Cl shows disorder with a herringbone structure likely given the similarity to 2-H;¹¹ the carbon atoms in the cation only show two-fold disorder compared to the four-fold disorder in 2-F. Projections of the crystal structure along the b and c axes are shown in Figure 1B. The Pb-I-Pb bond angles are 151.23(6)° and 151.21(6)°, indicating that 2-Cl is slightly more strained than 2-H; the Pb-I-Pb bond angles are more symmetric than in 2-F.

2-Br crystallizes in the monoclinic space group P2₁ (systematic absences $0k0$: $k = \text{odd}$) with $a = 8.8961(4)$ Å, $b = 8.1587(3)$ Å, $c = 17.9890(7)$ Å, $\beta = 94.847(2)^\circ$, $V = 1300.98(9)$ Å³, $Z = 2$, and $d_{\text{calc}} = 2.851$ g/cm³. The separation between inorganic layers is 17.925 Å, and the Pb-I-Pb bond angles are 139.92(3)° and 149.17(4)°, indicating significantly increased strain compared to 2-H, 2-F, and 2-Cl, consistent with Br's large size increasing the cross-sectional area of the cation.¹⁷ A further demonstration of the strain induced is that the equatorial and axial I-Pb-I bond angles are 174.09(3)° and 178.74(4)°, compared to the ideal 180° in 2-H, 2-F, and 2-Cl. Unlike the other compounds, 2-Br also exhibits a corrugated PbI₄²⁻ framework with out-of-plane distortions because the inorganic framework needs to buckle to accommodate the cation.

Figure 8.1 shows overlaid Pb-I frameworks of 2-H (red), 2-F (orange), 2-Cl (green), and 2-Br (blue), demonstrating that 2-H, 2-F, and 2-Cl have similar planar Pb-I frameworks while 2-Br exhibits out-of-plane buckling.

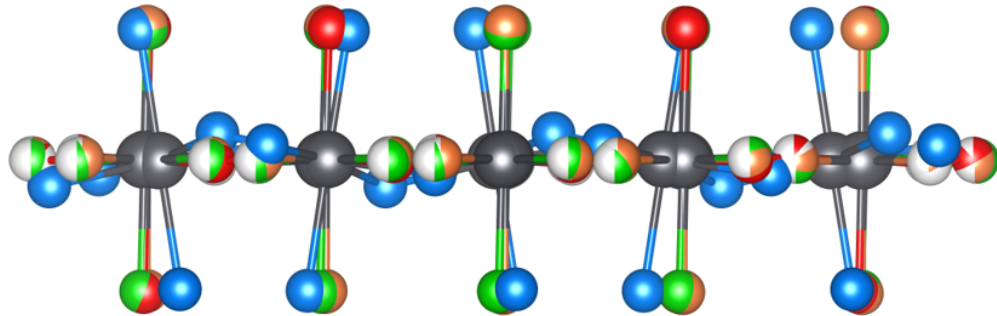


Figure 8.1: Overlaid Pb-I frameworks of 2-H (red), 2-F (orange), 2-Cl (green), and 2-Br (blue).

We perform our optical studies on thin films of 2-H, 2-F, 2-Cl, and 2-Br spin-cast out of acetonitrile. Room temperature powder diffraction patterns of thin-films of 2-H, 2-F, 2-Cl, and 2-Br on sapphire substrates (Figure 8.2) all exhibit regularly spaced reflections indicative of the layered structure, and the trend in interlayer spacing matches what is found from 100 K crystal structures.

8.3.2 Optical Characterization

Figure 8.3A shows room temperature excitonic absorption (solid) and PL (dashed) spectra for 2-H (red), 2-F (orange), 2-Cl (green), and 2-Br (blue). The spectra show a blue shift with increasing strain resulting from cations with large cross-sectional area. A similar blue shift is observed in Sn-based 2D hybrid perovskites with similar cations.¹⁷ The same spectra are plotted in Figure 8.3B with the absorption spectra overlaid. Like in our previous work on 4-substituted phenethylammonium lead iodides,¹¹ we find that increasing the interlayer spacing results in a disordered energy landscape, which can be seen by the greater width of the excitonic absorption of 2-F, 2-Cl, and 2-Br compared to 2-H. The increasing strain induced by larger cations does

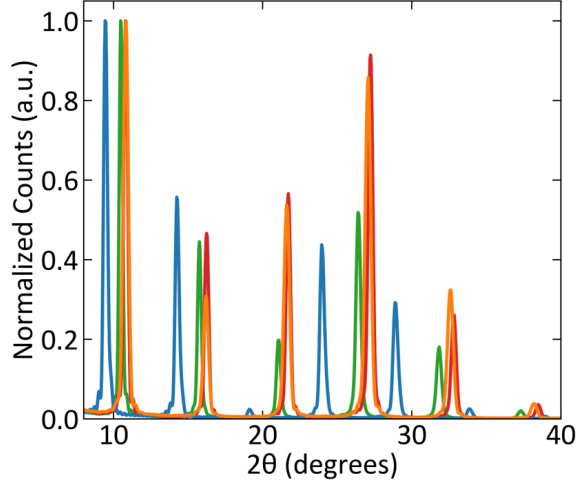


Figure 8.2: Room-temperature powder diffraction patterns of 2-H (red), 2-F (orange), 2-Cl (green), and 2-Br (blue) thin films deposited on sapphire.

not change this trend. Similarly, the Stokes shift also correlates with interlayer spacing. The widths of the PL spectra are more similar than those of the absorption spectra, indicating that excitons find energetic minima and may form polarons^{6,7,10,18–22} before recombining. The switch from 4-substitution to 2-substitution does not change these dynamics at room temperature.

As the temperature is decreased from 300 K to 10 K, the excitonic absorption and PL resonances for 2-F, 2-Cl and 2-Br linearly red-shift (Figure 8.4), indicative of negative coefficients of thermal expansion (α).^{6,23,24} We fit the excitonic absorption maxima to $E_g(T) = E_g(0) - \alpha T$. We previously observed this linear trend in 2-H and in 2-H derivatives with halogen or methyl substitutions in the 4-position of the PEA cation (Figure 7.15). A negative coefficient of thermal expansion and linear red shift with decreasing temperature have been observed in lead chalcogenides.^{25–27} 3D lead iodide hybrid perovskites also exhibit a negative coefficient of thermal expansion.^{28,29} Like in Figure 7.15, the excitonic absorption resonance can be used as a proxy to determine changes in the band edge. For 2-F, $\alpha = -0.080(2)$ meV/K, and similarly for 2-Cl, $\alpha = -0.076(2)$ meV/K. 2-Br shows smaller changes in the absorption maxima

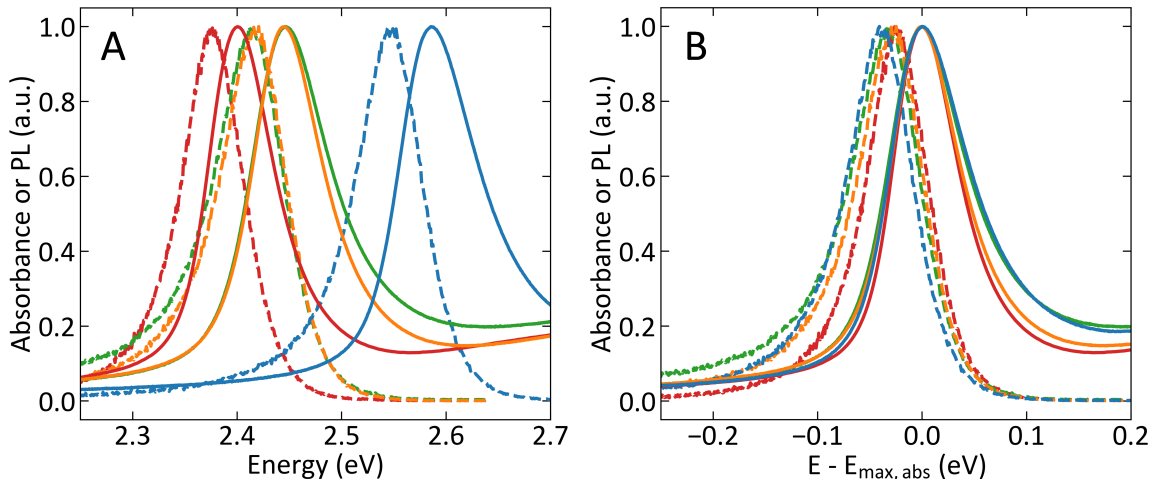


Figure 8.3: (A) Room-temperature absorption (solid) and PL (dashed) spectra of 2-H (red), 2-F (orange), 2-Cl (green), and 2-Br (blue). (B) Spectra with $E_{\max, \text{abs}}$ subtracted from absorption and PL energy.

with temperature, and $\alpha = -0.032(3)$ meV/K. α is much less negative than what we observed for 2-H and 2-H derivatives with halogen or methyl substitutions in the 4-position where α ranged from -0.14 to -0.16 meV/K. 4-substituted phenethylammonium lead iodides have similar degrees of inorganic lattice strain whereas 2-F, 2-Cl, and 2-Br exhibit increasing degrees of strain, indicating that a more strained inorganic framework results in a less negative α .

Figure 8.5A shows 10K absorption spectra for 2-H (red), 2-F (orange), 2-Cl (green), and 2-Br (blue). Differences in the fine structure are immediately evident, with the spacing between resonances much greater in 2-H than in 2-F and 2-Cl, and with no obvious fine structure present in 2-Br. For the fits in Figure 8.5, the zero in energy is fixed to the energy of the lowest energy discrete absorption resonance in each compound.

As we demonstrated in our prior work,⁶ the excitonic absorption spectrum of 2-H at 10 K (Figure 8.5B) shows three obvious features at 2.352, 2.395, and 2.435 eV, consistent with coupling to a 40-43 meV phonon that is located exclusively on the

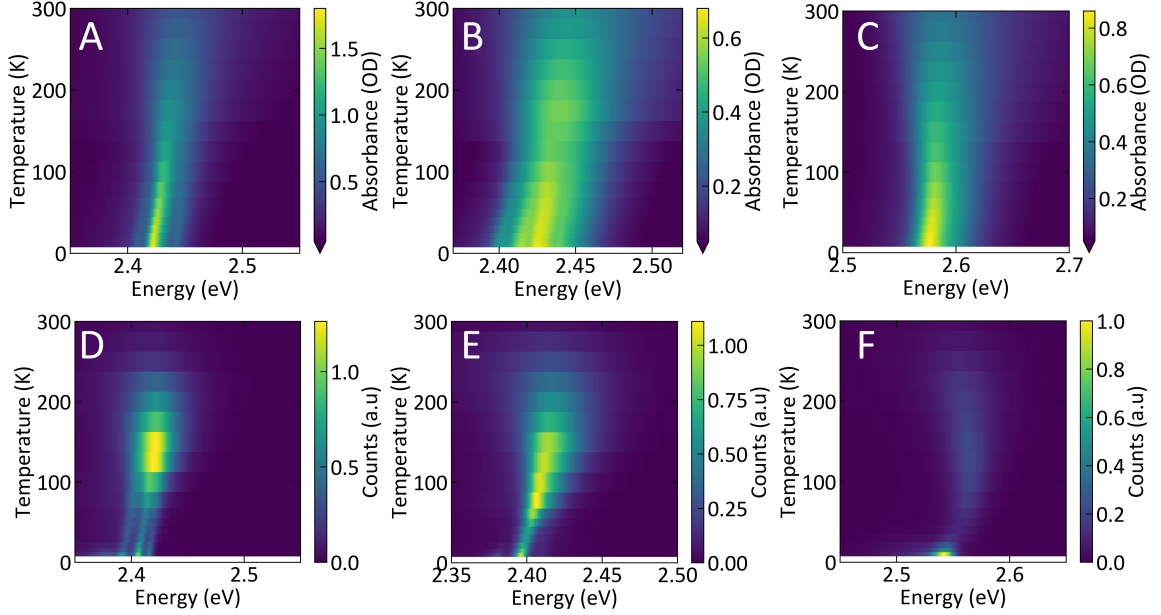


Figure 8.4: Temperature-dependent absorption spectra of 2-F (A), 2-Cl (B), and 2-Br (C). Temperature-dependent PL spectra of 2-F (D), 2-Cl (E), and 2-Br (F).

organic cation, in addition to a shoulder at 2.363 eV that we hypothesized originates from exciton coupling to a phonon of mixed organic and inorganic character. The 10 K excitonic absorption spectrum of 2-F shows five peaks or shoulders. A proposed fit is shown in Figure 8.5C, with the resonances separated by 6-16 meV from one another. 2-Cl shows four discrete peaks and three shoulders with a proposed fit in Figure 8.5D. The red, orange, green, and cyan resonances are separated by 12-13 meV and we hypothesize that these form a phonon progression. The absorption resonance centers are all within 50 meV in 2-F and 70 meV in 2-Cl of one another, precluding the existence of a central transition with two 40+ meV sidebands like in 2-H. The 10K absorption spectrum of 2-Br (Figure 8.5E) does not exhibit discrete fine structure resonances, and we fit the 10 K excitonic absorption spectrum to the sum of two Lorentzians, which are separated by 21 meV. Like we previously found in 2-H,⁶ the excitonic absorption spectra of 2-F, 2-Cl, and 2-Br fit to the sum of Lorentzian functions, indicative of homogeneous (*i.e.*, lifetime) broadening.³⁰

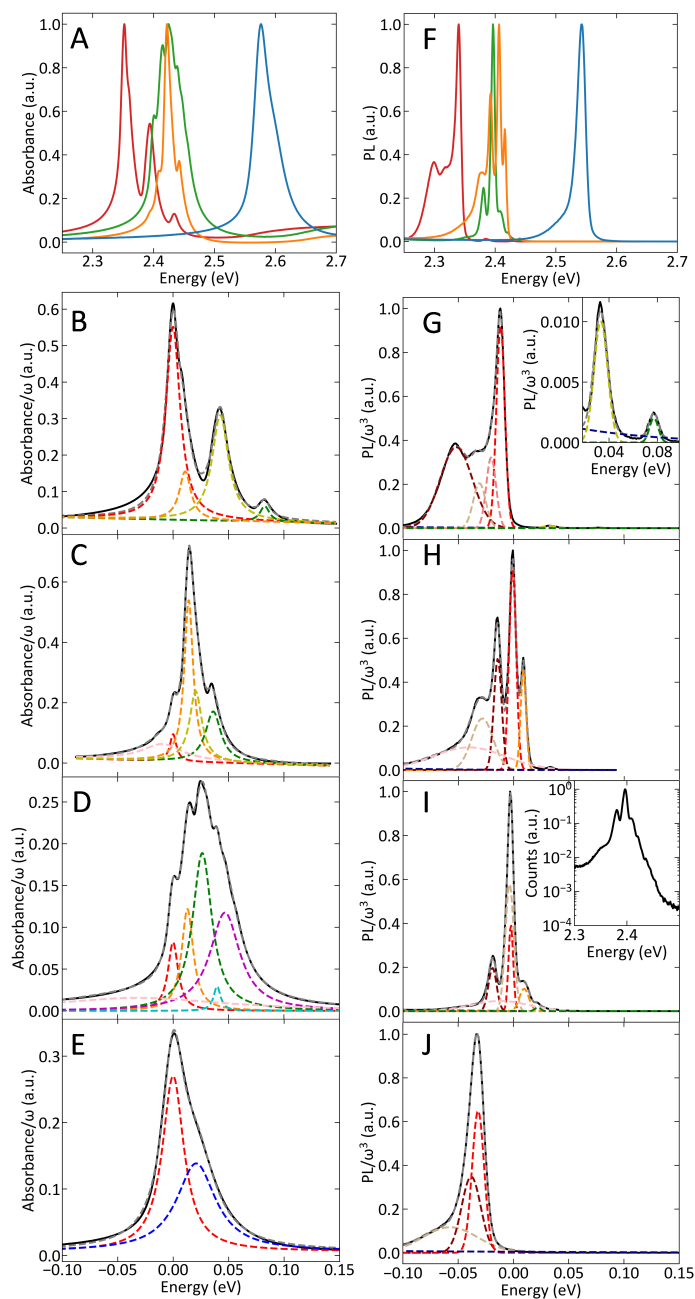


Figure 8.5: (A) 10 K absorption spectra of 2-H (red), 2-F (orange), 2-Cl (green), and 2-Br (blue), with fits of 2-H (B), 2-F (C), 2-Cl (D), and 2-Br (E). 10 K PL spectra (F), with fits of 2-H (G), 2-F (H), 2-Cl (I), and 2-Br (J). The zero of energy in each compound's absorption and PL fit is set as the center of the red resonance in absorption.

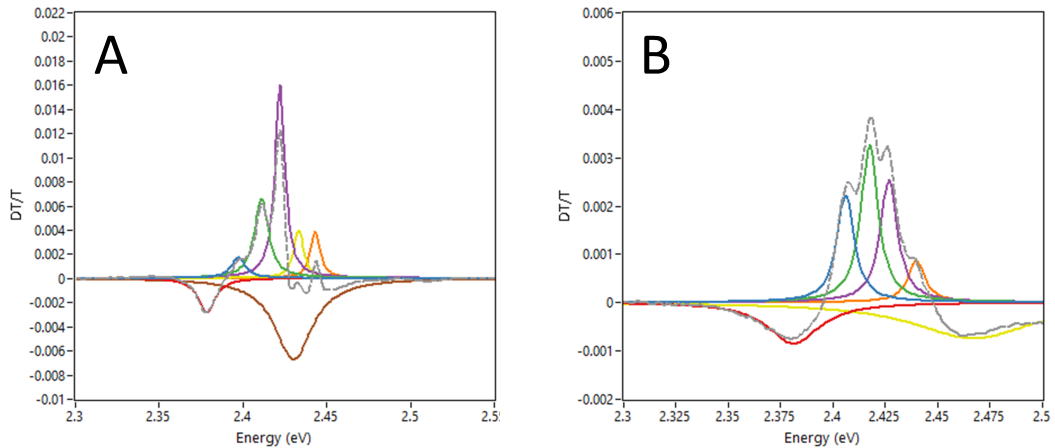


Figure 8.6: Transient absorption spectra ($\Delta t = 5$ ps) of (A) 2-Cl at 16 K and (B) 2-F at 15 K.

To better deduce the fine structure in 2-F and 2-Cl, we use transient absorption spectroscopy (Figure 8.6).³¹ Preliminary results show that in 2-F, there are five excitonic bleaches separated by 10-14 meV. In 2-Cl, we find four excitonic bleaches separated by 10-12 meV, similar to what we find in Figure 8.5D. The regular spacing supports that these resonances form a phonon progression.⁶

We also fit the 10 K PL spectra (Figure 8.5F). Figure 8.5G shows the 10 K excitonic PL spectrum for 2-H. In 2-H, we previously observed hot exciton PL at energies greater than the lowest energy excitonic absorption at the same energy as the higher energy sidebands in the absorption spectrum. The hot exciton PL results from competition between vibrational relaxation and radiative recombination,⁶ and at 10 K, 0.5% of the excitonic photoluminescence is emitted from hot resonances. In 2-F, we observe two hot exciton PL resonances (Figure 8.5H, orange and and unfit small resonance). The orange resonance is separated from the red resonance by 10 meV and from the unfit resonance by 25 meV; the unfit hot resonance and red resonances are separated from each other by 34 meV. Despite the different spacing, photoluminescence excitation

(PLE) spectra indicate that the excitonic resonances have a similar origin (Figure 8.7). The orange resonance accounts for 11% of the excitonic PL, and the 10 meV separation is consistent with the steady-state and transient absorption spectra. In 2-Cl, we also observe hot exciton PL (Figure 8.5I, green and orange), with resonances separated by 12-14 meV, which is consistent with the energetic spacing found in the absorption and transient absorption spectra. In 2-Cl, the hot exciton PL is 8% of the excitonic PL. We are therefore able to control the dynamics of relaxation to the lowest-lying vibrational state solely by introducing an F or Cl atom in the 2-position on the PEA cation, demonstrating that the cation greatly affects exciton dynamics and increases the amount of hot exciton PL by over an order of magnitude. In 2-Br (Figure 8.5J), we do not see fine structure, which may be related to the corrugated inorganic framework or to the heavy Br atom reducing the energy of the responsible vibrational mode such that the fine structure resonances are too close in energy to be observed discretely in optical spectra.

To investigate the dynamics of hot carrier PL, we use ultrafast time-resolved PL (TRPL) measurements.^{6,33} The TRPL spectrum of 2-Cl is shown in Figure 8.8A. Each slice of the TRPL spectrum is fit to the sum of Gaussian functions (the 0.19 ps spectrum is shown in Figure 8.8B), with the resonance centers shown in Figure 8.8C. At early times, we find a phonon progression consisting of four resonances (Figure 8.8B), three of which are above the energy of the central resonance at energies consistent with the peaks or shoulders observed in the steady-state PL spectrum (Figure 8.5I, inset). Because of the close spacing of the resonance, we set the FWHM of the sharp resonances (red, orange, green, cyan) to be equal, but let this shared FWHM and individual center locations vary freely. The lifetime of each resonance is determined by fitting the areas of each resonance versus time (Figure 8.8D). The highest energy (cyan) resonance is fit to the convolution of an exponential decay with

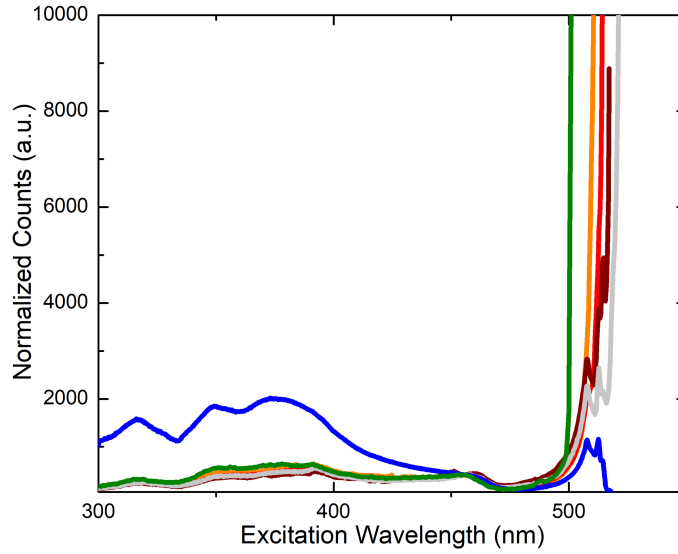


Figure 8.7: 10 K PLE spectra of 2-F. The color of each spectrum represents the PL energy according to the resonances in Figure 8.5H. The blue spectrum is the PLE spectrum from the broad self-trapped excitonic PL resonance³² and is collected at 2.0 eV.

the instrument response function (IRF). To account for vibrational selection rules, the green resonance is fit to an exponential decay convolved with both the IRF and the exponential decay used to fit the cyan resonance, with a similar procedure used to fit the orange and green resonances. These resonances are separated from one another and from the central PL resonance by 10-12 meV. The highest energy resonance (cyan) disappears first and has a lifetime of 0.78(5) ps, the next highest energy sideband (green) has a lifetime of 0.82(4) ps, the third sideband (orange) has a lifetime of 3.06(7) ps, and the central resonance (red) exhibits a biexponential lifetime of 3.6(2) ps and 17.0(6) ps. Importantly, the higher energy resonances decay while the lower energy resonances continue to rise, further supporting the competition between vibrational relaxation and radiative recombination because PL is occurring before the carriers cool to the lowest lying excited state,⁶ and our kinetic model incorporates these dynamics.

The resonances all red-shift in energy over time, consistent with the Burstein-Moss effect in which there is apparent blue-shift at early times because of state-filling.³⁴ The lifetimes of the cyan and green resonances are similar to what we previously measured for the hot resonances in 2-H, and the lifetime of the orange resonance is 3x longer than the lifetime for the hot resonances in 2-H. In addition, the lifetime for the central red resonance is significantly reduced from 13 ps in 2-H, indicating that the cause of increased hot exciton PL is that faster radiative recombination results in more hot PL before carriers relax to the lowest vibrational level. There is another resonance (tan) that decreases in energy by nearly 30 meV in energy over 200 ps, and this resonance likely accounts for emission out of other states separate from the phonon progression observed, such as the pink and dark red resonances in Figure 8.5I. Interestingly, the discrete dark red resonance in Figure 8.5I is missing in TRPL. The reason for the absence of this resonance is unclear.

The TRPL spectrum of 2-Br (Figure 8.9A) shows signatures of hot exciton photoluminescence despite the absence of discrete resonances in the steady-state PL spectrum. Like the TRPL spectrum in 2-Cl, we fit each time step to the sum of 1-3 Gaussian functions. There is a hot shoulder on the central Gaussian resonance (cyan, Figure 8.9B-C), which merges with the central (green) resonance within 4 ps (Figure 8.9B). Even after 4 ps when the hot shoulder disappears, the PL still cools over the next 5 ps which can be seen by the center of the Gaussian resonance moving nearly 20 meV (Figure 8.9C). Therefore, even though the fine structure is washed out with the introduction of Br onto the cation, hot carrier PL still is prevalent, demonstrating the competition between vibrational relaxation and radiative emission. The 20 meV cooling of the central resonance may be indicative of polaron formation.³⁵

We fit the temperature-dependent absorption FWHM to the model in Equation 7.1 that was developed to fit the excitonic absorption FWHM in 2D transition-metal

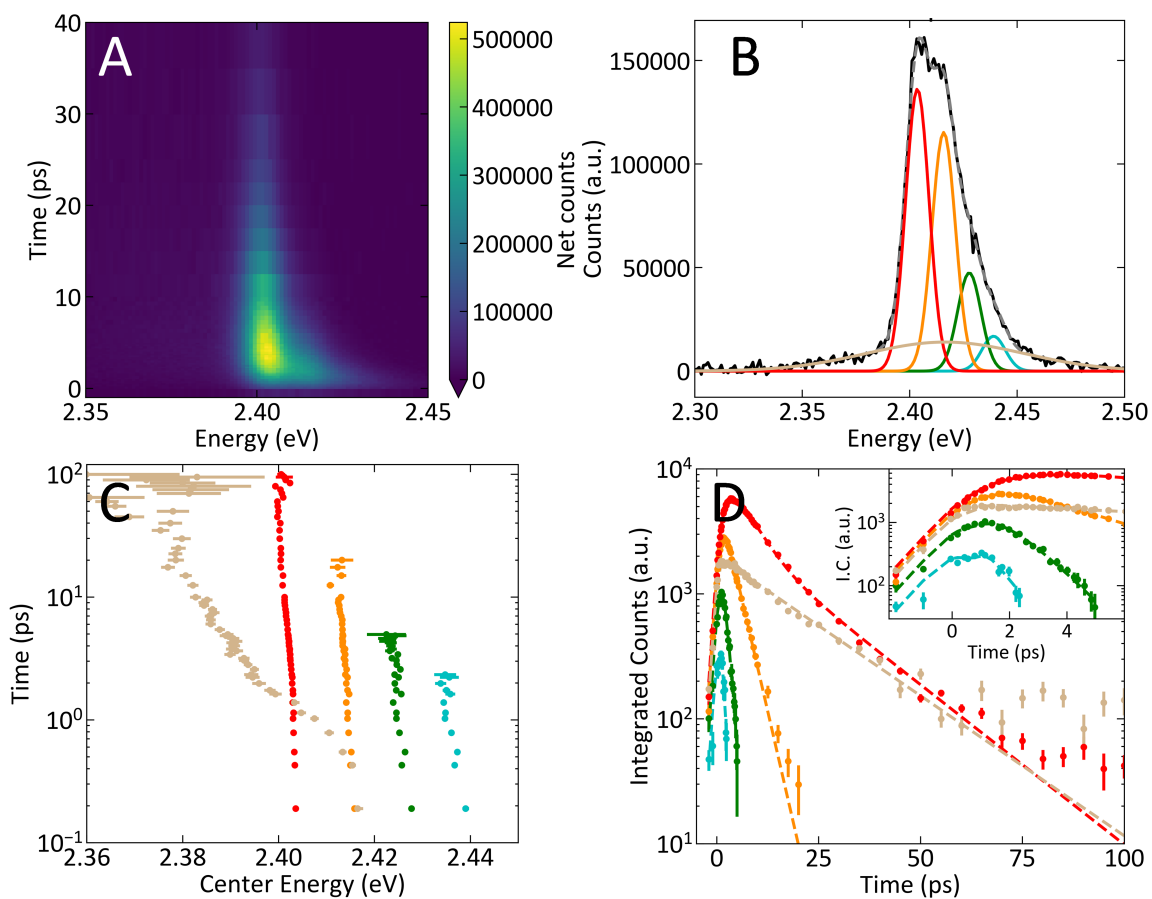


Figure 8.8: (A) 10K TRPL spectrum of 2-Cl. (B) Fit at $t = 0.19$ ps. (C) Centers of resonances over time. (D) Lifetime fits.

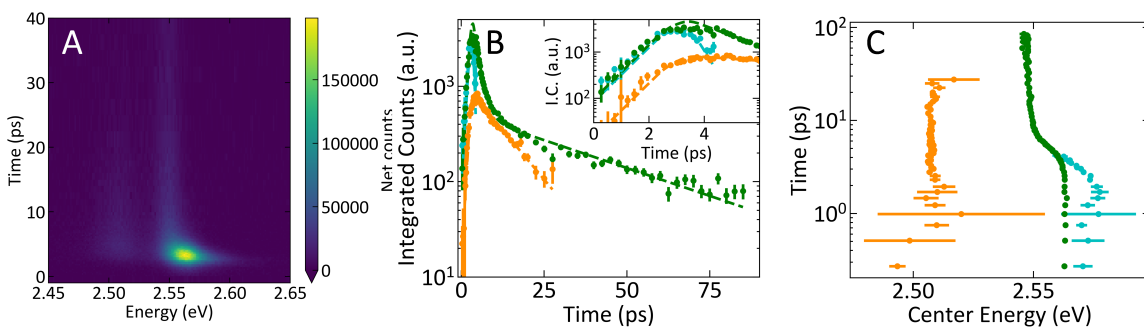


Figure 8.9: (A) 10K TRPL spectrum of 2-Br, with (B) lifetime fits and (C) centers.

dichalcogenides^{36,37} and more recently been applied to 3D²⁹ and 2D perovskites.^{7,38} Like in Chapter 7, contributions from the acoustic and impurity terms are small and do not match the data, so we fix $\gamma_{ac} = \gamma_{imp} = 0$. The FWHM fit results are summarized in Table 8.1. 2-F exhibits broadening to a 16(2) meV phonon, which is similar to the fine structure splitting seen in Figures 3B and F, with a coupling constant $\gamma_{LO} = 60(10)$ meV, and a small $\Gamma_0 = 16.2(7)$ meV. In contrast. 2-Cl is strongly broadened by a 59(3) meV phonon, with a large $\gamma_{LO} = 370(60)$ meV. Unlike 2-F and 2-Cl, 2-Br requires two LO phonons to be included in the model. Although 2-Br does not exhibit discrete fine structure at low temperatures, it is weakly broadened by a 7(2) meV phonon with a small $\gamma_{LO} = 12(4)$ meV. Although 2-Br does not exhibit discrete fine structure resonances, it still interacts with a phonon at low temperatures.

	2-F	2-Cl	2-Br	
E_{LO} (meV)	16(2)	59(3)	7(2)	54(8)
γ_{LO} (meV)	60(10)	370(60)	12(4)	150(40)
Γ_0 (meV)	16.2(7)	54.8(4)	39.7(3)	

Table 8.1: Results from fitting temperature-dependent FWHM of 2-F, 2-Cl, and 2-Br to the model in Equation 7.1.

The decrease in energy of the phonon modes that couple to the exciton at low temperature in 2-F, 2-Cl, and 2-Br can be rationalized using the harmonic oscillator model. In the simplest case of a diatomic molecule, the energy of a stretching vibration $E_{vib} \propto \sqrt{\frac{k}{m^*}}$, where k is the bond's force constant and m^* is the reduced vibrational mass ($m_1 m_2 / (m_1 + m_2)$). Under this model, introducing a heavy Cl or Br atom on the cation should reduce the energy of stretching modes of the organic cation because of the increased mass. Similarly, the energy of a torsional mode of a more complicated molecule $E_{vib} \propto \sqrt{\frac{k'}{I}}$, where k' is the torsional force constant and $I = \sum_i m_i r_i^2$ is the moment of inertia about an axis, where m_i is the atom's mass and r_i is the

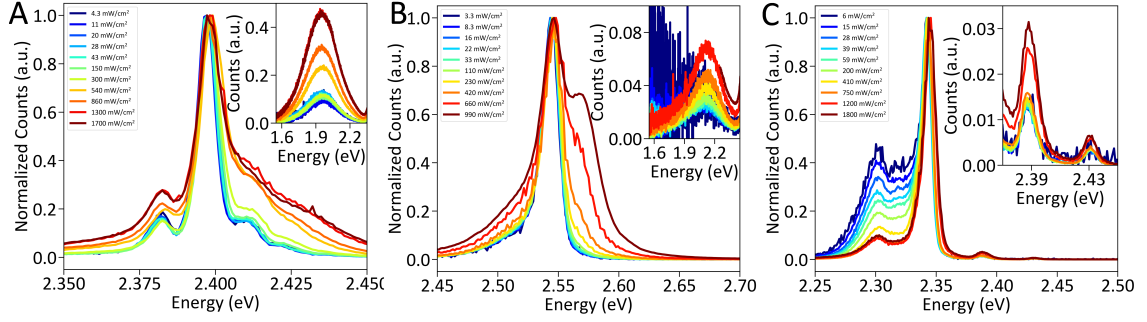


Figure 8.10: Power-dependent 10K PL spectra of 2-Cl(A), 2-Br (B), and 2-H (C).

atom's distance to the rotational axis. Introducing F, Cl or Br in the 2 position will increase the cation's moment of inertia I , decreasing the energy of the phonon mode. We therefore hypothesize that a torsional mode of the phenyl moiety couples to the exciton because the fine structure splitting decreases in energy with heavier 2-position substituents. This hypothesis is consistent with our previous findings in Chapter 7 that introducing F, Cl, Me, or Br substituents in the 4-position did not greatly change the ~ 40 meV energy of the phonon that couples to the exciton compared to 2-H because in a torsional mode, $r \approx 0$ for 4-position substitutions.¹¹

Lastly, we find that the power dependence of hot exciton PL is superlinear in 2-Cl. Using 378 nm excitation, we find that at powers ≥ 300 mW/cm² (5.7×10^{17} photons/cm²/s), the proportion of hot exciton PL increases, as does the proportion of PL from the lower energy self-trapped exciton resonance centered around 2 eV (inset, Figure 8.10A). We hypothesize two possible explanations. First, the high photon density heats the perovskite, increasing kT and causing phonon reabsorption, which is consistent with the small blue shift of the central PL resonance. This shift could also be a manifestation of the Burstein-Moss effect, as discussed earlier. Another possible explanation is that a hot phonon bottleneck occurs at high carrier density in which a large phonon emission rate in the presence of high carrier density causes phonon reabsorption and a resulting decrease in the rate of relaxation to the lowest vibrational

level.³¹ A similar phonon bottleneck is seen in the 3D perovskite methylammonium lead iodide at high photoexcitation density using transient absorption spectroscopy.³¹ We find similar hot exciton amplification in 2-Br and to a lesser extent in 2-H (Figure 8.10B-C).

8.3.3 Exploring Other Causes for Hot Exciton PL

In nanocrystals of the 3D perovskite CsPbX_3 ($\text{X}=\text{Cl}, \text{Br}, \text{I}$), it has been hypothesized that the bright exciton is not a singlet exciton, but instead a triplet exciton. Becker et al. found photoluminescence from three states separated by ~ 3 meV from one another in these nanocrystals, with PL lifetimes < 1 ns at 5 K.³⁹ We do not think this explanation is likely in the case of the 2D perovskites measured herein for several reasons. First, the crystal structures of 2-Cl and unsubstituted 2-H do not greatly differ in respect to the bond lengths and angles of the Pb-I framework, so we cannot rationalize why this substitution would reduce the splitting of a hypothetical triplet exciton from ~ 40 meV to ~ 14 meV. Second, our absorption and TRPL spectra of 2-Cl exhibit four regularly-spaced PL resonances, three of which are higher in energy than the lowest energy absorption resonance, when a triplet exciton should only show three regularly spaced resonances. Third, in both 2-H and 2-Cl, the higher energy PL resonances decay while the lower energy resonances continue to rise, supporting our hypothesis that excitons are relaxing from higher energy vibrational states to lower energy states; we expect a triplet exciton to have similar lifetimes and rise times for all energy levels because of conservation of angular momentum restricting interconversion between triplet levels, which may be why there is a strong orientational dependence to the number of PL resonances observed in CsPbX_3 nanocrystals. Our experimental evidence rules out triplet excitons explaining our findings here, and our

findings combined with our theoretical results suggest that exciton-phonon coupling and competition between carrier cooling and radiative recombination is the most likely explanation for our optical spectra. It is possible that the PL resonances in 2-F come from different origins or result from the unequal Pb-I-Pb bond angles, given the much more irregular spacing. Further studies are ongoing to decipher this mystery.

8.4 Conclusion

We demonstrate that the phonon modes that couple to optical transitions can be tuned through single atom substitutions on the PEA cation. Importantly, we confirm that phonon modes on the cation result in fine structure in 2D hybrid perovskites. By increasing the off-axis mass on the PEA cation, we reduce the energy of the phonon that couples to the exciton, which combined with our findings in Chapter 7 indicate that a torsional mode of the cation is responsible for causing the fine structure. In 2-Cl, PL occurs faster than in 2-H, which results in PL outcompeting vibrational relaxation, allowing us to increase the proportion of hot exciton PL by an over order of magnitude from 0.5% to 8%. Lastly, hot carrier amplification provides a further route to tune PL spectra in 2D hybrid perovskites and may allow for devices that use advanced energy transfer pathways to be created. The ability to narrow the PL width in 2-F and 2-Cl compared to 2-H is promising for narrowband LEDs, and increasing the degree of electron-phonon coupling may improve perovskite-based polariton lasers.⁴⁰

8.5 References

- (1) Papavassiliou, G. *Prog. Solid State Chem.* **1997**, *25*, 125–270.
- (2) Mitzi, D. B. *Prog. Inorg. Chem.* **1999**, *48*, 1–121.

- (3) Saparov, B.; Mitzi, D. B. *Chem. Rev.* **2016**, *116*, 4558–4596.
- (4) Straus, D. B.; Kagan, C. R. *J. Phys. Chem. Lett.* **2018**, *9*, 1434–1447.
- (5) Demchenko, A. P.; Tomin, V. I.; Chou, P.-T. *Chem. Rev.* **2017**, *117*, 13353–13381.
- (6) Straus, D. B.; Hurtado Parra, S.; Iotov, N.; Gebhardt, J.; Rappe, A. M.; Subotnik, J. E.; Kikkawa, J. M.; Kagan, C. R. *J. Am. Chem. Soc.* **2016**, *138*, 13798–13801.
- (7) Neutzner, S.; Thouin, F.; Cortecchia, D.; Petrozza, A.; Silva, C.; Srimath Kandada, A. R. *Phys. Rev. Mater.* **2018**, *2*, 064605.
- (8) Thouin, F.; Chávez, D. A. V.; Quarti, C.; Cortecchia, D.; Bargigia, I.; Beljonne, D.; Petrozza, A.; Silva, C.; Kandada, A. R. S. *Arxiv* **2018**.
- (9) Cortecchia, D.; Neutzner, S.; Srimath Kandada, A. R.; Mosconi, E.; Meggiolaro, D.; De Angelis, F.; Soci, C.; Petrozza, A. *J. Am. Chem. Soc.* **2017**, *139*, 39–42.
- (10) Ni, L.; Huynh, U.; Cheminal, A.; Thomas, T. H.; Shivanna, R.; Hinrichsen, T. F.; Ahmad, S.; Sadhanala, A.; Rao, A. *ACS Nano* **2017**, *11*, 10834–10843.
- (11) Straus, D. B.; Iotov, N.; Gau, M. R.; Carroll, P. J.; Kagan, C. R. *Prep.*
- (12) Iaru, C. M.; Geuchies, J. J.; Koenraad, P. M.; Vanmaekelbergh, D.; Silov, A. Y. *ACS Nano* **2017**, *11*, 11024–11030.
- (13) Gebhardt, J.; Kim, Y.; Rappe, A. M. *J. Phys. Chem. C* **2017**, *121*, 6569–6574.
- (14) Du, K.-Z.; Wang, X.; Han, Q.; Yan, Y.; Mitzi, D. B. *ACS Energy Lett.* **2017**, *2*, 2486–2490.
- (15) Ma, D.; Fu, Y.; Dang, L.; Zhai, J.; Guzei, I. A.; Jin, S. *Nano Res.* **2017**, *10*, 2117–2129.

- (16) Calabrese, J.; Jones, N. L.; Harlow, R. L.; Herron, N.; Thorn, D. L.; Wang, Y. *J. Am. Chem. Soc.* **1991**, *113*, 2328–2330.
- (17) Knutson, J. L.; Martin, J. D.; Mitzi, D. B. *Inorg. Chem.* **2005**, *44*, 4699–4705.
- (18) Munson, K. T.; Kennehan, E. R.; Doucette, G. S.; Asbury, J. B. *Chem* **2018**, 1–18.
- (19) Neukirch, A. J.; Nie, W.; Blancon, J.-C.; Appavoo, K.; Tsai, H.; Sfeir, M. Y.; Katan, C.; Pedesseau, L.; Even, J.; Crochet, J. J.; Gupta, G.; Mohite, A. D.; Tretiak, S. *Nano Lett.* **2016**, *16*, 3809–3816.
- (20) Nishida, J.; Breen, J. P.; Lindquist, K. P.; Umeyama, D.; Karunadasa, H. I.; Fayer, M. D. *J. Am. Chem. Soc.* **2018**, *140*, 9882–9890.
- (21) Soufiani, A. M.; Huang, F.; Reece, P.; Sheng, R.; Ho-Baillie, A.; Green, M. A. *Appl. Phys. Lett.* **2015**, *107*, 231902.
- (22) Zhu, H.; Miyata, K.; Fu, Y.; Wang, J.; Joshi, P. P.; Niesner, D.; Williams, K. W.; Jin, S.; Zhu, X.-Y. *Science* **2016**, *353*, 1409–1413.
- (23) Hong, X.; Ishihara, T.; Nurmikko, A. V. *Phys. Rev. B* **1992**, *45*, 6961–6964.
- (24) Varshni, Y. *Physica* **1967**, *34*, 149–154.
- (25) Gibbs, Z. M.; Kim, H.; Wang, H.; White, R. L.; Drymiotis, F.; Kaviany, M.; Jeffrey Snyder, G. *Appl. Phys. Lett.* **2013**, *103*, DOI: 10.1063/1.4858195.
- (26) Piccioli, N.; Besson, J.; Balkanski, M. *J. Phys. Chem. Solids* **1974**, *35*, 971–977.
- (27) Ravindra, N. M.; Auluck, S.; Srivastava, V. K. *Phys. Status Solidi* **1979**, *52*, K151–K155.
- (28) Dittrich, T.; Awino, C.; Prajongtat, P.; Rech, B.; Lux-Steiner, M. C. *J. Phys. Chem. C* **2015**, *119*, 23968–23972.

- (29) Wright, A. D.; Verdi, C.; Milot, R. L.; Eperon, G. E.; Pérez-Osorio, M. A.; Snaith, H. J.; Giustino, F.; Johnston, M. B.; Herz, L. M. *Nat. Commun.* **2016**, *7*, 11755.
- (30) Nitzan, A., *Chemical Dynamics in Condensed Phases*; Oxford University Press: New York, 2006.
- (31) Yang, Y.; Ostrowski, D. P.; France, R. M.; Zhu, K.; van de Lagemaat, J.; Luther, J. M.; Beard, M. C. *Nat. Photonics* **2015**, *10*, 53–59.
- (32) Smith, M. D.; Karunadasa, H. I. *Acc. Chem. Res.* **2018**, *51*, 619–627.
- (33) Diroll, B. T.; Turk, M. E.; Gogotsi, N.; Murray, C. B.; Kikkawa, J. M. *ChemPhysChem* **2016**, *17*, 759–765.
- (34) Abram, R.; Rees, G.; Wilson, B. *Adv. Phys.* **1978**, *27*, 799–892.
- (35) Emin, D.; Holstein, T. *Phys. Rev. Lett.* **1976**, *36*, 323–326.
- (36) Chemla, D.; Miller, D.; Smith, P.; Gossard, A.; Wiegmann, W. *IEEE J. Quantum Electron.* **1984**, *20*, 265–275.
- (37) Rudin, S.; Reinecke, T. L.; Segall, B. *Phys. Rev. B* **1990**, *42*, 11218–11231.
- (38) Dammak, T.; Koubaa, M.; Boukheddaden, K.; Bougzhala, H.; Mlayah, A.; Abid, Y. *J. Phys. Chem. C* **2009**, *113*, 19305–19309.
- (39) Becker, M. A. et al. *Nature* **2018**, *553*, 189–193.
- (40) Veldhuis, S. A.; Boix, P. P.; Yantara, N.; Li, M.; Sum, T. C.; Mathews, N.; Mhaisalkar, S. G. *Adv. Mater.* **2016**, *28*, 6804–6834.

Chapter 9

Concluding Remarks

This dissertation highlights the broadly tunable properties of quantum-confined systems. In Part I, we study zero-dimensional quantum dots (QDs), which exhibit a size-tunable band gap and large surface-to-volume ratio (Chapter 1) . While these traits allow for widely tunable optical and electronic properties, they also introduce many challenges, including how to best assemble and couple QDs to allow for efficient charge transport and how to passivate surface defects that lower the mobility and lifetime of charge carriers.

Chapter 2 describes the time-resolved microwave conductivity (TRMC) technique, which allows us to measure the mobility and lifetime of photogenerated carriers in semiconductors without needing to apply contacts or large electric fields, and we apply TRMC to QD assemblies in Chapters 3 and 4 and correlate the TRMC mobility and lifetime with more conventional field-effect transistor measurements.

In Chapter 3, we treat PbSe QD assemblies with the metal salts Na_2Se and PbCl_2 to vary the Pb:Se ratio in the QDs. Se-rich QDs are *p*-type and Pb-rich QDs are *n*-type, and we sweep the Fermi level from the valence to the conduction band and

measure the carrier mobility and lifetime. We demonstrate that moving the Fermi level closer to the valence or conduction band improves the mobility and lifetime of photogenerated charge carriers by electronically passivating defect states. Similarly, in Chapter 4, we dope CdSe QD assemblies with increasing amounts of indium and find that the field-effect and TRMC mobilities and TRMC lifetime increase with doping. Our findings reinforce that passivating surface defects and doping CdSe QD assemblies with indium increases the photogenerated carrier mobility and lifetime. These two studies indicate that surface passivation and doping are general methods to improve carrier transport in QD assemblies.

Part II examines two-dimensional organic-inorganic hybrid perovskites (2DHPs), which have fascinating optical and electronic properties owing in part to the contrast between the soft, heavy, ionic inorganic lattices as well as the much lighter, covalently bonded organic framework (Chapter 5). While carriers reside in the inorganic framework, the organic layers provide strong quantum and dielectric confinement effects for the carriers. In Chapter 6, we elucidate the complex relationship between the organic and inorganic frameworks using the 2DHP phenethylammonium lead iodide ((PEA)₂PbI₄). We find that at temperatures <75 K, strong fine structure resonances appear in the excitonic absorption and photoluminescence spectra, which result from the exciton coupling to vibrations located exclusively on the organic cations. We also observe hot exciton photoluminescence out of excited vibrational levels. Our findings illustrate that although carriers are confined to the inorganic framework, the organic framework is not inert and interacts with excitons.

In Chapter 7, we synthesize a family of (PEA)₂PbI₄ derivatives with longer, heavier cations that do not significantly change the inorganic framework. We find that intermolecular interactions between adjacent cations can be used to template the organic framework, yielding either a herringbone or face-on orientation of the

cations. Longer cations increase the energetic disorder in 2DHPs, proving that the organic cation can be used to tailor the optoelectronic properties of 2DHPs without perturbing the metal-halide octahedra. We also find that the predominant phonon mode that couples to the exciton in $(\text{PEA})_2\text{PbI}_4$ and these derivatives is not strongly sensitive to these cation modifications and is likely a twisting mode of the aromatic moiety of the cation.

Lastly, in Chapter 8, we investigate $(\text{PEA})_2\text{PbI}_4$ derivatives with wider cations, which strain the inorganic framework. These substitutions greatly increase the moment of inertia of the cation and decrease the energy of the phonon mode that causes excitonic fine structure. In 2-chloro- and 2-fluorophenethylammonium lead iodide, we increase the proportion of hot exciton photoluminescence by over an order of magnitude compared to $(\text{PEA})_2\text{PbI}_4$, further proving the importance of the cation on excitons in 2DHPs because in addition to altering the energy landscape (Chapter 7), the cation can be used to change the dynamics of excitons.

These and many other discoveries may realize the promise of quantum-confined materials including QDs and 2DHPs for next generation optical and electronic devices.

Appendices

Appendix A

Additional Tables

Table A.1: Complete SCXRD cell information, data collection parameters, and refinement data for structures in Chapter 7.

Empirical formula	C ₁₆ H ₂₄ I ₄ N ₂ Pb	C ₁₆ H ₂₄ I ₄ N ₂ Pb	C ₁₆ H ₂₂ F ₂ I ₄ N ₂ Pb	C ₁₆ H ₂₂ Cl ₂ I ₄ N ₂ Pb	C ₁₈ H ₂₈ I ₄ N ₂ Pb	C ₁₆ H ₂₂ Br ₂ I ₄ N ₂ Pb
Formula weight	959.16	959.16	995.14	1028.04	987.21	1116.96
Temperature/K	100	300	100	100	100	100
Crystal system	triclinic	triclinic	monoclinic	monoclinic	triclinic	monoclinic
Space group	P $\bar{1}$	P $\bar{1}$	P21/c	C2/c	P $\bar{1}$	C2/c
a	8.6863(2) Å	8.7437(2) Å	16.548(2) Å	33.3256(17) Å	6.1306(2) Å	34.1474(13) Å
b	8.6856(2) Å	8.7437(2) Å	8.5712(10) Å	8.6453(4) Å	6.1143(2) Å	8.6378(4) Å
c	32.3872(8) Å	33.0253(6) Å	8.7339(10) Å	8.7179(4) Å	17.5420(5) Å	8.6862(4) Å
α	85.2360(10)°	84.6160(9)°			81.582(2)°	
β	85.2760(10)°	84.6307(9)°	99.606(6)°	93.002(2)°	79.945(2)°	91.890(2)°
γ	89.4460(10)°	89.6320(9)°			89.980(2)°	
Volume	2426.75(10) Å ³	2502.68(9) Å ³	1221.4(2) Å ³	2508.3(2) Å ³	640.26(4) Å ³	2560.67(19) Å ³
Z	4	4	2	4	1	4
d_{calc}	2.625 g/cm ³	2.546 g/cm ³	2.706 g/cm ³	2.722 g/cm ³	2.560 g/cm ³	2.897 g/cm ³
μ	12.042 mm ⁻¹	11.677 mm ⁻¹	11.979 mm ⁻¹	11.867 mm ⁻¹	11.415 mm ⁻¹	14.536 mm ⁻¹
F(000)	1712	1712	888	1840	444	1984
Crystal size, mm	0.1 × 0.06 × 0.04	0.1 × 0.06 × 0.04	0.09 × 0.08 × 0.02	0.09 × 0.08 × 0.04	0.05 × 0.03 × 0.02	0.09 × 0.03 × 0.02
2θ range for data collection	4.706 - 55.386°	4.68 - 55.056°	2.496 - 55.122°	2.448 - 54.982°	4.77 - 54.99°	2.386 - 55.148°
Index ranges	-11 ≤ h ≤ 11, -11 ≤ k ≤ 11, -42 ≤ l ≤ 42	-11 ≤ h ≤ 11, -11 ≤ k ≤ 11, -42 ≤ l ≤ 42	-21 ≤ h ≤ 21, -11 ≤ k ≤ 10, -11 ≤ l ≤ 11	-43 ≤ h ≤ 43, 0 ≤ k ≤ 11, 0 ≤ l ≤ 11	-7 ≤ h ≤ 7, -7 ≤ k ≤ 7, -22 ≤ l ≤ 22	-44 ≤ h ≤ 40, -11 ≤ k ≤ 11, -11 ≤ l ≤ 11
Reflections collected	43310	44429	19063	21704	9054	31625
Independent reflections	11303[R(int) = 0.0367]	11511[R(int) = 0.0719]	2804[R(int) = 0.0500]	2885[R(int) = 0.0495]	2908[R(int) = 0.0457]	2955[R(int) = 0.0534]
Data/restraints/parameters	11303/456/378	11511/444/396	2804/0/116	2885/0/117	2908/103/184	2955/0/116
Goodness-of-fit on F²	1.11	0.921	1.083	1.242	1.064	1.014
Final R indexes [I ≥ 2σ (I)]	R ₁ = 0.0438, wR ₂ = 0.1088	R ₁ = 0.0488, wR ₂ = 0.1198	R ₁ = 0.0227, wR ₂ = 0.0497	R ₁ = 0.0266, wR ₂ = 0.0838	R ₁ = 0.0371, wR ₂ = 0.0831	R ₁ = 0.0198, wR ₂ = 0.0428
Final R indexes [all data]	R ₁ = 0.0529, wR ₂ = 0.1135	R ₁ = 0.0850, wR ₂ = 0.1315	R ₁ = 0.0313, wR ₂ = 0.0523	R ₁ = 0.0299, wR ₂ = 0.0928	R ₁ = 0.0471, wR ₂ = 0.0869	R ₁ = 0.0265, wR ₂ = 0.0447
Largest diff. peak/hole	3.53/-2.41 eÅ ⁻³	3.20/-2.08 eÅ ⁻³	1.17/-0.93 eÅ ⁻³	2.09/-2.62 eÅ ⁻³	3.81/-1.93 eÅ ⁻³	1.55/-0.75 eÅ ⁻³

Table A.2: Parameters for fits in Figure 7.10. Omitted errors for center and σ are less than instrumental uncertainty (0.0002 eV in absorption and 0.001 eV in PL).

	Absorption			Photoluminescence		
	Center (eV)	σ (eV)	Area (a.u.)	Center (eV)	σ (eV)	Area (a.u.)
4-H	2.3513	0.0105	0.01527(6)	1.899(1)	0.159(1)	0.0306(2)
	2.3926	0.0075	0.00294(5)	2.3	0.014	0.0203(1)
	2.4338(8)	0.003(1)	0.00009(3)	2.319	0.005	0.0044(1)
				2.333	0.005	0.0080(5)
				2.341	0.008	0.00419(5)
				2.387	0.005	0.00014(2)
				2.430(3)	0.004(3)	0.00002(2)
4-F	2.3526	0.0072(3)	0.0030(4)	1.919	0.228	0.0683(2)
	2.3607(3)	0.0107(5)	0.0060(7)	2.299	0.007	0.0027(3)
	2.3752(8)	0.0241	0.0068(5)	2.305	0.019	0.0346(3)
				2.338	0.009	0.0064(4)
				2.345	0.005	0.0078(3)
4-Cl	2.3529	0.0083	0.00117(6)	1.86	0.163	0.2430(5)
	2.3758(6)	0.0208(6)	0.0029(2)	2.301(2)	0.043(2)	0.016(1)
	2.3909(8)	0.0405(5)	0.0046(2)	2.305	0.014	0.021(1)
				2.342	0.007	0.0156(5)
				2.326	0.006	0.0037(7)
4-Me	2.3490(3)	0.0128(5)	0.0010(1)	1.873(1)	0.175(2)	0.128(1)
	2.376(1)	0.024(1)	0.0028(2)	2.300(3)	0.015(2)	0.018(7)
	2.401(1)	0.0500(5)	0.0044(1)	2.308(3)	0.033(5)	0.020(8)
				2.333(2)	0.013(2)	0.021(3)
				2.338	0.005(1)	0.003(2)
4-Br	2.3579	0.0123(4)	0.0016(1)	1.864(2)	0.166(3)	0.128(2)
	2.382(1)	0.0235(7)	0.0036(2)	2.299(9)	0.016(8)	0.02(2)
	2.4054	0.0513(5)	0.0053(1)	2.309(5)	0.033	0.022(2)
				2.315(2)	0.007(3)	0.005(5)
				2.337(1)	0.012(1)	0.022(5)

Table A.3: Parameters for PL fits in Figure 7.12. Omitted errors for center and σ are less than instrumental uncertainty (0.001 eV).

	Center (eV)	σ (eV)	Area (a.u.)
4-H	1.900(2)	0.159(2)	0.0304(4)
	2.299	0.014	0.0190(3)
	2.321	0.008	0.0076(4)
	2.339	0.006	0.0146(2)
	2.387(2)	0.005(2)	0.00014(4)
	2.430(7)	0.004(7)	0.00002(4)
4-F	1.922	0.23	0.0688(2)
	2.303	0.016	0.0339(2)
	2.336	0.01	0.0092(2)
	2.345	0.005	0.0080(2)
4-Cl	1.86	0.164	0.2442(6)
	2.3	0.006	0.0022(3)
	2.313	0.026	0.0424(5)
	2.342	0.006	0.0102(3)
4-Me	1.874(1)	0.127	0.175(2)
	2.305(1)	0.018(1)	0.023(9)
	2.312(3)	0.032(5)	0.02(1)
	2.336	0.01	0.016(2)
4-Br	1.864(2)	0.167(3)	0.128(2)
	2.31(1)	0.025(4)	0.04(2)
	2.334(6)	0.016(8)	0.02(2)
	2.340(1)	0.007(2)	0.005(4)

Appendix B

List of Publications

D. B. Straus, S. Hurtado Parra, N. Iotov, R. Fei, J. Zhang, A. M. Rappe, J. M. Kikkawa, C. R. Kagan. “Controlling Hot Exciton Photoluminescence, Vibrational Relaxation, and Phonon Energies Through Cation Modification in Two-Dimensional Hybrid Perovskites,” *In Preparation*.

D. B. Straus, M. Gau, R. Fei, J. Zhang, A. M. Rappe, P. J. Carroll, C. R. Kagan. “Temperature-Dependent Structural and Optical Properties of Two-Dimensional Hybrid Perovskites,” *In Preparation*.

D. B. Straus, T. Zhao, G. Liu, C. R. Kagan. “Rate Constants for Photogenerated Carrier Recombination in PbS Quantum Dot Thin Films,” *In Preparation*.

H. Wang, D. J. Butler, D. B. Straus, N. Oh, F. Wu, J. Guo, K. Xue, J. Lee, C. B. Murray, C. R. Kagan. “Air-Stable CuInSe₂ Nanocrystal Transistors and Circuits *via* Post-Deposition Cation Exchange,” *In Preparation*.

D. B. Straus, N. Iotov, M. R. Gau, P. J. Carroll, A. M. Rappe, C. R. Kagan.

“Tailoring the Organic Framework and Energetic Disorder in Excitonic 2D Hybrid Perovskites,” *Submitted*.

D. B. Straus, C. R. Kagan. “Electrons, Excitons, and Phonons in Two-Dimensional Hybrid Perovskites: Connecting Structural, Optical, and Electronic Properties,” *J. Phys. Chem. Lett.* **9** 1434 (2018). DOI: 10.1021/acs.jpcclett.8b00201

G. A. Elbaz, D. B. Straus, O. E. Semonin, T. D. Hull, D. W. Paley, P. Kim, J. S. Owen, C. R. Kagan, X. Roy. “Unbalanced Hole and Electron Diffusion in Lead Halide Perovskites,” *Nano Lett.* **17** 1727 (2017). DOI: 10.1021/acs.nanolett.6b05022

S. J. Oh, D. B. Straus, T. Zhao, J.-H. Choi, S.-W. Lee, E. A. Gaulding, C. B. Murray, C. R. Kagan. “Engineering the Surface Chemistry of Lead Chalcogenide Nanocrystal Solids to Enhance Carrier Mobility and Lifetime in Optoelectronic Devices,” *Chem. Commun.* **53** 728 (2017). DOI: 10.1039/C6CC07916D

D. B. Straus, S. Hurtado Parra, N. Iotov, J. Gebhardt, A. M. Rappe, J. E. Subotnik, J. M. Kikkawa, C. R. Kagan. “Direct Observation of Electron-Phonon Coupling and Slow Vibrational Relaxation in Organic-Inorganic Hybrid Perovskites,” *J. Am. Chem. Soc.* **138** 13798 (2016). DOI: 10.1021/jacs.6b08175

O. E. Semonin, G. A. Elbaz, D. B. Straus, T. D. Hull, D. W. Paley, A. M. van der Zande, J. C. Hone, I. Kymissis, C. R. Kagan, X. Roy, J. S. Owen. “Limits of Carrier Diffusion in *n*-Type and *p*-Type CH₃NH₃PbI₃ Perovskite Single Crystals,” *J. Phys. Chem. Lett.* **7** 3510 (2016). DOI: 10.1021/acs.jpcclett.6b01308

D. B. Straus^{*}, E. D. Goodwin^{*}, E. A. Gaulding, S. Muramoto, C. B. Murray, C. R. Kagan. “Increased Carrier Mobility and Lifetime in CdSe Quantum Dot Thin Films through Surface Trap Passivation and Doping,” *J. Phys. Chem. Lett.* **6** 4605

(2015). DOI: 10.1021/acs.jpcllett.5b02251 (* Equal Contribution)

F. S. Stinner, Y. Lai, D. B. Straus, B. T. Diroll, D. K. Kim, C. B. Murray, C. R. Kagan. “Flexible, High-Speed CdSe Nanocrystal Integrated Circuits,” *Nano Lett.* **6** 7155 (2015). DOI: 10.1021/acs.nanolett.5b03363

E. D. Goodwin*, D. B. Straus*, E. A. Gaulding, C. B. Murray, C. R. Kagan. “The Effects of Inorganic Surface Treatments on Photogenerated Carrier Mobility and Lifetime in PbSe Quantum Dot Thin Films,” *Chem. Phys.* **471** 81 (2016). DOI: 10.1016/j.chemphys.2015.07.031 (* Equal Contribution)

Appendix C

List of Figures

2.1	Rendering of the TRMC resonant cavity.	15
2.2	Schematic of the TRMC experiment.	18
2.3	Resonant microwave peak for the cavity loaded with a sample. The data are shown in blue, and the Lorentzian fit in red.	19
2.4	Simulated electric field distribution in TRMC resonant cavity.	23
2.5	Sensitivity constant K for a 1000 nm thick film with varying dielectric (ϵ_r) and σ_0 calculated by simulating $\Delta\sigma_{\text{sim}} = 0.01$ S/m.	25
2.6	A crystal of the perovskite methylammonium lead iodide attached to a glass substrate using double-sided Scotch tape. The width of the substrate is 25.2 mm.	27
2.7	Simulated electric field distribution for the crystal in Figure 2.6.	27
3.1	Deconvolution. The original TRMC trace is in blue, and the deconvolved sample response is in red.	40

3.2	<p>(a-d) TEM images and normalized (e) FTIR and (f) NIR absorption spectra of (a) an OA-capped PbSe QD thin film (black) and of PbSe QD thin films treated with (b) MPA (orange), (c) Na₂Se (red), and Na₂Se immediately followed by PbCl₂ for 1 min (green), 15 min (cyan), 1 h (blue), and 24 h (pink). The PbSe QD film shown in (d) is treated for 1 h in PbCl₂ immediately after Na₂Se treatment. Scale bars are 6 nm. (e) Inset: FTIR spectra highlighting the OA-capped PbSe QD thin film (black). Fourier-transform filtering is applied to the NIR absorption spectra to remove the interference pattern caused by the cover glass-QD film-glass stack.</p>	42
3.3	<p>(a) Diagram of a bottom-gate, top-contact FET fabricated from PbSe QD thin films. (b) Transfer curves of PbSe QD thin films treated with MPA (orange), Na₂Se (red), and Na₂Se followed by PbCl₂ for 1 min (green), 15 min (cyan), 1 h (blue), and 24 h (pink). $V_{DS} = -50$ V for QD thin films treated with Na₂Se and Na₂Se followed by PbCl₂ for 1 min and 15 min. $V_{DS} = +50$ V for QD thin films treated with MPA and Na₂Se followed by PbCl₂ for 1 h and 24 h.</p>	43

3.4	<p>(a) Diagram of the home-built, TRMC setup showing the VCO: voltage controlled oscillator (microwave source), I: isolator, At: 10dB attenuator, C: microwave circulator, microwave switch, spectrum analyzer, D: microwave power detector, A: amplifier, HP: high pass filter, S: oscilloscope, and computer. Also shown is the laser (532 nm) and optics for controlling and delivering the light to the sample. WP: rotating half wave plate, P: polarizer, BD: beam dump, FS: UV-fused silica window, and P M: power meter. (b) Example photoconductance transients of PbSe QD thin films treated with Na₂Se (red) and Na₂Se followed by PbCl₂ for 1 min (green), 15 min (cyan), 1 h (blue), and 24 h (pink). Inset: Photoconductance transient of MPA (orange) treated PbSe QD thin film. Dashed lines show fits (see text for details).</p>	44
3.5	<p>(a) $\phi\Sigma\mu$ product at the lowest photoexcitation density in PbSe QD thin films treated with MPA (orange), Na₂Se (red), Na₂Se followed by PbCl₂ for 1 min (green), 15 min (cyan), 1 h (blue), and 24 h (pink). (b) Photogenerated charge carrier lifetimes from nonlinear least-squares fits of the photoconductance transient data to: the sum of three exponential decay functions for MPA, Na₂Se, and Na₂Se followed by 1 min PbCl₂-treated (black, red, and blue showing lifetimes on the order of 100 ns, 1 μs, and 10 μs, respectively) and single exponential decay functions for Na₂Se followed by 15 min, 1 h and 24 h PbCl₂-treated PbSe QD thin films. Error bars are one standard deviation.</p>	45
3.6	<p>$\phi\Sigma\mu$ product vs photoexcitation density in PbSe QD thin films treated with MPA (orange), Na₂Se (red), Na₂Se followed by PbCl₂ for 1 min (green), 15 min (cyan), 1 h (blue), and 24 h (pink).</p>	46

3.7	Photogenerated charge carrier lifetimes from nonlinear least-squares fits of photoconductance transient data to the sum of three exponential decay functions for Na ₂ Se (red), and Na ₂ Se followed by 1 min PbCl ₂ (green) treatments and to a single exponential decay function for Na ₂ Se followed by PbCl ₂ treatment for 15 min (cyan), 1 h (blue) and 24 h (pink) of PbSe QD thin films. Lifetimes on the order of 100 ns are shown in (a), 1 μs in (b), and 10 μs in (c). Error bars are one standard deviation.	49
3.8	Photogenerated charge carrier lifetimes from nonlinear least-squares fits of photoconductance transient data to the sum of three exponential decay functions for MPA treated PbSe QD films. The shortest lifetime is shown in blue, the intermediate in green, and long in red. Error bars are one standard deviation.	50
3.9	NIR absorption measurements of PbSe QD films immediately after Na ₂ Se treatment (maroon), after Na ₂ Se treatment and storage in a nitrogen glovebox for 6 h (red), after Na ₂ Se treatment followed by immediate PbCl ₂ treatment for 1 h (blue), and after Na ₂ Se treatment and storage in a nitrogen glovebox for 24 h followed by 1 h PbCl ₂ treatment (light blue).	51
3.10	Quantum yield-mobility product for samples shown in Figure 3.9. . .	51
4.1	Frequency response (blue) of the fifth order Butterworth filter. A 40 MHz to 50 MHz cutoff frequency is used to filter the data. The cutoff frequency (here, 50 MHz) is shown in black.	63

4.2	Reflected microwave power transients as measured in TRMC showing the as-measured transient (blue), the transient after application of a Butterworth filter (black), and the sample response transient determined by deconvolution of the resonant cavity response from the filtered transient (green). Fit by non-linear least squares regression to a single exponential decay function of the deconvolved sample response transient (red).	63
4.3	Fourier transform infrared absorption spectra of as-synthesized, organic-capped CdSe QD film (light grey) and SCN-capped CdSe QD film (dark grey).	64

4.4 (a) Schematic of thermally-driven doping of evaporated indium onto SCN-capped, CdSe QD thin films. (b) Transmission electron micrographs of SCN-capped, CdSe QD assemblies that are annealed at 300 °C for 20 min in the absence (i) and presence (ii) of indium. Scale bars are 5 nm. (c) UV-Vis absorption spectra of CdSe QD thin films that are organic-capped (light grey), SCN-capped (dark grey) and SCN-capped and annealed at 300 °C for 20 min with 0 nm (black) and 5 nm (green) of evaporated indium. (d) XPS measurements monitoring the intensity of the indium 3d signal in SCN-capped, CdSe QD thin films doped with 0 nm to 11 nm of indium and annealed at 300 °C for 20 min. A linear fit to the XPS thickness is shown in red. Uncertainties represent standard deviations of three measurements. Inset: SIMS depth profile showing the intensity of the InO^{2-} ion as a function of depth into the CdSe QD thin film doped with 11 nm of indium and annealed at 300 °C for 20 min. The QD films are exposed to air for several days before SIMS measurements, and the InO^{2-} intensity represents that the indium has oxidized. 65

4.5 UV-Vis-NIR absorption spectra of SCN-capped CdSe QD films with a nominal thickness of 0 nm (black), 1 nm (red), 3 nm (orange), 5 nm (green), 7 nm (blue), 9 nm (purple), and 11 nm (pink) of indium after being annealed at 300 °C for 20 min. 66

4.6	(a) Transfer characteristics ($I_D - V_G$) and (b) FET mobilities of SCN-capped, CdSe QD thin films annealed at 300 °C for 20 min with nominal thicknesses of 0 nm (black), 1 nm (red), 3 nm (orange), 5 nm (green), 7 nm (blue), 9 nm (purple), and 11 nm (pink) of deposited indium. Uncertainties represent standard deviations of at least three measurements.	67
4.7	On/off ratio for CdSe QD thin film field effect transistors doped with a nominal thickness of 0 nm (black), 1 nm (red), 3 nm (orange), 5 nm (green), 7 nm (blue), 9 nm (purple), and 11 nm (pink) of indium after being annealed at 300 °C for 20 min. Uncertainties represent standard deviations of at least three measurements.	69
4.8	(a, b) Transfer characteristics (ID-VG) from Figure 4.6, reproduced on a linear scale, for SCN-capped, CdSe QD thin films annealed at 300 °C for 20 min with 0 nm (black), 1 nm (red), 3 nm (orange), 5 nm (green), 7 nm (blue), 9 nm (purple), and 11 nm (pink) of deposited indium.	69
4.9	TRMC (a) lifetime and (b) mobility for SCN-capped, CdSe QD thin films annealed at 300 °C for 20 min with nominal thicknesses of 0 nm (black), 1 nm (red), 3 nm (orange), 5 nm (green), 7 nm (blue), 9 nm (purple), and 11 nm (pink) of deposited indium. Uncertainties represent standard deviations of at least three measurements.	70
4.10	(a, b) Representative, deconvolved TRMC transients for CdSe QD thin films doped with 0 (black), 1 (red), 3 (orange), 5 (green), 7 (blue), 9 (purple), and 11 nm (pink) of indium. Single exponential fits are shown in gray.	71

4.11	(a) TRMC mobility-quantum yield product as a function of photoexcitation density product for CdSe QD thin films doped with 0 (black), 1 (red), 3 (orange), 5 (green), 7 (blue), 9 (purple) nm of indium, and 11 nm (pink) of indium at higher fluence, and (b) 11 nm at lower fluence. Uncertainties represent standard deviations of at least three measurements.	72
5.1	A) Schematic of a projection of the 3D hybrid perovskite, showing an inorganic network of corner sharing metal halide octahedra (red) with interstitial organic cations (blue, black). (green) Highlighting the restriction on cation size. B) Schematic of a projection down the <i>c</i> -axis of the 2D hybrid perovskite, showing the alternation of organic (blue, black) and corner-sharing inorganic (red) layers for $n = 1$ with inorganic layer thickness d and organic layer thickness L . (green) Highlighting the restriction solely on the cross-sectional area, but not the length of the organic cation. C) Energy diagram corresponding to the 2D structure in B). Labeling of the valence band VB, conduction band CB, electronic band gap E_g (grey) and the optical band gap E_{exc} (blue) of the inorganic framework, and the larger HOMO-LUMO gap of the organic cations (green). The organic framework (grey regions) has a dielectric constant ϵ_2 , which is smaller than the dielectric constant ϵ_1 of the inorganic framework (red regions).	80

5.2	A) Schematic showing distortion in the metal-halide framework to accommodate an organic cation with a larger cross-sectional area. B) Experimental energies of the excitonic absorption in (PEA) ₂ SnI ₄ -based 2D perovskites with functionalized cations that exhibit solely in-plane distortion (blue) and a combination of in- and out-of-plane distortion (red).	87
6.1	Measured instrument response function (black) for the Kerr-gate TRPL. The response is modeled as and fit to the convolution of a Gaussian with an exponential rise (blue).	102
6.2	(A) Schematic projection of the layered (PEA) ₂ PbI ₄ structure composed of lead iodide corner sharing octahedra (red) separated by phenethyl- (black) ammonium (blue) cations. Room temperature (B) absorption (black) and PL (blue) spectra.	104
6.3	X-ray diffraction pattern in $\theta - 2\theta$ geometry using Cu- $k\alpha$ radiation of a (PEA) ₂ PbI ₄ thin film deposited on a sapphire substrate. Bragg analysis yields an interlayer spacing of 1.64 nm, consistent with previous measurements for (PEA) ₂ PbI ₄	105
6.4	Room temperature (A) absorption (black) and (B) PL spectra of (PEA) ₂ PbI ₄ thin films. Spectra are fit to a Lorentzian (blue, dashed), and a linear background is used to fit absorption.	105
6.5	(A) Room temperature TRPL spectrum. Each time bin is fit to a single Lorentzian. (B) Integral of Lorentzian fit at each time (grey) fit to single exponential convolved with the instrument response (Figure 6.1) (black).	106

6.6	(A) 15K absorption (black) and PL (blue) spectra plotted on a linear and (inset) logarithmic scale to highlight the broad PL centered at 1.93 eV. (B) Excitonic absorption (black) and PL (blue) and PL $\times 60$ (purple) to highlight high energy structure. (C) The absorption spectrum in (B) fit to the sum of four Lorentzians with a linear baseline. (D) The PL spectrum in (B) fit to the sum of five Gaussians in addition to a linear term to correct for the slow rise of the broad feature at 1.93 eV. Inset resonances are fit separately from the three central peaks because of the large discrepancy in peak heights. The linear baseline is subtracted from the data in (C) and (D).	107
6.7	(A) PL spectra of a $(\text{PEA})_2\text{PbI}_4$ thin film at temperatures between 20 K and 300 K excited at 400 nm, using the Xe arc lamp in combination with the monochromator of the Fluorolog FL-3. (B) Highlight of the hot excitonic PL peaks. (C) Absorption spectra at temperatures between 20 K and 300 K.	108
6.8	15 K PL spectrum of a $(\text{PEA})_2\text{PbI}_4$ thin film excited at 2.40 eV (dashed black). The emission spectrum is fit (grey) to the sum of three Gaussians. The peaks are centered at 2.351 eV (red), 2.337 eV (orange), and 2.311 eV (maroon).	110

6.9	(A) Schematic detailing low temperature absorption and PL processes α (blue arrows), β (green arrows), γ (red arrows), and δ (maroon arrow) in $(\text{PEA})_2\text{PbI}_4$. δ is only shown in PL because there is no corresponding absorption. Nonradiative relaxation between vibrational states is shown by black curved arrows. (B) Computed phonon modes below 50 meV, with contributions from the Pb-I cage (blue) and the organic cations (green). EPC is shown in red. (C)(i) 41 meV phonon modes are rotation of NH_3^+ and phenyl moieties. (ii) 49 meV phonons are out-of-plane bending of phenyl groups.	111
6.10	PLE spectra divided by absorbance of a $(\text{PEA})_2\text{PbI}_4$ thin film collected at 2.44 (blue), 2.40 (green), 2.35 (red), 2.31 (maroon), and 2.00 (black) eV. All are normalized to the number of counts at 2.45 eV except for the spectrum collected at 2.44 eV which is normalized such that its value at 2.59 eV is the same as that for the PLE spectrum collected at 2.40 eV.	112
6.11	PL spectrum of a $(\text{PEA})_2\text{PbI}_4$ thin film spun by dissolving synthesized crystals in acetonitrile (black) and by mixing phenethylammonium iodide with an excess of lead iodide in acetonitrile (blue). (B) 15 K PL spectra of a $(\text{PEA})_2\text{PbI}_4$ thin film spun by dissolving synthesized crystals in acetonitrile excited at 3.10 eV (black) and 2.40 eV (blue). .	112
6.12	(A) Pseudocolor plot of 15K TRPL. Each time bin is fit to the sum of Gaussians. (B) Integral of each peak plotted at each time and fit (black) to a single or double exponential. Shaded area is 95% confidence interval of fit.	115
6.13	15K TRPL of (A) γ (2.35 eV resonance) and (B) δ (2.31 eV resonance) emissions.	115

6.14	(A) 20K TRPL of the broad emission centered at 1.93 eV. The increased counts at 1.79 eV are Cr ₂ ⁺ impurities in the sapphire substrate. Each time bin is fit to a single Gaussian. (B) The integral of the Gaussian is plotted versus time and fit to a triple exponential decay (Table 6.3).	116
7.1	Unsmoothed (solid) and smoothed (dashed) 300 K PL spectra for 4-H (black), 4-F (red), 4-Cl (orange), 4-Me (green), and 4-Br (blue).	129
7.2	(A) Overlaid 100 K crystal structures of 4-H, 4-F, 4-Cl, and 4-Br. Disorder in iodine not shown for 4-H. (B) Interlayer spacings at 100 K from SCXRD structures (green circles), at room temperature from powder diffraction patterns (red circles), and at 300 K from SCXRD structure for 4-H (black diamond). (C) Comparison of organic framework packing and thickness in 4-H (black), 4-F (red) and 4-Br (blue). Disorder in iodine not shown for 4-H. Structures in (A, C) visualized using VESTA.	130
7.3	Drawings of SCXRD structure or asymmetric unit with 50% thermal ellipsoids for (A) 4-H (100 K), (B) 4-H (300 K), (C) 4-F, (D) 4-Cl, (E) 4-Me, and (F) 4-Br.	132
7.4	(A) Disordered cation in 4-Me, with (B) the four conformers shown individually.	132
7.5	Overlaid SCXRD structures of 4-Cl (orange) and 4-Me (green).	133
7.6	(A) Room temperature powder XRD patterns of thin films of 4-H (black), 4-F (red), 4-Cl (orange), 4-Me (green), and 4-Br (blue) deposited on sapphire. (B) Scherrer grain sizes determined from patterns in (A).	134

7.7	300 K excitonic absorption (A) and PL (B) spectra and (C) their overlay, highlighting resonance maxima, and 10K excitonic absorption (D) and PL (E) spectra and (F) their overlay, highlighting resonance maxima, for 4-H (black), 4-F (red), 4-Cl (orange), 4-Me (green), and 4-Br (blue). All PL spectra use 3.10 eV excitation.	135
7.8	Summary of (A) maximum, (B) FWHM, and (C) Stokes shift of excitonic absorption (circles) and PL (diamonds) spectra from Figure 2 at 300 K (red) and 10 K (blue). Error represents instrumental uncertainty.	135
7.9	10K absorption (black) and PL (blue, $\times 60$ in purple) spectra of (A) 4-H, (B) 4-F, (C) 4-Cl, (D) 4-Me, and (E) 4-Br.	137
7.10	Fits of 10K absorption (top) and PL (bottom) spectra of (A) 4-H, (B) 4-F, (C) 4-Cl, (D) 4-Me, and (E) 4-Br. Absorption spectra are fit to the sum of 3 Lorentzian (4-H and 4-F) or Gaussian (4-Cl, 4-Br, and 4-Me) functions. PL spectra are fit to the sum of 5 Gaussian functions (7 for 4-H to account for the hot excitonic PL resonances).	138
7.11	Summary of 10 K absorption (circles) and PL (diamonds) fits, with (A) selected resonance centers, (B) FWHM, and (C) Stokes shift.	138
7.12	Fits of 10 K PL spectra of (A) 4-H, (B) 4-F, (C) 4-Cl, (D) 4-Me, and (E) 4-Br to the sum of 4 Gaussian functions (6 for 4-H to account for the hot excitonic PL resonances), one fewer than in Figure 7.10.	139
7.13	Full 10 K (A) absorption and (B) PL spectra of 4-H (black), 4-F (red), 4-Cl (orange), 4-Me (green), and 4-Br (blue).	139
7.14	Absorption (top) and PL (bottom) spectra from 10 K to 300 K for (A) 4-H, (B) 4-F, (C) 4-Cl, (D) 4-Me, and (E) 4-Br.	140

7.15	Excitonic absorption maxima for 4-H (black), 4-F (red), 4-Cl (orange), 4-Me (green), and 4-Br (blue) (circles; error indicates instrumental uncertainty), with linear fit (dashed lines with one-sigma uncertainties shaded). (B) Results of fits shown in (A). Error indicates one-sigma confidence intervals from the linear regressions. (C) Excitonic absorption FWHM (circles) of 4-H (black), 4-F (red), 4-Cl (orange), 4-Me (green), and 4-Br (blue). Error indicates instrumental uncertainty. Fits to model are indicated by the dashed lines with one-sigma uncertainties shaded. (D) Extracted fit parameters E_{LO} (blue circles), γ_{LO} (orange circles), and Γ_0 (green circles) from absorption for 4-H (≥ 175 K), 4-F, 4-Cl, 4-Me, and 4-Br. Error indicates one-sigma confidence intervals from the nonlinear regressions.	140
7.16	(A) Temperature-dependent PL maxima for 4-H (black), 4-F (red), 4-Cl (orange), 4-Me (green), and 4-Br (blue). Error bars represent instrumental uncertainty. (B, C) Results from linear fits of data in (A). Error bars represent one-sigma confidence interval from the linear regressions.	142
7.17	(A) Temperature-dependent PL FWHM of 4-H (black), 4-F (red), 4-Cl (orange), 4-Me (green), and 4-Br (blue). Error bars represent instrumental uncertainty. (B) Γ_0 (green), γ_{LO} (orange), and E_{LO} from fits of data in (A) for 4-H, 4-F, and 4-Cl from 125 K to 300 K. Error bars represent one-sigma confidence interval from the nonlinear regressions.	146
7.18	Room temperature Raman scattering spectra (lines) of single crystals or powders of 4-H (black), 4-F (red), 4-Cl (orange), 4-Me (green), and 4-Br (blue), with computed Raman spectra of cation (bars). Pink bar indicates mode shown in Figure 7.19.	146

7.19	Ring twisting vibrational mode in (A) 4-H, (B) 4-F, (C) 4-Cl, (D) 4-Me, and (E) 4-Br cations. Circles in (B) highlight differences in 4-F vibrational mode.	148
8.1	Overlaid Pb-I frameworks of 2-H (red), 2-F (orange), 2-Cl (green), and 2-Br (blue).	161
8.2	Room-temperature powder diffraction patterns of 2-H (red), 2-F (orange), 2-Cl (green), and 2-Br (blue) thin films deposited on sapphire.	162
8.3	(A) Room-temperature absorption (solid) and PL (dashed) spectra of 2-H (red), 2-F (orange), 2-Cl (green), and 2-Br (blue). (B) Spectra with $E_{\text{max,abs}}$ subtracted from absorption and PL energy.	163
8.4	Temperature-dependent absorption spectra of 2-F (A), 2-Cl (B), and 2-Br (C). Temperature-dependent PL spectra of 2-F (D), 2-Cl (E), and 2-Br (F).	164
8.5	(A) 10 K absorption spectra of 2-H (red), 2-F (orange), 2-Cl (green), and 2-Br (blue), with fits of 2-H (B), 2-F (C), 2-Cl (D), and 2-Br (E). 10 K PL spectra (F), with fits of 2-H (G), 2-F (H), 2-Cl (I), and 2-Br (J). The zero of energy in each compound's absorption and PL fit is set as the center of the red resonance in absorption.	165
8.6	Transient absorption spectra ($\Delta t = 5$ ps) of (A) 2-Cl at 16 K and (B) 2-F at 15 K.	166
8.7	10 K PLE spectra of 2-F. The color of each spectrum represents the PL energy according to the resonances in Figure 8.5H. The blue spectrum is the PLE spectrum from the broad self-trapped excitonic PL resonance and is collected at 2.0 eV.	168

8.8	(A) 10K TRPL spectrum of 2-Cl. (B) Fit at $t = 0.19$ ps. (C) Centers of resonances over time. (D) Lifetime fits.	170
8.9	(A) 10K TRPL spectrum of 2-Br, with (B) lifetime fits and (C) centers.	170
8.10	Power-dependent 10K PL spectra of 2-Cl(A), 2-Br (B), and 2-H (C).	172

Appendix D

List of Tables

3.1	Summary of the quantum yield-mobility products ($\phi\Sigma\mu$) and the carrier lifetimes (s) extracted from TRMC transients of ligand exchanged PbSe QD thin films. $\phi\Sigma\mu$ shown is calculated at the lowest photoexcitation density.	47
4.1	Summary of FET and TRMC results. Uncertainties represent standard deviations of at least three measurements.	67
6.1	Parameters for 15 K absorption and PL lineshape fits for (PEA) ₂ PbI ₄ thin films. Uncertainties are 95% confidence intervals of the regressions, although transition centers are given to meV precision because regression uncertainty is smaller than calibration precision (0.5-1 meV).	109

6.2	Tabulated fit parameters for lifetime fits shown in Figure 6.9B. Picosecond time-resolved photoluminescence is fit to the function $(\sum_i A_i \exp(t/t_i)) * \text{IRF}$ where $*$ represents convolution and IRF is the instrument response function (Figure 6.1). Amplitudes are normalized to the $\gamma + \zeta_3$ amplitude. Uncertainties are 95% confidence interval of the regressions.	114
6.3	Tabulated fit parameters for TRPL of the broad feature at 1.93 eV. The integrated amplitude is fit to the function $A(t) = A_1 \exp(-\frac{t}{t_1}) + A_2 \exp(-\frac{t}{t_2}) + A_3 \exp(-\frac{t}{t_3})$. Uncertainties are 95% confidence interval of the regression.	116
7.1	Select crystallographic parameters from SCXRD structures.	131
7.2	Extracted parameters from broadening model applied to absorption spectra. The FWHM of 4-F, 4-Cl, 4-Me, and 4-Br are fit from 10 K to 300 K. The temperature-dependent FWHM of 4-H is discontinuous between 100 and 150 K, so we fit the FWHM from 175 K to 300 K.	143
7.3	Extracted parameters from broadening model applied to PL spectra. The FWHM are fit for temperatures from 125 K and 300 K.	145
8.1	Results from fitting temperature-dependent FWHM of 2-F, 2-Cl, and 2-Br to the model in Equation 7.1.	171
A.1	Complete SCXRD cell information, data collection parameters, and refinement data for structures in Chapter 7.	183
A.2	Parameters for fits in Figure 7.10. Omitted errors for center and σ are less than instrumental uncertainty (0.0002 eV in absorption and 0.001 eV in PL).	184

A.3 Parameters for PL fits in Figure 7.12. Omitted errors for center and σ
are less than instrumental uncertainty (0.001 eV). 185